TECHNOLOGY DRIVEN. WARFIGHTER FOCUSED.

EDGEWOOD CHEMICAL BIOLOGICAL CENTER

IN-HOUSE LABORATORY INDEPENDENT RESEARCH PROGRAM ANNUAL REPORT FY11

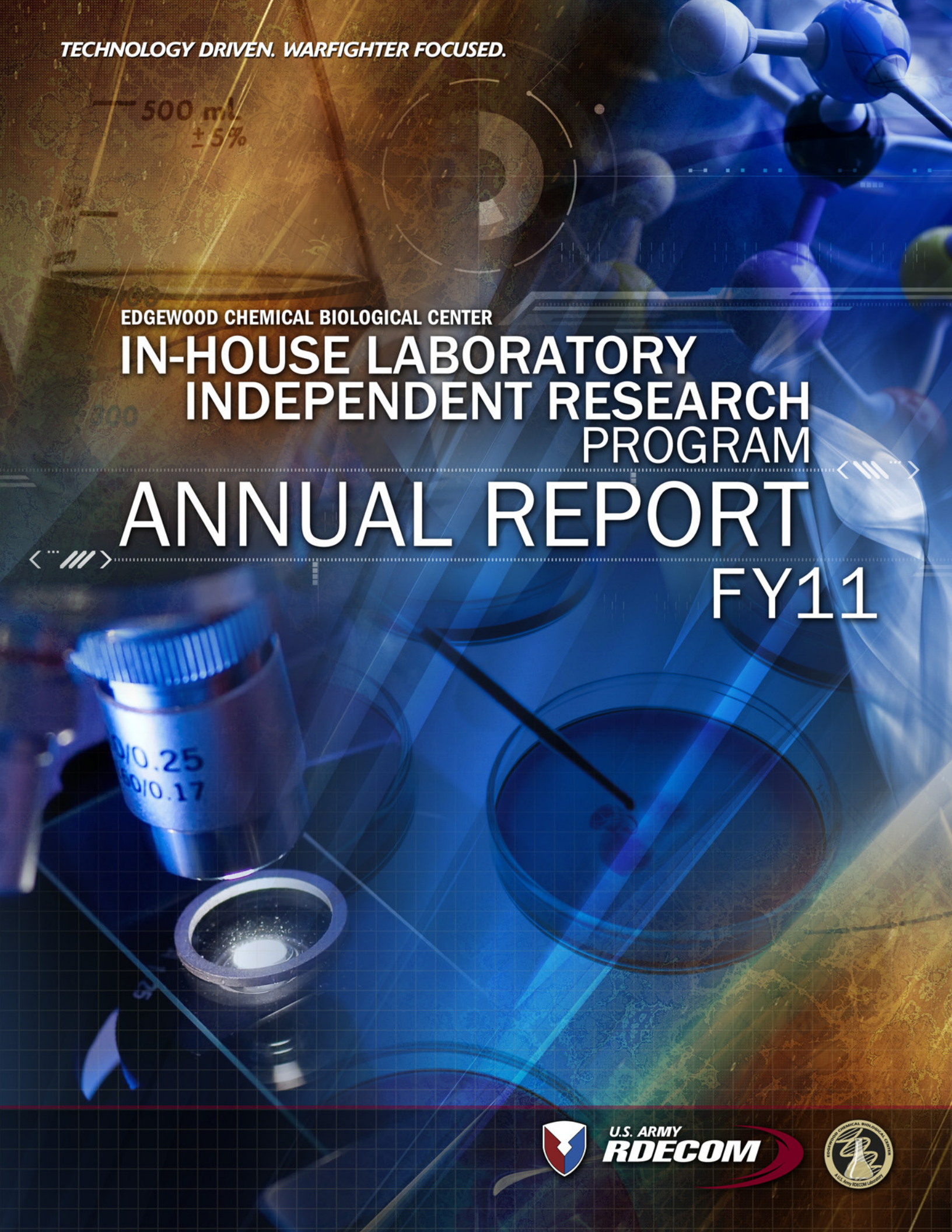

U.S. ARMY RDECOM

ECBC Strategic Mission and Vision

The U.S. Army Edgewood Chemical Biological Center (ECBC) functions as the nation's principal research, development, and engineering resource for non-medical chemical and biological warfare (CBW) defense applications. ECBC's mission is *to integrate life-cycle science, engineering, and operations solutions to counter CBRNE threats to U.S. forces and the nation.* This mission recognizes that ECBC's range of influence has grown to include military and homeland defense as well as expands research, development, and engineering needs beyond CB defense to include comparable technical solutions for radiological, nuclear, and explosives (RNE) hazards. ECBC's vision is *to be the premier resource for CBRNE solutions, uniting and informing the defense community*. As such, ECBC is charged with understanding the comprehensive threat to the warfighter and providing the scientific knowledge, technology, and materiel required to protect and enable the warfighter to effectively operate and implement strategic decisions while in the presence of CBW contamination.

ECBC's mission and vision are supported by the Center's core capabilities of research and technology, engineering, and program integration. The Research and Technology (R&T) capability provides integrated science and technology solutions that address CB defense knowledge gaps and vulnerabilities. The Center's R&T capability areas include Biosciences, CB Detection, CB Protection and Decontamination, Chemical Sciences, Physics, Computational Sciences, and Toxicology and Obscurants. Basic science research at ECBC contributes valuable information to the fundamental science knowledgebase, enabling the development of technologies that directly benefit the warfighter and further strengthen the Army's Science and Technology (S&T) mission. ECBC's unique set of core research and technology capabilities position it to be the Army's fundamental source of research in chemistry and biology.

ECBC ILIR Proposal Process

The In-House Laboratory Independent Research (ILIR) program is specifically designed to foster increased innovation within the ECBC Basic Research portfolio. The purpose of the ILIR program is to fund innovative basic research projects that are high risk and have high potential payoff for fulfilling Army needs. The Department of Defense (DoD) defines basic research as "the systematic study directed toward greater knowledge or understanding of the fundamental aspects of phenomena and of observable facts without specific applications toward processes or products in mind". ECBC views the ILIR program as a critical part of its efforts to ensure a high level of basic science, foster innovation in the areas of chemistry and biology, and mentor junior investigators in the art and practice of new technological innovations and new phenomenology at the boundaries of chemistry, biology, mathematics, or physics that will result in additional insights and advances in support of CBRNE defense missions.

The ILIR program solicits innovative proposals from the Center's principal investigators (PI) that correspond to ECBC's critical core capability areas: Inhalation Toxicology, Filtration Science, Threat Agent Chemistry and Bioscience, Aerosol Physics, and Agent Spectroscopy/Algorithm Development. Proposals are first reviewed internally by the Branch and Division Chiefs for their technical innovation, alignment to Army/ECBC S&T topic areas, and programmatic completeness. The proposals are then reviewed and critiqued by a panel comprised of resident and external Department of the Army members of the Scientific and Professional (ST) cadre of the Senior Executive Service, chief and/or senior scientists from other DoD organizations, and civilian and military faculty members at the U.S. Military Academy. Some of these same reviewers also serve on a Technical Advisory Board (TAB), which is convened in the fourth quarter of the program to assess the year-to-date performance of the basic science research projects.

The review panel evaluates and scores each proposal on its scientific objective, the scientific methods proposed, the qualifications of the investigator, and the budget, with the scientific objective and method weighted as the most important criteria. Only proposals deemed by the panel as basic research are considered for funding. Quality comments from the reviewers are compiled and used, with the numerical score, as a critical assessment of the proposal. The proposals are then ranked by score, according to merit. The written feedback and ranking is essential for ECBC's mentoring of researchers and for justifying the elimination of research programs that are not competitive. Quarterly reviews of project performance and the end-of-the-year TAB review provide additional guidance to the program's participants, ensuring projects meet significant milestones, and substantive new knowledge is produced and transferred to the ECBC and broader scientific community.

This cyclical review and assessment process was used to select and monitor the progress of new ILIR projects and projects already in existence. Internal funds were also used to support directed basic research projects, under the Surface Science Initiative (SSI) program, and "Seedling" projects, which are smaller-scale projects of high risk, high reward basic research. This Annual Review contains technical reports from ECBC-produced ILIR, SSI, and Seedling-funded projects.

FY11 ILIR Technical Report Executive Summary

The ECBC ILIR Program funded seven projects in FY11, the SSI Program divided funding between two projects, and internal "seedling" funding was distributed to seven projects. Together, the ILIR, SSI, and Seedling projects covered multiple areas of interest across the chemical, biological, and physical sciences, including abiotic systems design, molecular toxicology, computational method development, human stem cell research, aerosol sciences, and rational material design. Total FY11 funding in support of ILIR, SSI, and Seedling basic science projects performed at ECBC totaled approximately $3.36M. Projects with technical reports in this annual report are briefly summarized below:

In-House Laboratory Independent Research (ILIR) Projects

"Biotic-abiotic interfaces within a nanostructured polymer matrix platform: Towards a completely abiotic system" (PI: Sekowski). Chemically functionalized polystyrene-b-poly(2-vinyl pyridine) (PS-b-P2VP) block copolymers were used to develop glucose responsive and ovalbumin-specific color-changing thin films. Such functional abiotic polymers could be designed for use as autonomous sensor platforms or as integrated functional materials on or in the warfighter's kit.

"Fractional analysis of *Escherichia co*li O157:H7 by mass spectrometry-based proteomics" (PI: Bevilacqua). In this study, *E. coli* O157:H7 protein fractions were analyzed by liquid chromatography-tandem mass spectrometry (LC-MS/MS), followed by biochemical pathway mapping using the Kyoto Encyclopedia of Genes and Genomes (KEGG). The fimbriae-specific subset included proteins involved in carbohydrate metabolism, as well as inositol monophosphatase (IMP) and a glucose-specific phosphotransferase system (G-PTS). This research is expected to provide fundamental knowledge regarding extracellular proteins produced by Gram-negative bacteria, specifically those components important for bacterial survival.

"Molecular toxicology of toxic industrial chemicals (TICs) in human embryonic stem cells" (PI: Madren-Whalley). Undifferentiated WA09 human embryonic stem (hES) cells exposed to the widely-used organophosphate insecticide, methyl parathion (MP) and its active metabolite, methyl paraoxon (MPO) were studied using LC-MS and real time-polymerase chain reaction (RT-PCR). The results suggest that MP and MPO significantly and differentially impact the metabolism of hES cells, and that MP affects the expression of key genes involved in the differentiation and pluripotency of hES cells.

"Tuning the optical properties of multi-layered nanoparticles using exciton-plasmon coupling (PI: DeLacy). Colloidal suspensions of double-shell nano-composite structures were fabricated to demonstrate J-aggregation of a cationic cyanine dye onto a silver/silica or silver/ thiol bi-layered nanospheres. The interaction of the localized surface plasmon resonance exhibited by the metallic core with the absorption properties of the outer J-aggregate layer was elucidated by measuring their optical properties in the visible region. The researchers also developed a computational model predicting the interaction of electromagnetic radiation for the structures.

"Investigation of molecule-surface interactions with overtone adsorption spectroscopy and computational methods" (PI: Cabalo). The objective of this study was to understand how molecular interactions are reflected in overtone spectra and to use this information to predict overtone spectra from models of intermolecular interactions, especially of molecules on surfaces. The capability to predict changes in the overtone spectrum due to molecule-bulk and molecule-surface interactions permits the refinement and validation of the computational models of intermolecular interactions. The validated models allow other important properties, such as binding energies, to be predicted.

"Understanding the role of physical and chemical adsorption on the Raman enhancement from metallic nanoparticles and nanostructured surfaces" (PI: Guicheteau). Tethered gold nanoparticle substrates were

fabricated and used to analyze molecules that form charge transfer complexes (e.g., benzenethiol), and those that do not have strong charge transfer characteristics (e.g., aminoethanol). While resonance and pre-resonance effects related to low lying electronic states created by association with the metal cluster contributes to the Raman enhancement, the results of the modeling show that do not dominate. Sharing of electron density appears to also contribute, but it also does not fully account for the predicted enhancement.

"A computational approach to discovering useful self-assembling compounds" (PI: Banks). In this project, density functional theory at the B3LYP/6-31+G(d) level was used to explore the ability of molecules structurally derived from the purine and pyrimidine bases to self-assemble in linear chains on a graphene-like model surface, coronene. Preliminary data suggest that self-assembly of suitably chosen hybrid nucleobases under these conditions is likely.

Surface Science Imitative (SSI) Projects

"Identification of dynamic changes *in vitro* following exposure to the toxicant paraoxon" (PI: Dorsey). Human induced pluripotnet stem (IPS) cells, differentiated to form glial cells and neurons, were exposed to the pesticide paraoxon and assayed for cytotoxicity. Astrocytes and neurons were assayed using using both ATPlite and MTT cytotoxicity assays, which showed IC50 toxicity at 2 mM, consistent with previously reported findings. In addition to the toxicity studies, 17 proteins were found to have been affected, with significant alterations in expression (either up-regulated or decreased expression).

"A rational design approach to multifunctional nanostructured materials: Preparation and properties of luminescent lanthanide/graphene materials" (PI: Karwacki). In this study, graphene oxide was labeled with the luminescent lanthanides, europium and terbium. The surface morphology and physical properties of the graphene/lanthanide materials were investigated by scanning electron microscopy (SEM), transmission electron microscopy (TEM), and laser induced fluorescence. Efforts to model and direct the complexation of the newly prepared lanthanide graphene species with organic ligands, to enhance specificity and functionality of the luminescent complex, are planned.

Seedling Projects

"The role of turbulence intensity in establishing a critical Stokes number that demarks the breakdown of isokinetic sampling principles" (PI: Wise). In this study, inlet efficiency was measured for a range of thin-wall tube sampling probes, revealing that isokinetic sampling fails to provide the same aerosol concentration across scales of probe diameter. The inlet efficiency increased with increasing probe Stokes number for low levels of free stream turbulence, but not for high levels of turbulence.

"Enhanced recovery of agents by selective recombinatorial enrichment (ERASRE)" (PI: Redmond). The ERASRE procedure was developed to reduce the complexity of an environmental sample by enriching the DNA from one population by removing the DNA from the other population. Despite multiple methods for biotinylating capture DNA and multiple repeated attempts of the procedures, ERASRE did not enrich *Yersinia pestis* DNA via subtractive recombination from a mixture of *Bacillus anthracis* and *Y. pestis* DNA.

"Biodegradation of organofluorine compounds" (PI: Harvey). Enrichment cultures of a consortium of microorganisms were provided with various organofluorine compounds as the sole source of carbon for growth. Two of the organofluorine compounds, benzoyl fluoride and 1H, 1H, 2H, 2H-perfluorooctyltriethoxysilane, sustained microorganism growth. Benzoyl fluoride defluorinated very rapidly, suggesting that the microorganisms subsisted on the hydrolysis product, benzoic acid. Cultures grown from both organofluorine compounds appeared to be consortia; single colony isolates capable of growth on either compound were not identified.

"Aerosol particle size distribution in relation to material surface science" (PI: Wise). The goal of this study was to correlate aerosol particle surface properties, generically described as "Surface Energy" (which impacts the Hamaker Constant, Flow Quality number, and Geldhart classification of the material) to the characteristic aerosol cloud size distribution, for varied dissemination fluid shear stress parameters. The experimental results enhanced understanding of the relationship between intrinsic inter-particulate cohesion properties fundamental to resulting aerosol cloud characteristics and provided a more comprehensive aerosol cloud characterization for practical combinations of surface energy and dissemination shear force.

"Decontamination of single spores and bioclusters using UV-C and simulated sunlight" (PI: Kesavan). This study evaluated the effect of ultraviolet-C radiation (UV-C) and simulated sunlight on the decontamination (i.e., death) of organisms in different size clusters and as single spores of *Bacillus atrophaeous* (Bg). The results show that single spores are decontaminated faster than the clusters. The outer layers of clusters protected the organisms in the center, requiring a stronger and longer UV exposure to decontaminate all of the organisms in the clusters. Given these results, the kill curve predictions based on previous single spore tests may not be applicable for biocluster decontamination.

"Peptide selectivity study on the Cu_2O surface" (PI: Cabalo). Classical molecular dynamic (MD) simulations were performed for glycine, arginine, phenylalanine, and two-mer and three-mer peptides of these residues acting on the (1,1,1) face of Cu_2O. Within the simulations performed, no additional affinity for the surface was demonstrated by arginine or its two-mers or three-mers, in comparison to phenylalanine, glycine or their two-mers or three-mers. The results strongly suggest that charge transfer or chemistry involving the singly bound Cu atom is a factor in the selective binding, indicating that *ab initio* or Carr-Parrinello MD are necessary to fully account for the selectivity.

"Click chemistry on self-assembled monolayers (SAMs)" (PI: Hondrogiannis). Gold nanoparticle surfaces were modified with self-assembled monolayers (SAMs) of 1,7-dicarba-closo-dodecaborane m-9-carboranethiol by chemisorbing from a solution in acetone at room temperature. SEM and energy dispersive spectroscopy (EDS) was used to characterize the SAM-modified surfaces of the gold nanoparticles. Bulk results suggest that such reactions are feasible provided that sufficient heat and reaction times are allowed.

Table of Contents

In-House Laboratory Independent Research Projects

Biotic-abiotic interfaces within a nanostructured polymer matrix platform: towards a completely abiotic system
Omar Ayuub, Jennifer Sekowski, and Peter Kofinas 1

Fractional analysis of *Escherichia coli* O157:H7 by mass spectrometry-based proteomics
Vicky Bevilacqua, Rabih Jabbour, Mary Wade, Samir Deshpande, Patrick McCubbin 10

Molecular toxicology of TICs in human embryonic stem cells
Janna Madren-Whalley, Vicky Bevilacqua, Jessica Palmer, Robert Burrier, Alan Smith, Kevin Conard, Paul West, Jennifer Sekowski 15

Tuning the optical properties of multi-layered nanoparticles using exciton-plasmon coupling
Brendan DeLacy, Mary Soljacic, Wenjun Qiu 27

Investigation of molecule-surface interactions with overtone absorption spectroscopy and computational methods
Jerry Cabalo, Gary Kilper, Rosario Sausa 34

Understanding the role of physical and chemical adsorption on the Raman enhancement from metallic nanoparticles and nanostructured surfaces
Jason Guicheteau, Steven Christesen, John Kiser, Jerry Cabalo 44

A computational approach to discovering useful self-assembling compounds
Harold Banks 55

Surface Science Initiative Projects

Identification of dynamic changes *in vitro* following exposure to the toxicant paraoxon
Aisha Hajjij, Kristen Willis, Rabih Jabbour, Russell Dorsey 63

A rational design approach to multifunctional nanostructured materials: preparation and properties of luminescent lanthanide/graphene materials
Amanda Jenkins, Alex Balboa, Margaret Hurley, Chistopher Karwacki 73

Seedling Projects

The role of turbulence intensity in establishing a critical Stokes number that demarks the breakdown of isokinetic sampling principles
Daniel Wise, Daniel Weber, Elias Yoon, Donna Carlile 83

Enhanced recovery of agents by selective recombinational enrichment
Brady Redmond, Matthew Lux, Lauren McNew, Bryan Rivers, James Carney 90

Biodegradation of organofluorine compounds
Melissa Dixon, Steven Harvey 94

Aerosol particle size distribution in relation to material surface science
Daniel Wise, Brendan DeLacy, Daniel Weber, Elias Yoon, Donna Carlile 99

Decontamination of single spores and bioclusters using UV-C and simulated sunlight
Jana Kesavan, Deborah Schepers, Jerold Bottiger, Jason Edmonds 107

Peptide selectivity study on the Cu_2O surface
Jerry Cabalo 113

Click chemistry on self-assembled monolayers (SAMs)
George Hondrogiannis, Stanley Ostazeski, Erica Valdes 119


ILIR PROJECTS

Biotic-abiotic interfaces within a nanostructured polymer matrix platform: towards a completely abiotic system

Omar B. Ayyub[a], Jennifer Sekowski[b], and Peter Kofinas[a]
[a]University of Maryland, Fischell Dept of Bioengineering, College Park, MD 20742
[b]Edgewood Chemical Biological Center, Research & Technology Directorate, 5183 Blackhawk Rd., Aberdeen Proving Ground, MD 21010

ABSTRACT

Hybrid biotic/abiotic structures were fabricated using chemically functionalized polystyrene-b-poly(2-vinyl pyridine) (PS-b-P2VP) block copolymers. These polymer films induce a visible color change when exposed to aqueous media. The P2VP block of the copolymer was functionalized with either 2-bromomethylphenylboronic acid or bromoethylamine. The 2-bromomethylphenylboronic acid functionalization allowed the polymer films to respond to glucose with a change in color. When exposed to glucose, the films changed from green to orange. Ovalbumin antibodies were attached to films functionalized with bromoethylamine. These films responded to the ovalbumin protein with a color change.

1. INTRODUCTION

The overall goal of this research is to explore the basic rules governing the biotic-abiotic interfaces and other chemistry required to integrate different types of binding or capture reagents within a responsive, nanostructured block copolymer (BCP) matrix. The ease of processing the BCP at ambient temperature already allows the production of responsive shape-conforming thin films that can be processed as coatings or sheets, and distributed over a large area substrate. The principles we establish from this work will ultimately lead to the development of responsive flexible polymers that could form the basis for multiple or multiplexed "litmus test" polymers, configured as small "stickers", large coating sheets, or even integrated into the fabric or coatings used in the warfighter's uniform and kit.

To create a polymeric material that can successfully recognize ricin, anthrax, or any other biological or chemical molecule, it is necessary to combine a selective recognition element with a measurable output signal. The material we used achieves these needs by using the tunable reflectance of swollen functionalized BCPs. BCPs consist of two or more chemically distinct sequences of monomer repeat units linked together through a covalent bond. Upon evaporation from a solvent, BCPs will microphase separate into solid films displaying a number of different morphologies (e.g., hexagonal, cubic, gyroid, lamellar) depending on the relative volume fraction of each block. BCPs in which both blocks are of equal molecular weight generally exhibit the lamellar morphology. In this work, we used an A-B diblock copolymer that microphase separates into a lamellar periodic stack. The A block is water-insoluble polystyrene (PS) and does not contain any functional groups on the polymer chain that can interact with the biological/chemical threat compound. The B block contains the 2-vinyl pyridine (P2VP) functionality, which can be further chemically modified to serve as ionic interaction sites with known threat receptors.

Without modification, the refractive index contrast between subsequent A and B layers is too low to successfully reflect light in the visible wavelength. In addition, the spacing between these layers is not large enough to interact with visible light. Through selective chemical modification of the B block, the condition for visible light can be achieved, thus creating lamellar structures with tunable reflective properties. Upon binding a chemical or biological agent, the B layers swell, increasing the spacing

between the subsequent A layers. In addition, the refractive index contrast between alternating layers is increased. The ranges of wavelengths reflected are highly dependent upon the spacing between the AB layers and the refractive indices of subsequent layers. The color of the self-assembled polymer films can be modulated by simply changing the spacing (d) between subsequent layers. In the proposed system, this can be achieved by controlling the amount of swelling due to the CB threat binding event as shown in Figure 1.

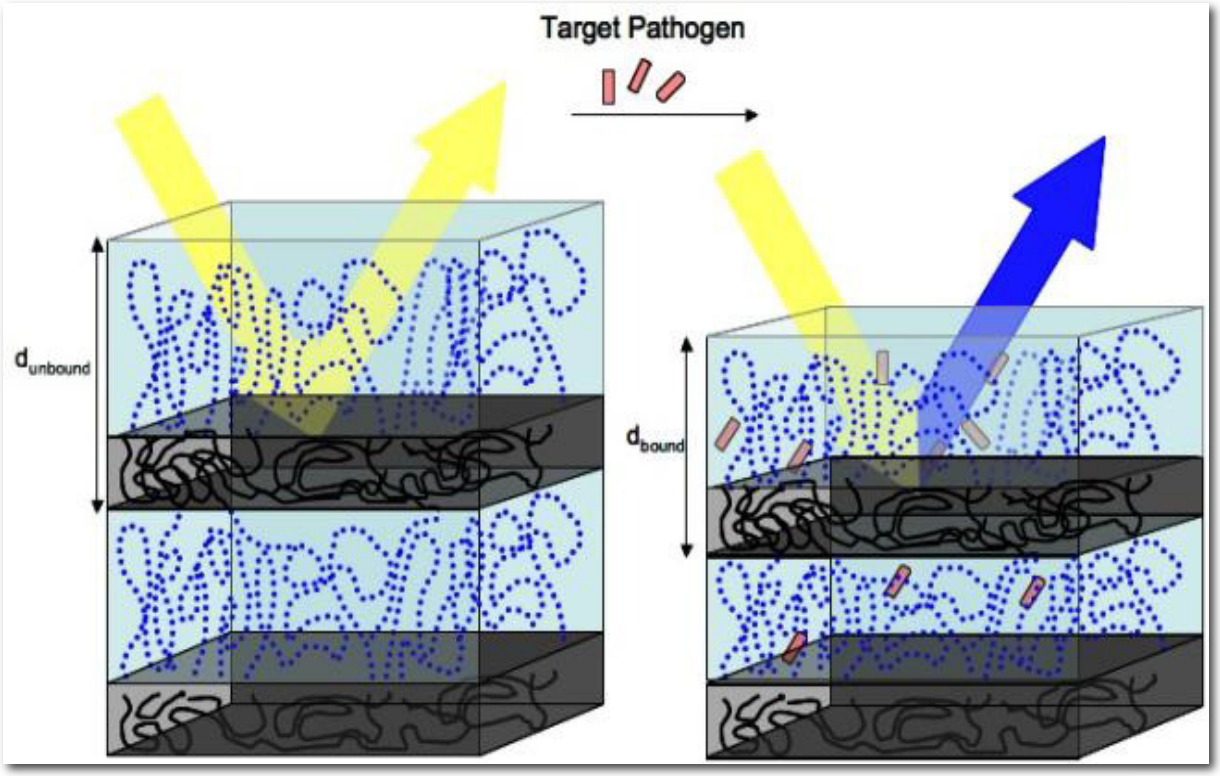

Figure 1. Schematic of BCP film in the unbound (left) and bound (right) state. The spacing (d), and refractive index contrast between subsequent layers changes as soon as the CB agent selectively binds to capture reagent in one of the layers.

In this study, films of the block copolymer PS-b-P2VP were fabricated to have a periodic lamellar structure, as seen in Figures 1 and 7. These solid films are then chemically functionalized. This functionalization only occurs on the P2VP block of the copolymer placing a positive charge on the nitrogen atom of the pyridine ring, which allows the film to swell in water and change color. The block copolymer films were functionalized with either 2-bromomethylphenylboronic acid or bromoethylamine, as seen in Figure 2. When functionalized with the 2-bromomethylphenylboronic acid, the films respond to the sugar glucose with a change in color. The bromoethylamine functionalization places a primary amine along the P2VP block. The primary amine can then have antibodies for proteins, such as ricin, attached to the polymer film. When the polymer film is exposed to a biological agent, the agent will bind to the antibody causing the polymer film to swell and change its color. In this study polyclonal ovalbumin antibodies were attached to the polymer films and the films were subsequently exposed to the ovalbumin protein. The films responded with a change in color.

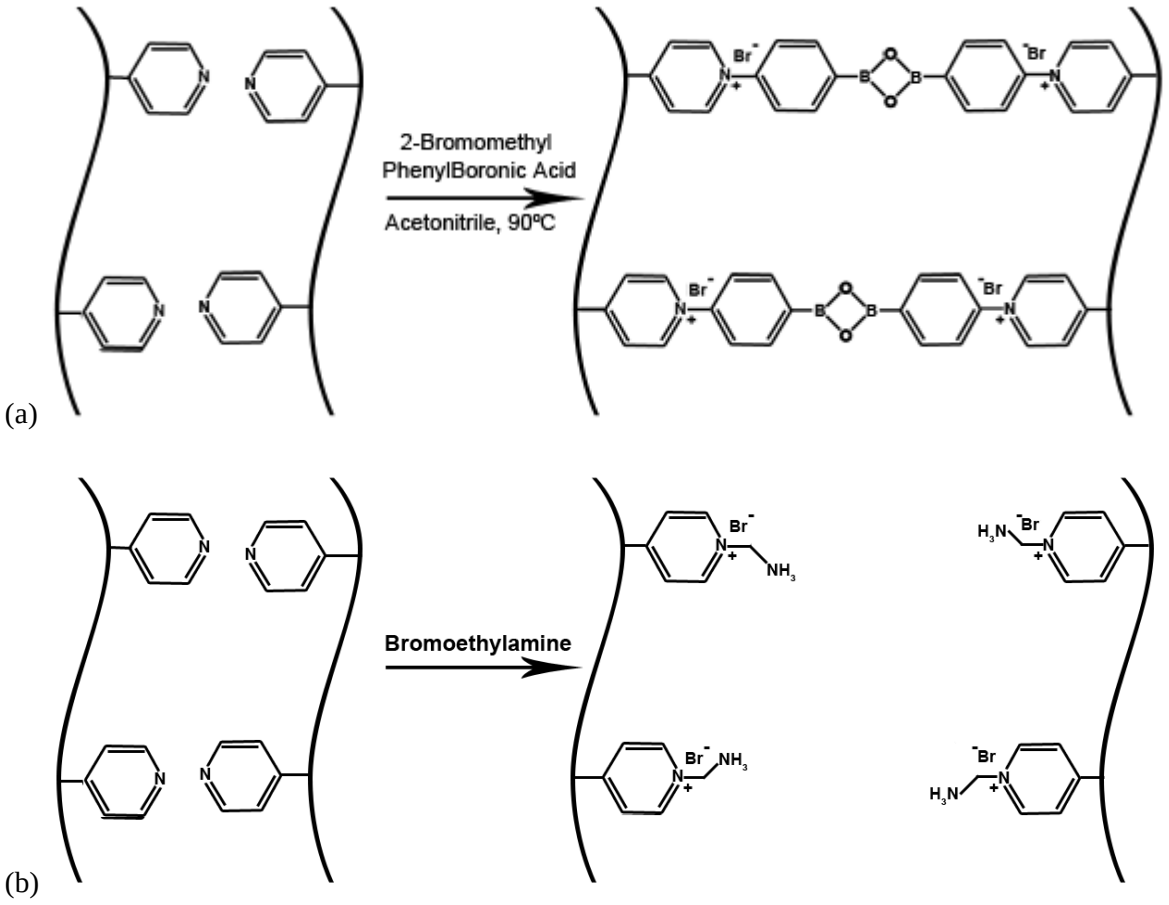

Figure 2. Functionalization of the 2-vinyl pyridine block with (a) 2-bromomethylphenylboronic acid (b) bromoethylamine.

2. METHODOLOGY

2.1 Fabrication of photonic BCP films

The procedure for fabrication of the PS-b-P2VP films was adapted from Kang et al.[1] The PS-b-P2VP block copolymers were purchased from Polymer Source. The molecular weight of each block of the polymer was 133,000. A 5% weight/volume stock solution of PS-b-P2VP was prepared in propylene glycol monomethyl ether acetate (PGMEA). The films were prepared by spin-casting 300 µL of the PS-b-P2VP solution was onto 1 "X1'' glass slides at 350 rpm for two minutes. The glass slides were purchased from Ted Pella, and were functionalized with 3-aminopropyl triethoxysilane. The spin-cast block copolymer films were subsequently annealed in chloroform vapor at 50°C for 24 hours to allow them to self-assemble into a lamellar structure.

2.2 Functionalization

The films were functionalized with either 2-bromomethylphenylboronic acid or bromoethylamine depending on the chemical or biological target. The 2-bromomethylphenylboronic acid functionalization allows the films to target sugars such as glucose, while the bromoethylamine functionalization allows for further modification of the films. To functionalize the P2VP block of the copolymer, a solution of 40 mg of either 2-bromomethyl-phenylboronic acid or bromoethylamine in 40 mL of acetonitrile was prepared. The block copolymer films were then immersed in the solution for 24 hours at 90°C. The chemical

ninhydrin was employed to verify the bromoethylamine functionalization. When ninhydrin comes in contact with primary amines, it generates a purple color. The films were tested for bromoethylamine functionalization by immersing them in a solution of 50 mg of ninhydrin in 30 mL of water. The solution was heated to 70°C, stirred for an hour, and then observed for generation of purple color.

2.3 Glucose detection

Once the films were functionalized with 2-bromomethylphenylboronic acid, they were exposed to glucose to observe if the films would respond with a color change. A 20 mL solution of 50 mg/mL of glucose was prepared. The polymer films functionalized with 2-bromomethylphenylboronic acid were immersed in this glucose solution and subsequently observed for a color change.

2.4 Antibody attachment and protein detection

Films quaternized with bromoethylamine were further modified by attaching polyclonal ovalbumin antibodies. The attachment was performed using 1-ethyl-3-(3-dimethylaminopropyl)carbodiimide (EDC) as well as N-hydroxysuccinimide (NHS). The ovalbumin antibody was placed in MES buffer solution using a slide-alyzer at a concentration of 1 mg/mL; 1.1 mg of NHS and 0.5 µL EDC were then added to the solution. The EDC was allowed to bind to the carboxylic acid groups on the antibody for 15 minutes. A film functionalized with bromoethylamine was the immersed in this solution for three hours. Once the antibody attachment reaction was complete, the film was introduced to a solution of 30 mg/mL of ovalbumin protein solution.

3. RESULTS AND DISCUSSION

3.1 Verification of bromoethylamine attachment

To determine whether the PS-b-2VP films were functionalized with bromoethylamine, the chemical ninhydrin was applied. When exposed to primary amines, ninhydrin will react with the amine to generate a purple color (called Ruhemanns's purple). After a PS-b-2VP film was exposed to the ninydrin solution for an hour, the color was observed. As seen in Figure 3a the films generated a purple color which was contained within the film. This indicates the attachment of the ethylamine group to the vinyl pyridine block of the polymer film. For further verification, the film was placed in deionized water. The attachment of the bromoethylamine on the nitrogen atom of the vinyl pyridine will generate a formal positive charge on the nitrogen atom. This will allow water to associate with the vinyl pyridine block which will, in turn, cause the film to swell. As the vinyl pyridine film swells in water, color is produced by Bragg's diffraction as seen in Figure 3b. A PS-P2VP block copolymer film that has not undergone the bromoethylamine functionalization will not change color upon exposure to water.

(a)  (b) 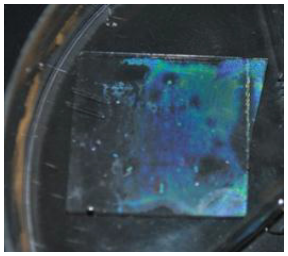

Figure 3. (a) PS-b-P2VP film functionalized with bromoethylamine after exposure to ninhydrin. (b) PS-b-P2VP film functionalized with bromoethylamine immersed in water.

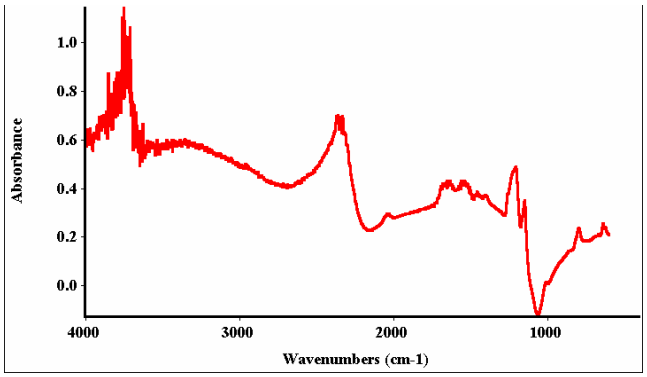

Figure 4. FTIR of the functionalized block copolymer using bromoethylamine and antibody

For additional verification, FTIR was utilized to determine functionalization with bromoethylamine as well as antibody attachment. As seen in Figure 4, there is a peak at 3600 cm^{-1}, which is associated with primary amines. The peaks after 2000 cm^{-1} could possibly be associated with the antibody.

3.2 Detection of glucose

The PS-b-2VP films functionalized with 2-bromomethylphenylboronic acid were exposed to a 20 mL 50 mg/mL aqueous solution of D-glucose. The films were initially green in pure deionized water due to the functionalization. Once exposed to the glucose solution, the films instantly swelled and became orange in color. This color change and proposed mechanism can be seen in Figures 4 and 5.

(a)

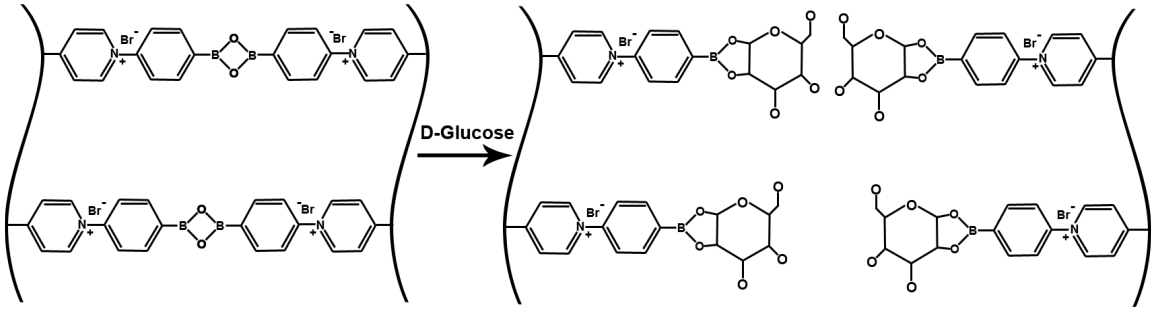

(b)

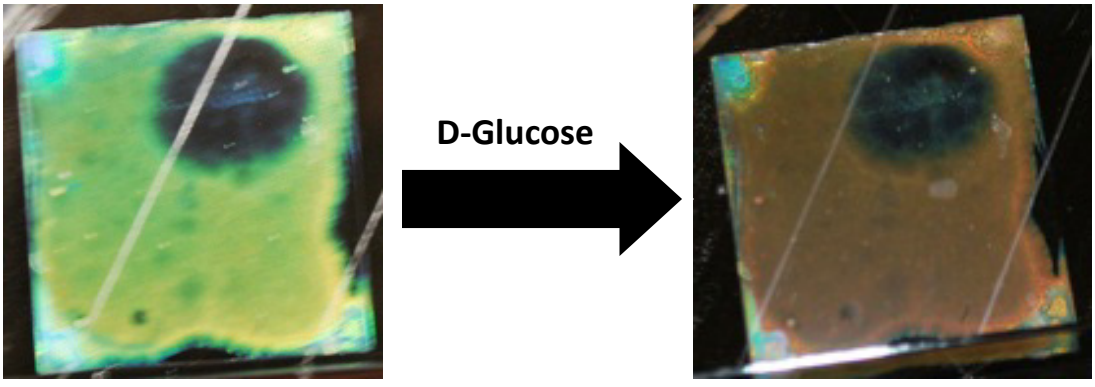

Figure 5. (a) Once the PS-b-2VP film is functionalized with 2-bromomethylphenylboronic acid, the boronic acid groups will reversibly bind to each other, cross-linking the film and inhibiting swelling. When exposed to glucose, the boronic acid cross-links are broken as the boronic acid groups bind to glucose allowing the film to swell. (b) PS-b-2VP film functionalized with 2-bromomethylphenylboronic acid. Once exposed to a 50 mg/mL D-glucose solution, the film changes from green (left) to orange (right).

The binding and color change to the sugar glucose demonstrates the concept of the PS-b-2VP films response to chemical or biological targets. This block copolymer functionalized with 2-bromomethylphenylboronic could eventually be modified to allow the PS-b-P2VP films to detect auto-inducer 2 (AI-2), which has been described as a "universal signal" for interspecies bacterial communication. AI-2 consists of molecules having chemical structures isomeric to simple sugars.

3.3 Detection of ovalbumin

PS-b-2VP films quaternized with bromoethylamine were further modified with polyclonal ovalbumin antibody using a carbodiimide reaction. When introduced to ovalbumin protein, the protein binds to the antibody causing a shift in mass and volume in the polymer film. This causes the film to swell and change color. As seen in Figure 6, the film swelled when introduced to ovalbumin, changing color from light greenish orange to red. The color change from orange to red could be difficult to discern. In Future experiments will involve optimizing a more obvious color change as well as measuring the shift in color using UV-Vis spectroscopy.

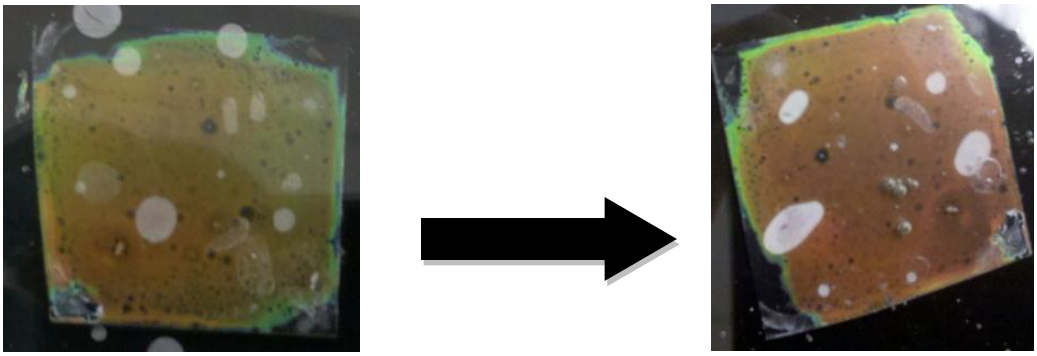

Figure 6. The antibody modified PS-b-2VP film is light green-orange before exposure to protein. After exposure the film is deep red orange.

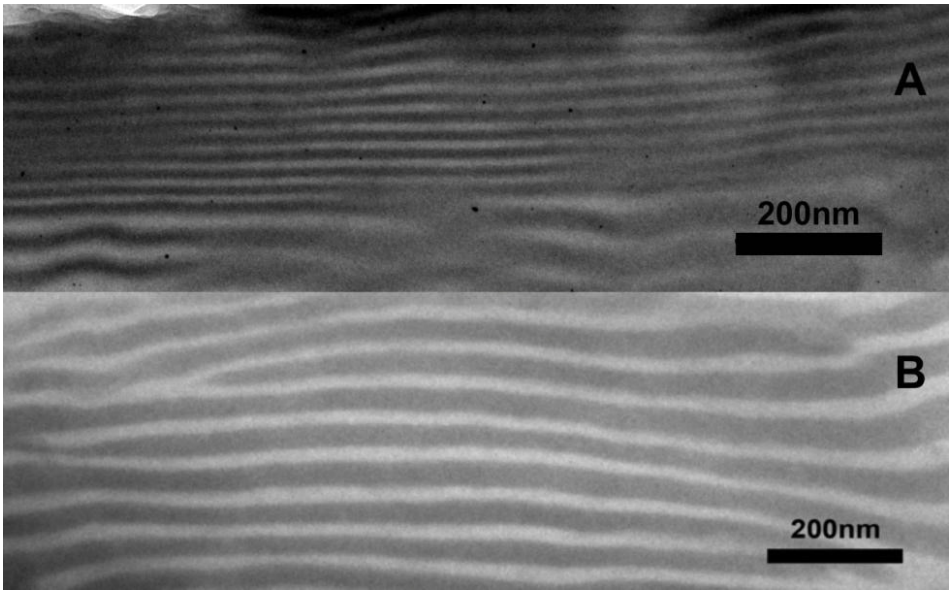

Figure 7. A) TEM of annealed, unmodified PS-b-P2VP film. B) TEM of PS-b-P2VP film functionalized with 2-bromomethylphenylboronic acid exhibiting a lamellar morphology. The darker iodine stained P2VP block appears thicker due to the increased mass of the P2VP block from the functionalization as compared to the cross section seen in the unmodified film, A.

3.4 Tuning the polymer film's color

Demonstrating control over the optical properties or color of the BCP film is vital for producing a reliable chemical sensor. To tune the color of the functionalized BCP film, varying degrees of crosslinking were introduced into the P2VP block. The BCP was exposed to various molar ratios of 1,4-dibromo-2-butanol (crosslinker) to 2-(bromomethyl)phenylboronic acid (quatenizer). Increasing or decreasing the mole fraction of the crosslinker allows the collapsing or swelling the polymer film in water, which tunes the color of the BCP.

The BCP films can be fabricated to exhibit different colors by controlling the swelling of the polymer film through variations in crosslink density. The BCP films have successfully been tuned to blue, green, yellow, orange, or infrared colors. Figure 8 shows each of the colored BCP films and their corresponding visible spectra. As seen the BCP film's color is intense and easy to recognize by eye. There is no need for extraneous equipment to distinguish one color from another. This allows the simple fabrication sensor to be utilized by individuals who would not need specific training to determine if the BCP film has responded to a specific analyte.

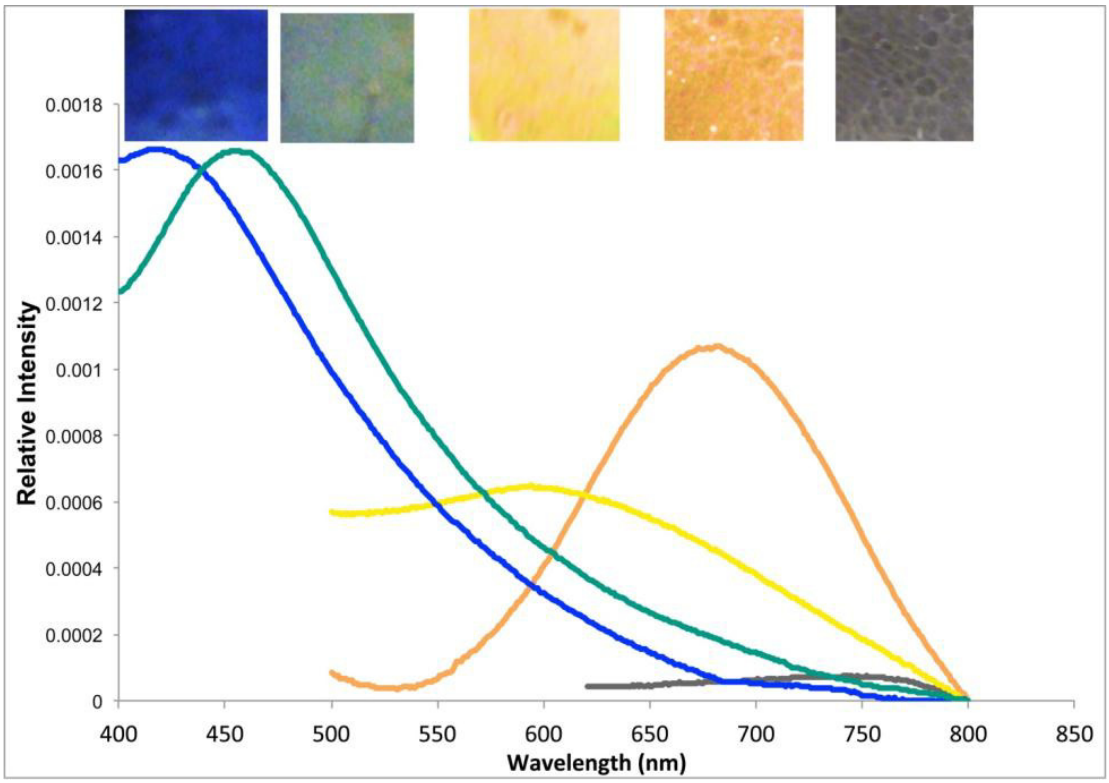

Figure 8. The BCP film color can be tuned to blue, green, yellow, orange or transparent (infrared) colors depending on the degree of crosslinking. Increasing the crosslink density inhibits swelling which blueshifts the color of the polymer film. Each BCP film displays a different color and visible spectra depending on the molar ratio of crosslinker to quaternizer.

3.5 Sensor selectivity towards simple sugars

The phenylboronic acid functionality introduced to the P2VP block of the BCP can covalently bind to any diol-containing sugar such as glucose, fructose, mannose, and galactose. The K_{eq} of boronic acid binding to each one of these sugars varies depending on the sugar. This suggests that the boronic acid functionalized film should have a selective response to each simple sugar. To observe this effect, a BCP film functionalized and crosslinked to yield a blue color in water was exposed to 50 mg/mL solution of

either glucose, fructose, mannose, or galactose. After 30 minutes of exposure, the BCP film's visible spectra was measured using UV-Vis spectroscopy. The peak difference in wavelength was then calculated as the difference between the peak wavelength of the film in water and in the sugar solution.

As seen in Figure 9, the BCP film exposed to fructose gave the largest response of a 200 nm redshift in wavelength. The film exposed to galactose exhibited a 70 nm redshift in color. The smallest responses were in from films exposed to glucose and mannose, which exhibited 44 nm and 37 nm decreases, respectively. This difference in response between fructose, galactose and glucose is expected. It has been reported that fructose has the highest K_{eq} to bind to boronic acid, followed by galactose, and then glucose.[2]. This difference in binding is due to the steric structure of each sugar. Boronic acid can bind to both 1,2 and 1,3 cis diols but preferentially binds to 1,2 cis diols. Fructose, for example, has a planar 1,2 cis diol. Glucose does not have a 1,2 cis diol but has a 1,3 cis diol in its dominate pyranose form. Generally glucose binds to boronic acid in its furanose form, which does contain a planar 1,2 cis diol.[3] This result signifies that for a given concentration, the boronic acid functionalized BCP film can differentiate between glucose, galactose and fructose.

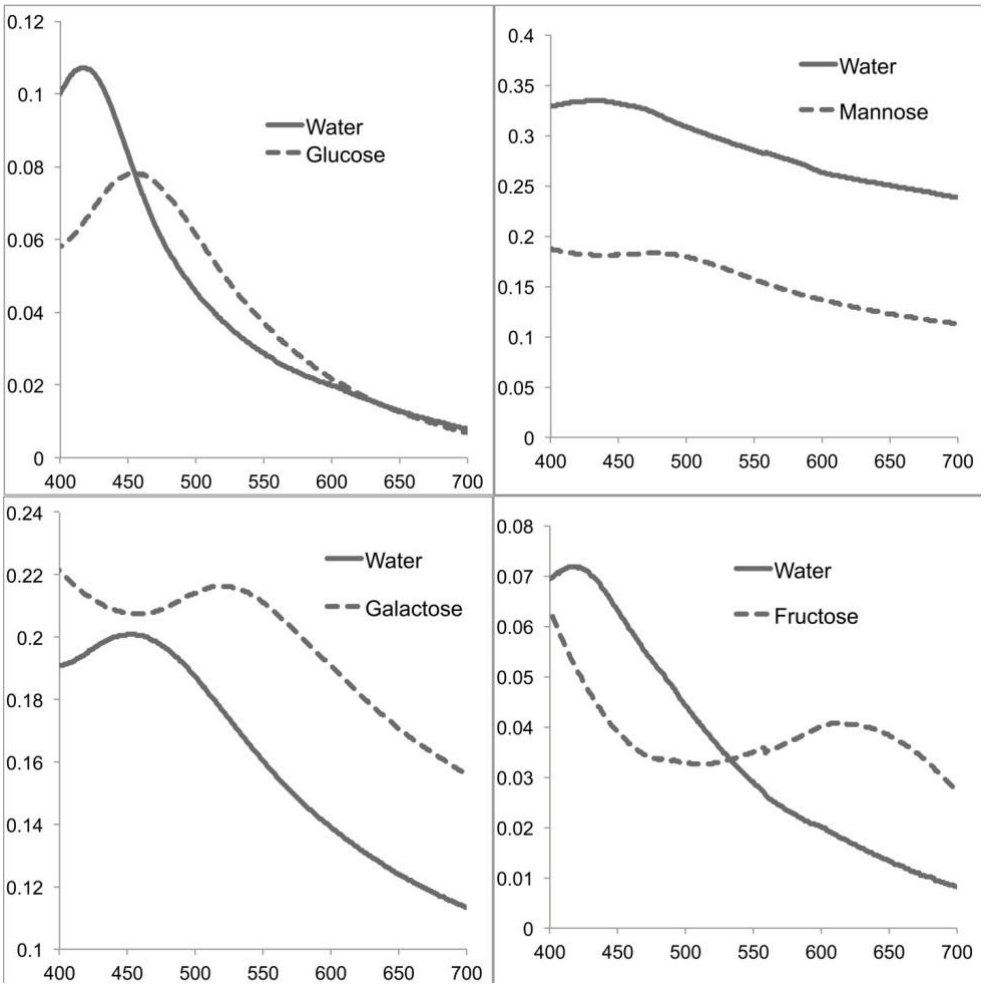

Figure 9. An initially tuned-blue BCP film was exposed to four different sugar solutions containing either glucose, fructose, galactose, or mannose at the same concentration. The difference of the peak wavelength observed in water versus that observed in the sugar solution was calculated to obtain the shift in wavelength. As seen in the figure, fructose gave the largest response of an approximately 200 nm redshift in wavelength. Galactose induced a 70 nm increase in wavelength and mannose and glucose induced smaller increases of approximately 40 nm each. This indicates that the BCP film can differentiate between fructose, galactose, and glucose for a given concentration.

4. CHALLENGES

In order for the BCP film to diffract light towards the observer, the lamellar morphology must be oriented parallel to the glass substrate. The 3-(aminopropyl)triethoxysilane functionalization on the glass substrate interacts with the P2VP block of the BCP by influencing the morphology to be parallel to the substrate. The BCP film is then annealed by exposing it to cholorform vapor, mobilizing the polymer chains and allowing them to form the parallel lamellae. This annealing process is very specific, requiring precise conditions to be successful. Environmental factors such as room humidity and evaporation rate of the annealing solvent can cause the BCP film to have poor morphology or break the interactions between the BCP and the substrate.

It was found that low humidity, approximately 20%, and relatively slowed evaporation rate of the chloroform dramatically improved morphology. After completion of the annealing process the BCP film is chemically functionalized by attaching 2-(bromomethyl)phenylboronic acid to the P2VP block. This chemical modification requires that the BCP film be exposed to acetonitrile at an elevated temperature. Such harsh conditions could potentially damage the BCP film or disrupt its delicate lamellar morphology. If the lamellar morphology is disrupted by the chemical modification, then the photonic properties of the BCP film will be diminished.

5. CONCLUSION

The PS-b-P2VP films show promise for detecting chemical or biological threats. The films functionalized with the 2-bromomethylphenylboronic acid demonstrated the ability to respond to glucose with a change in color without the use of any supplementary enzymes such as glucose oxidase. Functionalization with bromoethylamine was further modified with polyclonal ovalbumin antibodies. This film responded to the ovalbumin protein with a change in color. Future experiments will involve attaching other more operationally important antibodies (e.g., anti-ricin A chain antibody) to the polymer film instead of the ovalbumin antibody as well as optimizing the shift in color when exposed to the target protein.

WORK CITED

[1] Kang, Y. et al. 2007. *Nat. Mater.* 6(12), 957-960.
[2] Springsteen, G. and Wang, B.H. 2002. *Tetrahedron* 58(26), 5291-5300.
[3] Bielecki, M. et al. 1999. *J. Chem. Soc., Perkin Trans.* 2(3), 449-455.

REFERENCES

- Bates, F.S. and Fredrickson, G.H., 1990. *Annu. Rev. Phys. Chem.* 41, 525-557.
- Bosch, L.I. et al. 2004. *Tetrahedron* 60(49), 11175-11190.
- Chen, W. et al. 2009. *Langmuir* 25(12), 6863-6868.
- Cui, Q. et al. 2009. *Analyst* 134(5), 875-880.
- Edrington, A.C. et al. 2001. *Adv. Mater.* 13(6), 421-425.
- Endo, T. et al. 2010. *Sensor Actuat. B-Chem.* 148(1), 269-276.
- Kim, Y. et al. 2007. *Chem. Commun.* (22), 2299-2301.
- Lee, K. and Asher, S.A. 2000. *J. Am. Chem. Soc.* 122(39), 9534-9537.
- Lee, M. and Fauchet, P.M. 2007. *Opt. Express* 15(8), 4530-4535.
- Li, Y.Y. et al. 2003. *Science* 299(5615), 2045-2047.
- Urbas, A. et al. 2000. *Adv. Mater.* 12(11), 812-814.

Fractional analysis of *Escherichia coli* O157:H7 by mass spectrometry-based proteomics

Vicky L. H. Bevilacqua[a], Rabih E. Jabbour[a], Mary M. Wade[a], Samir V. Deshpande[b], Patrick E. McCubbin[c]
[a]Edgewood Chemical Biological Center, Research & Technology Directorate, 5183 Blackhawk Rd., Aberdeen Proving Ground, MD 21010
[b]Science and Technology Corporation, Edgewood, MD
[c]Optimetrics, Inc., Abingdon, MD

1. INTRODUCTION

Certain extracellular proteins of pathogenic bacteria have been shown to function in survival mechanisms such as host immune system modulation [1] and biofilm formation.[2] In addition, Gram-negative bacteria release a subset of extracellular proteins as MV components. Gram-negative bacteria form MVs by pinching off of the outer membrane to form liposomes. Bacteria form MVs at an energy loss and MVs contain periplasmic space components including enzymes, which suggest a functional role for MVs. Pathogenic Gram-negative bacteria produce more MVs than their non-pathogenic counterparts. Not surprisingly, several studies have provided evidence for a number of roles for MVs [3], such as transfer of antibiotic-resistance enzymes to other bacteria [4] and directed intercellular transport of virulence factors.[5] In addition, work by Schooling and Beveridge [6] indicates that membrane vesicles (MVs) shed by Gram-negative bacteria are a ubiquitous component in the biofilms of these bacteria. Levin and Rozen cite biofilm formation as one of three means by which bacterial populations can attain non-inherited antibiotic resistance.[7]

Our hypothesis is that the binding of intracellular, MV proteins or secreted proteins could contribute toward mechanisms of antibiotic resistance. To address this possibility, we are characterizing the MV proteins, other extracellular proteins, and whole cell lysate proteins produced by the pathogenic Gram-negative bacterium *E. coli* O157:H7 in terms of proteomics and binding of antibiotics. The expression and antibiotic binding capability of the MV proteins and other extracellular proteins will be compared with whole cell and fimbriae protein fractions from *E. coli* O157:H7 in search of differences indicative of unique functions for these extracellular components in resistance and virulence. Here we report on a comparison of the whole cell lysate, secreted, and fimbriae protein fractions of *E. coli* O157:H7 as determined by mass spectrometry-based proteomics. This research is expected to provide fundamental knowledge regarding MVs and extracellular proteins produced by Gram-negative bacteria. In particular, the work seeks to characterize these proteins and the role they may play with regard to virulence and resistance. In addition, this effort will further the development of a high-throughput platform for analyzing samples for the presence of biological constituents and enhance development of nanoparticle technologies by identifying molecular level components important for recognition and encapsulation.

2. METHODS

2.1 *E. coli* O157:H7 growth and protein fraction preparation

E.coli O157:H7 was grown in trypticase soy broth (TSB) to the late exponential phase (~10^8 cfu/mL) in an orbital shaker (125 rpm) at 37°C. The cell culture was stored at 4°C until fractionation. For isolation of the whole cell lysate and secreted protein fractions, 30 mL of culture was centrifuged at 11,300 x *g*/hr using a Beckman J2-MC centrifuge. The supernatant was decanted to separate it from the pellet. This

supernatant containing the secreted proteins is referred to as the secreted fraction. The pellet was re-suspended in ~3.5 mL of 100 mM ammonium bicarbonate (ABC). This suspension was divided into three aliquots of approximately equal volume. The cell pellet suspension samples were thawed and lysed by ultrasonication (25 s on, 5 s off, 4 min total) using a Branson Digital Sonifier® (Danbury, CT). The lysate was centrifuged at 14,000 rpm for 20 min at 10°C using a Beckman GS-15R centrifuge. This fraction is referred to as the whole cell lysate fraction. A microwave lysis procedure was also attempted in which the sample was subject to microwaves using a Discover™ System (CEM Corporation, Matthews, NC) was performed at 55°C for time periods of 5, 10, and 15 minutes rather than being subjected to sonication.

For isolation of fimbriae, cell culture aliquots (3 x 30 mL) were centrifuged at 15,000 x *g*/30 using a Beckman J2-MC centrifuge. Each pellet was re-suspended in 7 mL of ABC. These solutions were sheared through a 2 in, 22 gauge needle, 10 times each. Samples were divided into 1.5 mL centrifuge tubes and centrifuged at 15,000 x *g*/15 min using a Beckman GS-15R centrifuge. The supernatants were combined and filtered through a 0.45 µm acetate syringe filter. The filtrate was then heated at 60°C/hr in a block heater. These samples are referred to as the fimbriae fraction. Samples were frozen at -25°C for up to four days.

2.2 Liquid-chromatography/mass spectrometry sample preparation

Samples were prepared for liquid-chromatography tandem mass spectrometry (LC-MS/MS) in a similar manner to that previously reported.[8] Briefly, proteins were extracted from the whole cell lysate and secreted fractions by transferring each sample to a separate Microcon® YM-3 filter unit (Millipore, Billerica, MA) and centrifuging at 14,100 x *g*/20-30 min. The filter membrane was washed with ABC and centrifuged at 14,100 x *g*/20 min. For the fimbriae fraction, the frozen samples were thawed and pipetted into Microcon® YM-3 filter units (Millipore, Billerica, MA) for purification. The filters were each centrifuged at 14,000 x *g*/25 min three times with a 200 µL ABC wash in between centrifugations.

Generally, the proteins in the retentate were denatured at 40°C for 1 hr with 300 µL of 7.2 M urea and 3 µg/mL dithiothreitol in ABC. The urea was removed by centrifugation (14,100 x *g*/30-40 min) and the retentate was washed three times with ABC (150 µL ABC followed by centrifugation at 14,100 x *g*/30-40 min using an Eppendorf centrifuge 5415C or 5415D, Eppendorf North America, Westbury, NY). The filter unit was then transferred to a new receptor tube, and the proteins in the retentate were digested overnight at 37°C with 5 µL sequencing grade trypsin (Product # 511A, Promega, Madison, WI) in 10 µL acetonitrile and 240 µL ABC. The tryptic peptides were isolated by centrifuging at 14,100 x *g*/20-30 min. Alternative digestion protocols involved adjusting trypsin concentration, incubation time, and temperature.

2.3 Liquid-chromatography/mass spectrometry experiments

The tryptic peptides were separated in a similar manner to that previously described [8] on a capillary column using the Dionex UltiMate 3000 (Sunnyvale, CA) and the resolved peptides were electrosprayed into a linear ion trap mass spectrometer (LTQ XL; Thermo Scientific, San Jose, CA). Product ion mass spectra were obtained in the data-dependent acquisition mode, with a survey scan followed by MS/MS of the top five most intense precursor ions.

2.4 Proteomics analysis

A protein database was constructed as previously described [8] in a FASTA format using the annotated proteome sequences derived from the genomes in the National Center for Biotechnology Information (NCBI, http://www.ncbi.nlm.nih.gov, accessed November 16, 2010). For this task, an in-house PERL (http://www.activatestate.com/ActivePerl, accessed November 16, 2010) program was used to automatically download proteome sequences from the NCBI. The database was constructed by translating

putative protein-encoding genes and contains amino acid sequences of potential tryptic peptides obtained by the *in silico* digestion of all proteins, assuming up to two missed cleavages. The acquired mass spectra were searched against this database with the SEQUEST algorithm (Thermo Scientific). The SEQUEST thresholds for searching the product ion mass spectra were Xcorr, deltaCn, Sp, RSp, and deltaMpep. These parameters provide a uniform matching score for all candidate peptides. The generated outfiles with candidate peptides were validated using the PeptideProphet™ algorithm.[9] Peptide sequences with probability scores of 95% and higher were retained and used to generate a binary matrix of sequence-to-bacterium (STB) assignments. The binary matrix was populated by matching the peptides with corresponding proteins in the database and assigning a score of one. A score of zero was assigned for a nonmatch. The column in the binary matrix represents the proteome of a given bacterium, and each row represents a tryptic peptide sequence from an LC product ion mass spectral analysis. A sample microorganism is matched with a database bacterium by the number of unique peptides that remained after filtering of degenerate peptides from the binary matrix. Verification of the classification and identification of candidate microorganisms is performed through hierarchical clustering analysis and taxonomic classification.

2.5 Biochemical pathway mapping

An algorithm was developed in-house for automated comparison of proteins observed in samples from a given fraction (whole cell, secreted, fimbriae). This algorithm was used to compare the proteins observed by LC-MS/MS in the three fractionas and to determine which proteins were common between two or three fractions and which proteins were specific to a given fraction (fraction-specific proteins). Fraction-specific proteins were mapped to *E. coli* metabolic pathways using the Kyoto Encyclopedia of Genes and Genomes database (KEGG, www.genome.jp/kegg/, accessed November 16, 2011, Copyright 1995-2011 Kanehisa Laboratories).

3. RESULTS AND DISCUSSION

Three whole cell, three fimbriae, and five secreted fraction peptide samples were prepared for LC-MS/MS experiments and proteomics analysis. From these samples, more than 200 *E. coli* proteins were identified. The percentages of strain- and species-unique proteins identified in each fraction are shown in Figure 1, with the majority being in the fimbriae fraction. The strain-unique proteins represent biomarkers of *E. coli* O157:H7.

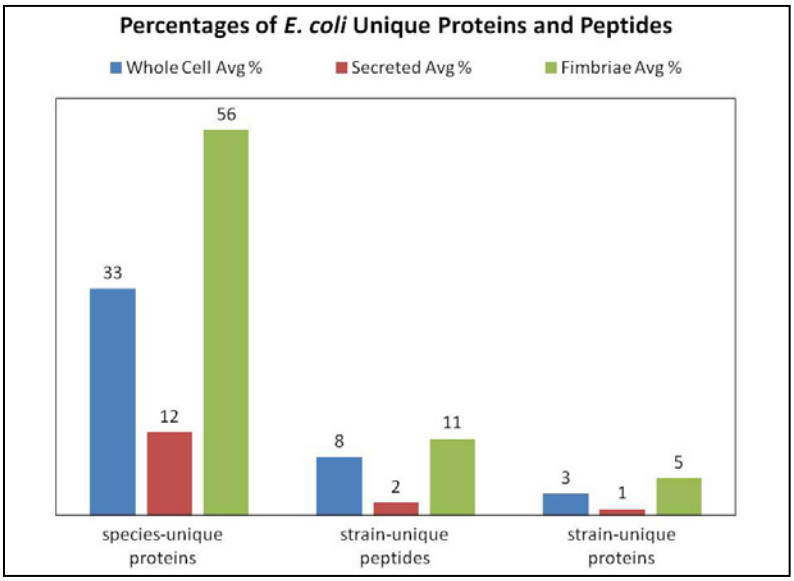

Figure 1. Approximate average percentages of *E. coli* unique proteins and peptides identified in *E. coli* O157:H7 whole cell, fimbriae, and secreted fractions.

For further analysis, proteins present in at least two of three samples for the fimbriae and whole cell fractions, and in at least three of five samples for the secreted fraction, were considered. Of these 201 proteins, 15% were common to all fractions. In addition, proteins specific to each fraction were observed: 3%, 5%, and 29% of the 201 in the secreted, fimbriae, and whole cell fractions, respectively. The percent of proteins localized to each fraction and shared between various fractions is shown in Figure 2.

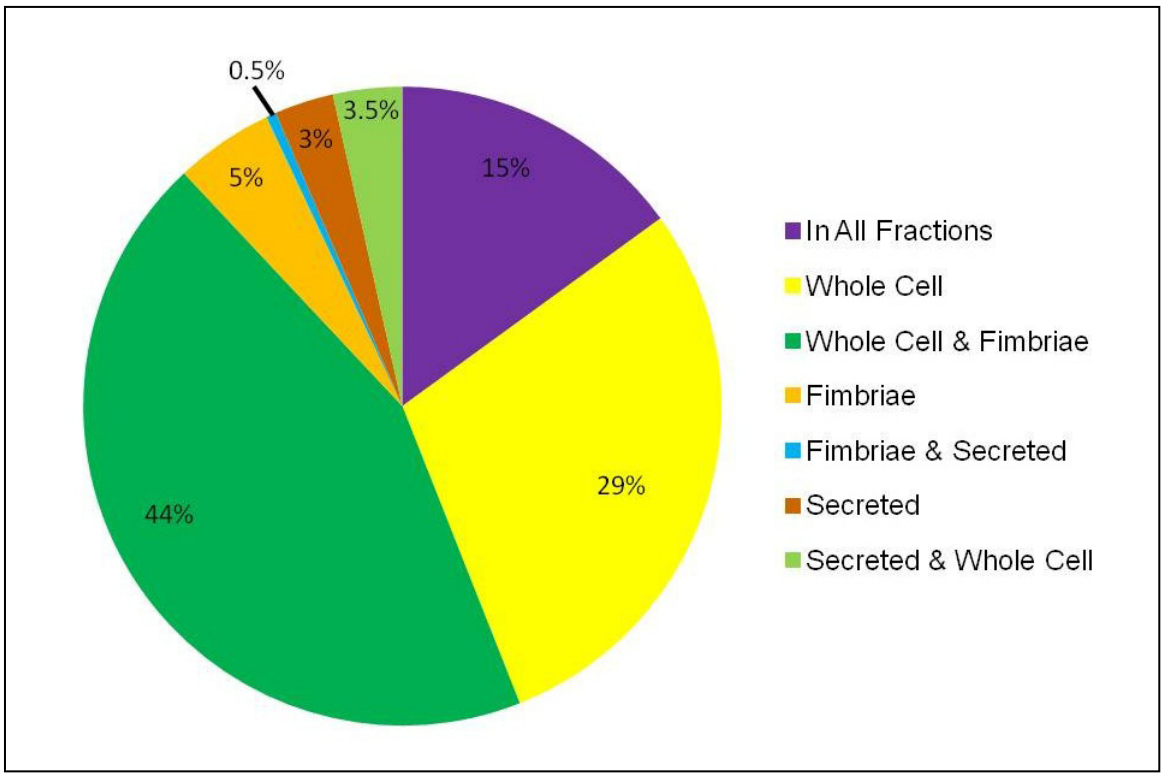

Figure 2. Percentage of observed proteins localized to various fractions of *E. coli* O157:H7.

The fraction-specific proteins were mapped to *E. coli* metabolic pathways using the KEGG. Table 1 summarizes the numbers of proteins mapped for each fraction. For a given protein, the NCBI protein identification (ID) number was used to obtain the KEGG ID number. The KEGG ID number was then used to determine the KEGG pathway identification and pathway map. The mapping of one example protein is shown in Figure 3.

Table 1. Number of Proteins Mapped to *E. coli* metabolic pathways.

Fraction	# of Proteins Mapped
Whole Cell	57
Fimbriae	14
Secreted	6
Total	**77**

Of particular interest are two proteins identified in the fimbriae fraction: the glucose-specific phosphotransferase system (G-PTS) component protein given in the example (Figure 3) and inositol monophosphatase (IMP). In addition, ~35% of pathway hits for the fimbriae fraction involved carbohydrate and energy metabolism, compared to ~18% and ~7% of whole cell and secreted fraction hits.

ID#	Fimbriae Protein Name
YP_002270949.1	aspartyl-tRNA synthetase
YP_002402495.1	hypothetical protein EC55989_1415
YP_002403827.1	Inositol monophosphatase
YP_669175.1	2-dehydro-3-deoxyphosphooctonate aldolase
YP_669361.1	hypothetical protein ECP_1453
YP_669553.1	phosphoenolpyruvate synthase
YP_669562.1	putative glutathione peroxidase
YP_669684.1	hypothetical protein ECP_1780
YP_670126.1	50S ribosomal protein L25 (could be impurities)
YP_670331.1	**glucose-specific PTS component**

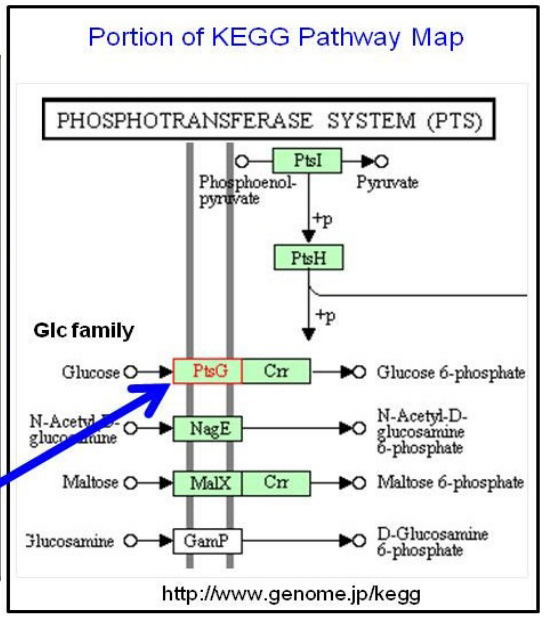

Figure 3. Mapping of a protein to its corresponding metabolic pathway.

4. CONCLUSIONS

We analyzed *E. coli* O157:H7 whole cell, fimbriae, and secreted protein fractions by LC-MS/MS. Proteomics analysis of the LC-MS/MS data resulted in the identification of 201 proteins, of which ~15% were common to all three fractions, and ~10% were strain-unique. In addition, ~30%, ~5%, and ~3% were specific to the whole cell, fimbriae, and secreted protein fractions, respectively. Biochemical pathway mapping using KEGG was carried out for 77 proteins. The fimbriae-specific subset included proteins involved in carbohydrate metabolism, which would be important in providing energy for fimbriae motion. Moreover, IMP, which has a role in streptomycin synthesis, and G-PTS, involved in environmental processing, were also identified. The functions IMP, G-PTS, and a recently-identified putative stress protein in the suspension would be expected to be part of survival mechanisms. This research is expected to provide fundamental knowledge regarding extracellular proteins produced by Gram-negative bacteria and further the development of a high-throughput platform for analyzing samples for the presence of biological constituents. The identification of molecular level components important for survival mechanisms could prove useful in arenas such as vaccine and antibiotic development.

WORK CITED

[1] Vranakis, I; et al.; July 27, 2011, *J. Proteome Res.* Web publication ahead of print. DOI 10.1021/pr200422f.
[2] Ostrowski, A.; et al.; 2011, *J. Bacteriol.* 193, 4043.
[3] Kuehn, M.J. & Kesty, N.C., 2008, *Genes & Development* 19, 2645.
[4] Ciofu, O.; et al., 2000, *J. Antimicrob. Chemother.* 45, 9.
[5] Sidhu, V. K.; et al.; 2008, *BMC Microbiology* 8, 87-92.
[6] Schooling, S.R. & Beveridge, T.J., 2006, *J. Bacteriol.* 188, 16.
[7] Levin, B.R. & Rozen, D.E., 2006, *Nature Reviews Microbiology* 4, 556.
[8] Jabbour, R.E. et al. 2010. *Appl. Environ. Microbiol.* 76, 3637-3644.
[9] Keller, A. et al. 2002. *Anal. Chem.* 74, 5383-5392.

Molecular toxicology of TICs in human embryonic stem cells

Janna S. Madren-Whalley[a], Vicky L. H. Bevilacqua[a], Jessica A. Palmer[b], Robert E. Burrier[b], Alan M. Smith[b], Kevin R. Conard[b], Paul R. West[b], and Jennifer W. Sekowski[a]
[a]Edgewood Chemical Biological Center, Research & Technology Directorate, 5183 Blackhawk Rd., Aberdeen Proving Ground, MD 21010
[b]Stemina Biomarker Discovery, Inc., Madison, WI, USA 53719

ABSTRACT

Given their wide spread use, lack of barriers for procurement, and potential for serious health consequences if deployed by a terrorist, TICs represent a real threat to the warfighter and civilians at home and abroad. Unfortunately, for a vast number of TICs, including the widely-used organophosphate (OP) insecticide MP, which is used in crop spraying, mosquito control, etc., there is incomplete knowledge regarding the basic molecular toxicological consequences of exposure in humans.[1-4] While the literature suggests diverse toxicological consequences for MP exposure, it is all based on human epidemiological studies, *in vivo* animal studies, or *in vitro* studies using immortal cell lines. Thus, there remains no definitive connection to the molecular events that occur during MP exposure in "normal" human cells. Here we have studied the effects of MP and its active metabolite, MPO, on undifferentiated WA09 hES cells utilizing LC-MS and real time (RT)-PCR. Our results suggest that MP and MPO significantly and differentially impact the metabolism of hES cells and that MP affects the expression of key genes involved in the differentiation and pluripotency of hES cells.

1. INTRODUCTION

Chemicals that have certain known effects in adults can have dramatically different toxic effects during embryonic and prenatal development. For example, the successful adult anti-epileptic drug, valproate, has a dramatic toxic effect on embryonic development, leading to neural tube deficits, autism, and cognitive dysfunction.[5] Cezar et al. used LC-MS to examine the metabolites in spent medium from pluripotent hES cells exposed to valproate and found a blockage of the serotonin production pathway. Therefore, an important part of any complete toxicological evaluation must include examination of the compound's effect on human embryonic development. The use of hES cells to explore human embryonic molecular toxicological endpoints is promising in the field of toxicology. Since pluripotent hES cells contain the ability to differentiate into any somatic cell in the body, they provide a unique window into the influence of toxicants on the entire early human development process. In this study, we hypothesize that by using pluripotent WA09 hES cells to measure molecular toxicological endpoints, we will begin to understand the impact TICs have on early processes influencing pluripotency and differentiation pathways in human development. We collected both metabolomic and transcriptomic data from exposed and control pluripotent WA09 hES cells. By comparing metabolomic data from the secretome (in spent medium) with the intracellular transcriptome, we will more completely and accurately illustrate the functional consequences of exposure to operationally relevant TICs during early human development.

2. METHODS

2.1 Metabolomics

Cell viability and dosing curves
Cell viability assays were performed to establish three concentrations to dose hES cells for metabolomic studies. First, hES cells were plated in 96-well format at 250,000 cells/well and dosed with eight concentrations of MP (0.01, 0.1, 0.5, 1, 10, 50, 100, 200 µM) dissolved in DMSO. These doses were

chosen after a literature review of *in vitro* experiments on MP covering the dose range used in those experiments.[6-9] A dose response was not seen in the first set of doses. A second set of dose curve experiments at higher dose levels was performed. In the second set of dose curve experiments, hES cells were treated with another eight doses of MP, spanning 0-1000 μM. After 72 hours of compound exposure, cell viability measurements were taken using the MultiTox-Fluor cell based assay (Promega). Additionally, the number of cells/well was determined following treatment. Concentration curves were calculated to determine the three concentrations for the metabolomics analysis. The final concentrations employed in the study were those that caused no cell death and minimal cell death, if possible. The general aim of this study was to evaluate the metabolome of hES cells exposed to chemicals which may cause developmental toxicity; therefore, doses were employed which are not likely to reflect major metabolic or biochemical injury as a result of cytotoxicity or cell death. An experiment to determine if hES cells were metabolizing MP into its active metabolite, MPO, was conducted. To determine if hES cells were metabolizing MP to MPO, hES cells were treated with eight concentrations (0-500 μM) of MP and the response was assessed. Following 72 hours of compound exposure, viability was measured using the MultiTox-Fluor cell viability assay. Additionally, cells were counted to determine the number of cells/well remaining following treatment.

Cell culture for metabolomic analysis
For metabolomic analysis, hES cells were dosed at the three concentrations for each chemical compound based on the cell viability data. Media controls (no cells), dosed media controls (no cells with dosed media), and controls (cells with undosed media) were also included in the experimental design. Additionally, a positive and negative control was included on the plate. In both the viability and metabolomics steps, 96-well plates were seeded with 250,000 cells/well of WA09 hES cells. These cells were exposed to compound for three days. Each day, the spent media was removed and replaced with mTeSR®1 media containing the designated compound. Each compound stock solution was made in DMSO and each final solution used to dose hES cells contained 0.1% DMSO. Spent media samples were collected on the fourth day and quenched with 40% acetonitrile. Quenched samples were stored at -80°C until they were prepared for metabolomic analysis. Viability was measured after sample collection using the MultiTox-Fluor viability assay.

Sample preparation
To isolate the small molecular weight compounds (<10 KDa) from samples for metabolomics experimentation, the Millipore Multiscreen Ultracel-10 molecular weight cut-off plates were used. These plates were first washed with a 0.1% sodium hydroxide solution and then twice with water to remove contaminant polymer product. The quenched samples were added to the washed filter which was centrifuged at 2000 x g for approximately 200 minutes at 4°C; the flow-through was collected, and then dried overnight in a SpeedVac. Lastly, the dried samples were reconstituted in 70 μL of 1:1 0.1% formic acid in water: 0.1% formic acid in acetonitrile and transferred to a 96-well plate compatible with the Agilent LC-QTOF-MS system.

LC-MS experimental
Samples were analyzed in both ESI positive and ESI negative modes on the Agilent QTOF Model G6530A, serial number US10162003, operated in high resolution, extended dynamic range mode. A Phenomenex Luna HILIC column; 100 x 3mm; P/N 00D-4449-Y0, 512587-1 was used for the analysis.

2.1.1 Data processing

Data preprocessing
This section outlines how the raw LC-MS data files were handled and evaluated during the data analysis process prior to statistical analysis for differential feature identification.

mzData file creation
Agilent raw data files were converted to the open source mzData file format using Agilent MassHunter Qual software version 3.0. During the conversion process, deisotoping (+1 charge state only) was performed on the centroid data and peaks with an absolute height less than 400 (approximately double the typical average instrument background level). The resulting mzData files contain centroid data of deisotoped (+1 charge state only) peaks that have an absolute height greater than 400 counts.

Mass feature creation and integration
Peak picking and feature creation were performed using the open source software library XCMS. Mass features (peaks) were detected using the centWave algorithm. Following peak picking deviations in retention times were corrected using the obiwarp algorithm that is based on a non-linear clustering approach to align LC-MS samples. Mass feature bins or groups were generated using a density based grouping algorithm. After the data had been grouped into mass features, missing features were integrated based on retention time and mass range of a feature bin using the iterative peak filling. Feature intensity is based on the Mexican hat integration values of the feature extracted ion chromatograms.

Adduct and higher charge state isotope filter
This algorithm evaluates feature groups and calculates the probability that related features are due to common adducts or isotopes using a correlation based method. The abundance levels for the related features are summed and the redundant features are removed from the XCMS dataset. Features that are the result of the combining isotopes and adducts contain an "_A" or "_I" in the feature ID.

Mass defect filter
The filter combines both linear and polygon based filters to exclude or include mass features. The filter was trained using all of the chemical formulas in the Stemina MetDB and creates a conservative filter that allows many endogenous metabolites, peptides, drugs, and drug metabolites through while removing features of unlikely biological origin.

Solvent/extraction blank filter
The extraction blank filter removes ions associated with the sample extraction process and background ions present in the LC-MS system. Features were removed from the metabolomics dataset if the average in the experimental samples was less than five times the average abundance in the extraction blanks.

Contamination DB filter
The contamination DB filter removes features with a mass match within 20 ppm to entries in Stemina's proprietary database which contains a number of contaminants such as plasticizers and PEG compounds identified in previous studies. Features were removed without respect to retention time if they matched a contaminant or a common charge specific adduct of a contaminant.

2.1.2 Statistical analysis and identification of differential features

Abundance and reproducibility filter
Prior to statistical analysis, features were filtered by factor (e.g., experimental compound by dose) to remove features that did not exhibit abundance greater than 20,000 in 65% of the LC-MS runs for at least one dose level (L, M, H) of at least one experimental compound (e.g., MP or MPO). This filter selects against spurious low abundance features at the level of detection that are not reproducibly measured, and features that may not have peak shapes amenable to reproducible detection and/or integration. This filter typically removes a large portion of the metabolomics dataset, and focuses the analysis on the most reliable and valuable features. For example a feature with abundance values greater than 20,000 in 70% of the negative mode LC-MS samples in one dose level of one experimental compound and abundance values greater than 20,000 in none of the other experimental compound by dose combinations would pass the filter because at least one experimental compound by dose factor satisfies the filter criteria.

Data transformation and normalization
All data was log base two transformed. Normalization for each factor level was performed by subtracting the column (sample) mean and dividing by the row (feature) standard deviation for each value.

Differential analysis of mass features (univariate)
Mass features were evaluated under the null hypothesis that no difference is present between the means of experimental classes and the alternative hypothesis that there is a difference between experimental classes. Welch two sample T-tests were performed as a parametric method that does not assume equal variances of the experimental classes. False discovery rates were controlled for multiple testing using the Benjamin–Hochberg (1995) method of p-value correction of the ANOVA and Welch T-tests.

Analysis of mass features (multivariate)
Multivariate (or chemometric) analysis is the application of statistical/machine learning procedures to identify a group of features that have valuable experimental information. These methods differ from univariate methods in that they consider the importance of a given feature with respect to all of the mass features present in the experimental comparison. This information is typically displayed graphically by separation of groups, but the measure of a given features importance to the separation of the experimental classes in multivariate space is evaluated by ranking a features contribution. Two different multivariate methods were applied to the data to evaluate the importance of features, a supervised method and an unsupervised method by dose and experimental compound. Principal component analysis (NIPALS PCA) was the unsupervised method used to evaluate the contribution of a feature by ranking the loadings values of features over three principle components. The supervised linear classifier method partial least squares-discriminant analysis (PLS-DA) was used to rank the importance of features based on their ability to discern experimental classes. The PLS-DA scored mass features based on the variable importance in projection (VIP) scores.

Identification of Mass Features
Annotation of mass features was carried out by comparing the m/z mass values of the mass features to Stemina's internal metabolite database containing records from multiple public databases such as HMDB, KEGG, PubChem Compound, and METLIN and company-specific metabolite data. The features were annotated with respect to the appropriate adducts for each ESI mode. The identities of all mass features were not validated; therefore, all annotations are putative.

Prediction of Developmental Toxicity
Prediction of teratogenicity was performed using a random forest (RF) classification model based on metabolic changes observed in the spent cell culture media (secretome) from WA09 hES cells treated with pharmaceutical agents. The RF classifier model was trained on the secretome of hES cells treated with the published therapeutic circulating doses of 22 pharmaceutical agents of known teratogenicity that included 10 known teratogens (accutane, 5-fluorouracil, busulfan, hydroxyurea, rifampicin, cyclophosphamide, methotrexate, retinoic acid, thalidomide, and valproate) and 12 known non-teratogens (ascorbic acid, caffeine, diphenhydramine, doxylamine, folic acid, isoniazid, levothyroxine, penicillin G, retinol, saccharin, thiamine, DMSO). The devTOX™ version 1.0 model is based on the median fold change (median treatment abundance versus its associated intra-experimental median control value) of 138 mass features common among the secretome of hES cells treated with pharmaceutical agents and unknown chemical compounds.

Pathways analysis
Pathways enrichment analysis was performed by mapping annotated mass features for each experimental compound to human metabolic pathways using KEGG compound ids. Hypergeometric p-values and false discovery rates (FDR) were used to assign a quantitative measure of statistical significance to each pathway. Features derived from ESI negative and positive mode for each experimental compound were pooled for this analysis. False positive results can be generated by isobaric compounds that generate

multiple "hits" in a pathway from the same mass, so unique masses instead of unique compound ids were used for these calculations. The relevant parameters used to calculate hypergeometric p-values for each pathway were: the number of unique mass "hits", the number of unique masses in the pathway, and the total number of unique masses in all of the human pathways in the KEGG database. For each experimental compound, the p-values for the derived pathways were converted to FDR using the Benjamini and Hochberg (1995) correction.

Selection of interesting features
Feature selection was performed on a compound by dose basis using Welch T-tests and fold changes. Features were selected for further evaluation if they had a Welch FDR<.05 with at least a 75% fold change. If a feature was selected as interesting in a drug or dose level comparison it was then evaluated experiment wide for fold changes. Following feature selection, only significant features putatively annotated as human in origin and present on KEGG pathway diagrams were further evaluated. Pathway enrichment analysis was then performed on the selected features and features in pathways exhibiting a statistically significant enrichment were further evaluated for fold changes. These selection criteria focused the analysis on biochemical pathways.

2.2 Transcriptomics

Cell culture
hES cells (WA09) were purchased from the WiCell Institute, Madison, WI and were grown in mTeSR®1 medium (STEMCELL Technologies, Inc.) according to WiCell protocols. To determine the dose response, small colonies of hES cells were seeded into Nunc six-well plates that were coated with Matrigel™ (BD) according to WiCell protocols. Cells were exposed to 1 mM, 500 μM, 250 μM, 100 μM, 50 μM, 25 μM, 10 μM, and 5 μM MP to determine three concentrations to be used for transcriptomics experiments (RT-PCR). Vehicle and untreated controls were exposed to 0.5% DMSO and cell culture medium only, respectively. Cells were counted and viability determined using a Beckman Coulter Vi-CELL XR® after exposure. Final concentrations of MP selected for the study were those that caused minimal or no cell death. For RT-PCR experiments, cells were seeded into six-well plates and on day four post-seeding, cells were exposed for 24 hrs to 100 μM, 10 μM or 1 μM MP (dissolved in DMSO) or 0.5% DMSO (vehicle control) in mTeSR®1 medium. Untreated controls were exposed to cell culture medium (mTeSR®1) only. After exposure, cells were trypsinized, washed once in DMEM and once in mTeSR®1 medium and pelleted by centrifugation at 2000 rpm for 2 min. Cell lysates were prepared by adding lysis buffer (Qiagen, RNeasy® Mini Kit, cat #74104), following kit protocol, to the cell pellets and mixing 10 x with a 20 g needle and 1 mL syringe. Cell lysates were frozen at -80°C until the following day.

RNA preparation
Cell lysates were thawed on ice and RNA was extracted using an RNeasy® Mini Kit (Qiagen, cat #74104) and Qiagen protocols. The RNA was quantitated and checked for purity using an Experion™ RNA StdSens Analysis Kit and protocol (Bio-Rad, cat# 700-7103) and run on an Experion™ (Bio-Rad) Automated Electrophoreseis System.

RT-PCR
cDNA was synthesized from the mRNA using an RT^2 First Strand Kit (Qiagen, cat#330401). The cDNA was quantitated using the SA Biosciences RT^2 Profiler RT- PCR array (Qiagen) using an ABI 7900 PCR instrument. This array (cat# PAHS-081) measures the expression of 84 key genes involved in the pluripotency and differentiation of human embryonic stem cells.

Data Analysis
Raw RT-PCR data were analyzed using RT^2 Profiler Data Analysis Software (Qiagen). This free, web-based data analysis software automatically performs all ΔΔCT based fold-change calculations from the raw threshold cycle data.

The data were normalized and pair-wise comparisons between all groups and pairs of experimental replicates made using fold-change and statistical significance threshold of p=0.05 with Bonferroni correction. While a fold significance cut-off of 2 is typically used in transcriptomic analysis, genes exhibiting significant, but lower, fold changes were included in this manuscript. It is becoming recognized that small measured transcriptomic trends may be indicative of significant biological trends when the data are compared with other 'omics data. In year two, these data will be compared to the Phase II metabolite identification work that will be completed in year two. All samples used and all assay steps have passed Quality Control (QC) measurements such as quality of RNA, absence of genomic DNA, reverse transcription efficiency and positive PCR control data.

3. RESULTS

3.1 Metabolomics

Dose response curves

After compound exposure, cell number and viability was determined. The Multitox-Fluor assay was used to determine the viability and cytotoxicity present after treating the cells for 72 hours with MP or MPO. The relative fluorescence units (RFU) for viability (live cell protease) are normalized to the 0.1% DMSO control readout by dividing the viability RFU of each well by the average 0.1% DMSO viability RFU. To determine the average number of cells/well, the three wells for each treatment were trypsinized and pooled. An aliquot was taken from this sample and added to trypan blue to determine the number of viable cells/well. Cell counts were performed on each treatment sample using an automated cell counter (Nexelcom Cellometer Auto T4). Treatment of hES cells with 0-200 μM MP did not identify a decrease in cell viability or cell number. In the next set of experiments, hES cells were treated with 0-1000 μM MP. A decrease in cell viability was seen at starting at 100 μM. The data from these two experiments was combined to determine the EC_{30}, EC_{10}, and EC_0 for metabolomics treatment. In the third set of viability experiments, hES cells were treated with MPO, the active metabolite of MP. As expected, MPO was found to be more cytotoxic than its parent compound. A sharp decrease in cell viability is seen between 125 and 250 μM. Very few (~14000) cells survived treatment with 500 μM MPO. These results suggest that hES cells do not efficiently metabolize MP into its active metabolite.

LC-MS evaluation of MP and MPO

We plotted the m/z values for MP and MPO to determine if hES cells are indeed converting parathion to the active paraoxon form. Based on EICs for the high and low doses of MP and MPO in plate D112, corresponding to M+H, M+Na and M-H, there was a chromatographic peak at 4 min. that is consistent with MPO (M-H) and present in only the MPO high dose samples. This peak was not present in any dose of MP and not detected in any sample under these LC-MS conditions. This is consistent with the hypothesis that MPO exposure is necessary for toxicity.

Prediction of teratogenicity

The prediction of teratogenicity of MP and MPO was performed utilizing the random forest based devTOX™ version 1.0 model. Two positive controls treatments (valproate and penicillin G) of known teratogenicity and a solvent control were added to confirm accuracy of prediction. Evaluation of the control samples suggests that the model was performing normally on this set of data by predicting the positive and solvent control correctly (Table 1). The model conclusively predicted that MPO is teratogenic at each dose level utilized in this experiment. The prediction of MP, however, did not yield a conclusive prediction (confidence > 0.1) at 1 μM and 50 μM treatment levels. Since a conclusive prediction was not determined for MP the treatments were repeated and tested using the predictive model. The second replication did not produce a conclusive prediction at 50 μM, but produced a conclusive prediction at 1 μM. Based on these results, we predict that a dose of 500 μM MP is teratogenic, a dose of 1 μM is non-teratogenic, and that the teratogenicity of 50 μM MP cannot be determined at this time.

Table 1. The prediction of teratogenicity by the devTOX™ version 1.0 random forest model. The replication column denotes if a sample was repeated. The effect column denoted a test compound's developmental toxicity, if it is known. The prediction column provides the developmental toxicity prediction of the model as Ter (Teratogen), Non (Non-teratogen), or I for inconclusive followed by the model prediction. The random forest generated class probabilities are % Non and % Ter. Confidence values less than 0.1 are considered inconclusive with respect to the class prediction and are marked with an asterisk (*).

Treatment	Dose	Replication	Effect	Prediction	% Non	% Ter	Confidence
Methyl paraoxon	180 µM	1	Unknown	Ter	0.18	0.82	0.64
Methyl paraoxon	130 µM	1	Unknown	Ter	0.24	0.76	0.52
Methyl paraoxon	72 µM	1	Unknown	Ter	0.28	0.72	0.44
Methyl parathion	500 µM	1	Unknown	Ter	0.38	0.62	0.24
Methyl parathion	50 µM	1	Unknown	I/Ter*	0.47	0.53	0.06*
Methyl parathion	1 µM	1	Unknown	I/Ter*	0.46	0.54	0.08*
Methyl parathion	500 µM	2	Unknown	Ter	0.22	0.78	0.56
Methyl parathion	50 µM	2	Unknown	I/Non*	0.54	0.46	0.08*
Methyl parathion	1 µM	2	Unknown	Non	0.57	0.43	0.14
Penicillin G	48 µM	1	non	Non	0.74	0.26	0.48
Valproate	1000 µM	1	Ter	Ter	0.22	0.78	0.56
DMSO	0.10%	1	non	Non	0.74	0.26	0.48

3.2 Transcriptomics

Dose response curve

Cells exposed to 1 mM, 500 µM, 250 µM, 100 µM, 50 µM, 25 µM, 10 µM, and 5 µM MP were counted and cell viability determined using a Beckman Coulter Vi-CELL XR® four days after exposure. Cells exposed to the three highest concentrations of MP (1 mM - 250 µM) showed a sharp decrease in viability and cell number after four days in culture. Cell viability and counts were comparable to controls for the cells receiving concentrations of MP at 100 µM and lower. Final concentrations of MP (100 µM, 10 µM, 1 µM) selected were those that would cause minimal or no cell death.

RT-PCR

cDNA was quantitated using an SA Biosciences RT^2 Profiler RT-PCR array which measures the expression of 84 key genes involved in the pluripotency and differentiation of hES cells. Some genes were up-regulated in cells exposed to DMSO (0.5%, VC, Figure 1) while other genes were up-regulated in cells exposed to only the highest concentration of MP (Figure 2). Genes down regulated in cells exposed to the lowest dose of MP (1 µM) are shown in Figure 3. DDX4, a DEAD box protein belonging to a gene family involved with many processes, including translation initiation, nuclear/ mitochondrial splicing, and ribosome and spliceosome assembly was up regulated in cells receiving the lowest dose of MP (1 µM, Figure 4). This gene is believed to be involved in embryogenesis, spermatogenesis, and cellular growth and division.

Table 2. Pathways exhibiting statically significant enrichment as evaluated at each dose level of each drug treatment. FDR values are based on pathway enrichment analysis of the individual drug by dose level evaluation.

Treatment	Dose	Kegg Pathway	Pathway Description	Hits	# in Path	P value	FDR
MethylParathion	L	hsa00020	Citrate cycle (TCA cycle)	3	15	0.002165	0.02
MethylParathion	L	hsa00030	Pentose phosphate pathway	3	23	0.007362	0.05
MethylParathion	L	hsa00053	Ascorbate and aldarate metabolism	3	25	0.009242	0.05
MethylParaoxon	H	hsa00260	Glycine, serine and threonine metabolism	6	40	0.006188	0.10
MethylParathion	H	hsa00260	Glycine, serine and threonine metabolism	3	40	0.010283	0.07
MethylParathion	H	hsa00280	Valine, leucine and isoleucine degradation	3	24	0.002486	0.02
MethylParaoxon	H	hsa00290	Valine, leucine and isoleucine biosynthesis	5	18	0.000802	0.02
MethylParaoxon	M	hsa00290	Valine, leucine and isoleucine biosynthesis	6	18	0.00015	0.01
MethylParathion	H	hsa00290	Valine, leucine and isoleucine biosynthesis	3	18	0.001066	0.02
MethylParathion	L	hsa00410	beta-Alanine metabolism	3	31	0.016307	0.07
MethylParathion	L	hsa00561	Glycerolipid metabolism	3	13	0.001408	0.02
MethylParaoxon	H	hsa00620	Pyruvate metabolism	6	24	0.000431	0.01
MethylParaoxon	M	hsa00620	Pyruvate metabolism	5	24	0.005066	0.07
MethylParathion	L	hsa00620	Pyruvate metabolism	4	24	0.000743	0.02
MethylParathion	L	hsa00640	Propanoate metabolism	3	28	0.012509	0.06
MethylParathion	L	hsa00650	Butanoate metabolism	4	31	0.001964	0.02
MethylParaoxon	H	hsa00760	Nicotinate and nicotinamide metabolism	8	37	0.000134	0.01
MethylParaoxon	M	hsa00760	Nicotinate and nicotinamide metabolism	7	37	0.001661	0.04
MethylParathion	L	hsa00760	Nicotinate and nicotinamide metabolism	4	37	0.003737	0.03
MethylParaoxon	M	hsa00770	Pantothenate and CoA biosynthesis	5	24	0.005066	0.07
MethylParathion	M	hsa04142	Lysosome	2	4	0.002426	0.10
MethylParaoxon	M	hsa04930	Type II diabetes mellitus	3	5	0.001157	0.04
MethylParaoxon	M	hsa05211	Renal cell carcinoma	2	3	0.007339	0.08
MethylParathion	L	hsa05211	Renal cell carcinoma	2	3	0.000993	0.02

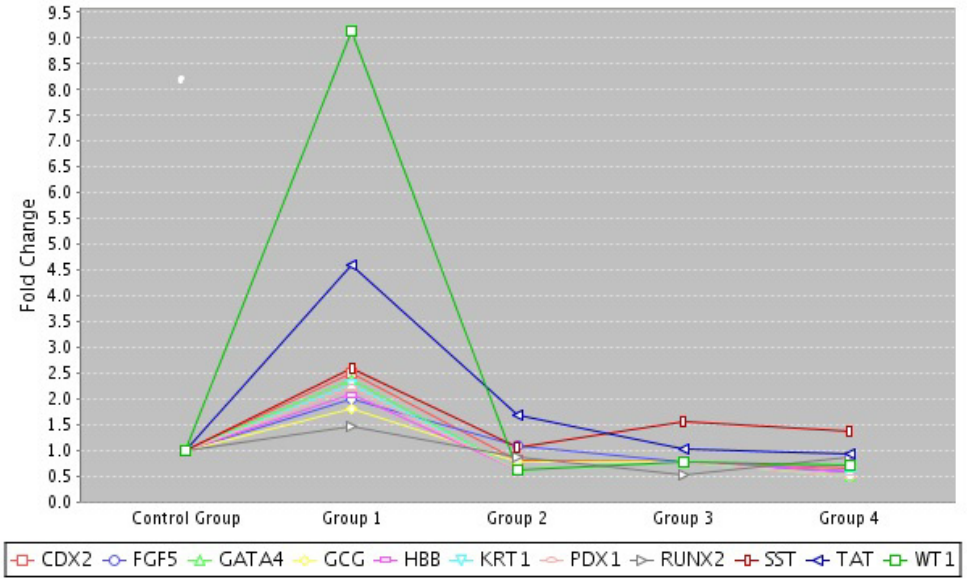

Figure 1. Genes up-regulated in cells exposed to DMSO (0.5%). WT1 = Wilm's Tumor 1 protein, a transcription factor, TAT = encodes a mitochondrial tyrosine aminotransferase, SST = somatostatin, a widespread hormone regulator, CDX = caudal type homobox, binds to the insulin promoter, GATA4 = encodes a transcription factor, important in embryogenesis and myocardial differentiation.

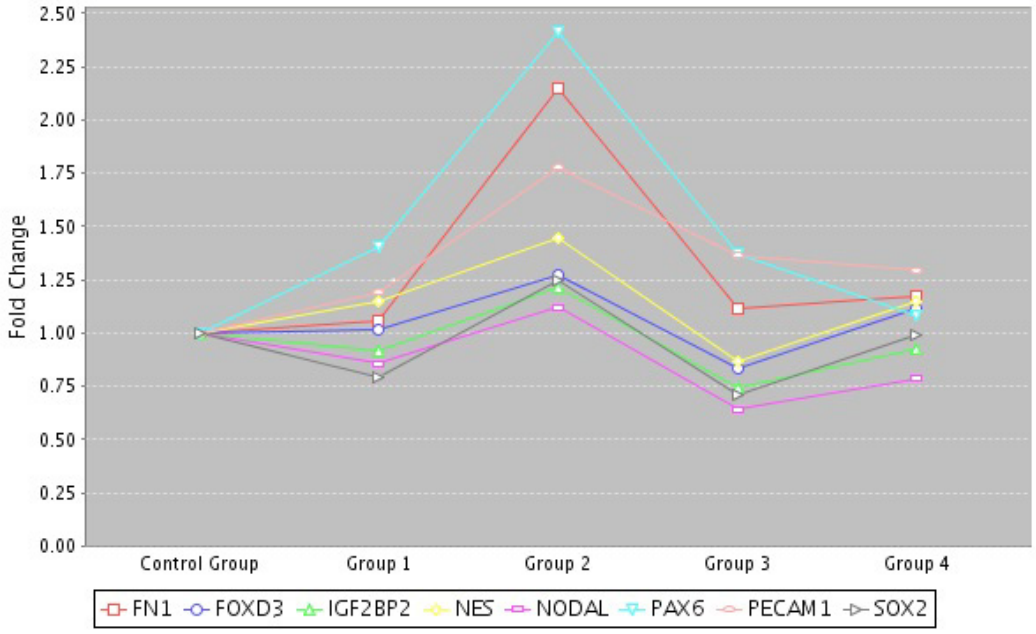

Figure 2. Genes up-regulated in cells exposed to 100 µM MP. PAX6 = Paired Box 6, a regulator of gene transcription in nervous/ocular system, FN1 = fibronectin 1, a glycoprotein involved in embryogenesis, PE-CAM1 = platelet/endothelial cell adhesion molecule, protein of IG superfamily, NES = Nestin, an inter-medicate filament protein in central nervous system (CNS) stem cells.

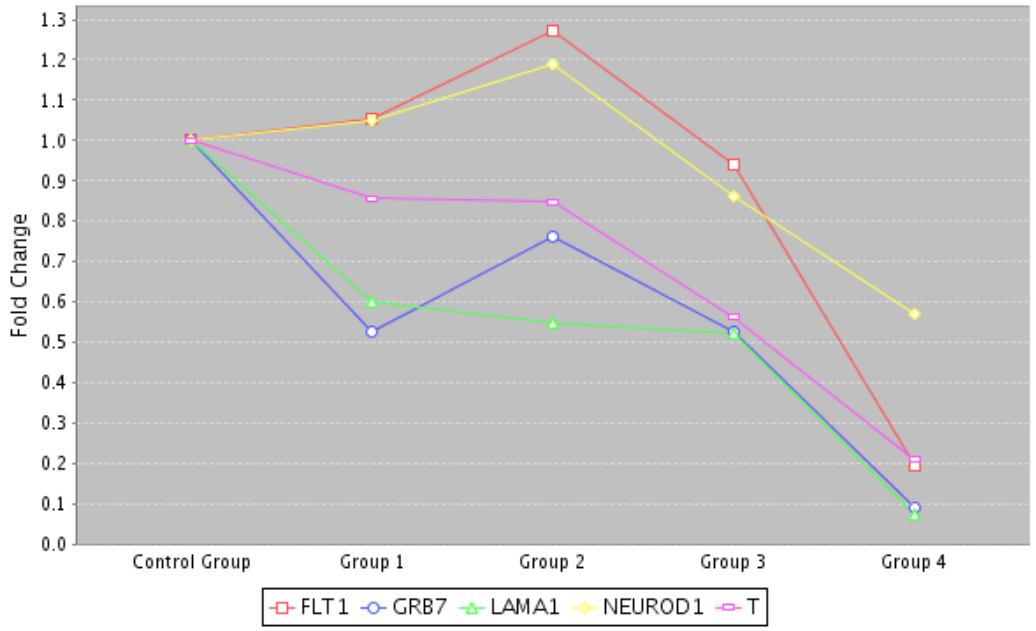

Figure 3. Genes down-regulated in cells exposed to 1 µM MP. FLT1 = fms-related tyrosine kinase 1, a vascular endothelial growth factor receptor protein, NEUROD1 = Neurogenic differentiation 1, transcription factor for the insulin gene, T = Brachyury homolog, embryonic nuclear transcription factor, effects genes required for mesoderm formation, GRB7 = growth factor receptor-bound protein 7, adaptor protein interacts with a number of receptor tyrosine kinases, LAMA1 = Lamin alpha-1, functions in differentiation.

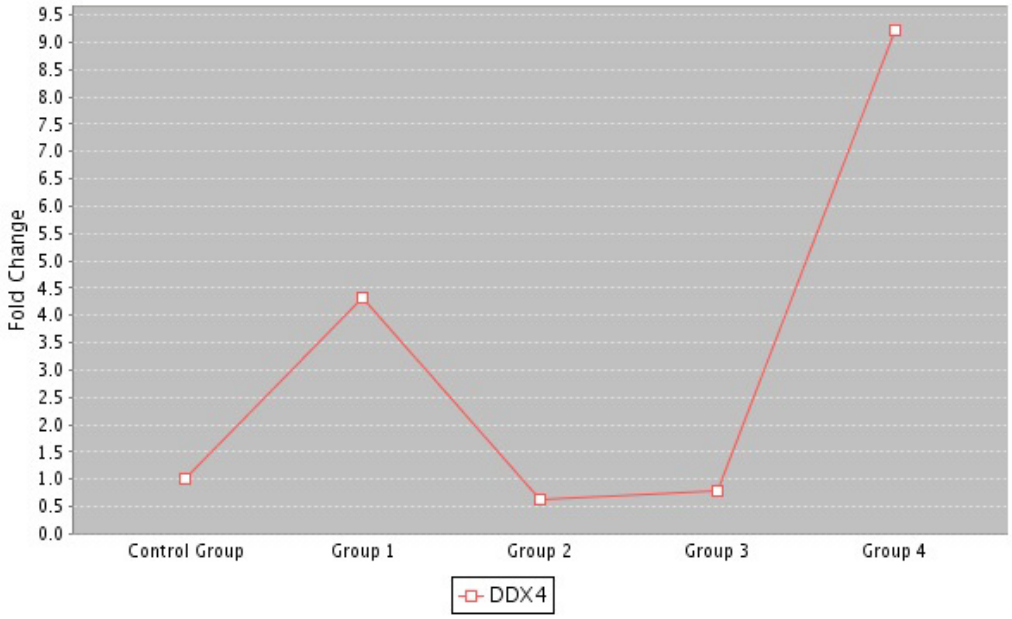

Figure 4. Genes up-regulated in cells exposed to 1 µM MP. DDX4 = DEAD box proteins, characterized by the conserved motif Asp-Glu-Ala-Asp (DEAD). An RNA helicase, this gene family is involved with many processes, including translation initiation, nuclear/mitochondrial splicing, and ribosome and spliceosome assembly. Based on their distribution patterns, this gene is believed to be involved in embryogenesis, spermatogenesis, and cellular growth and division.

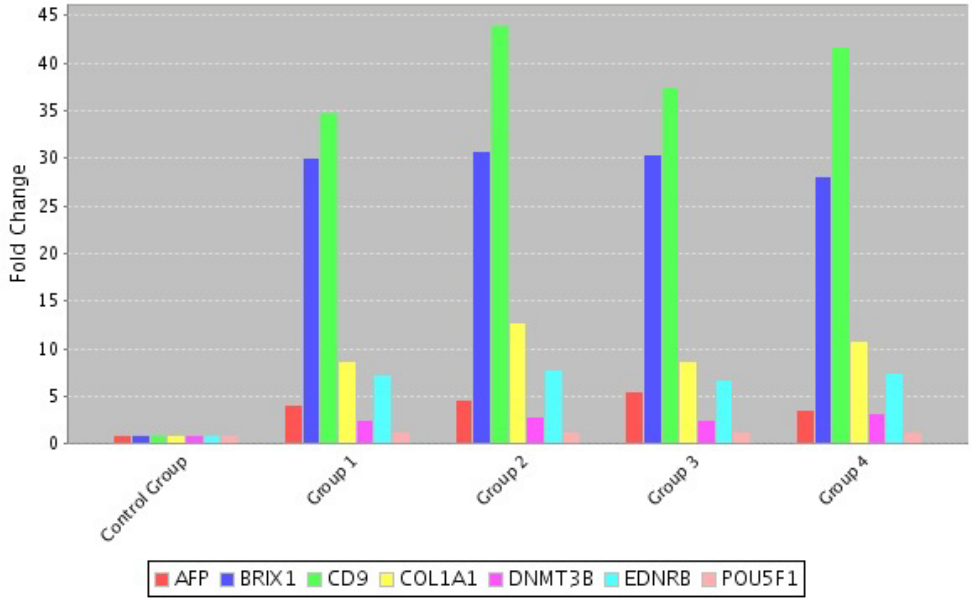

Figure 5. Genes up-regulated in all groups compared to control group. AFP = encodes alpha-fetoprotein, BRIX1 = required for biogenesis of the 60S ribosomal unit, CD9 = encodes cell surface glycoproteins, COL1A1 = encodes type 1 collagen pro-alpha 1 chains, DNMT3B = DNA (cystosine-5-) methyltransferase 3 beta, EDNRB = endothelium receptor type B, POU5F1 = POU class 5 homeobox 1.

Figure 6. Heat Map of relative gene expression in all groups.
RED = up-regulated gene
GREEN = down-regulated gene

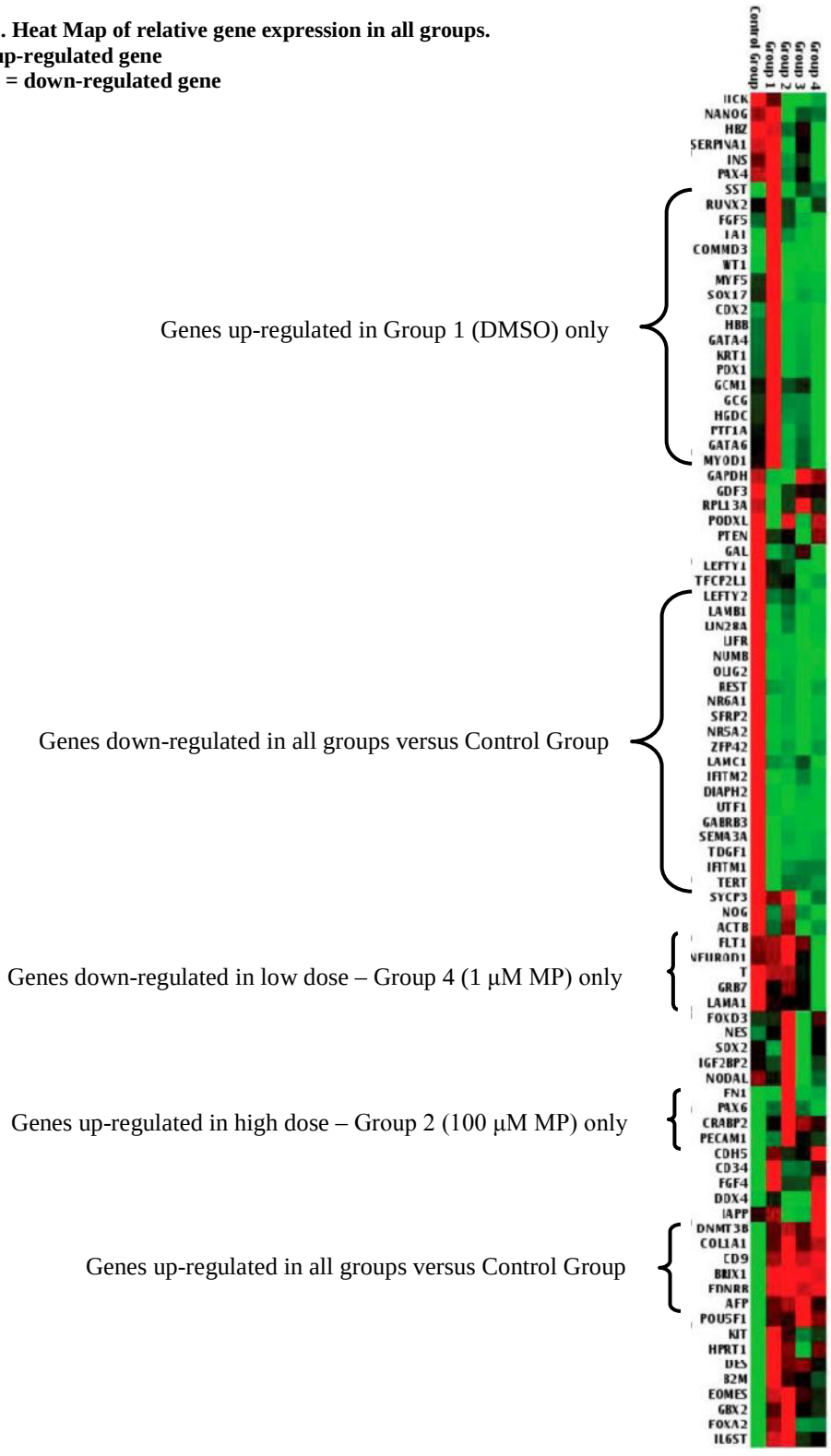

4. CONCLUSIONS

Our results indicate that exposure to MP and MPO significantly and differentially impact the metabolism of human embryonic stem cells. Data also suggest that MP alters the expression of a number of key genes involved in pluripotency and differentiation pathways of undifferentiated hES. These initial results have opened a new avenue toward a better understanding of how exposure to toxic industrial chemicals (such as MP and MPO) may interfere with early human embryonic growth and development.

5. ACKNOWLEDGEMENTS

The authors would like to thank the ILIR program for funding and Dr. A. Way Fountain, Dr. Laura Borland and Mr. Roy Thompson for administrative support.

WORK CITED

[1] Slotkin, T.A. et al. 2007. *Env. Health Pers.* 115(1), 93-101.
[2] Edwards, F.L. et al. 2005. *Int. J. Env. Res. Pu. Health* 2(3-4), 430-41.
[3] Galloway, T. and Handy, R. 2003. *Ecotoxicology* 12 (1-4), 345-63.
[4] Johnson, F.O. et al. 2009. *Tox. Sci.* 109(1), 132-42.
[5] Cezar, G. et al. 2007. *Stem Cells Dev.* 16(6), 869-92.
[6] Isoda, H. et al. 2005. *Environ. Sci.* 12(1), 9-19.
[7] Calaf, G.M. and Roy D. 2007. *Mol. Med.* 13(5-6), 255-265.
[8] Hreljac, I. et al. 2008. *Environ. Mol. Muta.* 49, 360-367.
[9] Guizzetti, M. et al. 2005. *Toxicology* 215, 182-190.

Tuning the optical properties of multi-layered nanoparticles using exciton-plasmon coupling

Brendan G. DeLacy[a], Marin Soljacic[b], Wenjun Qiu[b]
[a]Edgewood Chemical Biological Center, Research & Technology Directorate, 5183 Blackhawk Rd., Aberdeen Proving Ground, MD 21010
[b]Massachusetts Institute of Technology, 77 Massachusetts Ave, Cambridge, MA 02139

ABSTRACT

Colloidal suspensions of double-shell nano-composite structures were fabricated and their optical properties measured in the visible region. The double-shell structures consisted of a silver core, an intermediate silica or thiol layer, and an exterior cyanine dye layer. The goal of this work was to first demonstrate the J-aggregation of a cationic cyanine dye onto a silver/silica or silver/ thiol bi-layered nanosphere. An additional goal was to elucidate the interaction of the localized surface plasmon resonance exhibited by the metallic core with the absorption properties of the outer J-aggregate layer. Silver nanoparticles were synthesized using an aqueous citrate reduction technique. The silver nanoparticles were then coated with a range of thiols. The thiols varied in chemical content and alkyl chain length. Thiols investigated were sodium mercaptopropionate, 3-mercaptopropionic acid, 6-mercaptohexanioc acid, 8-mercaptooctanoic acid, 12-mercaptododecanoic acid, and 16-mercaptohexadecanoic acid. A cationic cyanine dye, 1,1-diethyl-2,2-cyanine iodide (PIC), was then self assembled onto the thiol intermediate layer. The formation of the aggregated form of the dye was observed for sodium mercaptopropionate, 3-mercaptopropionic acid, and 6-mercaptohexanioc acid. Silica coated silver nanoparticles were also coated with PIC and the formation of the J-aggregate was also observed. Finally, a computational model predicting the interaction of electromagnetic radiation for the structures was developed.

1. INTRODUCTION

Silver and gold nanoparticles have been extensively studied for their unique optical properties which arise from localized surface plasmon resonance (LSPR).[1] This resonance results in a large extinction in the visible and near infrared regions due to the strong enhancement of the local electric field both inside and near the surface of the particle. LSPR is described as the resonance between the collective oscillation of conduction electrons and the incident light. This phenomenon has been employed in surface-enhanced Raman scattering (SERS) and enhanced fluorescence spectroscopy.[2,3] The size and morphology of the silver and gold nanoparticles have a significant impact on LSPR and therefore have a great significance on such fields as sensors and photonic devices.

Cyanine dyes are a class of dyes which are known to form J-aggregates in solution.[4] J-aggregates are so named because of their tendency to form a characteristic optical absorption called the J-band, which is °C red-shifted from the monomer band (Figure 1).

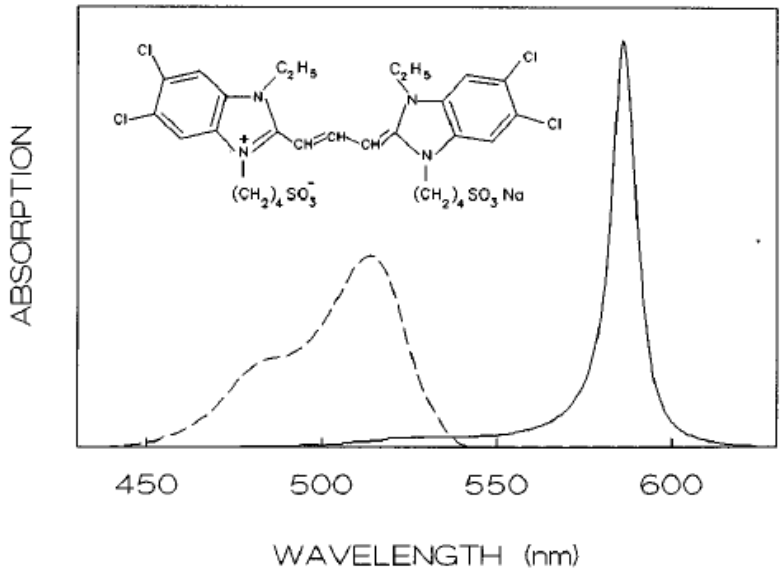

Figure 1. Absorption spectra of a J-aggregate (TDBC) in water. At low concentration (c<<10-6) absorption of monomers is observed (dashed line). At a concentration of c = 5 x 10^{-5} M, little monomer absorption is observed (solid line), since the molecule aggregated into long chains. The red-shifted absorption at 587 nm is due to the excitation of Frenkel excitons on these chains. The molecular structure of TDBC is provided in the inset. Figure Courtesy of van Burgel et al.

These J-aggregates also exhibit resonance fluorescence with small Stokes shifts, ultra short radiative lifetimes, and nonlinear optical properties.[4] Their properties are described in terms of the delocalization of Frenkel excitons, which are derived from the strong coupling between transition dipole moments of the aggregated dye molecules. J-aggregates are relevant to various applications including imaging materials, dye-sensitized solar cells, and optoelectronic devices.

Multi-layered nanoparticles composed of both the J-aggregate dyes and the metal particles offer the potential for impacting a wide range of areas such as optoelectronic materials, nanophotonic materials, solar cell development, and sensors to name a few. In light of the unique optical properties observed for both silver and gold nanoparticles and the J-aggregates dyes, recent efforts in the literature have focused on the synthesis of complex systems composed of J-aggregate/metal nanoparticles. For example, Hranisavljevic et al. measured the absorption spectra of colloidal suspensions containing Ag/J-aggregate composite nanoparticles.[5] Wurtz et al. examined the spectroscopic properties of gold nanorods coated with J-aggregates.[6] In these works, it was observed that the colloidal absorption of the nanoparticles was not the simple sum of the absorption of the metal nanoparticle and the J-band of the aggregate. This is apparent in work done by Kometani et al. where an Au/J-aggregate particle exhibited an absorption “dip” at the position of the J-band but an Ag/J-aggregate nanoparticle exhibited an absorption “peak” at the position of the J-band.[7] The Maxwell-Garnett treatment for both of these systems predicted these unique “dips” and “peaks”.

In another recent work by Yoshida et al, the impact of a spacer layer between the metal core and the J-aggregate dye was explored.[8] In this work, they demonstrated the use of a cationic alkanethiol for facilitating the J-aggregation of four kinds of anionic cyanine dyes at the metal nanoparticle interface. It was also concluded from this work that the spectral line shape of these composite nanoparticles near the J-band depends on the strength of the exciton-plasmon coupling between the metal core and the J-aggregate shell.

In work done by Tischler et al., the optical properties of a multi-layered thin film were explored.[9] The thin film consisted of a dielectric Bragg reflector as a base, a spacer layer, and a J-aggregate absorbing top

layer. Using this structure, it was demonstrated that for a given incident wavelength of 591 nm, 1% of the incident light was transmitted, and only 2% of the light was reflected. These structures offer tremendous potential for the selective attenuation of electromagnetic radiation. An analogous structure is the so-called critically coupled resonator, in which a silver mirror replaces the dielectric Bragg reflector base.

Our focus in this work was to first demonstrate the J-aggregation of a cyanine dye onto a silver/silica or silver/thiol bi-layered nanosphere. More specifically, the goal was to demonstrate the J-aggregation of a cationic form of a cyanine dye onto an anionic surface, which represents a variation from what has been previously reported. Additionally, the focus was to expand on the work done by Yoshida et al. by exploring the impact of spacer layer thickness on the exciton-plasmon interaction. To achieve this, a wide range of mercaptoalkyl carboxylic acids that varied in alkyl chain length were explored as spacer layers. Carboxylic acid functional groups were chosen since they would largely be deprotonated at aqueous pH, and subsequently allow for the adsorption of the cationic cyanine dye. The mercaptoalkyl carboxylic acids used in the study included 3-mercaptopropionic acid, 6-mercaptohexanoic acid, 8-mercaptooctanoic acid, 12-mercaptododecanoic acid, and 16-mercaptohexadecanoic acid. Other mercaptoalkyl surfactants that were explored included 3-mercaptopropanesulfonate (also for its anionic functionality) and 3-mercaptopropane-1-trimethyoxysilane (3-MPTMS). 3-MPTMS was included in the study as a control, since it was not expected that the trimethoxy functionality would result in a negatively charged Ag/thiol surface. 1,1'-diethyl-2,2'-cyanine iodide was the main cyanine dye studied for the adsorption onto the Ag/thiol surface.

Additionally, as an alternative to the use of mercaptoalkyl carboxylic acids, silica (SiO_2) was also used as a spacer layer in the study. The use of silica as a spacer layer is pertinent since the sol-gel technique used to fabricate the silica layer is amenable to controlling the spacer layer thickness. A schematic of the proposed double-shell structures is provided in Figure 2.

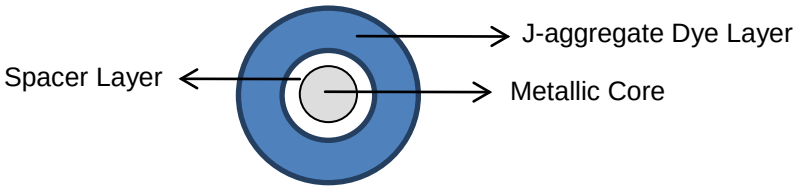

Figure 2. Schematic of the double-shell structure. Silver was used as the metallic core, either a mercaptoalkly carboxylic acid or silica was used as the spacer layer, and 1,1'-diethyl-2,2'-cyanine iodide was used as the exterior dye layer. Note – the schematic is not to scale.

Finally, in order to elucidate the impact of spacer layer thickness on Plasmon-exciton coupling, a computational code describing the interaction of electromagnetic radiation with the multi-layered nanoparticles was developed. The code makes use of the transfer matrix method for spherical nano-particles and can handle an arbitrary number of layers and arbitrary material dispersions. The code was compared to the well established Mie-plot calculations and identical results were obtained. Advantages of the code over the Mie-plot calculations include the ability to handle more complicated geometries and the ability to incorporate nonlinear optics code.

2. EXPERIMENTAL

2.1 Materials

Silver nitrate, trisodium citrate tribasic dihydrate, methanol, ammonium hydroxide (28% NH_3), sodium 3-mercaptopropionic acid, 3-mercaptopropionic acid, 3-mercaptopropyl-trimethoxysilane, 6-mercaptohexanoic acid, 12-mercaptododecanoic acid, 16-mercaptohexadecanoic acid, and 1,1'-diethyl-

2,2'-cyanine iodide were purchased from Sigma Aldrich (St. Louis, MO). Silica coated silver nanospheres were obtained from Nanocomposix (San Diego, CA).

2.2 Synthetic procedure

Silver Nitrate Solution – placed approximately 113 mg $AgNO_3$ and 400 mL H_2O in an Erlenmeyer flask and magnetically stirred. *1% Trisodium Citrate Tribasic Solution* – placed 1.14 g trisodium citrate dihydrate in a 100 mL volumetric flask and diluted to volume with H_2O. *Silver Sol* – transferred silver nitrate solution into a 1 L three-neck flask. Magnetically stirred and heated the solution to 100°C using a heating jacket and temperature controller (Glass-Col, Terre Haute, IN) while refluxing. Once the boiling point was reached, 10 mL of 1% trisodium citrate solution was added dropwise. The mixture was heated for an additional hour at 100°C. The solution was then cooled to room temperature and stirring was continued for an additional hour. *Sodium Mercapto-1-propanesulfonate solution* – placed 210 mg of sodium mercapto-1-propanesulfonate in a 25 volumetric flask and diluted to volume with methanol. *3-mercaptopropionic acid solution* – placed 100 µL 3-mercaptopropionic acid in 25 mL volumetric flask and diluted to volume with methanol. *3-mercaptopropyl-trimethoxysilane solution* – placed 200 µL 3-mercaptopropyl-trimethoxysilane in a 25 mL volumetric flask and diluted to volume with methanol. *1,1-diethyl-2,2'cyanine iodide (PIC) standard solution* – placed 23 mg PIC dye in a 100 mL volumetric flask and diluted to volume with H_2O. *Ag/Thiol Suspension* – transferred 50 mL Ag/citrate solution into a 50 mL centrifuge tubed. The sample was centrifuged at 4000 RPM for 10 minutes, and the supernatant removed using a pipette in order to remove excess citrate. The precipitate was re-suspended in 5 mL methanol and sonicated. The suspension was again centrifuged at 4000 RPM for 10 minutes, and the supernatant removed. Added 5 mL of sodium mercapto-1-propanesulfonate to the silver precipitate and the solution sat overnight. The suspension was again centrifuged at 4000 RPM for 10 minutes and the supernatant removed. Added 5 mL of H_2O to the precipitate, followed by sonication. This procedure was repeated for each of the thiol spacer layers, i.e. 3-mercaptopopionic acid, 3-mercaptopropyl-trimethoxysilane, 6-mercaptohexanoic acid, 12-mercaptododecanoic acid, and 16-mercaptohexadecanoic acid. *Ag/Thiol/PIC Dye Suspension* – 4 mL PIC dye solution was added to 1 mL Ag/thiol solution in centrifuge tube and shaken by hand. The solutions sat overnight in order to enhance the adsorption of PIC dye to the surface of the Ag/thiol nanoparticles. The mixture was then centrifuged at 4000 RPM for 10 minutes, and the supernatant was removed. The precipitate was then re-suspended in 10 mL H_2O with sonication. This procedure was repeated for each of the Ag/thiol combinations. *0.2M NH_4OH* – Diluted 30 mL NH_4OH(28% NH_3) to 1L with H_2O. *Silver/Silica/PIC dye Suspension* – Placed approximately 3 mL silica-coated silver (1.46 mg/mL) suspension in a 50 mL centrifuge tube. Centrifuged at 4000 RPM for 10 minutes and then removed the supernatant. Re-suspended the solid in 5 mL of 0.2M NH_4OH for about 1 hour. Again centrifuged at 4000 RPM for 10 minutes and removed the supernatant. Next, suspended the solid in 5 mL PIC standard solution overnight. Then centrifuged the sample at 4000 RPM for 10 minutes and removed the supernatant. Finally the solid was re-suspended in 10 mL H_2O and sonicated.

2.3 Instrumentation and measurements

UV/Vis absorption spectra of the colloidal suspensions in a quartz cuvette (10 mm optical path length) were measured using an Ocean Optics HR2000CG-UV-NIR spectrophotometer (Dunedin, FL).

3. RESULTS

3.1 Nano-composite spectral results

The absorption spectrum for 1,1'-diethyl-2,2'-cyanine iodide (PIC), the silver sol, various silver/thiol/PIC nano-composites, and the silver/silica/PIC nano-composite are provided in Figure 3. The adsorption of the monomer form of PIC dye was observed for all silver/thiol/PIC nano-composites and silver/silica/PIC

nano-composite at ~518 nm. In addition to the adsorption of the monomeric form, absorption peaks at 569 nm, 575 nm, 579 nm, and 582 nm occurred when silica, 3-mercaptopropanesulfonate, 3-mercaptopropionic acid, and 6-mercaptohexanoic acid were used as the spacer layer, respectively. The location of these peaks corresponds to the J-aggregation of PIC, which typically occurs at 575 nm on various substrates such as gold or montmorillonite clay.[8,11]

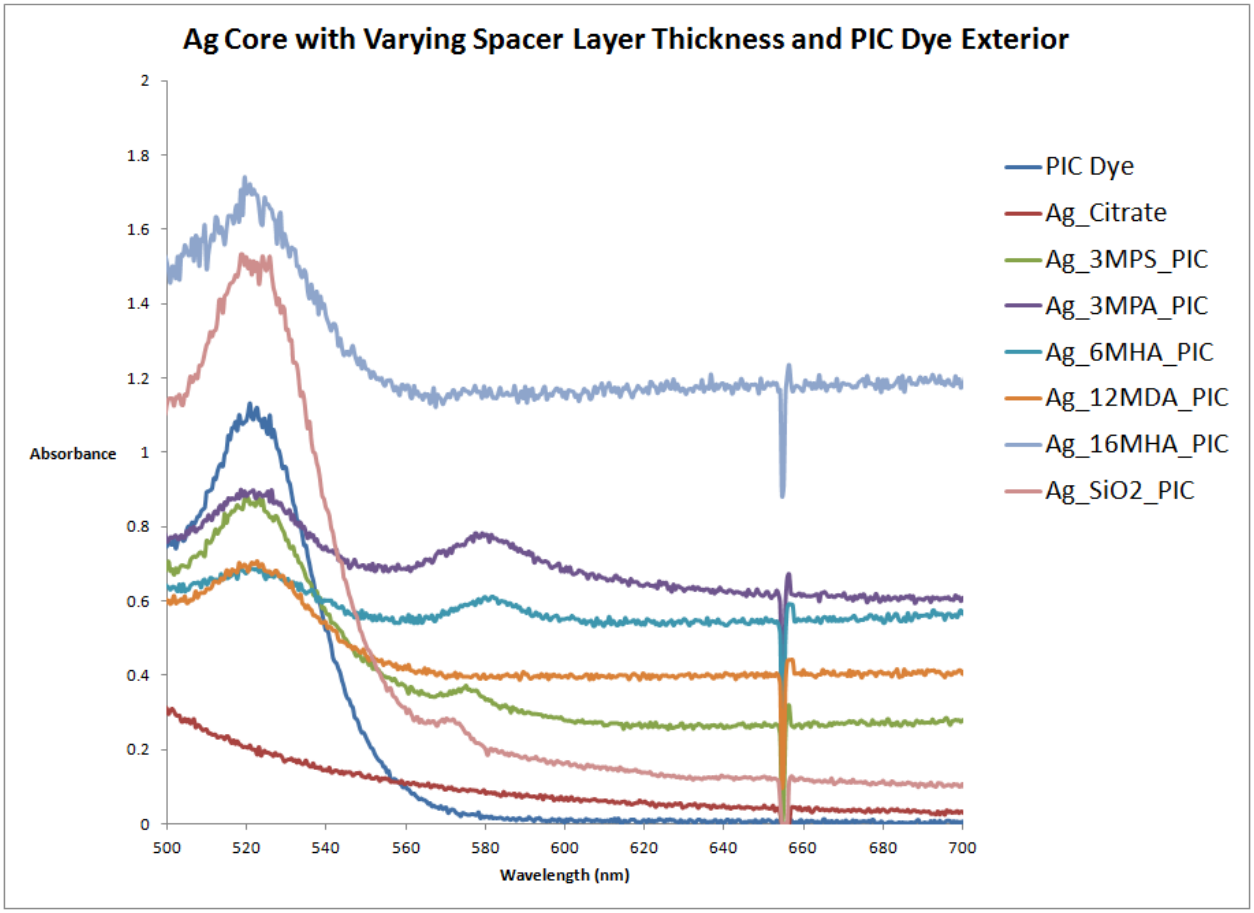

Figure 3. Absorption spectra of silver/mercapto/PIC Dye nanocomposites. Note – Spectra are offset and are not normalized to mass. PIC = 1,1'-diethyl-2,2' cyanine iodide, Ag_Citrate = silver nanoparticles fabricated using citrate method, 3MPS = 3-mercaptopropanesulfonate, 3MPA = 3-mercaptopropionic acid, 6MHA = 6-mercaptohexanioc acid, 12MDA = 12-mercaptododecanoic acid, 16MHA = 16-mercaptohexadecanoic acid.

3.2 Computational results

A computational model describing the interaction of electromagnetic radiation with multi-layered spherical nanoparticles was also developed during the previous research period. For nanoparticles with spherical symmetry, the electrical field can be decomposed into vector spherical harmonics. The radial function of vector spherical harmonics is a linear combination of first and second kind spherical Bessel functions. The coefficients of Bessel functions on the two sides of an interface are connected by a transfer matrix. By multiplying the transfer matrices of all interfaces, the transfer matrix of the nanoparticle may be obtained. Subsequently, the radiative cross-section, absorptive cross-section, resonant frequencies, and efficiency factors may be calculated from the transfer matrix. The code can be implemented for spherical nanoparticles with an arbitrary number of layers and arbitrary material dispersions. The code was compared with the well-established Mie-plot calculation, and identical results were obtained using both techniques. Additionally, a strong correlation was observed when the experimental determination of

extinction for silica coated silver was compared to computational results obtained from the code. Figure 4 provides the experimental and computational results for silica-coated silver. The small deviation in the computational results from the experimental results is due to the fact that a normal distribution of diameters was used in the computation. In reality, the diameters of the silica-coated silver were not normally distributed.

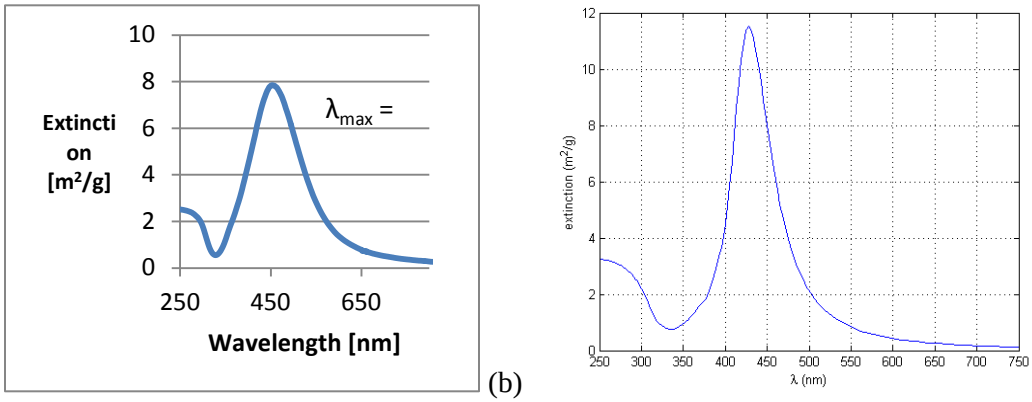

Figure 4. (a) Experimental determination of extinction for silica-coated silver nanoparticles. (b) Computational results for silica-coated silver.

4. DISCUSSION AND CONCLUSIONS

Novel double-shell spherical nano-composites consisting of a silver core, an anionic thiol spacer layer, and a cationic PIC dye exterior were fabricated. A nano-composite comprised of a silver core, a silica spacer layer, and a PIC dye exterior was also demonstrated. Inspection of Figure 3 reveals that the J-aggregate of PIC was observed when silica, 3-mercaptopropanesulfonate, 3-mercaptopropionic acid, and 6-mercaptohexanoic acid were used as the spacer layers; however, the absorption wavelength of the J-aggregate varied for each of these spacer layers. Namely, absorption wavelengths for the J-band were observed at 569 nm, 575 nm, 579 nm, and 582 nm when silica, 3-mercaptopropanesulfonate, 3-mercaptopropionic acid, and 6-mercaptohexanoic acid were used as the spacer layer, respectively. This is in contrast to results obtained in the literature, in which the absorption wavelength of the J-aggregate consistently occurred at 575 nm. The J-band at 575 nm, however, was observed for systems in which either the dye was directly absorbed to the surface of the core particle, or the distance between the core and the dye was fixed. The experimental results obtained herein imply that either, 1) the distance between the silver core and the J-aggregate layer (i.e., the plasmon-exciton interaction distance) impacts the location of the J-aggregate absorption peak, or 2) the type of spacer layer (mercaptoalkyl carboxylic acid or silica) impacts the degree of J-aggregation (i.e., the number of dye molecules that aggregate). Equation 1 describes the red-shifted energy of the J-band, which is directly proportional to the number of dye molecules that form the aggregate.

$$\varepsilon = \varepsilon_0 - 2V\cos\left(\frac{\pi}{N_c+1}\right) \qquad \text{(Eq. 1)}$$

Here, V is the nearest neighbor coupling energy, and N_c is the number of coherently coupled molecules. Modeling efforts during the next research period will focus on elucidating whether or not the distance between the silver core and the cyanine dye exterior impacts the absorption wavelength of the J-aggregate. If the code does not reveal a dependence of red-shifted energy for the J-band on the spacer layer thickness, it is hypothesized that the red-shifted energy is due to the extent of aggregation of the dye molecules on the spacer layer.

Inspection of Figure 3 also demonstrates that the J-aggregate of PIC did not form when 12-mercaptododecanoic acid or 16-hexadecanoic acid were used as spacer layers. This may be rationalized by the fact that all double-shell structures were suspended in water. It is hypothesized that as the alkyl chain length in the spacer layer is increased, and hydrophobicity of the surface is increased, and the propensity of the spacer layer to interact with the cationic dye in solution is minimized. Future research will focus on ensuring that the carboxylic acid group of the spacer layer is fully deprotonated via pH modification. This will enhance the "solubility" of the spacer layer in an aqueous environment.

Future efforts during the next research period will focus on: 1) determining the optimum Ag:PIC ratios for maximizing the J-aggregate peak, 2) normalizing all optical responses to mass [i.e., determine extinction (m^2/g) as a function of wavelength in order to determine if extinction is enhanced at either the silver peak wavelength or the J-aggregate peak wavelength], 3) varying the thickness of a silica spacer layer to determine the impact on J-aggregation, and 4) exploring the impact of gold as an alternative core metal.

5. ACKNOWLEDGEMENTS

This work was made possible through support from the ECBC ILIR Program.

WORK CITED

[1] Kerker, M. *The Scattering of Light, and Other Electromagnetic Radiation*, Academic Press, New York, 1969.
[2] Kneipp, K. et al. 1999. *Chem. Rev.* 99, 2957-2975.
[3] Lakowicz, J.R. 2005. *Anal. Biochem.* 337, 171-194.
[4] Kobayashi, T. *The J-Aggregate*, World Scientific, Singapore, 1996.
[5] Hranisavljevic, J. et al. 2002. *J. Am. Chem. Soc.* 124, 4536-4537.
[6] Wurtz, G.A. et al. 2007. *Nano Lett.* 7, 1297-1303.
[7] Kometani, N. et al. 2001 *Langmuir* 17, 578-580.
[8] Yoshida, A. et al. 2009. *Langmuir* 25(12), 6683-6689.
[9] Tischler, J.R. et al. 2006. *Opt Lett*. 31(13), 2045-2047.
[10] Hench, L.L. and West, J.K. 1990. *Chem. Rev*. 90, 33-72.
[11] Dixon, A. et al. 2005. *American Journal of Undergraduate Research* 3(4), 29-34.

Investigation of molecule-surface interactions with overtone absorption spectroscopy and computational methods

Jerry Cabalo[a], Gary Kilper[a], Rosario Sausa[b]
[a]Edgewood Chemical Biological Center, Research & Technology Directorate, 5183 Blackhawk Rd., Aberdeen Proving Ground, MD 21010
[b]US Army Research Laboratory, RDRL-WML-B, APG, MD 21005

ABSTRACT

Vibrational overtone spectroscopy is a potentially powerful tool for studying intramolecular and intermolecular interactions. We report on a combined experimental and modeling study of the C-H stretch first overtone of bulk 1,3,5-trinitrotoluene (TNT), TNT on fumed silica powder, ε-CL20, and RDX for the final year of this program. We recorded the overtone spectra for these materials by laser photoacoustic spectroscopy and compared them to those predicted with the Harmonically Coupled Anharmonic Oscillator model in the 5600-6600 cm^{-1} region. The model systems for TNT and RDX utilized a hybrid quantum mechanical/classical mechanical (QM:MM) approach with the MP2 method and the Universal Force Field. For CL20, only Density Functional Theory (DFT) methods produced results. Since the QM:MM approach introduces severe errors into the DFT calculated electron correlation energy and the calculated molecular dynamic dipole moment, a purely quantum mechanical model was used for CL20. In order to replicate the physical forces between molecules in the bulk crystal as well as on surfaces in the model, and bring the predicted overtone spectra into agreement with the experiment, it was necessary to obtain a unit cell geometry as close as possible to experimental measurements, to average the contributions of each molecule in the crystal unit cell, and to correctly assign partial charges to each of the molecules in the model. Due to the effort to understand the intermolecular interactions occurring in the neat crystal, a full understanding of molecule-surface interactions was not obtained in the course of this study; although, several key insights were obtained for intermolecular interactions in the bulk crystal.

1. INTRODUCTION

Intermolecular interactions play an integral part in physical and chemical processes such as adsorption, corrosion, and heterogeneous catalysis.[1-6] An understanding of these processes has profound implications for the properties, functions, and reactivities of molecules. Vibrational overtones are uniquely sensitive to a molecule's local environment, and are potentially an effective tool in examining intermolecular and molecule-surface interactions because they involve higher vibrational energy levels than the ground state levels. Knowledge of how these interactions are reflected in the overtone spectra permits the refinement and validation of computational models that are in turn used to predict other important properties such as molecular orientation, molecular motion, and binding energies.

When the surrounding molecules perturb a molecule's vibrational potential energy surface, the higher energy levels experience more change than the lower levels. The molecule's average bond lengths increase with vibrational level, and thus the molecule experiences greater mechanical interactions with the surroundings. This intermolecular interaction also affects the nuclear wavefunctions that in turn modify the transition dipole moment and the absorption intensities. As a result, the magnitude of the perturbation from the surroundings to the vibrational spectrum increases as higher vibrational levels are involved.

The Vibrational Self Consistent Field (VSCF) method [7-10] and the Harmonically Coupled Anharmonic Oscillators (HCAO) method [11-14] are two theoretical approaches that can be used to predict overtone

spectra. The VSCF approach seeks solutions to the vibrational Hamiltonian by making the approximation that the nuclear wavefunction can be treated as the product of single, mass weighted normal coordinate wavefunctions. The vibrational Hamiltonian is broken into a series of one dimensional vibrational Hamiltonians that are solved with a self-consistent field approach. This is analogous to the Hartree Fock approach where the electronic wavefunction is treated as the product of single electron wavefunctions. HCAO is a much simpler, local mode model that applies only to bond stretches between a hydrogen atom and a heavier atom such as carbon, and treats them as a diatomic Morse Oscillator. HCAO additionally corrects for coupling between oscillators by treating that coupling as a harmonic, second order interaction. Although VSCF is more general than HCAO, HCAO was implemented in this study because of its simplicity and applicability to the C-H stretches that were the focus of this study.

The previous results in this study [15] were performed with a quantum mechanical/classical mechanical (QM:MM) approach. Vibrational spectra were calculated from a single molecule that was treated quantum mechanically, and the intermolecular interactions were accounted for by allowing electrostatic charges in the classical layer act on the molecule in the quantum mechanical layer. It was found that in this approach the electrostatic charges in the classical layer affected the electron correlation energy calculated in the quantum mechanical layer when using the Hartree Fock (HF) or Density Functional Theory (DFT) methods. The MP2 method which provides a perturbative correction for electron correlation gave results in agreement with data. In addition, the assignment of partial charge and intermolecular positioning were critical to correctly predicting the overtone spectra. Although much progress was made in including the proper physical description of the interaction between a molecule undergoing vibrational analysis in a quantum mechanical region and molecules in a classical mechanics region, there was still disagreement between predicted spectra and experimental measurement. To obtain a better physical description of the intermolecular interactions, additional work was performed.

The objective is to obtain an understanding of how molecular interactions are reflected in the overtone spectra and to use this understanding for predicting overtone spectra from models of intermolecular interactions, especially of molecules on surfaces. The capability to predict changes in the overtone spectrum due to molecule-bulk and molecule-surface interactions permits the refinement and validation of the computational models of intermolecular interactions. The validated models in turn allow other important properties, such as binding energies, to be predicted.

2. METHODS

2.1 Experimental methods

In order to validate results of the computational modeling, it was necessary to generate photoacoustic spectra from the materials under study. In order to provide a basis for comparison with the synthetic spectra, overtone and fundamental vibrational spectra were collected using photoacoustic spectroscopy in a commercial MTEC 300 cell that was flushed with Argon gas to remove water vapor. Photoacoustic spectroscopy was used because it is suitable for powdered samples. Tunable near IR laser light was obtained from the idler output of a 10 Hz Nd:YAG pumped Continuum Sunlite EX OPO laser system in the range of 5600 cm^{-1} to 6600 cm^{-1}. The pulse energy varied from 600 μJ/pulse at 6430 cm^{-1}, to 150 μJ/pulse at 5700 cm^{-1}. A Schott glass filter removed residual visible light from the near IR beam. Laser pulse energy was measured using a Coherent Field-Max II meter with a J-10 energy sensor.

The MTEC 300 had an onboard preamplifier with an amplification setting of 20. The output was directed to a Tektronix 5104B digital storage oscilloscope and a Stanford Research boxcar integrator, with a maximum gate setting of 3 μs and a delay of 10 ms. The output of the boxcar was digitized and recorded on a computer. Power spectra were recorded by scanning over the tuning range and monitoring the laser energy with a photodiode directed into the boxcar. To calibrate the power curve, the average pulse energy of the IR idler beam was measured with the pulse energy meter at 5 nm intervals of the visible output

wavelength. All spectra were normalized with the power curve. Background spectra were recorded with an empty sample cup, and subtracted from the sample data. Near IR overtone spectra were collected from ~50 mg pure, recrystallized TNT, RDX, and ε CL20 (confirmed by FTIR measurements) obtained from the Weapons Materials Research Directorate at the Army Research Laboratory. For preparation of TNT on silica, 12 mg of the munitions grade TNT was dissolved in 10 mL of acetone, and 9 mL of this solution was added to 35 mg of Cabosil™ 5 M fumed silica, and the acetone was evaporated, leaving a coating TNT on the fumed silica.

2.2 Theoretical methods

Theoretical calculations were performed using Gaussian 2009 version A.02 on a LAN Parallel cluster utilizing up to 112 Intel processors.[16] For all quantum mechanical models with periodic boundary conditions, DMOL3 was used on the High Performance Computing Center at the Army Research Laboratory in Aberdeen. Overtone vibrational frequencies of TNT and RDX were calculated from cluster models formed 64 molecules (Figure 1). The large clusters were formed from eight unit cells of TNT or RDX. This was done to ensure the molecules used to calculate spectra for the crystalline material would be completely enclosed by other molecules, as occurs in the bulk crystal. It was assumed the interior of the large cluster would be a reasonable model of the bulk crystal. The initial unit cell structures for TNT and RDX were provided by Accelrys, which is the vendor for Materials Studio, and then both the unit cell and the molecules were geometry optimized with the PBE functional and the double numerical basis set with polarization functions (DNP) within the DFT code DMOL3. The results were then used to form the large cluster models. These models were then passed to the Gaussian 2009 code. A single point ab intio calculation using the HF/3-21G* method with the Merz-Singh-Kohlman (MSK) population analysis was performed to assign partial atomic charge to the entire system.

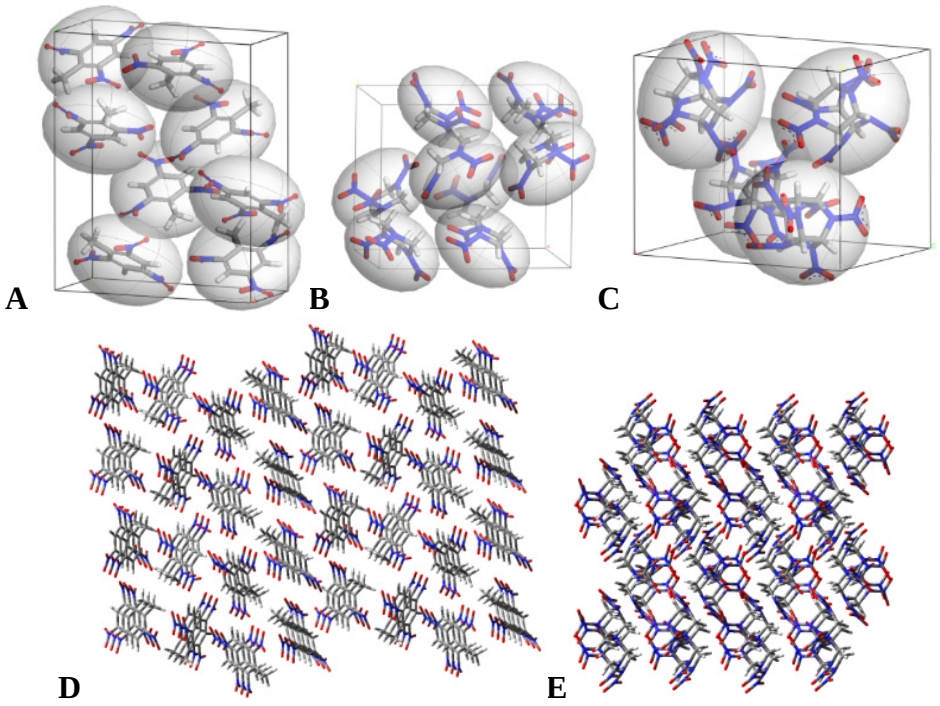

Figure 1. Unit cell and cluster models. A) Unit cell model for TNT, B) Unit cell model for RDX, C) unit cell model for CL20, D) cluster model for TNT, and E) cluster model for RDX.

Calculations on CL20 did not use a cluster approach and were either based on the unit cell with periodic boundary conditions and a purely quantum mechanical model or on an isolated molecule. For the isolated CL20 molecules, spectra were calculated using the B3LYP functional with the 6-31+G(d,p) basis set.

Because only the MP2 method worked with the QM:MM approach, and because no results could be obtained for CL20 using the MP2 method for any basis set, the QM:MM approach was not used. The crystal structure of CL20 had to be calculated and validated by comparison to the literature. This was performed first using classical molecular dynamics (MD), followed by quantum mechanical DFT optimization of the crystal cell and the molecules. The structure of the molecule itself and that the CL20 crystal has four molecules in its crystal unit cell is known from the literature. To calculate the structure of the cell, molecular dynamics were used. First, the individual molecule was optimized with PBE/DNP and its partial atomic charge was assigned. The molecules were then treated as rigid units and the orientation and rough molecular positions were optimized using five cycles of annealing with the Universal Force Field. Once the molecules had found an optimal orientation and position, both the unit cell and the molecules were optimized with PBE/DNP.

To calculate the overtone absorption spectra, the HCAO model was used. This is based on the observation that the high frequency hydrogen stretches, where hydrogen is bound to a heavier atom such as carbon or oxygen, are energetically independent of the other vibrational modes of the molecule. Thus, these modes can be treated as if they were vibrations of a simple diatomic molecule. Based on this assumption, the solutions of for the Morse Oscillator model can be used to calculate both the vibrational frequencies and the intensities. Because the collection of C-H oscillators in a typical organic molecule has similar vibrational frequencies, a correction for coupling between them may need to be introduced. This is especially true if several hydrogens are attached to the same carbon as occurs in a methyl or methylene group. This coupling can be assumed to be harmonic (i.e., described by a second order polynomial) and corrections have been formulated.

For TNT and RDX, spectra were calculated from one molecule at a time, sampled from different positions so that each position within the crystal unit cell would get representation in the predicted overtone spectrum. For the RDX or TNT molecule that was the focus of a frequency analysis, it was treated quantum mechanically with MP2/6-31+G(d,p) and geometry optimized. The rest of the molecules in the calculation were described with the UFF and were not optimized. To calculate the overtone vibrational spectrum, the potential energy surfaces (PES) along each of the C-H bond stretches were calculated for the molecule treated quantum mechanically. This was accomplished by performing a rigid scan of the energy and dipole moment as a function of C-H bond length ±0.30 angstroms around its equilibrium position, in steps of 0.05 angstroms. The resulting potential energy surfaces and dipole moment as a function of bond length were fitted to polynomial functions. The second and third order derivatives of the PES were used to calculate force constants that lead to the harmonic constants and anharmonicities. These were in turn used to get the frequencies. For TNT and RDX, two bond lengths were scanned concurrently, which allowed the calculation of any coupling on the PES. The two dimensional PES was fitted with a polynomial that contained up to the quadratic terms that was a function of both coordinates. Force constants that were a mix of the two coordinates indicated coupling. To calculate the absorption intensities, the matrix elements of the dynamic dipole moment were calculated. The solutions for the Morse Oscillator Hamiltonian and the calculated vibrational frequencies were in turn used to get the vibrational wavefunctions used in the calculation of the elements of the dynamic dipole moment. For RDX, it was important to account for combination bands. Combination bands are similar to overtones, except, instead of multiple quanta of vibrational energy going into a single vibrational mode in an absorption event, multiple quanta of vibrational energy are absorbed and distributed to multiple vibrational modes. The HCAO model easily accommodated combination bands. The Hamiltonian was written to include multiple modes, and multiple modes are permitted to absorb a quantum of vibrational energy.

The HCAO approach to calculate the spectrum CL20 was similar, except that a purely quantum mechanical model with periodic boundary conditions was used to determine the C-H stretch PES and dipole moment. The DMOL3 code with the PBE functional and the DNP basis set was used. A script was

written in Materials Studio 5.5 to perform a potential energy scan and at the same time capture the change in the dipole moment as the bond length was scanned. The results of these calculations were post-processed in the same way as the Gaussian 2009 produced data for TNT and RDX, except that the harmonic coupling corrections were neglected.

3. RESULTS AND DISCUSSION

The effect of charges in the classical layer of QM:MM models on the calculation of electron correlation energy was the first important result. Figure 2 shows the PES calculated along one of the C-H stretch coordinates for either single molecule or cluster models for different levels of QM theory. For single molecule models, the three QM methods produce similar results, with a significant anharmonic component in the PES for all QM methods. The same is not true for the cluster models, where only the MP2 method PES maintained its anharmonicity. When the manner in which electron correlation is determined for the QM methods are considered, the reason for the errors in electron correlation energy becomes clear.

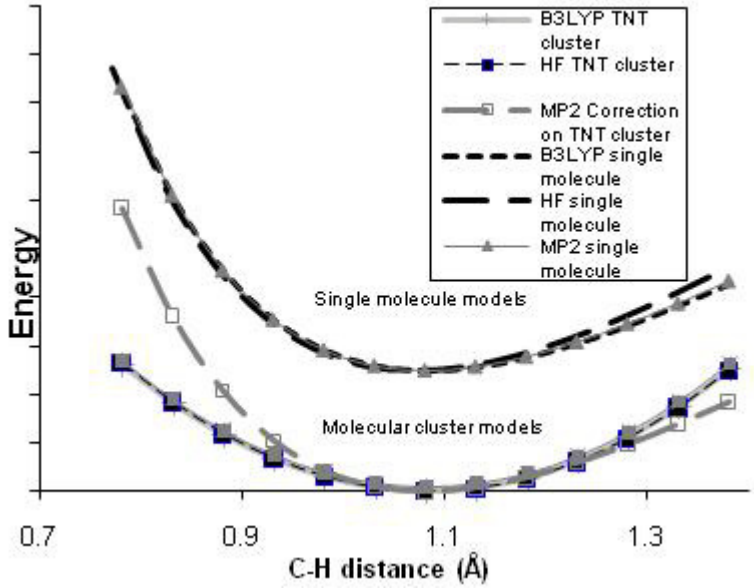

Figure 2. PES along a C-H stretch coordinate for the HF, B3LYP, and MP2 methods. The effect of charges in the classical layer in the QM:MM calculations on the electron correlation energy are illustrated by the loss of anharmonicity in the PES for cluster models using the HF and B3LYP methods. The PES for MP2 retains anharmonicity.

To make solution of the Schrodinger equation manageable, the overall many-electron Schrodinger equation is approximated as a series of single electron Schrodinger equations. The effect of the electron repulsion from the other electrons is approximated as a mean electric field that is added into the single electron Schrodinger equations. The MP2 method applies an additional correction factor from perturbation theory. When the electrostatic charges in the classical layer of a QM:MM calculation are permitted to interact with the QM portion, the electrostatic charges contribute to the mean field used to account for electron correlation. Significant errors result, and the predicted PES has little or no anharmonicity. The MP2 method on the other hand, applies a correction for electron correlation, and compensates for the error introduced by the charges in the classical layer.

In a similar manner, the electrostatic charges in the classical layer interfere with the calculation of the dipole moment in the QM layer. When the Mullekin population analysis is performed, the partial atomic charges in the molecule that are in turn used to calculate the dynamic electric dipole moment are

calculated directly from the molecular orbitals in the QM layer. This approach does not account for the interaction with charges in the MM layer, and for cluster models, there is a significant difference in the slope of the dipole moment along the C-H stretch coordinate, as shown in Figure 3. As a result, incorrect absorption intensities are predicted. In contrast, the Merz-Singh-Kollman population analysis determines charge based on the local electrostatic potential. This directly accounts for the interaction with electrostatic charges in the MM layer of the QM:MM model, thus similar results are obtained for either single molecule or cluster models.

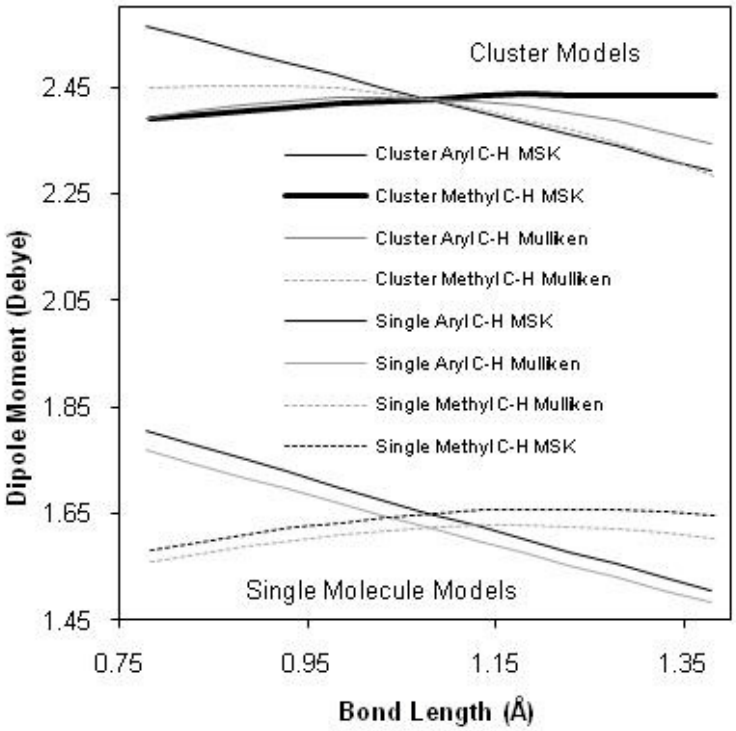

Figure 3. Predicted molecular dipole moment in Debye as a C-H bond is stretched around its equilibrium position. The predicted change in dipole moment for the QM:MM cluster model is affected by the method for calculating partial atomic charge.

The results of modeling the energetic materials show how sensitive the predicted overtone spectra are to the molecular arrangement. TNT with a cluster cut out of a crystal structure optimized with periodic boundary conditions is shown in Figure 4. The resulting spectrum is scaled with a correction factor of 0.99 for the sake of comparison to the experimental data. In comparison to the data previously reported in this program, this result is in better agreement with the data. The primary difference between the models is that the newer model utilized a purely quantum mechanical calculation to determine the geometry of the overall system. The purely quantum mechanical model should yield better results because it does not rely on parameterization. In further support of this, the spectra calculated from individual molecular positions in the model are drastically different from each other, and an average of many of the individual spectra is necessary to account for the number of features in the experimental spectrum. Although the result presented includes additional refinements to what was previously published, there are still remaining disagreement with experiment.

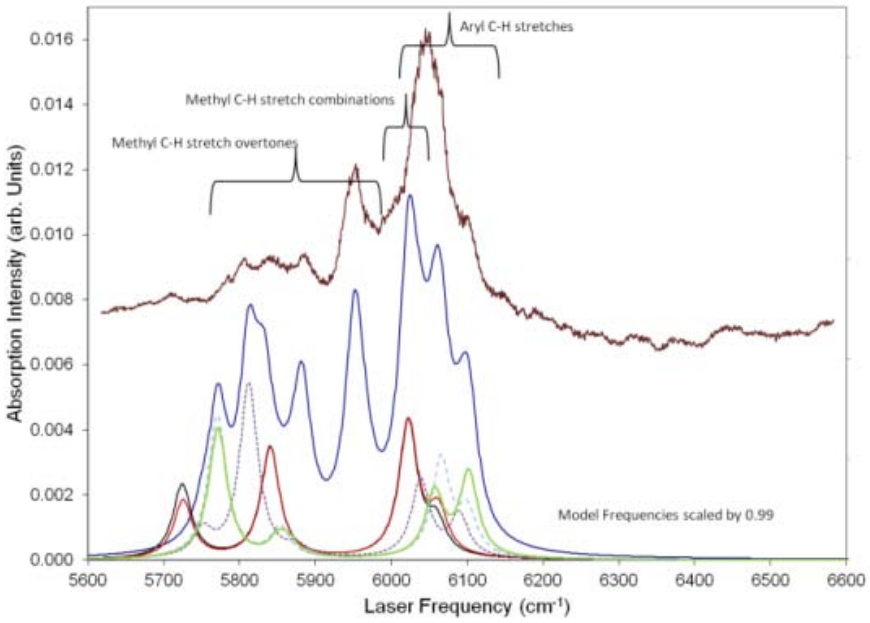

Figure 4. Predicted first overtone spectrum from solid TNT. The blue trace is the sum of spectra generated from several positions in the model TNT cluster, intended to be representative of the distinct positions within the crystal unit cell. Examples of the spectra from single molecules are shown also illustrating the observed spectrum is an ensemble average.

The influence of combination bands were investigated for both TNT and RDX. In the case of TNT, a negligible difference was introduced by including combination bands. However, inclusion of combination bands were essential for accounting some of the main features in the experimental RDX spectrum, especially the peak centered at 5900 cm^{-1}, which is not present at all in spectra predicted from models that neglect combination transitions. This result makes sense when the molecular geometry differences between TNT and RDX are considered. For TNT, the aryl hydrogens are part of a rigid aromatic ring where there is very little coupling between them. Coupling between the aryl hydrogen stretches and the methyl hydrogen stretches is unlikely because of the separation between the C-H oscillators. Combinations are highly probable for the C-H oscillators sharing the methyl carbon, but due to the high symmetry around the C-H oscillators there is significant degeneracy between overtones and combination bands. In other words, the combination bands for TNT are obscured by the overtone absorptions. For RDX, each of the carbons in the molecule have two distinct types of C-H stretches, where three of the C-H stretches are directed within the plane of the molecule, and three and directed outward. There is a distinct difference in vibrational frequency between the two C-H oscillators centered on each carbon, so that the combination bands do not overlap with the pure overtone bands. Thus, the combination bands contribute significantly to the predicted spectrum.

Figure 5 is a molecular model of RDX where the C-H oscillators in the molecule are numbered and the corresponding peaks are labeled in the spectrum. Although there is excellent agreement in terms of frequency between the experimental spectrum and the predicted spectrum, there is disagreement in terms of intensities. For the peaks between 5850 cm^{-1} and 6000 cm^{-1} that correspond to oscillators 2, 3, 6, which are in the plane of the molecule, the agreement between predicted and experiment are good. For the peaks between 5800 cm^{-1} and 5820 cm^{-1}, the predicted intensities are much less than measured, which corresponds to oscillator 4. For the peaks predicted between 5620 cm^{-1} 5700 cm^{-1}, there are no peaks shown in the experimental spectrum. These peaks correspond to oscillators 1 and 5. The disagreements arise from the pure overtones of oscillators directed above the plane of the molecule. This result points to an incorrect representation of the intermolecular interactions above the individual molecules.

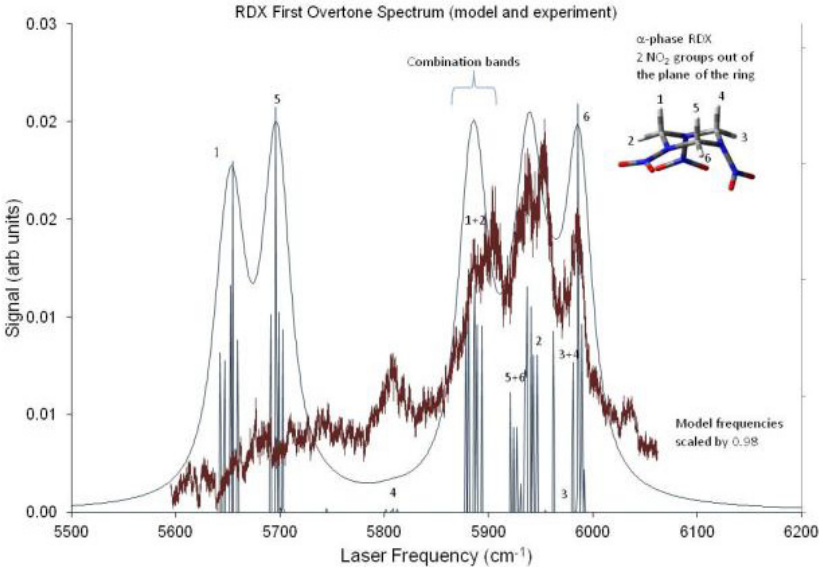

Figure 5. Comparison of the experimentally measured predicted overtone and combination band vibrational spectra for RDX from eight positions in a cluster model.

The previous results were determined from models that rely on two-layer models which use electrostatic interactions to account for intermolecular interactions. Van der Waals interactions were accounted for as forces that affected the geometric arrangement of the molecules, but the direct effect of these interactions were not accounted for in the electronic description of the model. Thus, the effect of van der Waals interactions on the dynamic dipole moment was not explicitly treated. To better account for van der Waals interactions, a purely quantum mechanical model was first attempted on the CL20 system.

The results of predicted overtone spectra from single molecule models of CL20 are shown in Figure 6 for four different crystal polymorphs of CL20. The spectrum predicted for the ε polymorph is mostly consistent with the experimental spectrum. However, there are some general features in the data that are not accounted for. This is not surprising since the single molecule model does not account for intermolecular interactions in the solid crystal.

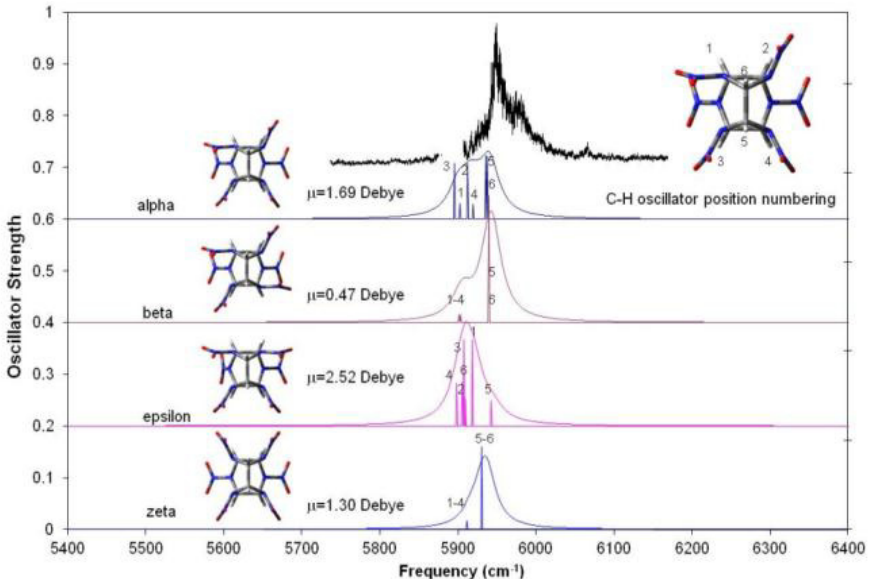

Figure 6. Predicted vibrational spectra from single molecule models of four crystal polymorphs of CL20 compared to experimental measurement.

To remedy this problem, a pure DFT model with periodic boundary conditions and the PBE functional was attempted. The result of a single molecule position in the crystal unit cell is shown in Figure 7. The first observation that can be made from Figure 7 is that there are more absorption features predicted than were predicted with the single molecule models. The presence of intermolecular interactions accounts for the breaking of molecular symmetry that leads to a wider variety of interactions. However, it should also be noted that there is a difference on the order of 200 cm^{-1} between that predicted with the PBE functional and experiment. This disagreement is greater in magnitude than between experiment and single molecule models calculated with the B3LYP functional. The disagreement can either be due to the PBE functional used or to differences in the basis set used in the calculation. Most likely, the increased disagreement with experiment when using a purely quantum mechanical model for the crystal unit cell is the result of the choice of functional, since a double ζ basis set was used for both the cluster and periodic boundary condition calculations. Furthermore, neither B3LYP nor PBE have been known to account well for van der Waals interactions, so that either an electron correlation corrected functional such as the X3LYP functional should be used, or the calculation should be performed with a plane-wave basis set, which is known to accurately calculate the electron correlation energy.

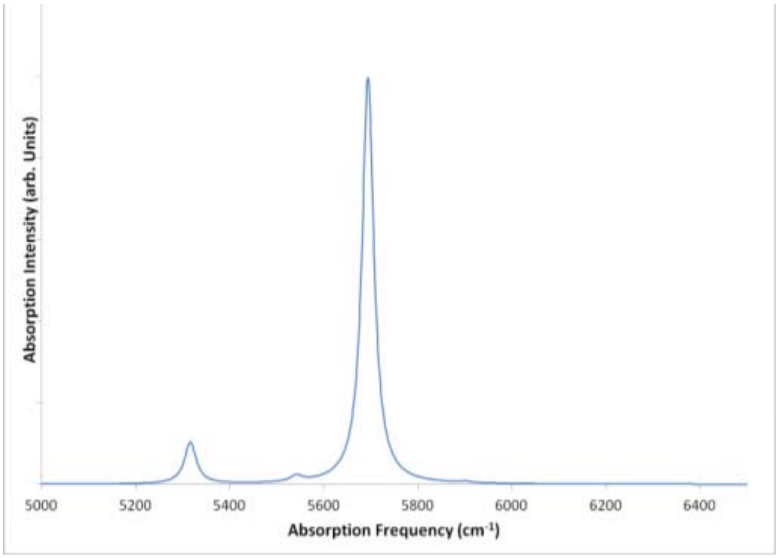

Figure 7. Spectrum calculated from a purely quantum mechanical model with periodic boundary conditions for the ε polymorph of CL20. Unlike spectra predicted from single molecule models, more features are visible in this spectrum.

4. CONCLUSIONS

In summary, three different approaches were used to model intermolecular interactions in crystalline bulk solids. In the first, the bulk crystal was modeled as a large cluster of molecules, and the structure was optimized as a cluster. Overtone vibrational spectra were calculated using a two layered QM:MM approach. In the second approach, a cluster model was still used, but it was optimized with three dimensional boundary conditions and a fully quantum mechanical model using DFT, followed by the same QM:MM analysis. The results of these two methods showed that the QM:MM approach introduced difficulties in how electron correlation energy was accounted for and how partial atomic charge was calculated. These issues were resolved by using the MP2 *ab initio* method and population analyses that assign charge based on the local electrostatic potential, such as the MSK population analysis. Some modest improvements were obtained for the TNT spectrum, but a number of large differences remained between experiment and predicted overtone spectra from RDX. Since CL20 could not be modeled at all with QM:MM model, this system was first examined with a purely QM model. Disagreement with experiment was increased for this model, but this is likely due to the selection of functional in the

calculation. It is expected that a better selection of functional or the use of a plane-wave basis set should improve results for this approach.

The objective of determining a clear method for predicting changes in overtone spectra that arise from intermolecular interactions on surfaces was not obtained. An understanding of how intermolecular interactions in bulk crystalline systems are reflected in the overtone and combination band absorption spectra is necessary before applying vibrational analysis to molecules on surfaces. The problem of understanding how to correctly represent the intermolecular forces in bulk crystals in a computational model is not trivial, and accounting for electron correlation in both QM:MM and purely QM models is a major component of this.

WORK CITED

[1] Roddick-Lanzilotta, A. D. et al. 1998. *Langmuir* 14(22), 6479-6484.
[2] Johnson, W. G. et al. 1990. *J. Chem. Phys.* 93(12), 9167-9179.
[3] Sung, C. Y. et al. 2009. *J. Phys. Chem. C* 113(35), 15643-15651.
[4] Bermudez, V. M. *J. Phys. Chem. C* 113(5), 1917-1930.
[5] Tao, Y. T. et al. 1997. *J. Phys. Chem. B* 101(47), 9732-9740.
[6] Fujita, S. et al. 2006. *J. Phys. Chem. B* 110(6), 2533-2540.
[7] Lundell, J. et al. 2000. *J. Phys. Chem. A* 104(34), 7944-7949.
[8] Gerber, R. B. et al. 1986. "Mean-field approach to vibrational energy levels and tunneling dynamics in polyatomic systems", 25-38.
[9] Gerber, R. B. et al. 1990. "Vibrational states of van der Waals and hydrogen bonded clusters: A self consistent field approach", 343-354.
[10] Ratner, M. A. and Gerber, R. B. 1986. *J. Phys. Chem.* 90(1), 20-30.
[11] Kjaergaard, H. G. et al. 1994. *J. Chem. Phys.* 100(9), 6228-6239.
[12] Kjaergaard, H. G. and Henry, B. R. 1992. *J. Chem. Phys.* 96(7), 4841-4851.
[13] Petryk, M. W. P. and Henry, B. R. 2005. *J. Phys. Chem.-A* 109(18), 4081-4091.
[14] Petryk, M. W. P. 2006. *Pro. Biomed. Opt. Imag.* 7(43), 637818.1-637818.14.
[15] Cabalo, J. and Sausa, R. 2011. *J. Phys. Chem. A* DOI: 10.1021/jp2025895.
[16] *Gaussian 2009, Revision A.02,* Gaussian, Inc.: Wallingford CT, 2009.

Understanding the role of physical and chemical adsorption on the Raman enhancement from metallic nanoparticles and nanostructured surfaces

Jason Guicheteau[a], Steven Christesen[a], John Kiser[b], and Jerry Cabalo[a]
[a]Edgewood Chemical Biological Center, Research & Technology Directorate, 5183 Blackhawk Rd., Aberdeen Proving Ground, MD 21010
[b]University of Maryland, Baltimore County, Department of Chemistry and Biochemistry, 1000 Hilltop Circle Baltimore, MD 21250

ABSTRACT

The enhancement of the Raman signal resulting from analyte adsorption onto nano-structured metallic surfaces was first discovered in 1977. Since then, surface-enhanced Raman spectroscopy (SERS) has developed into an exceptionally fertile area of scientific investigation producing hundreds of refereed publications yearly. This research, however, has not yet transformed SERS into a tool for routine chemical analysis. Much of the reason for this has to do with lack of substrate reproducibility and the highly analyte specific enhancement factors. While most of the SERS enhancement can be explained by the enhanced electric field produced by the metallic nanostructures, the role of physical and chemical adsorption is less well understood. Because the enhanced electric field drops off sharply with distance, the adsorption is critical to observing enhanced Raman spectra. This research is aimed at a quantitative understanding of the effects of both physical and chemical adsorption on the SERS enhancement. We investigated a select number of simple molecules with varying degrees of polarity to provide an improved experimental and theoretical understanding of the physical phenomena that govern the adsorption and interaction of analytes with metallic nanoparticles and nanostructured metallic surfaces.

1. INTRODUCTION

The SERS effect was first observed when the scattering intensity from an adsorbed species onto a roughened silver electrode increased by a factor of 10^6 over a non-adsorbed species. Originally reported by Fleishmann [1] and described in detail by Jeanmaire and Van Duyne [2], and Albrecht and Creighton [3] the SERS effect was eventually generalized in that virtually any noble metal substrates roughened on the nanometer scale or suspension of nanoparticles can provide enhancement of the Raman signal.

SERS is generally attributed to two enhancement mechanisms: chemical enhancement (CE) and electromagnetic enhancement (EM). The principal controversy concerning the mechanisms stems from the partitioning of the greater than 10^6 enhancement factor between the CE and an EM enhancement mechanism.[4-7] The electromagnetic enhancement is more general than the chemical enhancement and is believed to account for the majority ($>10^4$) of the SERS effect and involves both the molecular polarizability tensor and the electric field of the radiation. The enhancement of the electric field experienced by the adsorbate is a result of a localized electric field at the surface of the nanostructure. The EM enhancement is dependent on the nanoscale's surface roughness features or the particle size and shape of a colloidal suspension.[8,9] Because the intensity of the Raman scattering from an adsorbed analyte molecule is proportional to the square of the local electromagnetic field (EMF), the increase in the magnitude of the EMF at the metal surface increases the number of photons that are Raman scattered. If the correct wavelength of light strikes a metallic roughness feature, the plasma of conduction electrons will oscillate collectively. The collective oscillation of the plasma electrons is localized at the surface, and

is known as a localized surface plasmon resonance (LSPR).[10] This, combined with the free-electron property of a SERS active metal (ε is negative), leads to a large polarization field in the particle and allows the resonant wavelength to be absorbed and scattered, creating large electromagnetic fields around the roughness feature. The net effect is that a molecule localized within these large electromagnetic fields produces an enhanced Raman signal. Even though Raman spectroscopy can be performed using virtually any excitation wavelength, the best SERS is accomplished through a coordination of the surface plasmon resonance of the substrate with the excitation wavelength being used.

Unlike the EM effect, the CE is related to specific interactions between the metal and the formation of a molecule-metal complex creating a charge-transfer state between the two species that can resonantly enhance the Raman scattering signal from analyte molecules. Differing from the EM, the molecule must be directly adsorbed to the roughened metal surface in order to experience the CE enhancement and is believed to only contribute to the enhancement effect at most 10^2. Sites of atomic scale roughness, such as metal clusters or adatom defects, are thought to act as chemical active sites that facilitate the creation of charge transfer complexes, but the nature and identity of these sites has not been conclusively determined.

Even without the formation of a strict charge-transfer complex, the analyte molecule must adsorb onto the metal to take advantage of the EM which falls off rapidly with distance. Chemicals that do not adsorb to the metal nanoparticle will not be enhanced. This is why most SERS studies are performed with analytes that bind strongly to the metal particles or nanostructures. The nanoparticle surface charge plays a critical role in the determining the adsorptivity of the analyte as well as the stability of the colloidal suspension. This surface charge on the nanoparticle results in a relative increase in the concentration of counter-ions close to the surface and the formation of an electrical double layer. The potential difference between the stationary layer of solvent and the mobile layer or slipping plane is referred to as the zeta potential and provides information about the charge on the nanoparticle which in turn affects the stability of the colloid and the binding of the analyte molecule. To describe both these physical and chemical adsorption effects, the Langmuir isotherm can be used to characterize the binding of the analyte to the substrate [11]:

$$\theta = \frac{Kc}{Kc+1} \tag{1}$$

In this equation, the analyte concentration is given by c, the fractional surface coverage by θ, and the adsorption equilibrium constant by K. The fractional coverage is calculated as the ratio of the SERS peak intensity divided by the intensity at full surface coverage (I/Imax). K can be determined from experimental data by fitting K and Imax using a nonlinear regression technique as shown in Figure 1a for trans-1,2-bis(4-pyridyl) ethylene (BPE) on a gold nanostructured SERS substrate. The calculated adsorption equilibrium constant is 1.2 x 107 M^{-1}. While the plot of SERS intensity vs. concentration yields the adsorption equilibrium constant, the rate constant for adsorption can be extracted from the time dependence of the SERS signal via the time-dependent Langmuir equation [12]:

$$\theta = 1 - \exp(-\mathrm{kt}) \tag{2}$$

where k is the rate constant and t the time delay between exposure of the SERS substrate to the analyte solution and data collection. Figure 1b shows the results for BPE adsorbed onto Klarite™ (not the same substrate as in Figure 1a) and the fit of the data to Equation 2.

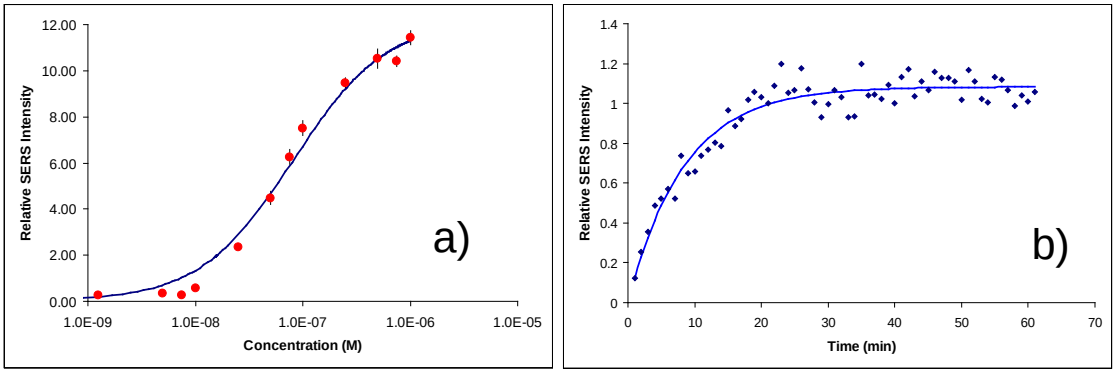

Figure 1. Dependence of SERS signal with fits to Langmuir isotherm and time-dependent Langmuir equation on a) concentration and b) time.

In utilizing Langmuir isotherms, zeta potential, and both colloidal solutions and constructed 2-D nonmetallic planar arrays, we investigated several molecules with varying degrees of polarity in order to seek an improved experimental and theoretical understanding of the physical phenomena that govern the adsorption and interaction of analytes with SERS active surfaces. The following describes a brief account of the first year's efforts [13], followed by a detailed summary of the second year's.

2. RESULTS

2.1 Year one summary

We demonstrated that it is possible to reproducibly fabricate two-dimensional SERS substrates based on tethering gold nanoparticles to quartz slides. While work still needs to be done to improve intra- and inter-substrate reproducibility and tethering silver particles, these substrates can be used to analyze molecules that form charge transfer complexes (e.g., benzenethiol), and molecules that do not have strong charge transfer characteristics (e.g., aminoethanol). We successfully synthesized silver and gold colloids and performed preliminary analysis of the binding kinetics of aminoethanol on a gold nanoparticle planar substrates. Complementing the experimental research in this project, we used computational modeling to understand how the interaction between an analyte molecule and the SERS substrate controls signal enhancement. DFT was employed to simulate the interaction between 2-aminoacetic acid (glycine) and a SERS substrate. Additional work is being performed in several areas including: silver tethering to 2D planar substrates, kinetic measurements on remaining chemicals, and predicative calculations using larger clusters of atoms. Figure 2 shows the preliminary Langmuir isotherm calculated from aminoethanol measurements performed on a gold substrate and the frequency Gaussian calculation mercaptoethanol bound and unbound to a single silver atom.

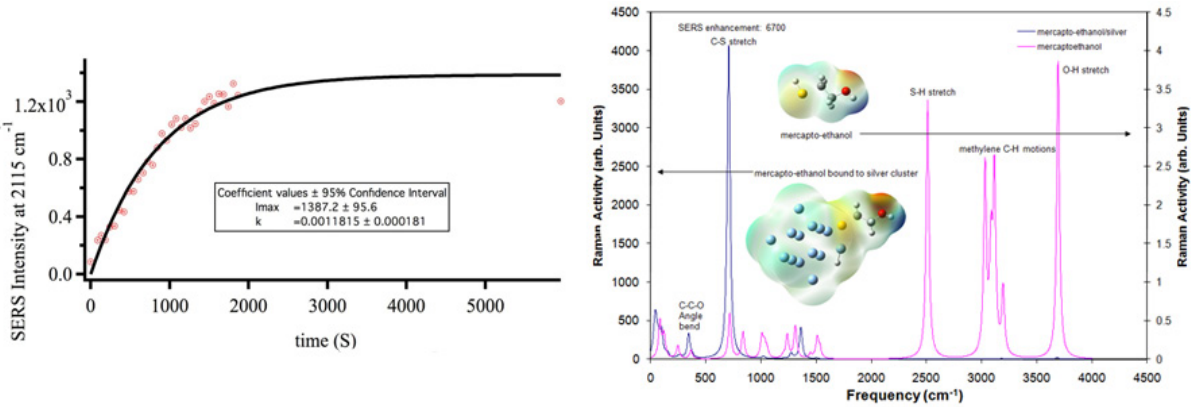

Figure 2. Langmuir isotherm of binding kinetics for ethanolamine on gold, and DFT calculation for mercaptoethanol bound and unbound to one silver atom.

2.2 Year two results

We concentrated on the originally proposed molecules of interest, 2-aminotethanol, 2-mercpatoethanol, 2-aminoacetic acid, and 2-mercaptoacetic acid and attempted adsorption measurements and DFT calculations in Gaussian. Initially we performed zeta potential measurements with both silver and gold colloidal solutions which yielded immediate differences concerning each metals binding/adsorption abilities. Figure 3 shows comparisons results for 2-mecptoethanol adsorbed onto the nanoparticles. The silver colloids (Figure 3a), showed an instantaneous effects upon analyte addition resulting not only in a color change, but zeta potential, size, and absorption shifts. The particle size was observed to increase from approximately 30 nm to 55 nm, and the zeta potential increased from -65.5 mV to -26.0 mV indicating less particle stability (closer to zero = less stable). The increase in particle size produced a shift to longer wavelengths of the colloids absorption maximum (400 nm to 405 nm). The original gold colloids used (20 nm) did not show binding ability to the 2-mercptoethanol. However, larger particles were synthesized (30 nm) and did show dramatic increase in binding. Figure 4b, details the shift in particle size from 30 nm to 1.1 µm and the zeta potential from -39 mW to +23 mW. Also observed are the spectral differences between the two analytes as relative intensity of the vibrational bands at 623 cm^{-1} and 715 cm^{-1} is reversed. Conclusions from the other molecules are still being finalized but these results clearly show the effect of particle size on the adsorption of analytes to metallic nanostructures.

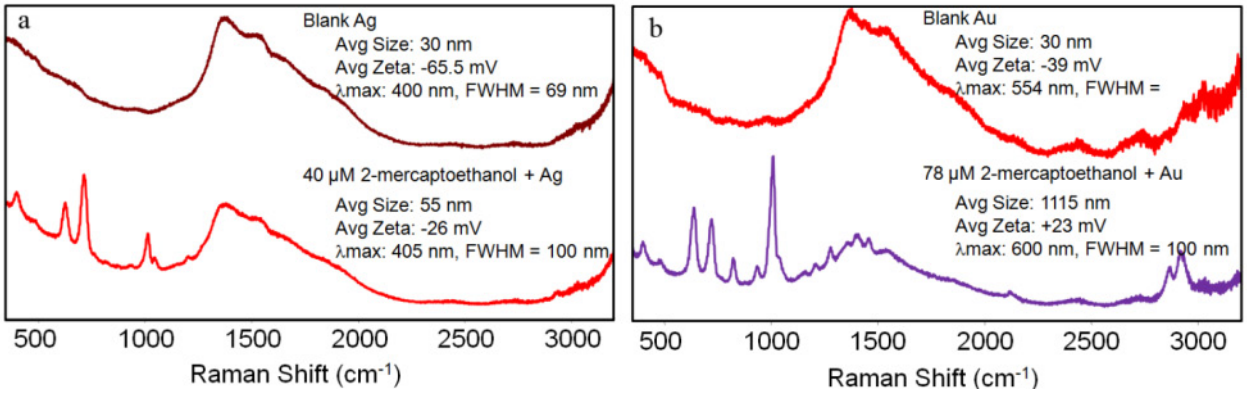

Figure 3. Pre- and post-analyte adsorption data for silver (a) and gold (b) colloids to 2-mercaptoethanol.

2.3 Silver nanoparticle substrate fabrication & tethering

Following last year's gold nanoparticle tethering and fabrication successes, studies continued on tethering silver nanoparticles to functionalized quarts substrates as well as increasing tethering efficiency of the gold nanoparticles. A new process for the silver colloid functionalization yielded positive results which eventually allowed for kinetic measurements on 2-mercpatoethanol. Quartz slides were Piranha (4:1 H_2SO_4: 30%H_2O_2) cleaned four times before placement into an oven to be dried. Functionalization was performed by immersing the cleaned/dried slides in 15 mL aminopropyltrimethoxysilane (APTMS) with 45 mL of methanol and placed into a sonicator overnight. Following this, the APTMS/MeOH solution was removed, and the slides re-immersed in clean methanol. Sonication was carried out for an additional 2 hours. Before addition of the nanoparticles the slides were rinsed with copious amounts of deionized (DI) water and methanol.

Silver nanoparticle suspensions were prepared following a modified procedure of Lee and Meisel.[9] Briefly, 90 mg of silver nitrate (99+ %, Aldrich) was dissolved in 400 ml of DI water (18.3 MΩ), and 10 ml of 1% sodium citrate was added to the solution upon boiling. Heating and constant stirring were maintained for 45 minutes after which time the reaction flask was removed from heat and allowed to cool to room temperature. The resulting nanoparticle suspensions appeared yellowish-brown with an electronic

absorption λ_{max} of 399 nm and an average full width half maximum of 65 nm with an average particle size of 36 nm (as measured on a Malvern Zetasizer nano-ZS).

The silver colloids were prepped for tethering to the cleaned slides by the following method: 10 mL of colloid was centrifuged at 10000 RPM for 20 minutes. A small pellet formed at the bottom of the tube, from which 9.5 mL of the supernatant removed. The remaining 0.5 mL pellet was then re-suspended in methanol and ready for tethering to the functionalized quartz slide.

Tethering
A cleaned slide was placed onto a hotplate, brought up to a low temperature, and 100 µL aliquots of the methanolic colloid is deposited onto the slide and allowed to rapidly dry. This is followed by 19 more 100 µL aliquots onto the slide for a total volume of 2 mL. The fully functionalized/tethered slide is removed from heat, cooled to room temperature and placed in a desiccator prior to analyte analysis.

2.4 Gold nanoparticle substrate fabrication and tethering

As mentioned above, typical gold nanoparticles were synthesized at a size of approximately 20 – 30 nm using a standard citrate reduction reaction of auric acid in boiling aqueous solution. This year we extended this work to not only increase the particle size, but prepare the gold solutions in digitubes instead of the normal glassware as before. The reason to employ plastic in the preparation is to remove any potential active sites from the glassware that could react during the reduction process. The digitube process is described here. A sterilized 50 mL digitube is pre-cleaned with aqua regia followed by copious amounts of water to ensure all the acid is removed. A solution of HAuCl4 is pippetted into the tube and capped with a rubber septum and a 25.5 gauge needle is inserted. A 50:50 ethylene glycol water bath is prepared. The digitube is placed in the water bath being heated by a hot plate. Upon the temperature reaching a boil, sodium citrate is injected into the gold solution. A color change occurs within 5 minutes from a gold color to a purple and finally a dark red. After 5 minutes, the sample is removed from heat and allowed to cool. The final volume is adjusted to 50 mL.

Tethering
Quarts slides were pre-cleaned as described above. Following cleaning, the slides were suspended in a 4:1 solution of methanol and aminopropyltrimethoxysilane. The quartz slides were then sonicated for 5 hours for batches. The sonication increases the motion of the solution and adds heat to the silanization procedure. After the derivatization, the slides were sonicated two times in 50 mL aliquots of methanol for at least 60 minutes each time to remove any unbound aminopropylsilane. Following the methanol cleaning the slides were rinsed with copious amounts of water followed by methanol. The functionalized slides were then coated with 2 mL of gold colloid in the same manner as the silver slides described above.

2.5 Analysis of tethered nanoparticle substrates

During the previous year ethanolamine (2-aminoethanol) was investigated both experimentally and theoretically solely on gold, as tethering problems plagued silver investigations and it was observed that ethanolamine showed low binding efficiency to silver. Since this year's zeta potential results showed that 2-mecptoethanol bound strongly to both silver and gold, experiments and theoretical calculations were focused in that area.

2.6 Kinetic analysis of ethanolamine binding to tethered gold nanoparticle substrates

In this set of experiments, the kinetics of the of 2-mercaptoethanol binding was measured by monitoring the SERS response as a function of time. These experiments were conducted using a scanning Raman microscope using with a 4× objective and 785 nm excitation. Sample preparation consisted of placing the substrate into a Pyrex Petri dish and covering with 5 mL of aqueous 2-mercaptoethanol solution.

Prior to the SERS kinetic analysis, normal Raman spectra were obtained using a plain quartz slide as a substrate. This was done to keep the optical path length consistent between the normal Raman measurements and the SERS measurements. The spectral results at concentrations between 1 mM and 5 mM over a 12 minute time frame for 2-mercptoethanol are shown in Figure 4. Interesting to note are the subtle ratio shifts between the bands 850 cm^{-1} and 940 cm^{-1}.

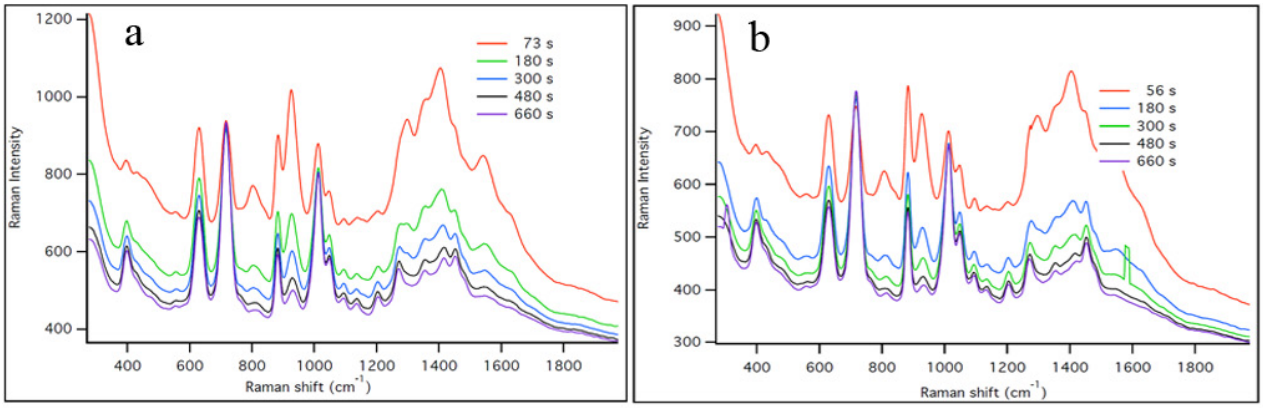

Figure 4. SERS spectra of 1.0 mM (a) and 5.0 mM (b) 2-mercaptoethanol obtained from planer substrates of tethered silver nanoparticles.

To calculate the binding kinetics the integrated intensity at 710 cm^{-1} (C-S) was used to construct time dependant intensity curves, as shown in Fig. 5. The data shown in this figure were fit using a time dependent Langumir isotherm of the form.

$$S_{(t)} = I_{max} (1 - e^{-kt^{0.5}})$$

This equation was adapted from the work of Karpovich et al.[10] Using this equation, the observed rate constant was determined to be 0.0619 ± 0.00076 s^{-1} at the 95% confidence interval for 1 mM and 0.0238 ± 0.0075 s^{-1} at the 95% confidence interval for 5 mM.

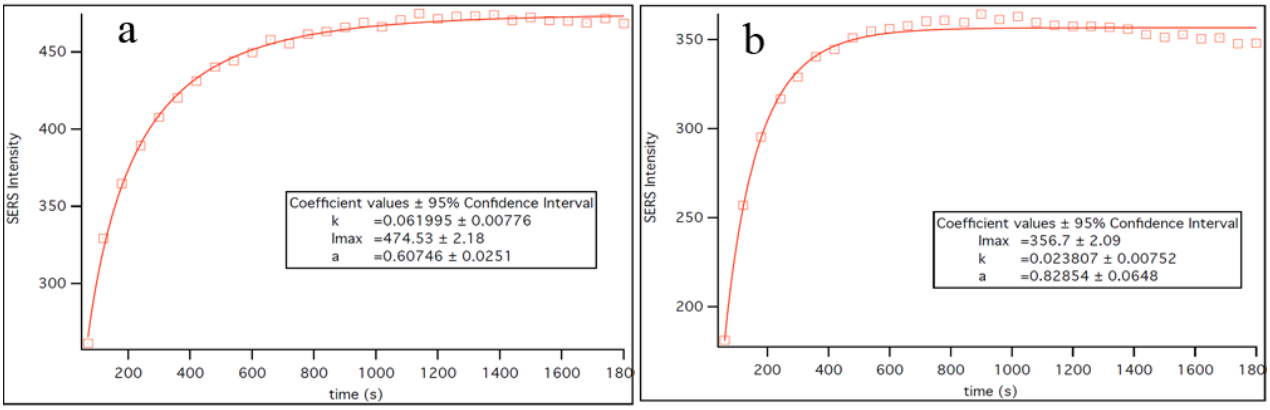

Figure 5. Vg(C-S) band fit to a modified Langmuir isotherm for 1.0 mM (a) and 5.0 mM (b) 2-mercpatoethanol solution calculated from tethered silver planar arrays.

Gold substrates were also, tested; however, delamination problems continued to occur and the causes are still under investigation. However, similar kinetic measurements were carried out in solution at various concentrations over a 20 minute time frame. Figure 6 plots these results using the 710 cm^{-1} (c-s) vibration

show good agreement between the tethered silver data. Additional experiments are being conducted to enhance the tethering capability of the gold.

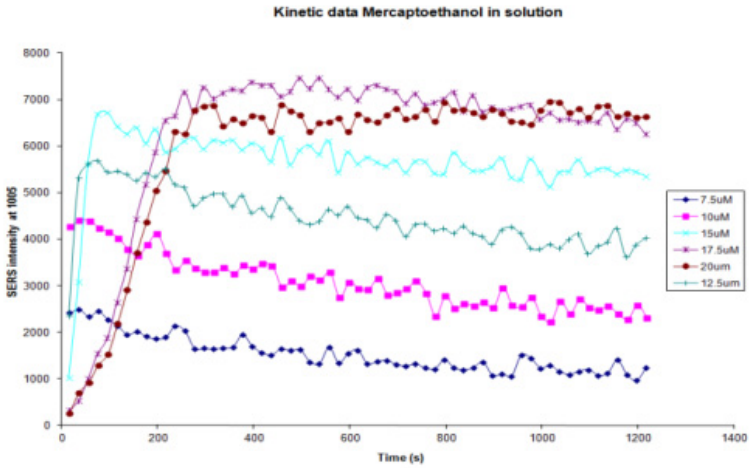

Figure 6. Kinetic data performed on gold nanopartilces for 2-mercaptoethanol over a 20 minute period.

2.7 Theoretical work

The objective of the theoretical component of this effort is to help explain observed SERS signal returns from individual normal modes as a function of molecular orientation on the SERS substrate, and the influence of the substrate and substrate surface structure on the electronic states of the analyte molecules. The theoretical treatment of SERS, however, is as complex as the experimental understanding of the EM and CE competing effects discussed earlier.[14]

The contribution to the signal from resonance Raman can be calculated from first principles. For Raman scattering that takes a molecule from an initial vibrational state |I,0> to a final vibrational state |F,0>. The Raman scattering factor is proportional to $|\langle F,0|\alpha_{\alpha\beta}|I,0\rangle|^2$, which is the matrix element of the polarizability tensor $\alpha_{\alpha\beta}$. An expression for this polarizability was published by Kramers, Heisenberg, and Dirac (KHD) [15,16], but in practice, this expression is very difficult to calculate; however, Placzek [17] introduced an approximation where the overall polarizability is approximated with the electronic polarizability which is in turn expanded in a Taylor series around the equilibrium geometry. This approximation only holds true for the situation where the excitation laser is not in resonance with any states in the molecule. As a result, predicted Raman scattering factors from standard quantum mechanical modeling packages do not produce good results for systems involving resonance with excited states. Fortunately, using time-dependent Raman scattering theory, it is possible to form an approximation to the KHD expression that holds for cases of resonance Raman. Using the short time approximation, the excited electronic state Hamiltonian is included in the calculation and then approximated with its classical equivalent. This is the approach of Schatz [18] and coworkers and it is necessary for modeling the effect the SERS substrate on the electronic states of the analyte molecule.

2.8 Year two results

To date, work has been done in the study of mercaptoethanol, mercaptoacetic acid, aminoethanol, and glycine interacting with nanoclusters of silver SERS substrates as models, using Gaussian 2009 for an excitation wavelength of 785 nm when that wavelength is not in resonance with any low lying states, and the ADF code to calculate Raman scattering factors as well as the energies of the electronic states and oscillator strengths. This work involved calculating the Raman scattering factors with the input laser wavelength at 785 nm while progressively adding silver atoms to the model with both the Gaussian 2009 [19] and ADF 2010 quantum mechanical codes.[20,21] For calculations performed with Gaussian 2009,

the B3LYP/LANL2DZ and the BP86/LANL2DZ levels of theory were used to calculate Raman scattering factors. The coupled-perturbed Hartree-Fock equations were utilized to account laser excitation at 785 nm in the Raman scattering factor. For calculations performed with ADF 2010, the BP86/TZ2P level of theory was used with effective core potentials. To account for relativistic effects on the heavy silver atoms, the relativistic ZORA facility in ADF was utilized. Raman scattering factors that take into account resonance with low lying electronic states were calculated with the AORESPONSE module within ADF. A laser frequency of 785 nm and a lifetime constant of 0.0034 Hartrees were used as inputs. The AORESPONSE module in ADF is not currently able to handle unpaired electrons and unbalanced electron spin with the relativistic scalar ZORA algorithm. To maintain zero electron spin, only odd numbers of silver atoms are used with the sulfur containing molecules, and even numbers of silver atoms are used with the amine containing compounds. To model spectra that can be compared to the experimental data, Lorentzian lineshapes with a FWHM of 30 cm^{-1} are located at the normal mode frequencies, scaled with the predicted intensities, and then summed to produce the predicted Raman spectra. For the same model systems, time dependent DFT calculations were performed with both Gaussian and ADF for the 50 lowest energy singlet-singlet electronic excitations. The energies and oscillator strengths of transitions to these electronic states determine whether resonance Raman is occurring at the modeled wavelength of 785 nm.

The expected behavior of the enhancement from the purely plasmonic point of view would be a monotonic increase in Raman scattering as silver atoms were added to the model. As atoms were added, more and more mobile electrons would be available, increasing the density of the plasmonic states, and increasing the probability they could influence the polarizability. Of the results from mercaptoethanol, mercaptoacetic acid, aminoethanol, and zwitterionic glycine, only the aminoethanol results followed this pattern and showed a clear cause and effect between silver cluster size and Raman enhancement. As shown in Figure 7, the system of aminoethanol on a silver nanocluster followed the expected trend as silver atoms were added to the model. Figure 8 shows the results of the time dependent DFT calculations on the excited states for the same systems modeled in Figure 7. Although the aminoethanol is not chemically bound to the nanocluster, the nanocluster does indeed change the electronic structure of the overall system. For the bare aminoethanol molecule, the electronic absorptions fall deep within the UV and no resonance effects can be expected. As metal atoms are added to the system, the electronic transitions are shifted towards the visible wavelengths, and several absorptions become accessible to the 785 nm excitation wavelength modeled and can participate in resonance and pre-resonance enhancement. The electronic absorptions become progressively closer to the modeled wavelength as atoms are added, and the result of Figure 2 would suggest that the Raman enhancement is driven by a resonance effect.

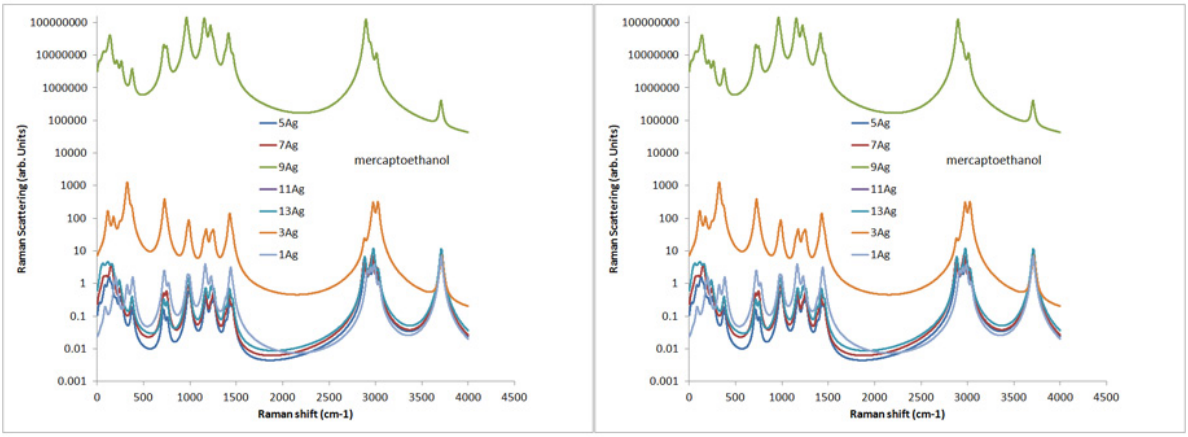

Figure 7. Comparison of calculated Raman spectra for aminoethanol, and aminoethanol associated with various sizes of silver metal clusters, and the same for mercaptoethanol. For aminoethanol, there appears to be a monotonic increase in Raman scattering as silver is added to the metal cluster. For mercaptoethanol, the pattern of increase is not monotonic.

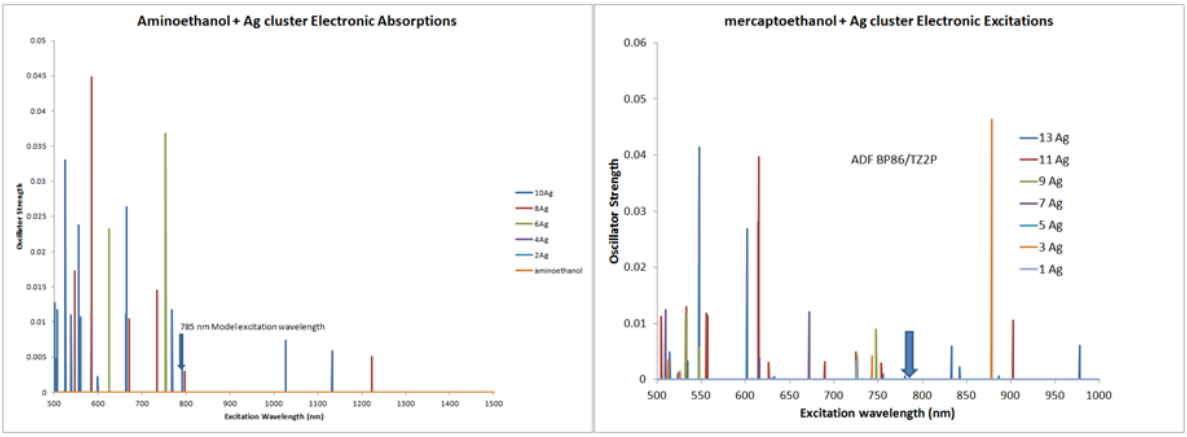

Figure 8. Results of time-dependent DFT calculations in ADF for aminoethanol and mercaptoethanol associated with various sized metal clusters. For each cluster size, 50 singlet-singlet transitions were calculated.

Figure 9 shows a series of isodensity surfaces for the highest occupied molecular orbital (HOMO) and the lowest unoccupied molecular orbital (LUMO) each for aminoethanol associated with two silver atoms and for aminoethanol associated with eight silver atoms. For the smaller silver cluster, there is no sharing of electron density between the metal cluster and the aminoethanol molecule for either the HOMO or the LUMO. In contrast, the HOMO and LUMO of the eight atom silver cluster associated with aminoethanol shows significant sharing of electron density between the metal cluster and the aminoethanol. As expected, the amount of Raman enhancement increases as the electron density is shared. This result would suggest charge transfer or charge sharing to be a major drive for the enhancement.

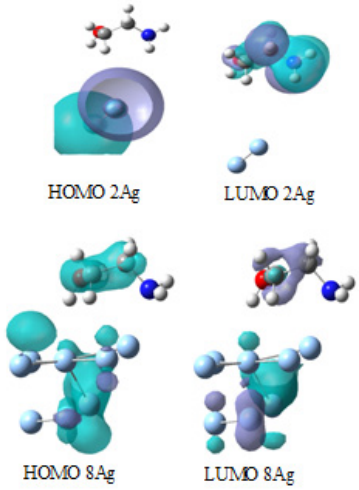

Figure 9. Electron isodensity surfaces for the HOMO and the LUMO for aminoethanol associated with a 2- and 8-atom cluster of silver. For the smaller cluster, there is little sharing of electron density between the metal cluster and the aminoethanol. For the larger cluster, there is significant sharing of electron density.

While the trends observed with aminoethanol seem to indicate the phenomena that drives enhancement involve resonant enhancement and charge sharing between the analyte molecule and the metal cluster, the connection between enhancement and these phenomena is not clear for mercaptoethanol, metcaptoacetic acid, or glycine. For clusters of 1 to 3 silver atoms and mercaptoethanol or mercaptoacetic acid, there is an increase in the Raman scattering factors. For 5, 7, 11, and 13 atoms in the metal cluster, very little enhancement was observed. Yet, the model having nine silver atoms produces enhancements of 7 orders of magnitude, so that there does not appear to be a monotonic relationship between the number of silver atoms in the cluster and Raman signal return. A similar pattern is observed for zwitterionic glycine, where for clusters of 2 and 4 silver atoms, there is an increase in Raman scattering factors, but not for a cluster

of 6 silver atoms. An examination of isodensity surfaces of these compounds show electron sharing for systems that have little or no enhancement, and thus weakening any link between sharing of electric charge density and Raman enhancement. In addition, time dependent Raman spectra were calculated for mercaptoethanol and mercaptoacetic acid associated with silver clusters of 1 to 13 atoms.

An examination of the electronic structure shows that resonance enhancement is not sufficient to explain the calculated Raman enhancement that occurs by associating analyte molecules with the metal nanoclusters. The results of time-dependent calculations with Gaussian 2009 and the B3LYP/LANL2DZ level of theory (not shown) shows that for the clusters that are weakly enhanced, the electronic absorptions fall at much different optical wavelengths than the modeled 785 nm. For systems that are strongly enhanced, absorptions of strong oscillator strength occur close the modeled excitation wavelength. Although this result is consistent with the hypothesis that the main driver for the enhancement involves resonance Raman effects, the results of these calculations were produced with Gaussian, and Gaussian does not account for time dependent effects on the Raman scattering. Excited state calculations were also performed with ADF and the same conditions that were used to calculate the resonant Raman spectra for comparison to the Raman spectra predicted from ADF. The resulting absorption lines from these calculations do not follow the same pattern as the previous Gaussian calculations in the case of mercaptoethanol. For example, although the cluster with thirteen silver atoms experiences a small amount of enhancement, there is an absorption line close to 785 nm. If resonance effects indeed were the main driver for enhancement in the model, the cluster of 13 atoms should have produced a very strong Raman signal. The 3 silver atom cluster produces two very strong electronic absorptions close to the 785 nm excitation used in the model, and these are much stronger than the single absorption near 785 nm that the 9 atom cluster has; however, the predicted Raman signal from the 9 atom cluster is many orders of magnitude stronger than the 3 atom cluster. Thus, we do not expect resonance with an electronic state to be the primary driver for Raman enhancement.

Given that the conventional understanding of SERS involves electric field enhancement, the interaction of the electric field and path of atoms involved in the normal modes must be examined. Figure 10 shows aminoethanol associated with a cluster of 6 silver atoms, including arrows that indicate the motions of atoms that compose two vibrational modes. Superimposed on the plane that contains the motions of interest is a contour plot of the potential energy field where the electric field is orthogonal to the equipotential lines. The atomic motions involved for the two normal modes are indicated by vectors where the magnitude is proportional to how much the atoms are displaced along the normal coordinate.

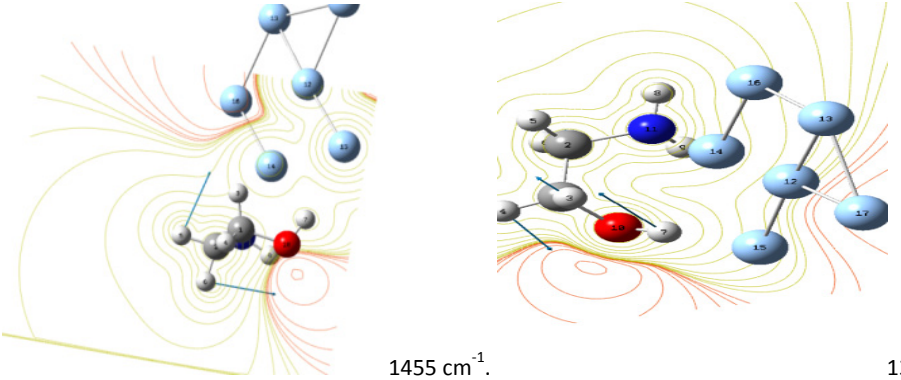

1455 cm^{-1}. 1354 cm^{-1}

Figure 10. A weakly enhanced mode at 1455 cm^{-1} compared to a strongly enhanced mode at 1354 cm^{-1} for the aminoethanol + 6 Ag system. The atomic motions for the mode are indicated by vectors; the magnitude of the vectors is indicated by their length. A contour plot of the electrostatic potential is shown in the plane of the normal mode motion, where the electric field is directed normal to the equipotential lines and the magnitude of the field is indicated by the spacing of the equipotentials. For the mode that is strongly enhanced, atomic motions are mostly aligned with the electric field, and as indicated by the equipotential lines, the overall electric field is directed in one direction.

The first mode predicted for 1455 cm^{-1} is very weakly enhanced. The second mode at 1354 cm^{-1} is very strongly enhanced. As shown by the equipotential lines in Figure 4, where the equipotential lines are mapped out in a plane that contains the motion along the normal coordinate, the atomic motion for the second mode has a significant component aligned with the local electric field. The electric field is also, on average, directed in a single direction along the aminoethanol. The atomic motions along the first normal mode coordinate that is weakly enhanced are also aligned with the local electric field, but this field is symmetric about the molecule and the hydrogen bending is also symmetric about the molecule, resulting in little net change in overall polarizability. Given that the electric field around two modes of the same cluster system, where electron sharing and resonance Raman effects are the same, this result qualitatively supports the understanding that electric field enhancement is the primary driver for SERS enhancement.

3. CONCLUSIONS

We have demonstrated that it is possible to reproducibly fabricate tethered silver and gold nanoparticle substrates. Using these substrates, binding kinetics of 2-mercptoethanol to the silver nanoparticle surface was evaluated. The primary qualitative result from the computational modeling of aminoethanol, glycine, mercaptoethanol, and mercaptoacetic acid is that modes that experience Raman enhancement by association with a metal nanocluster are those where the atomic motions along the normal mode have a significant component along a local electric field that propogates in a single direction. While resonance and preresonance effects related to low lying electronic states created by association with the metal cluster certainly make a contribution to the Raman enhancement, the results of the modeling show that they by no means dominate. Sharing of electron density appears to make a contribution, but it also by no means fully accounts for the predicted enhancement.

In the next year, we will incorporate new molecules, taking advantage of different polarities while enahancing the tethering ability of the silver and gold nanoparticles enabling additional binding kinetic measurements along with additional computational modeling with increasing metallic clusters.

WORK CITED

[1] Fleischmann, M. et al. 1974. *Chem. Phys. Let* 26(2), 163-6.
[2] Jeanmaire, D. L. and Van Duyne, R. 1977. *J. Electroanal. Chem. Inter. Electrochem.* 84(1), 1-20.
[3] Albrecht, M. G. and Creighton, J. A. 1977. *J. Am. Chem. Soc.* 99, 5215-5217.
[4] Gersten, J. and Nitzan, A. 1980. *J. Chem. Phys.* 73(7), 3023-37.
[5] Wang, D. S. and Kerker, M. 1981. *Phys. Rev. B* 24(4), 1777-90.
[6] Cline, M. P. et al. 1986. *J. Opt. Soc. Am. B:* 3(1), 15-21.
[7] Hulst, Van de. 1981. Light Scattering by Small Particles. Dover Publications Inc. New York.
[8] Carey Lea, M. 1889. *Amer. J. Sci*. 37, 476-491.
[9] Lee, P.C. and Meisel, D. 1982. *J. Phys. Chem.* 86, 3391-3395.
[10] Rohr, T. E. et al. 1989. *J. Anal. Biochem.* 182, 388-398.
[11] Adamson, A.W. and Gast, A.P. Physical Chemistry of Surfaces. Wiley Interscience, New York, 1997, 6th ed., p. 599.
[12] Biggs, K.B. et al. 16 March 2009. *J. Phys. Chem. A*, Article ASAP.
[13] ECBC In-House Laboratory Independent Research Program Annual Report FY10.
[14] Itoh, T. et al. 2007. *Phys. Rev. B* 76.
[15] Kramers, H. A. and Heisenberg, W. 1925. *Zeitschrift fur Physik* 31(1), 681-708.
[16] Dirac, P. A. M. 1927. *Proc. R. Soc. Lond.* 114, 710-728.
[17] Placzek, G. 1934. *Handbuch der Radiologie;* Leipzig.
[18] Jensen, L. et al. 2005. *J. Chem. Phys.*123, 174110-1-174110-5.
[19] *Gaussian 2009, Revision A.02,* Gaussian, Inc.: Wallingford CT, 2009.
[20] *Amsterdam Density Function Code,* v. 2010. Vrije Universiteit: Amsterdam, Netherlands, 2010.
[21] van Gisbergen, S. J. A. et al. 1999. *Comp. Phys. Comm.* 118, 119.

A computational approach to discovering useful self-assembling compounds

Harold D. Banks
Edgewood Chemical Biological Center, Research & Technology Directorate, 5183 Blackhawk Rd., Aberdeen Proving Ground, MD 21010

ABSTRACT

The ability of molecules structurally derived from the purine and pyrimidine bases found in DNA to self-assemble was explored computationally using density functional theory at the B3LYP/6-31+G(d) level. To further increase the likelihood of self-assembly of hybrid nucleobases in linear chains, the possibility of this process occurring on a graphene surface was considered. Due to the staggering cost of calculations on graphene itself, a reasonable model, coronene, was used for preliminary calculations. Our findings at this level of sophistication indicate that self-assembly of suitably chosen hybrid nucleobases under these conditions is likely.

1. INTRODUCTION

The broad potential applications of nanotechnology [1] in the development of quantum computers, advanced materials, drug delivery, and filtration, etc. has led to vigorous pursuit of many avenues of research. Nanotechnology promises to deliver results at vastly reduced weight and volume with significantly reduced energy consumption. The present research effort was inspired by two Nobel Prizes: the elucidation of the structure of DNA [2] and the development of a method for preparation and study of grapheme [3], the two-dimensional, one-molecule thick product of exfoliation of graphite (Figure 1). The base pairs that are responsible for the helical double strands of DNA employing hydrogen bonding are a reasonable starting point to investigate self-assembly mechanisms. Because these bases are aromatic, one would expect them to interact favorably with the aromatic graphene surface by means of $\pi - \pi$ interactions. Both self-assembly and the extended planar structure of graphene have important nanotechnological implications. Some of the present and anticipated applications of nanotechnology are quantum computers, novel drug delivery mechanisms, ultrafiltration, and the discovery of advanced materials.

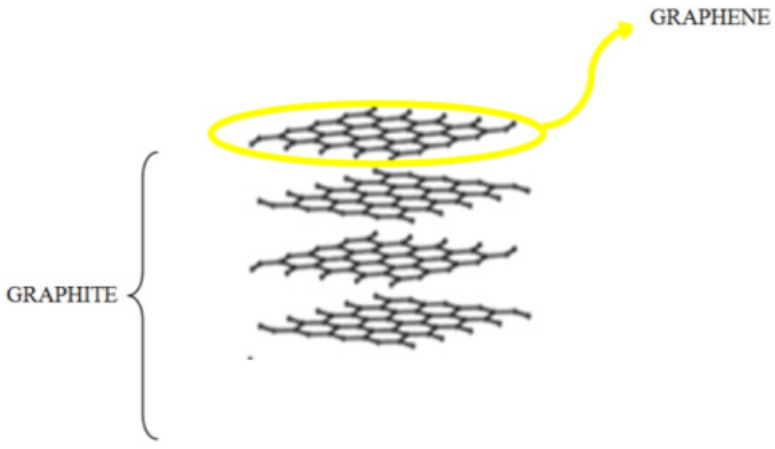

Figure 1. Preparation of graphene from graphite.

Self-assembly is a bio-inspired approach to assembling supramolecular structures. Biological cells function by utilization of a plethora of self-assembly processes. Growth of surface quantum dots is an additional example of this process. Since self-assembly occurs on a molecular scale, is a powerful, unique method for generating nanostructures. It is also useful in the formation of smart materials and design of computer components. Additional potential applications are in the areas of robotics, sensors, and microelectronics. Simple mixing initiates these processes, resulting in non-covalent associations; this is in sharp contrast to the thermal, photochemical or microwave energy input that often characterizes covalent bond formation.[4]

Potential mechanisms of self-assembly are hydrogen-bonding, halogen bonding, metal-ligand interactions, hydrophobic effects, electrostatic interactions, and $\pi - \pi$ interactions. Several of these possibilities were studied in the present investigation.

In order for self-assembly to proceed, the head and tail of a given molecule must have complementary interactions. The regiochemistry must be considered in targeting the shape, linear, circular, etc., of the final assembly.

2. COMPUTATIONAL METHODOLOGY

The enthalpy and free energy changes for the optimized structures upon formation of complexes were calculated in the gas phase at 298.15 K and 1 atm at the B3LYP/6-31+(d) level by means of the Gaussian 03 suite of programs.[5] Initial geometry was determined at the AM1 level using Spartan 06.[6] The criterion for ground state structures was the absence of imaginary frequencies. The structures of starting compounds and their complexes were visualized and analyzed with GaussView 3.09.[7] Basis set superposition energies (BSSE) were calculated using the counterpoise method.[8] The BSSE are due to the fact that, when the basis sets of two species interact, the wavefunction of the complex becomes expanded such that it has available more basis sets than that of the component; this leads to an erroneously low energy for the associated species. The counterpoise method is an approach to approximate the basis set of the complex with a size equivalent to the uncomplexed molecules. An additional contribution to the total energy of the complex is non-bonded interactions or dispersion. For purposes of initial screening, these effects were ignored since their evaluation would add to the computational cost.

3. RESULTS AND DISCUSSION

One possible mechanism for self-assembly is halogen bonding. In this non-covalent interaction, one halogen atom acts as the electron pair donor while the other atom plays the role of electron acceptor. Since iodine is the best donor, a molecule containing this halogen was employed to assess the importance of this type of interaction (Figure 2). Halogen bonding can be quite strong; the largest value determined at present is 31 kJ/mol.[9] An appraisal of the importance of this effect is important given the findings of Kool that certain isosteric substitutions with halogenated compounds can be made for the nucleobase pairs without significant loss of stabilization (*vide infra*). The results of the calculations demonstrate that the halogen bonding is rather weak for these types of compounds, as evidenced by their enthalpies of formation and rather large interatomic distances.

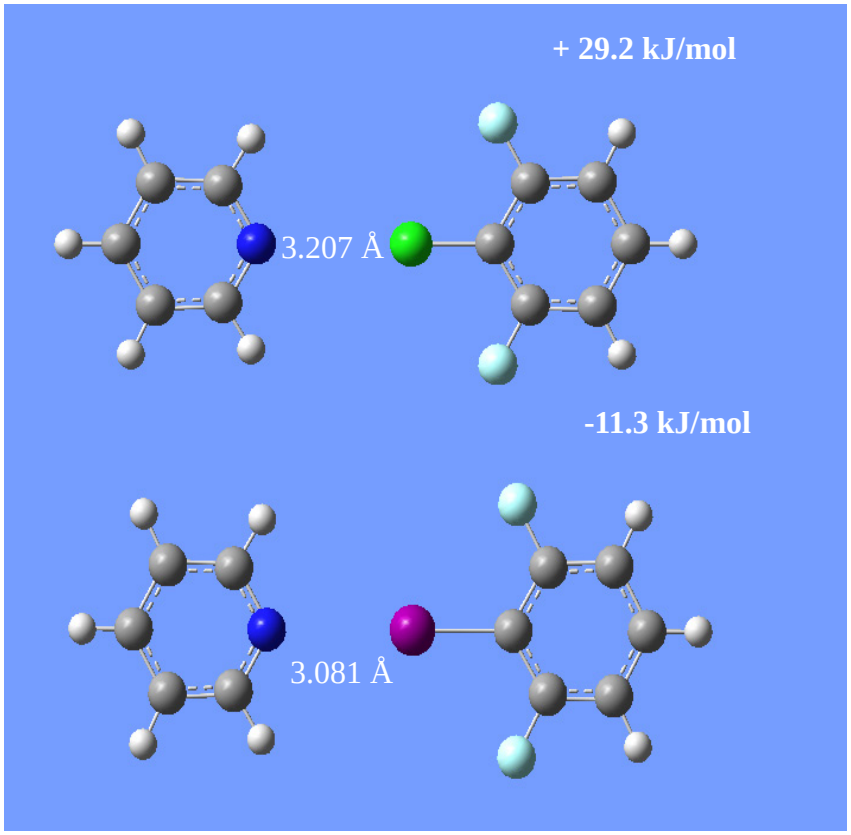

Figure 2. Distances between halogen atoms and enthalpies of complex formation or pyridine with 2-chloro-1,3-difluorobenzene and 2-iodo-1,3-difluorobenzene.

Table 1 presents the results of computations of the enthalpy and free energy of formation, as well as the entropy and basis set superposition energies for complex formation for nucleobases and hybrid molecules. Unless otherwise noted, the complexes are Watson-Crick. Since these values were obtained in the gas phase, the entropies are quite large; the free energies are thus distorted positively relative to expectations in the condensed phase. The enthalpies were thus chosen for comparison. The Watson-Crick and Hoogsteen complexes of adenine and thymine are computed to be quite similar in energy, in accord with reported results.[10] Our finding of the greater stability of the guanine-cytosine pair relative to that of adenine-thymine qualitatively agrees with previous *ab initio* calculations.[11] These results provide confidence that the remaining calculations of Table 1 are reasonable. It is useful to note that substitution of fluorine results in lowered complex stability. Fluorine is often employed as a vastly more electronegative mechanistic probe that is only somewhat larger than hydrogen. In the examples studied herein it is reasonable to assume that this halogen decreases hydrogen bonding by rendering one member of the pair a poorer electron pair donor. As expected, comparison of the triazines reveals that the ΔH values are proportional to the number of hydrogen bonds formed by the corresponding dimer. The bicyclic amide result demonstrates that the planarity of aromatic rings is not required for reasonably strong complex formation; the shape of the complex is necessarily nonlinear. Finally, 2,6-dihydro-pyridine represents an OH hydrogen bond donor.

Table 1. Calculated thermodynamic parameters for complexes

COMPLEXES	ΔH(AB) kJ/mol	ΔS(AB) J/mol-K	ΔG (AB) kJ/mol	BSSE kJ/mol
Adenine-Thymine	-45.27	-157.34	1.64	3.59
Adenine-Thymine (Hoogsteen)	-48.35	-159.36	-0.83	4.02
Cytosine-Guanine	-98.55	-164.90	-49.39	5.29
2-Fluoroadenine-Thymine	-35.81	-145.63	7.61	3.64
Guanine-Thymine (Hoogsteen)	-23.53	-132.06	15.84	2.58
Adenine-6-Fluorothymine	-47.04	-157.77	0.00	3.64
6-Fluorothymine-Difluoroadenine	-33.43	-158.33	13.77	3.61
Trifluorothymine-Difluoroadenine (Hoogsteen)	-38.34	-158.33	8.86	4.17
Trifluorothymine-Difluoroadenine	-33.81	-145.22	9.49	3.61
Trifluorocytosine-Guanine	-95.77	-175.38	-43.48	5.18
Diguanine-Dicytocytosine	-98.79	-158.46	-51.54	5.48
Adenine-22-Difluorothymine	-45.87	-155.03	0.36	3.81
Adenine-2-(Difluoromethylene)thymine	-41.71	-159.08	5.72	3.88
Adenine-4-DiFmethylenethymine	-19.86	-145.36	23.48	3.36
Triazine-Triazine (2 H-bonds) [see text]	-66.11	-140.10	-24.34	4.16
Triazine-Triazine (3 H-bonds) [see text]	-95.81	-167.95	-45.74	5.55
2-Iodo-1,3-difluorobenz-Pyridine	-11.32	-105.96	20.27	2.35
2-Chloro-1,3-difluorobenz-Pyridine	29.18	-90.10	56.04	0.95
3-Azabicyclo[2.2.2]octan-2-one Dimer	-51.48	-154.01	-5.56	4.52
2,6-Dihydroxypyridine Dimer	-93.19	-192.99	-35.65	7.45

Because assembled structures approaching linearity were deemed desirable, only aromatic structures whose enforced planarity limited molecular degrees of freedom were considered. Figure 3 presents the structures of isomers derived from cytosine having different symmetry elements. The results of a calculation to evaluate hydrogen bonding with guanine were also provided. The interatomic distances of the appropriate atoms are well within the expected range for this type of non-bonded interaction. The structure has a relatively large ΔH of -90.8 kJ/mol.

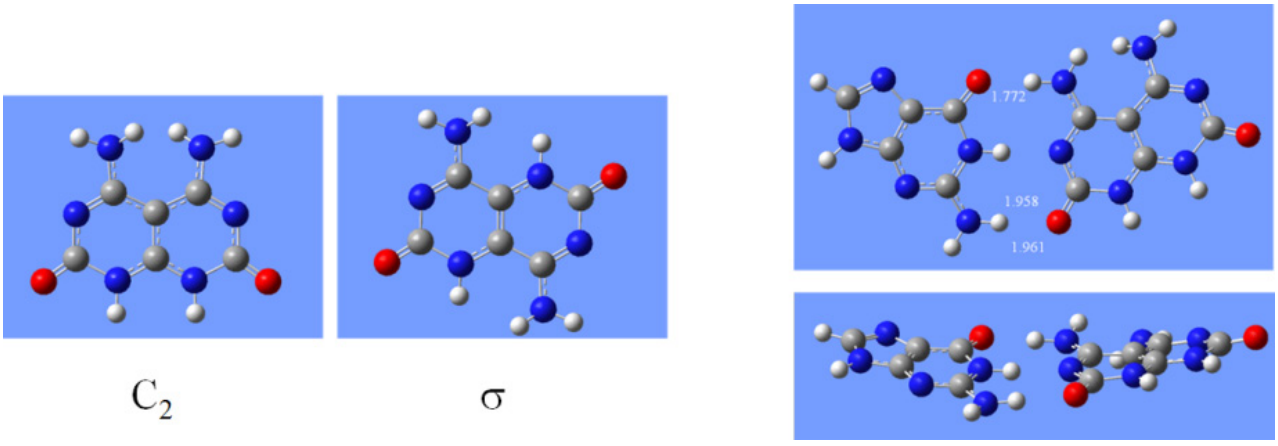

Figure 3. Two hybrid structures derived from cytosine. The complex of σ isomer with guanine.

It is interesting to note that the complex departs slightly from planarity. It might be expected that interaction with a surface such as graphene would tend to force this complex to assume a structure that approaches planarity. The arrangement of extended complexes is not necessarily linear. Guanine, for example, self-associates into two ribbons with zigzags in an averaged linear direction; however, it also forms a cyclic tetramer, the G-quartet.[12] The regioisomeric adenine-thymine hybrids provided in Figure

4 have the potential to take advantage of the strong interactions of this base pair. The anticipated zigzag structure resulting from self-assembly of the second isomer is also provided.

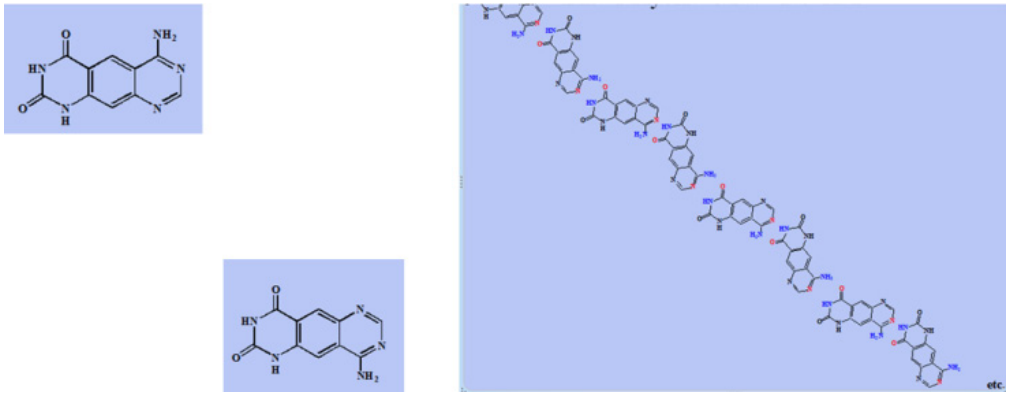

Figure 4. Hybrid structures derived from adenine and thymine and self-assembly of lower compound.

Calculations in which coronene is used as a model for graphene are available at a modest computational cost, but come with liabilities. Coronene is similar in size to hybrid nucleobase candidates. As such, one would expect the heterocyclic molecule to exert a considerably larger perturbation on the structure of this polycyclic aromatic hydrocarbon than anticipated for graphene. Additionally, the base would necessarily be susceptible to the edge effects of this graphene model. An example that illustrates these problems is presented in Figure 5.

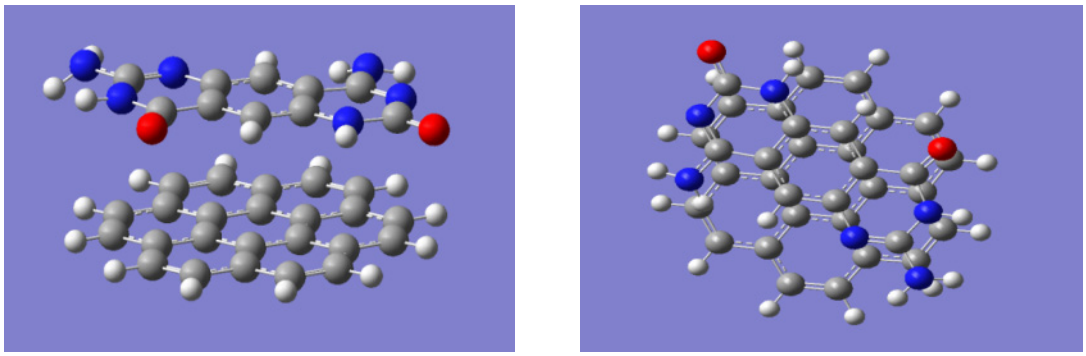

Figure 5. Perpendicular views of a hybrid nucleobase and coronene. The planes are 4.5 Å apart.

Kool [13] discovered that pairs such as 4-methylbenzimidazole (MBI) and 2,4-difluorotoluene (DFT) that are isosteric with adenine and thymine, respectively pair with each other in spite of the absence of hydrogen bonding possibilities, apparently by favorable hydrophobic interactions. This interaction was calculated to be slightly unfavorable in the gas phase (ΔH = 1.21 kJ/mol), whereas for the adenine-2,2-difluorothymine complex , ΔH = -45.9 kJ/mol.) Computations for interactions with the coronene surface found ΔH = -24.4 kJ/mol for MBI and -1.18 kJ/mol for DFT. The complex of MBI and DFT with coronene resulted in ΔH = -24.4 kJ/mol; apparently DFT had no effect on the favorable interaction of MBI, however, the complex of nuclebase isosteres was disrupted as evidenced by an increased intermolecular distance (Figure 6). These findings suggest that isosteric substitutions are effective in part because of the unique structure of DNA in which these compounds are tethered on the chains and $\pi - \pi$ stacking interactions can occur. To the extent that coronene is a surrogate for graphene, one would deem these types of molecules poor choices for surface self-assembly. A recent report [14] that calculated distances between the nucleobases and larger polynuclear aromatic hydrocarbon models for graphene gave an average distance between the planes of 3.5 Å. In hybrid nucleobase-coronene studies we have

found the interplanar distances to be 4.3 – 4.6 Å. One of the difficulties of using coronene is that its size and that of the surface molecule are comparable. Edge effects should introduce a large contribution to the surface effects.

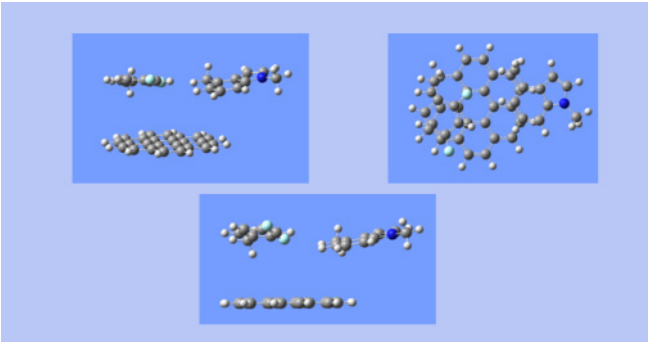

Figure 6. Interaction of MBI and DFT with coronene. The closest distances between MBI and DFT, DFT and coronene and DFT and coronene are 3.30, 5.67, and 4.32 Å, respectively.

A more reasonable model for graphene is the 5x5x1 supercell provided in Figure 7 with the triazine (6-amino-1,3,5-triazine-2,4(1H,3H)-dione) dimer held together by three hydrogen bonds on its surface. Clearly edge effects are less important than in the case of coronene, however 118 atoms are incorporated into this calculation. Computations for this type of system may be handled by DMol^3 that is ideally suited for modeling surface interactions.[15,16] These calculations are facilitated by recent access to the supercomputer network at ARL. DMol^3 offers the additional advantage that DFT-D calculations can be routinely performed. This approach corrects for the dispersion [17] or nonbonding interactions that occur in sytems containing more than one molecule. Geometry optimization results in determination of all the intermolecular (and interatomic) distances in addition to the total energy of the system. The enthalpy of formation is then calculated from the energies of the individual components. Because the size of the basis sets tend to be smaller than those of Gaussian, the BSSE values are smaller.[17b]

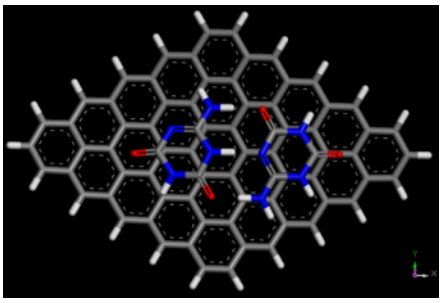

Figure 7. Triazine dimer with three hydrogen bonds on 5x5x1 supercell

One interesting possibility for self-assembly is the tethering of a molecule to the surface that will serve to initiate the process. Azomethine ylides [18] are known to react readily with the graphene surface.[19] This idea is illustrated in Figure 8. It is assumed that, as the hybrids assemble, favorable $\pi - \pi$ interactions with the graphene surface will cause the chain to coat the surface.

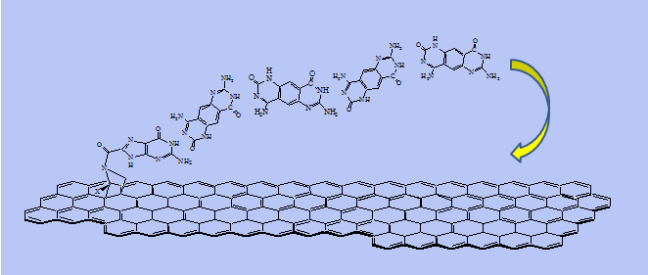

Figure 8. Self-assembly of a guanine-cytosine hybrid nucleobase by means of surface tethering.

Finally, it should be noted that many compounds that are within the purview of this study have been prepared and offer experimental opportunities. The triazine, for example, has a CAS registry number of 645-93-2. An incomplete list of other possibilities are 57978-32-2, 30201-64-0, 73619-61-1, 645-93-2, 626-06-2, 45893-20-7, 28285-95-2, 67116-20-5, 872277-14-0, 5926-95-4, 591-28-6.

4. CONCLUSIONS

Density functional theory calculations (B3LYP/6-31 were used to study the relative strengths of complexes formed between the nucleobases and derived hybrid structures. Halogen bonding was found to be nonexistent. Hydrogen bonding was found to be the most effective means of stabilizing dimeric complexes. The strongest complexation was determined to occur between guanine and cytosine, although the triazine that formed three hydrogen bonds was almost as stable. A pair of aromatic compounds (MBI and DFT) that do not hydrogen bond, which were found to be effective substitutes for the nucleobases when incorporated into DNA, were found to associate poorly in the gas phase and on the coronene surface. While use of coronene as a surrogate for graphene has the advantage of greatly reducing computational cost, it was demonstrated that its size is comparable to that of most reasonable assembly candidates. This introduces the possibility of edge effects that could potentially change the energies found in geometry optimization calculations. More reasonable models for graphene are the 5x5x1 and 6x6x1 supercells, although this raises the level of difficulty of the calculation that must necessarily handle more than 100 atoms. The recently available DMol^3 program appears to be a viable solution to this problem. Molecules must be chosen for their ability to associate in a linear (zigzag) manner. They must possess a complementary head and tail for propagation of the chain.

This technical report describes our results after roughly 10 months of research. Promising hybrid nucleobases for self-assembly have been identified. It has been decided to proceed with calculations using supercells as models for graphene. The results of these investigations are ongoing and will be reported in due course.

WORK CITED

[1] (a) Ozin, G.A. et al. 2009. *Nanochemisty*, Royal Society of Chemistry, London. (b) Müller, A.; Cheetham. 2007. *Nanomaterials Chemistry*, Wiley-VCH, Weinheim. (c) Cademartiri, L. et al. 2009. Lehn, J-M. *Concepts of Nanochemistry*, Wiley-VCH, Weinheim. (d) Sergeev, G.B. 2006. *Nanochemistry*, Elsevier, Amsterdam. (e) Barone, V. et al. 2011. *Acc. Chem. Res.* 44, 269. (f) Hong-Bin et al. 2011. *Chem. Soc. Revs*. 40, 3764. (g) Love, J. C. et al. 2005. *Chem. Rev.* 105, 1103. (h) Lallana, E. et al. 2011. *Angew. Chem. Int. Ed*. 50, 8794.

[2] Watson, J.D. and Crick, F.H.C. 1953. *Nature* 171, 737.

[3] Geim, A.K. and Novoselov, K.S. 2007. *Nat. Mat.* 6, 183.

[4] Whitesides, G.M. and Grzybowski, B. 2002. *Science* 295, 2418.

[5] *Gaussian 03, Revision C.02*. Gaussian, Inc., Wallingford CT, 2004.

[6] *Spartan 06*, Wavefunction, Inc., 18401 Von Karman Avenue, Suite 370, Irvine, CA 92612 USA.

[7] *GaussView 3.0*, Gaussian Inc., Carnegie Office Park, Blg 6, Pittsburgh, PA 15106.
[8] Boys, S.F. and Bernardi, F. 1970. *Mol. Phys*, 19, 553.
[9] (a) Riley, K.E. and Merz, Jr., K.M. 2007. *J. Phys. Chem. A* 111, 1688 and references cited therein. (b) Lu, Y. et al. 2010. *Phys. Chem. Chem. Phys.* 111, 1688. (c) Metrangolo, P. et al. 2005. *Acc. Chem. Res.* 38, 386.
[10] Kratochvíl, M. et al. 2000. *J. Am. Chem. Soc*. 122, 3495.
[11] Kabelá, M. and Hobza, P. 2001. *J. Phys. Chem. B* 105, 5804.
[12] Kwan, I.C.M. et al. 2007. *J. Am. Chem. Soc*. 129, 2398-2407. Smaller thymine and uracil can form quintets: See Qui, E. et al. 2009. *Chem. Commun*. 2863.
[13] (a) Kreuger, A.T. and Kool, E.T. 2009. *Chem. & Biol*. 16, 242. (b) Kool, E.T. 1997. *Chem. Rev*. 97, 1473. (c) Schweitzer, B.A. and Kool, E.T. 1994. *J. Org. Chem.* 59, 7238.
[14] Gowtham, S. et al. 2007. *Phys. Rev. B B76*,033407.
[15] Accelrys Software Inc., 10188 Telesis Court, Suite 100, San Diego, CA 92121.
[16] For recent examples using DMol^3 see (a) Wu, M. et al. 2010. *J. Am. Chem. Soc*. 132, 5554. (b) Inada, Y. and Orita, H. 2008. *J. Comput. Chem*. 29, 225. (c) Clare, J.P. et al. 2009. *J. Org. Chem.* 74, 6637. (d) Zhang et al. 2005. *J. Phys. Chem. A.* 109, 6592.
[17] (a) Grimme, S. 2004. *J. Comput. Chem*. 25, 1463. (b) Grimme, S. 2006. *J. Comput. Chem*. 27, 1787. (b) Mackie, I.D.; DiLabio, G.A. *J. Phys. Chem. A.* 2008, *112*, 10968.
[18] See (a) Banks, H.D. Org. 2011. *Biomol. Chem*. 6335. (b) Banks, H.D. 2010. *J. Org. Chem*. 75, 2510 and references cited therein.
[19] See Cao, Y. and Houk, K.N. 2011. *J. Mater. Chem*. 21, 1503.


SSI PROJECTS

Identification of dynamic changes *in vitro* following exposure to the toxicant paraoxon

Aisha Hajjaj[c] Kristen Willis[a,b] Rabih Jabbour[a], and Russell Dorsey[a]
[a]Edgewood Chemical Biological Center, Research & Technology Directorate, 5183 Blackhawk Rd., Aberdeen Proving Ground, MD 21010
[b]Defense Threat Reduction Agency, Fort Belvoir, VA
[c]Science Applications International Corporation, Aberdeen Proving Ground, MD

ABSTRACT

Currently, the Chemical Abstract Services (CAS) Registry contains over 63 million organic and inorganic substances. There is considerable concern because the majority of these substances have not been evaluated for potential toxic effects and, in particular, the toxicity of chronic low level exposures and combinations of chemicals are seldom examined. In addition to the chemicals found on the registry, novel, unpublished chemicals are proliferating globally, some of which are designed for specific detrimental effects. Current toxicity testing protocols rely primarily on animal models, typically requiring months to test a single compound; this approach struggles to meet the demand. Moreover, cost and ethical concerns associated with the use of animal resources are becoming limiting factors to scientific progress. Thus, incentive is mounting to develop methods employing *in vitro* techniques. To date, the development of *in vitro* screening approaches that accurately recapitulate the complex processes of vertebrate organ systems have presented a significant challenge. The use of stem cells will, in part, allow technological barriers to be broken. Although work with stem cells has largely focused on use in replacement therapies for disease states of the central nervous system, recent studies demonstrate the utility of stem cells in assessing neurotoxicity *in vitro* and provide support for the development of this technology. Therefore, we are developing technologies that employ human pluripotent stem cells (hPSC) to assess neurotoxic outcomes. hPSC's are immortal and can be differentiated into the major neural cell types, which will eliminate the variability of using surgically removed cells or tissue. Stem cells are karyotypically normal, in contrast to all other human cells lines, which have genetic abnormalities. Also, the use of human cells will eliminate the error of extrapolation from animal to human. Initially, we assessed the OP class of chemicals, which are utilized industrially, agriculturally, and as warfare agents. Because of their ubiquity and toxicity, much research has been invested into the OPs, providing an understanding into many of their neurotoxic mechanisms. This will facilitate linking observed cellular aberrations in model systems to neurotoxic outcomes. Subsequent to *in vitro* model characterization, in conjunction with the New York Structural Biology Center (NYSBC), we will identify and determine the molecular structure of cellular proteins of interest, thus enabling *in silico* screening for OP chemical to protein interaction. A tiered approach of *in silico* screening at a rate of 10,000 per second followed by *in vitro* screening at hundreds per day is envisioned. By applying our recently garnered knowledge of stem cells combined with innovative analytical techniques, we have the opportunity to develop technology that could enable a wide range of screening, from untested combinations and exposure scenarios of known compounds to novel warfare agents of unknown toxicity.

1. INTRODUCTION

Concern is growing regarding adverse health effects from exposure to synthetic chemicals. CAS, a division of the American Chemical Society (ACS), assigns identifiers to every chemical that has been described in the literature. The CAS Registry currently contains over 50 million compounds, and by their

estimates, a novel substance is either isolated or synthesized every 2.6 seconds.[1] Currently, little is known regarding the potential hazard for a large portion of the registry.

The Danish Environmental Protection Agency carried out a study aimed at determining the hazards for 100,000 substances by analyzing two of the world largest sources of publicly available test data (Registry of Toxic Effects of Chemical Substances (RTECS) 2000 and AQUIRE, 1994). Based on their analysis, 25.1% of chemicals were found to cause deleterious health effects.[2]

Applying the percentages of the Danish EPA study to the CAS registry, 12.5 million harmful chemicals may be contained in the registry (Table 1). Given that chemicals do not exist in single pure form, but occur in mixtures in the environment, the potential for additive, synergistic, and potentiating effects logarithmically increases the chances for toxic outcomes. To control the risk of chemical effects on human health, recent legislation in both the United States and Europe dictates increased testing of chemicals and chemical products to predict their potential hazards.[3]

Table 1. Chemical hazards as percentages of RTECS, and AQUIRE and potential number of hazardous chemicals in the CAS registry, in millions.

Hazard type	% of RTECS and AQUIRE	Number of hazardous chemicals (in millions)
Acutely toxic	13.4%	6.7
Toxic to reproduction	2.5%	1.3
Mutagenic	3.9%	2.0
Carcinogenic	1.8%	1.0
Dangerous to the aquatic environment	3.5%	1.8
Total	25.1%	12.8

Traditional approaches for hazard identification and risk assessment are based on toxicity tests using *in vivo* animal models. These tests are designed to generate data relevant to specific adverse outcomes (e.g., cancer, reproductive toxicity, and neurotoxicity). While providing useful information, *in vivo* models struggle to address several competing demands, to characterize chemical toxicity while minimizing the cost, time, and number of animals utilized. Typically, six months are required to screen a single compound at a cost of $250K per compound. This information, combined with the Animal Welfare Act National Defense Authorization Act, which calls for aggressive programs to replace, reduce, and refine current animal usage, makes *in vivo* testing unfeasible for screening the millions of compounds for which there is no toxicity data. Additional obstacles to *in vivo* testing are: high doses (doses are administered based on animal body weight, which limits experimental flexibility and adds to the costs and the hazards of the testing); interspecies variation (animal models are selected based on end point similarity to those in humans, but invariably there is error associated with this extrapolation); and apical endpoints (e.g., observed ataxia does not provide information on the underlying molecular mechanism).

A potential solution for minimizing and possibly replacing animal use, while also promising high throughput (HT), are *in vitro* models. In addition to HT adaptability, *in vitro* systems are able to provide more mechanistic determinations of biological perturbations. Other benefits are the uniform and defined chemical and physical environment that comes with using cell culture techniques and a greater number of dosage ranges and chemical combinations that can be studied. By employing human progenitor stem cells, the error associated with animal to human extrapolation could be eliminated and progenitor cells can be regenerated in perpetuity while maintaining genotypic and phenotypic stability.

To date, a validated *in vitro* approach for assessing neurotoxicity does not exist, leaving an area of critical need. Several significant challenges have prevented development of *in vitro* neurotoxicity screens: (1) developing appropriate human cell-based models, (2) designing screening approaches that accurately recapitulate the complex processes of nervous system reactions to chemical exposures, and (3) developing

high-throughput screening approaches that are both time and cost efficient. Significant advances in our understanding of neurobiology and stem cell biology, coupled to innovative analytical instrumentation, will allow these challenges to be addressed.

Of the three major classes of chemicals, metals, pesticides, and solvents, the OP pesticides will receive our initial attention. Approximately 2.5 million tons of OP pesticides are applied globally per year, causing 3 million poisonings and 220,000 deaths.[4,5] Included in this class of chemicals are the cholinergic chemical warfare agents and other small molecules of DoD interest. The enormous usage and rapidly increasing development of novel OP compounds dictates the need for more intense research into their toxic effects on humans. Organophosphorus compounds have three distinct neurotoxic actions. First is the irreversible inhibition of acetylcholinesterase, resulting in the accumulation of acetylcholine and subsequent overstimulation of the nicotinic and muscarinic acetylcholine receptors, resulting in cholinergic effects. The effects of cholinergic stimulation include vasodilation of blood vessels, slower heart rate, constriction of bronchioles, reduced secretion of mucus in the respiratory tract, intestinal cramps, secretion of salvia, sweat and tears, and constriction of eye pupils. The second action of these compounds arises from single or repeated exposure, causing a delayed onset of ataxia, accompanied by a Wallerian-type degeneration of the axon and myelin in both the central and peripheral nervous systems. This is known as organophosphorus-induced delayed neuropathy (OPIDN). Finally, many studies have reported long-term, persistent, chronic symptoms of neurotoxicity in individuals following acute exposure to high doses resulting in acute cholinergic toxicity. Identical outcomes are also seen from long-term, low-level, subclinical doses of these chemicals which are known as organophosphorus-induced chronic neuropathy (OPICN), which leads to long-term neurological and neurobehavioral deficits. While the mechanisms of this neurodegenerative disorder have yet to be established, the available data suggest that large toxic doses of organophosphorus compounds cause acute necrotic neuronal cell death in the brain, whereas sub-lethal or subclinical doses produce apoptotic neuronal cell death and involve oxidative stress.

OPIDN is prevalent in farmers, particularly those involved with dipping their animals in pesticides, and veterans from the Persian Gulf War. Symptoms of OPIDN that parallel Gulf War Illness (GWI) are ataxia and upper motor neuron spasticity. Additionally, GWI includes difficulty with balance, memory, and headaches. The specific cause of GWI is unknown, but is associated with exposure to OPs potentiated by DEET, pyridostigmine bromide (PB) pills, and atmospheric hydrocarbons. Unfortunately, no effective treatment has been identified for Gulf War illness and studies indicate that few veterans have recovered over time. As an Army research facility, we are ideally suited to apply an hESC screening technology to identify the cause and potential treatments for GWI.

The use of *in vitro* cell culture models to study neurotoxicity is based on the premise that although neurotoxicants may act on a multitude of molecular targets, the final outcome will be reflected in alterations in one or more critical events leading to neurotoxicity. This principle has been demonstrated in the area of embryotoxicity by differentiating stem cells into contractile cardiomyocytes and simply assessing beating versus non-beating following exposure. This one functional endpoint captures many mechanisms involved in embryotoxicity and this model became formally validated as an *in vitro* test for embryotoxicity.

A distinct advantage of *in vitro* cell-based models will be the ability to consistently and precisely replicate events of neurotoxicity. Initially hPSCs will be differentiated into the three major types of cells found in the brain: oligodendrocytes, neurons, and astrocytes. Gains made in understanding central nervous system (CNS) development and biology will be applied to advancing the *in vitro* screening model system with possible utilization of mixed cell populations or neural spheres. To differentiate neurotoxicants from general cytotoxicants, non-neural cells will be included to index basal level activity.

Possible end points that can be measured include cellular morphology, biochemical markers, neurotransmission, and molecular events (gene expression and intracellular signaling). Based on the

current knowledge of OPIDN and OPICN, endpoints that will be initially assessed are necrosis, apoptosis, and neurite outgrowth. Following, we will examine differentiated neuronal specific cell function endpoints such as neurotransmission, axonal transport, receptor and channel activation, enzyme activity, synaptogenesis/myelination, excitotoxicity, and neuronal-glial interactions. Recent studies have shown that many of the mechanisms underlying neurotoxicity ultimately affect neuronal electrical activity. Similar to the singular endpoint of the cardiomyocyte assay for embryotoxicity, measurements electrical activity may serve as a general but still neuronal specific endpoint for in vitro neurotoxicity evaluation. HT measurement of electrical activity is not yet a reality; however, this is an endpoint we will assess in preparation to the eventual development of the platform technology.

Necrosis is a violent form of cell death that is associated with rupturing of cellular membranes, swelling of the cells, and random destruction of the cellular structures. The cytosolic proteins of the dying cell are released extracellularly. Apoptosis is a coordinated process in contrast to necrosis. It occurs in single cells and, rather than swelling, an apoptotic cell loses volume. Concurrently, the intracellular matrix is actively dismantled by caspases. Finally, neighboring cells or macrophages will phagocytize the apoptotic bodies, averting an inflammatory response. The numerous florescent dyes available to label and differentiate between healthy, apoptotic, and necrotic cells, will also enable HT assessment (Figure 1).

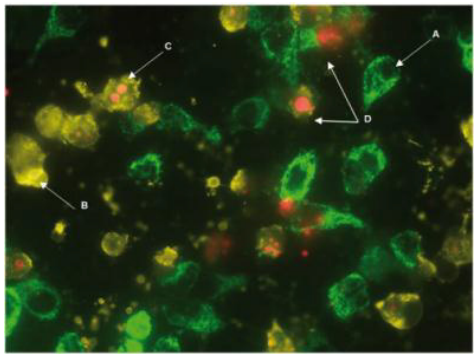

Figure 1. Florescent staining of healthy (A), apoptototic (B), late-stage apopototic (C), and necrotic cells (D).

Tied to formation of memory, neurite outgrowth is a process that not only occurs in the developing brain but also in the adult brain. As with apoptosis and necrosis, measurement of neurite outgrowth can be performed by fluorescent labeling. The neurite outgrowth assay is based on the measurement of microtubule-associated protein 2 (MAP2), a well-characterized neuron-specific cytoskeletal protein. Incidentally, the loss of MAP2 immunoreactivity has been demonstrated to be directly proportional to neuronal death (Figure 2).

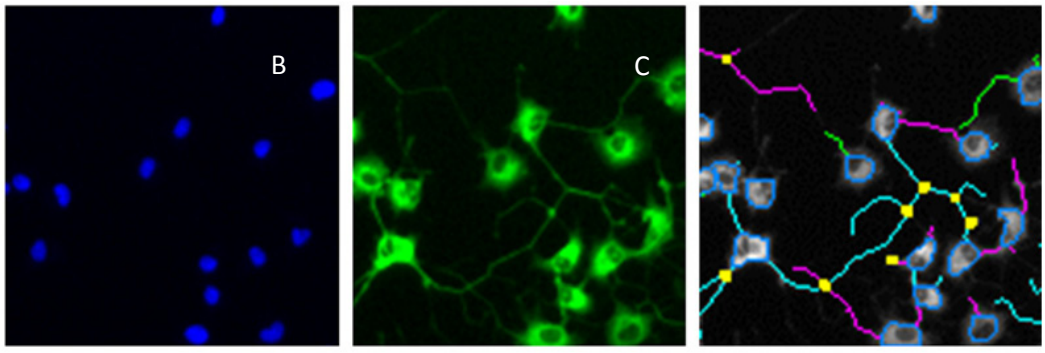

Figure 2. Screening for neurite outgrowth. PC12 cells in 96-well plates were treated with neural growth factor (NGF). (A) Nuclei are labeled blue with Hoescht 33258 to identify viable cells. (B) Cell bodies and processes are labeled green using anti-bIII tubulin antibody labeled with Alexa 488. (C) The image captured and analyzed using the Cellomics ArrayScan VTiW identifies the cell body and measures a number of parameters including cell body size, neurite number, length, and branch points for each identified cell.

Measurement of lactate dehydrogenase (LDH) and neuropathy target esterase (NTE) are published cellular markers of neurotoxicity and will also be considered, but the use of either carry caveats of uncertainty. In a study of workers exposed to the defoliant DEF, inhibition of lymphocyte NTE was observed but was considered a false positive because no clinical or electrophysiological signs of OPIDN were detected in exposed workers.[6] Measuring LDH efflux lacks neuronal specificity, unless one is confident that the toxin used is only lethal to neurons. In addition, various chemicals may interfere with the LDH assay by directly oxidizing NADH to give falsely elevated LDH activity.

In addition to the *in vitro* methods, we will apply omics technologies. Omics have already been applied in various *in vitro* cell culture systems for different purposes. A global evaluation of biomarkers, such as expression of a gene, a protein, or a metabolite becomes feasible with such technologies and can provide a more comprehensive study of combined alterations induced by a toxicant. Moreover, the methodology might provide a means to identify new biomarkers or underlying mechanisms of neurotoxicity, which are difficult to determine with conventional toxicological methods. Through ECBC's existing collaboration with the New York Consortium on Membrane Protein Structure (NYCOMPS) at the NYSBC, we will isolate all expressed proteins of our hES cell lines. Approximately 1000 proteins per week can be isolated and crystal structures can be generated in as little as three days. ECBC will then use the structures of the membrane-bound proteins in the *in silico* model construct an HT model of the small molecule-protein interactions and screen small molecule databases for molecules binding hES cell surface proteins. With Over 7 million compounds presently in databases, *in silico* modeling can be used to screen >10,000 interactions per second for a given transmembrane protein (Figure 3).

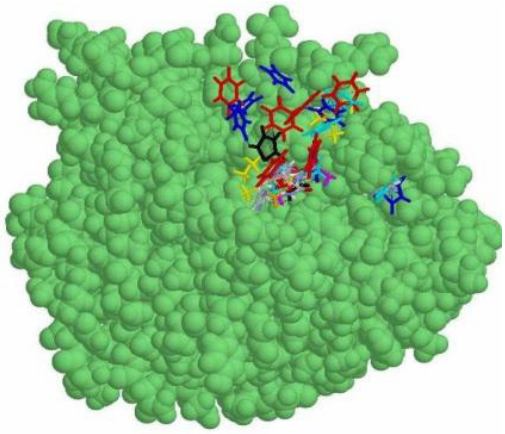

Figure 3. *in silico* model of small molecule-protein interactions.

A tiered approach is envisioned utilizing high-throughput *in silico* modeling followed by *in vitro* procedures to screen large numbers of chemicals for toxicity. Results of these screening assays would be used to prioritize resources to those chemicals most likely to result in adverse health effects. Ultimately, new testing paradigms based on computational models and *in vitro* assays have the potential to eliminate the need for traditional animal tests and may allow for the identification of preventative measures and treatments.

2. METHODS

Neural progenitor cells characterized for normalcy were treated in triplicate with paraoxon at the indicated concentrations for 24 hours. Cytotoxicity was assayed using the Invitrogen LIVE/DEAD cytoxocity kit, which utilizes both propidium idodie and calcein AM. Prodium idodide (red) is an indicator of membrane permeability and stains dead cells. Calcein AM (green) is an indicator of intracellular esterase activity and stains live cells. Cells were imaged using the Perkin Elmer Operetta

imaging platform. The black line represents the mean response and the dotted red lines give the 95% confidence interval on the mean.

2.1 2D Difference Gel Electrophoresis (2D-DIGE)

T-7 culture flasks containing 2×10^7 cells were scraped and suspended in 500 mL of lysis buffer (7 M urea, 2 M thiourea, 30 mM Tris, 4% CHAPS, 5 mM magnesium acetate, pH 8.5) and then sonicated. Samples were left on a shaker for 1 hr at room temp to allow extraction to take place, and then centrifuged at approximately 14,000 rpm (or equivalent g) for 15 min at 10°C to remove insoluble material. The supernatant was removed and stored at -80°C until required for use. Protein concentrations were determined using the thiourea-compatible Bradford protein assay and found to be similar among all samples. As a result, 50 μg of protein was used per sample on each 2D-DIGE gel for comparative proteomic analysis experiments. Immobilized 18 cm linear pH gradient (IPG) strips (GE Healthcare), pH 4-7, were chosen for 2D-DIGE analysis as these gave good resolution of protein spots in a relatively broad pI range using the total cellular lysate protein extraction procedure described above. IPG strips were rehydrated in rehydration buffer (7 M urea, 2 M thiourea, 4% CHAPS, 0.5% IPG buffer, 50 mM DTT) overnight. Three biological replicate samples from each time point were labeled with either Cy3 (clones 1.14 and 5B5) or Cy5 (clones 3B12 and 2.8) dyes and a pooled internal standard was labeled with Cy2 dye to aid image matching and cross-gel statistical analysis. Reverse labeling was also carried out on each sample to reduce dye bias. 2D-DIGE was then carried out according to manufacturer's instructions (GE Healthcare) and as previously described. Gels were scanned with a Typhoon 9400 variable mode imager (GE Healthcare) and the subsequent Cy2, Cy3, and Cy5 gel images were analyzed using the Differential In-gel Analysis (DIA) and Biological Variation Analysis (BVA) modules of DeCyder 6.5 software. Proteins were defined as differentially expressed if the observed average ratio was greater than 2.

2.2 Protein identification by mass spectrometry

LC-MS/MS was performed on an Ultimate 3000 nanoLC system (Dionex), interfaced to an LTQ Orbitrap XL (Thermo Fisher Scientific). 2D gel spots were excised from Coomassie-stained preparative gels containing 400 μg of protein per gel, then de-stained with a solution containing 100 mM ammonium bicarbonate/acetonitrile (ACN) (1:1, vol/vol) and incubated with occasional vortexing for 30 min. Samples were then dehydrated by the addition of neat ACN and swelled by rehydration in a digestion buffer containing 12.5 ng/μL of trypsin (Promega, sequencing grade) in 10 mM ammonium bicarbonate containing 10% (vol/vol) ACN at 37°C overnight. Peptides were extracted in extraction buffer (1:2 (vol/vol) 5% formic acid/ACN), incubated for 15 min at 37°C on a shaker and dried down in a vacuum centrifuge. Tryptic peptides were re-dissolved in 10 μL of 0.1% formic acid containing 2% CAN, and 5 μL of sample was loaded onto a trapping column packed with C18, PepMAP100 (Dionex), at a flow rate of 20 μL/min in 0.1% formic acid. After 5 minutes of washing, peptides were eluted into a C18 PepMAP100 nanocolumn (15 cm × 75 μm ID, 3 μm particles) (Dionex) at a flow rate of 350 nL/min. Peptides were separated using the mobile phase gradient: from 5 to 50% of solvent B in 30 min, and from 50 to 90% B in 5 min. Solvent A was 98:2 H_2O:ACN (v/v) containing 0.1% formic acid; solvent B was 2:98 H_2O:ACN (v/v) containing 0.1% formic acid. LC-MS/MS data was acquired in data-dependent acquisition (DDA) mode controlled by Xcalibur 2.0.7 software (Thermo Fisher Scientific).

3. RESULTS

Experimental evidence has been generated showing OP toxicity to human central nervous system cells. Human cells were confirmed to be normal and to possess pluripoentcy. Those cells plated to 96-well plates differentiated to both glial cells and neurons (Figure 3). Glial cells were included because they are the most abundant cell type in the brain and have been shown to play an important role in the function and health of neurons. In culture, glial cells are the differentiated cell type that matures earliest and, therefore,

received the preponderance of tests. To date, the IPS cells, glial cells, and neurons have all been exposed to the pesticide paraoxon and assayed for cytotoxicity. Paraoxon was tested on human astrocytes and neurons using both ATPlite and MTT cytotoxicity assays (Figure 4).

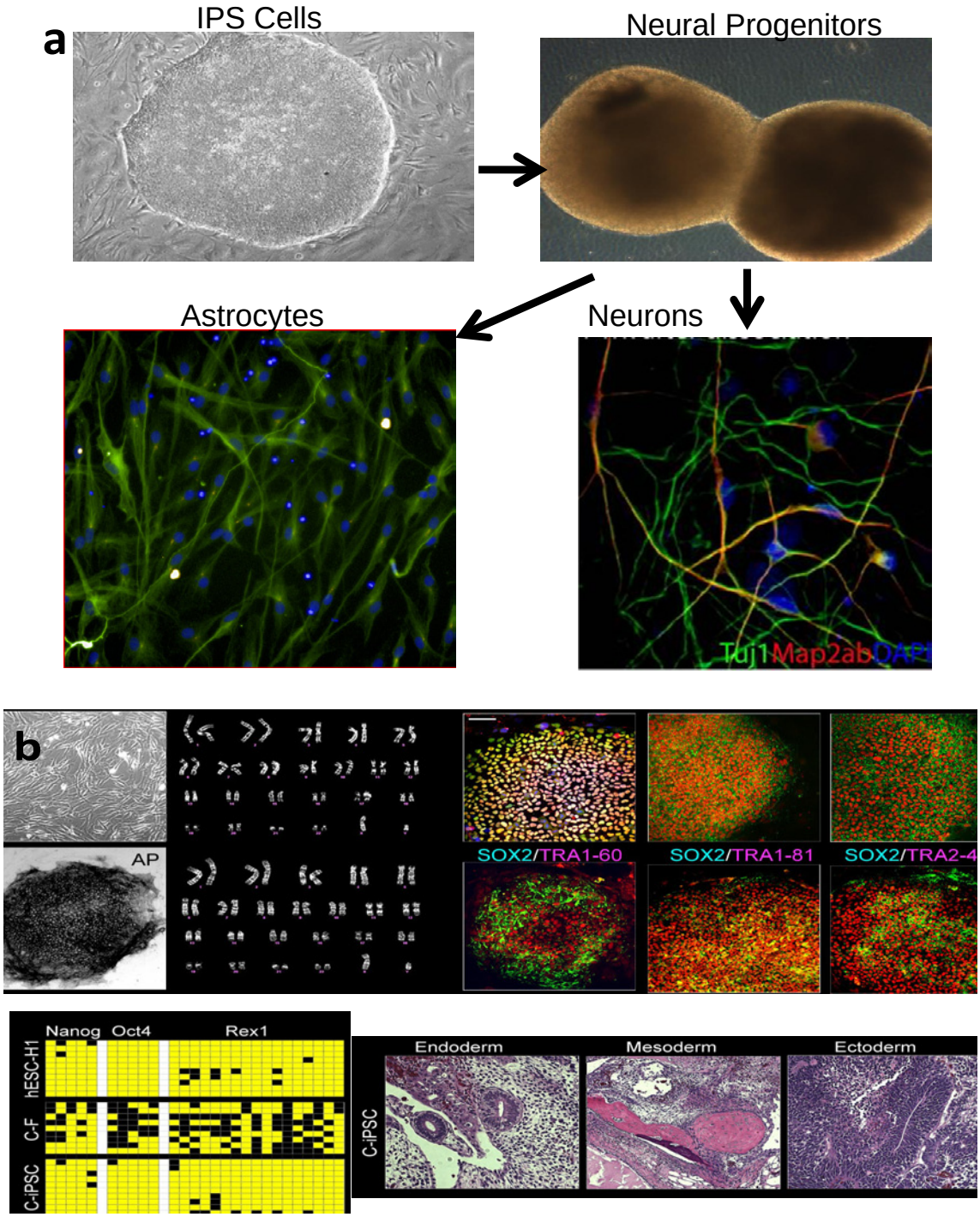

Figure 3. IPS cells differentiated to neural progenitors to terminally differentiated glial or neurons (a). Karyotyping, immunostaining, DNA methylation, and teratogenic tumor formation demonstrating normality, and pluripotency of IPS cells (b).

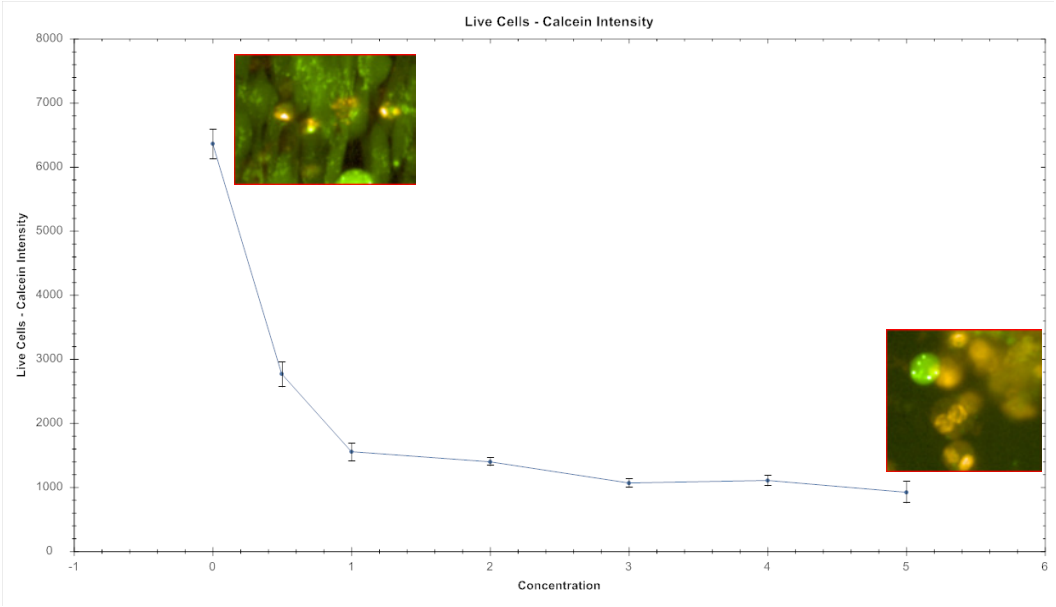

Figure 4. Paraoxon dose response versus neural progenitor cell viability showing an IC50 of 2mM.

Results show toxicity at IC50 of 2 mM, which is consistent with previously reported findings. To determine target protein for crystallization determinations, Differential In-gel Analysis (DIGE) was performed (Figure 5).

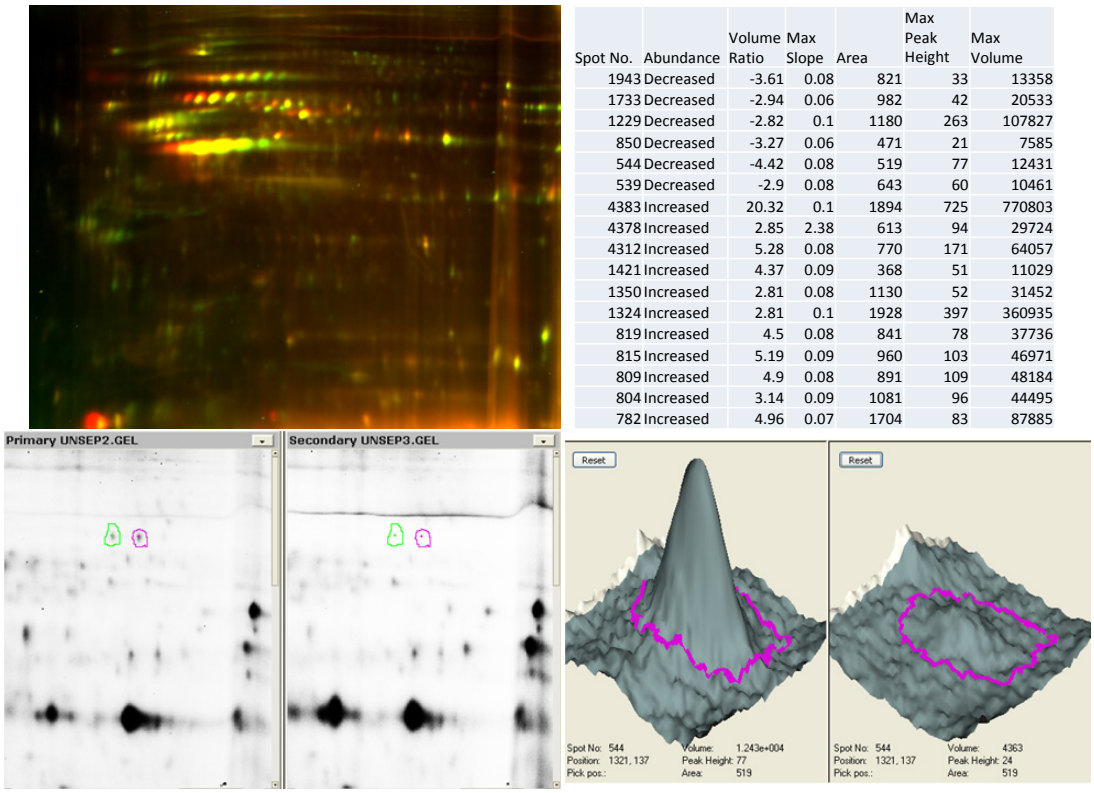

Spot No.	Abundance	Volume Ratio	Max Slope	Area	Max Peak Height	Max Volume
1943	Decreased	-3.61	0.08	821	33	13358
1733	Decreased	-2.94	0.06	982	42	20533
1229	Decreased	-2.82	0.1	1180	263	107827
850	Decreased	-3.27	0.06	471	21	7585
544	Decreased	-4.42	0.08	519	77	12431
539	Decreased	-2.9	0.08	643	60	10461
4383	Increased	20.32	0.1	1894	725	770803
4378	Increased	2.85	2.38	613	94	29724
4312	Increased	5.28	0.08	770	171	64057
1421	Increased	4.37	0.09	368	51	11029
1350	Increased	2.81	0.08	1130	52	31452
1324	Increased	2.81	0.1	1928	397	360935
819	Increased	4.5	0.08	841	78	37736
815	Increased	5.19	0.09	960	103	46971
809	Increased	4.9	0.08	891	109	48184
804	Increased	3.14	0.09	1081	96	44495
782	Increased	4.96	0.07	1704	83	87885

Figure 5. DIGE analysis of paraoxon treated cells identifying 4248 proteins and showing an effect on 17 proteins. Plot and analysis for spot 544 shown.

For image analysis of the 2D-DIGE gels, the Differential In-gel Analysis (DIA) module of Decyder was first used to merge the Cy2, Cy3, and Cy5 images for each individual gel and to detect spot boundaries, to calculate normalized spot volumes (protein abundance). The Biological Variation Analysis (BVA) module of Decyder was then used to match spot patterns across all gels for comparative cross-gel statistical analysis with protein abundance differences normalized against the Cy2 intensity for any given spot. Comparison of normalized Cy3 and Cy5 spot volumes with the corresponding Cy2 standard spot volumes within each gel gave a standardized abundance. The number of detected spots on each gel averaged around 4248 per gel. After spot matching and filtering, 17 proteins were found to have been affected; expression was either up-regulated or decreased. Points of interested were excised from gels and trypsin digested for LC-MS identification (Figure 6).

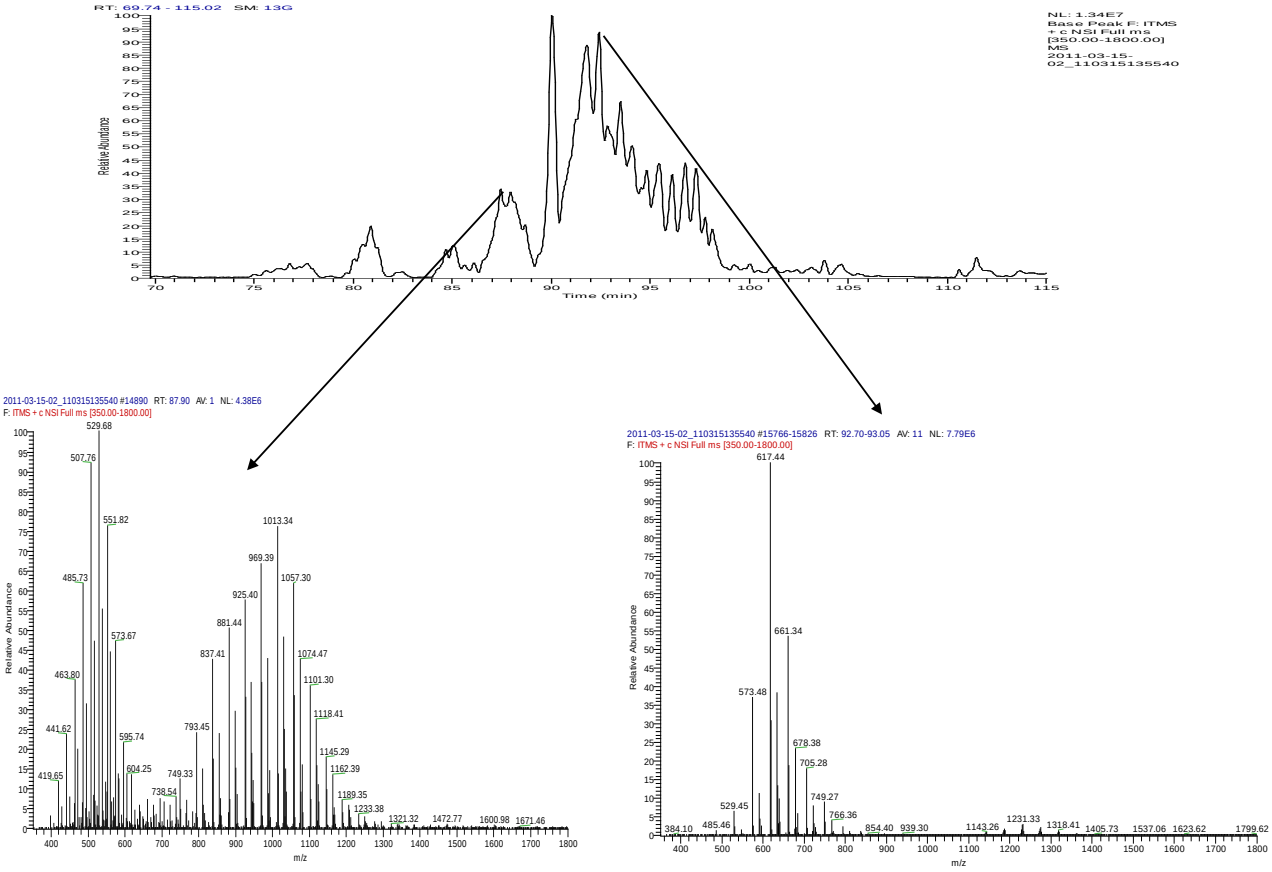

Figure 6. LC-MS identification of proteins extracted from polyacrylamide gels.

4. DISCUSSION

There is an urgent need for cheaper, faster, and more mechanism-based approaches in toxicology. Despite the major advances in the field of biotechnology, molecular biology, and information technology, the concepts of toxicology have not changed over the previous several decades. Today, companies and agencies still largely use animal studies to assess toxicological risk, despite cost (in the US about $1 billion a year) and the inability to provide answers to the complex toxicological questions posed. This has led to the current dearth of toxicological information, which is required to safeguard human health and regulatory decision making on chemicals. Toxicologists have become increasingly aware of these limitations and have brought forward new concepts and innovative approaches to overcome them. The National Research Council vision report on Toxicity Testing in the 21st Century (Tox-21c) from 2007 [7] now principally forming the novel EPA toxicity-testing paradigm, suggests moving to a pathway-based

testing strategy away from traditional animal-based methods too slow for testing large numbers of chemicals or their combinations in mixtures. We see broad future applications of stem cell technology to screen for a multitude of potential outcomes on all human organ systems. The power afforded by this will likely have a profound impact on the welfare of our citizens, warfighters, and national and global security.

WORK CITED

[1] The American Chemical Society Home Page. http://www.acs.org/ (accessed Nov 10, 2011).
[2] Hayo, M. G. van der Werf. 1996. *Agri. Ecosyst. Environ*. 60, 81-96.
[3] Hengstler, J.G. et al. 2006. *Toxicology* 220, 232–239.
[4] Roberto, B. et al. 2008. *Ann Ist Super Sanità* 44, 13-15.
[5] The World Health Organization Home Page http://www.who.int/en/ (accessed Nov 10, 2011).
[6] Lotti, M. et al. 1983. *J. Occup. Med.* 25, 517-522.
[7] Toxicity Testing in the 21st Century: A Vision and a Strategy Committee on Toxicity Testing and Assessment of Environmental Agents, National Research Council. 2007. http://www.nap.edu/catalog/11970.html (accessed Nov 21, 2009).

A rational design approach to multifunctional nanostructured materials: preparation and properties of luminescent lanthanide/graphene materials

Amanda L. Jenkins*[a], Alex Balboa[b], Margaret M. Hurley[c], and Christopher J. Karwacki[b]
[a]ASK Incorporated, 7447 Rockawalkin Rd. Hebron, MD 21830,
[b]Edgewood Chemical Biological Center, Research & Technology Directorate, 5183 Blackhawk Rd., Aberdeen Proving Ground, MD 21010
[c]US Army Research Laboratory, Aberdeen Proving Ground, MD 21005

ABSTRACT

Graphene based materials have been receiving a lot interest recently because of their unique mechanical and electrical properties. These properties give rise to many possible applications ranging from field emission displays [1-3], sensors, thin film transistors [4], solar cells [5], touch panels [6-7], electrostatic dissipation [8], and transparent electrodes for optoelectronic devices. In an effort to better understand the binding sites, to add chemical selectivity and detection capabilities, luminescent lanthanides have been complexed with graphene oxide. The luminescent graphene/lanthanide complexes were made from the reaction of the graphene carboxylate with europium and terbium in a methanol solution under basic conditions.[9] The coordination of the graphene carboxylate with the lanthanide was verified by laser induced fluorescence. The surface morphology and physical properties of the graphene/lanthanide materials have been investigated by SEM and TEM measurements. Molecular modeling of the systems was conducted to better understand the binding of the lanthanide to the graphene system and to provide direction on further enhancements of the system by organic ligands.

1. INTRODUCTION

Lanthanides comprise the largest naturally occurring group in the periodic table, comprised of elements 57-71.[10] The similarities in the lanthanides arise from a resemblance in the electronic configurations of the elements which consists of the xenon levels, filled 6s sublevel, and a varying amount of electrons occupying the 4f sublevel. Generally, the optical absorption and emission spectra of the ions formed by the triply charged free lanthanide ions consist of very narrow lines (0.1-0.01 nm). Quantum mechanical calculations have indicated that the energies and the radial extensions of the 4f eigen functions dramatically drop at the beginning of the lanthanide series so that the maxima of the 4f eigen functions no longer exceed those of the 5s and 5p eigen functions. The 4f orbitals are therefore not the outermost shell, but are largely shielded from the external environment by the filled 5s and 5p shells. Since these 4f orbitals are shielded, the electrostatic field induced by coordinating ligands causes only small perturbations in the 4f electrons energy levels, and as a result, they retain their semi “atomic” nature responsible for the narrow bands observed in lanthanide emission and excitation spectra.[11-13] These narrow features result in analyses which are both selective and sensitive. The spectral position and intensity of these features are dependent on the environmental symmetry of the lanthanide complex.[14]

When a lanthanide ion is placed in a molecular environment, it is subject to a number of influences that are absent in the free ion. Although, as previously mentioned, the 4f levels are shielded from the outside influences by the 5s and 5p levels, aspects of the external environment can cause small shifts and splittings in the free ion states. Since the external environment produces an electric field, the free ion levels can be split into Stark components. The exact nature and degree of these splittings are due not only to the magnitude of the electric field but also to symmetry considerations. Since the magnitude of the

external field can cause shifts in line position, it follows that line positions can be affected by the identity of any external ions. This behavior has been observed in crystals that have been doped with a lanthanide ion and some analytes as well as in a number of rare earth chelate complexes.[15-16]

The magnitude of the splittings of the Stark components associated with lanthanide compounds is much greater than the magnitude of these same splittings in the case of transition metal compounds. This is because, in the case of the lanthanides, the contribution to the energy of the orbital made by the spin-orbit interaction is of the same order of magnitude as the coulomb interaction (electron-electron repulsion). The exact character and degree of these spectral changes are a function of the complexing species, the major factors being the coordination number, symmetry, geometry, and the type of coordinating molecule. Although the ligand field is sufficient to produce these shifts, splits, and intensity changes, the ligand to f electron coupling doesn't result in broadening of the lines. Detailed descriptions and the theoretical foundations of lanthanide spectroscopy are described by Deike, Hufner, and Wybourne.[17-19]

As a result of this unique chemistry, lanthanides have been used for a variety of purposes such as catalysts, optical components, alternatives to radioisotopes, and as scientific probes for a wide variety of phenomenon including temperature probes [20-24] and structure [25-34] often at parts per trillion (ppt) levels or lower.[35] Trace analysis techniques based on lanthanide spectroscopy have also found application for detection of pharmaceuticals, biological molecules, toxic chemicals, and many others.[36-40] The ability of the luminescent lanthanides to accurately and sensitively indicate events in their coordination sphere is being combined with the excellent electrical and mechanical properties of graphene to create a material with a wide range of uses.

2. EXPERIMENTAL

2.1 Reagents

Unless otherwise indicated, materials were obtained from commercial suppliers and used without further purification. Analytical reagent grade chemicals were used along with deionized water to prepare solutions. The lanthanides were obtained from Aldrich (Aldrich, Milwaukee, WI). The graphene oxide was prepared by Teresa Bandosz at the City College of New York (CUNY) and used as received.[10] $Eu(NO_3)_3 \cdot 5H_2O$ was prepared by taking Eu_2O_3 and dissolving it in water with heat and just enough nitric acid to produce a clear solution. The resulting solution was dried and evaluated spectroscopically to confirm the conversion.

2.2 Instrumentation

Luminescence was excited using a model 35-LAP-321-120 argon ion laser (Melles Griot, Carlsbad, CA). Spectra were collected using an *f*/4, 0.5-m monochromator (Chromex, Albuquerque, NM) equipped with a model ST-6 CCD (Santa Barbara Instruments Group, Santa Barbara, CA) using Kestrel Spec Software (K&M Co., Torrance, CA). Spectra were also obtained with a StellarNet Blue wave miniature fiber optic spectrometer (StellarNet, Tampa, FL) with a range 500-700 nm equipped with a 2400 g/mm ruled grating, a 2048 element detector array, integrated order sorting filter, 16-bit digitizer, and a 25 µm slit and running SpectraWiz software. The excitation and emission light was carried to and from the sample using a 400 µm bifurcated multimode fiber (Thor Labs, Newton, NJ). Scanning electron micrographs were obtained using a JEOL 6300F Field Emission Scanning Electron Microscope SEM (JEOL, Ltd., Tokyo). Transmission Electron Micrographs are currently being completed by David Zeigler's group at the U.S. Army Natick Soldier Systems Center (Natick, MA).

2.3 Compound preparation

Graphene carboxylic acid was prepared by Teresa Bandosz, (City College New York) and used as obtained. Graphene/europium materials were first prepared by the following the procedure outlined by

Jang Yong Kim et al.[9] The graphene carboxylic acid (0.5 g), water (20 mL), and NaOH (1 M aqueous solution, 1 mL) were sonicated for 30 minutes in a Cole-Parmer sonicator at 200 W. Europium nitrate, $Eu(NO_3)_3 \cdot 5H_2O$ (0.428 g, 1 mmol) was added and stirred overnight. The solids were centrifuged, washed with water and acetone. The graphene/europium solids were dried on a watch glass overnight. This procedure was repeated with increasing amounts of europium nitrate (1.0 g, 1.25 g, 1.5 g, and 2.0 g). The same procedure was repeated for the terbium graphene oxide compound. Terbium nitrate was used as purchased and 0.5, 1.0, 1.5, and 2.0 g respectively were reacted with the graphene oxide as described above.

The resulting europium samples were then reacted with α-pyridion in an attempt to recreate the results presented in the Jang Yong Kim paper.[9] The europium graphene oxide samples prepared with 0.5 g (as done in the paper) and samples made with 1.0 and 1.5 grams of europium were selected for this study. Graphene/europium/picolinate materials were prepared by dissolving (0.420 g, 2 mmol) α-pyridoin in methanol (20 mL), with 2 mL of 1.0 M NaOH. The graphene/europium solids and methanol (20 mL) were sonicated for 30 minutes followed by the addition of the α-pyridoin anion methanol solution. The reaction mixture was stirred overnight and the resulting solids were washed with methanol several times and then water to remove any residual α-pyridoin and/or europium compounds detached from the graphene. This process was repeated with varying amounts of α-pyridoin in methanol (0.25 g, 0.75 g, and 1.0 g).

2.4 Compound evaluation

The graphene oxide, europium oxide, europium nitrate, terbium nitrate, and the resulting europium graphene oxide and terbium graphene oxide samples as well as the samples with the α-pyridoin were evaluated using the laser induced fluorescence system described above. Excitation wavelengths of 465.8 nm, 488 nm, 496 nm, and 514 nm were evaluated with 465.8 nm selected as optimal for the europium complexes and 514 nm selected for the terbium samples. The compounds with the highest luminescent intensity were selected for further study. The resulting europium and terbium graphene oxide samples were submitted for SEM and TEM evaluation.

2.5 Molecular modeling

The second phase of the work, run concurrently with the synthesis, uses various modeling techniques such as quantum mechanics methods (*ab initio* and DFT) and molecular dynamics. This approach expands an understanding of lanthanides and their interactions with graphene oxide and other relevant ligands. Multiple targeted levels of modeling are being used for different levels of the size continuum. Quantum mechanical approaches can be used to understand the electronic interaction of the lanthanides, ligands and solvents, and how this affects the photoluminescence of the systems. From this work, binding energies and predicted photoluminescence properties of different combinations of lanthanides, graphene model compounds and coordinating ligand molecules, will be directly used to predict performance of a candidate combinations. On the multi-atom scale, methods like molecular dynamic simulations will allow prescreening of targets and allow the choice of lanthanide and ligand to be directed towards those that give the best binding and photoluminescence. Using the various different levels of modeling will allow information gained at one level to guide the work at the other levels. The results can then be used to guide the selection of solvent and templating molecules from phase one and the experimental results in turn can be used to refine the models. Presently, the electronic structure program Gaussian 09 [41] was used to gather preliminary geometry structures using the default geometry optimization criteria shown in Table 1.[42] The optimized structure(s) used the Universal Force Field (UFF) [43], which treats the europium atom as an octahedral europium (+3) cation.

Table 2. Geometry optimization threshold values

Item	Threshold
Maximum Force	0.000450
RMS Force	0.000300
Maximum Displacement	0.001800
RMS Displacement	0.001200

3. RESULTS AND DISCUSSION

3.1 Compound Preparation

The conversion from europium oxide to europium nitrate was relatively easy and confirmed spectroscopically by a comparison with the spectra published by Bunzli et al.[43] Europium samples were evaluated using excitation wavelengths of 465.8 nm, 472 nm, 488 nm, and 514 nm. As previously published, excitation at 465.8 was determined to have the best luminescence intensity and give the best peak resolution.[35] Complexation between the lanthanide and the graphene was determined by spectral changes and increased luminescence from the lanthanide (Figure 1). The europium graphene samples with the best luminescent intensity were those prepared with 1.5 g of europium nitrate. The sample prepared with 0.5 g showed no spectral difference from the graphene oxide sample itself. In comparing the spectra of graphene oxide, europium nitrate and the optimized europium graphene oxide, the $^5D_0 \rightarrow {}^7F_1$ transition of the europium from about 590-595 nm was evaluated. In this region, a 1nm shift is seen the europium peak of the nitrate at 592 nm and the GO at 591 nm. Additionally, the two peaks in the 595 nm region are better resolved in the GO complex. The Eu(GO) peak at 595 nm is also higher in intensity, however this could be due to the fact that the GO itself has a fluorescence peak at that wavelength.

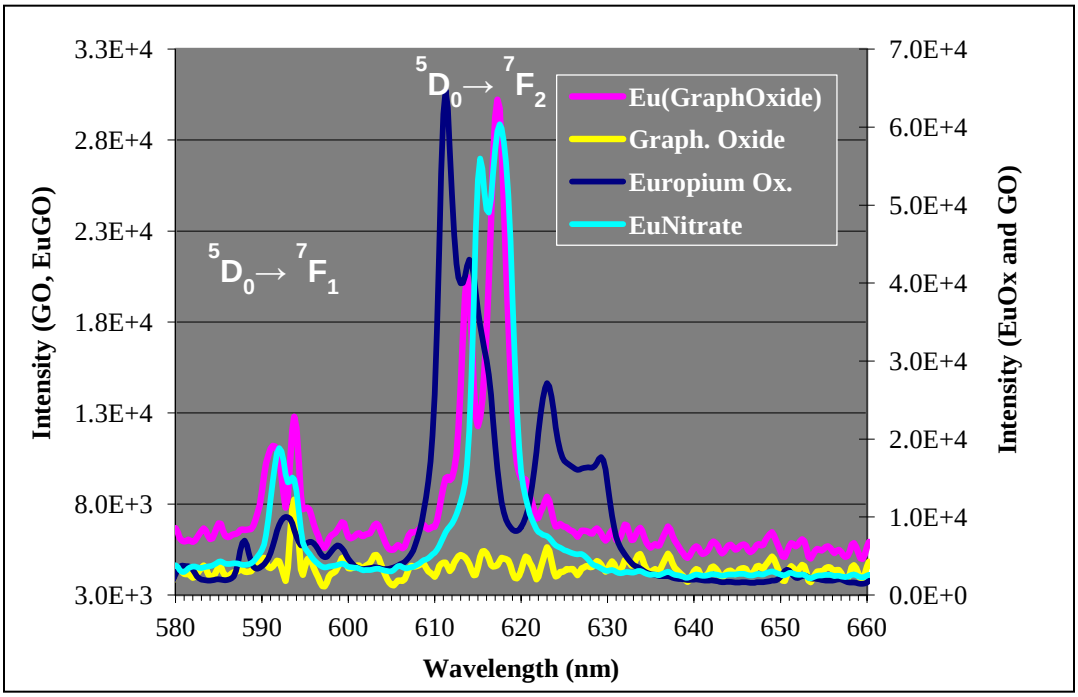

Figure 1. Results of the europium study. Excitation wavelength was 465.8 nm.

The hypersensitive $^5D_0 \rightarrow {}^7F_2$ europium transition was also used to determine binding. The europium nitrate peak at 615 nm was not only shifted one nanometer to the blue (614 nm) in the Eu(GO) but also reduced in intensity relative to the peak at 617.5 nm. The peak at 617 nm was shifted 0.1 nm to the blue in

the nitrate complex. Comparing these splitting patterns with the calculations done by Stump et al [14] (and taking into account no peaks were seen in the $^5D_0 \rightarrow {}^7F_1$ transition) the site symmetry for both molecules is likely D_2 or D_2d with either a tetragonal or rhombic crystal system. For this study, all samples were excited using 488 nm.

The terbium samples performed in a similar manner with sampled prepared with 0.5 g terbium showing no spectral response and the sample prepared with 1.5g of terbium showing the optimal luminescence. GO, terbium nitrate, and Tb(GO) were all excited at 465.8, 488, 496, and 514 nm. The best wavelength for the terbium was 514 nm and was used for comparison of the terbium complexes and the GO (Figure 2). The first transition $^5D_4 \rightarrow {}^7F_5$ had the strongest luminescence. In this spectral region, three peaks were seen for the terbium nitrate (541.5, 543.25, and 545.75) while only two peaks were noted for the TbGO complex (544.5 and 547.0 nm). The intensity of the largest peak also shifted from the left (nitrate) to the right (TbGO). In the $^5D_4 \rightarrow {}^7F_4$ transition, the terbium nitrate has 2 unresolved peaks (581 and 585.25 nm) while the TbGO complex has only one (585.0 nm). The $^5D_4 \rightarrow {}^7F_3$ transition has one peak at 621.5 nm for the nitrate and two unresolved peaks at 621.25 and 622.75 nm in the TbGO complex. The GO and TbGO both had weak peaks at 536.75 and 593.75 nm which were not seen in the terbium nitrate spectrum.

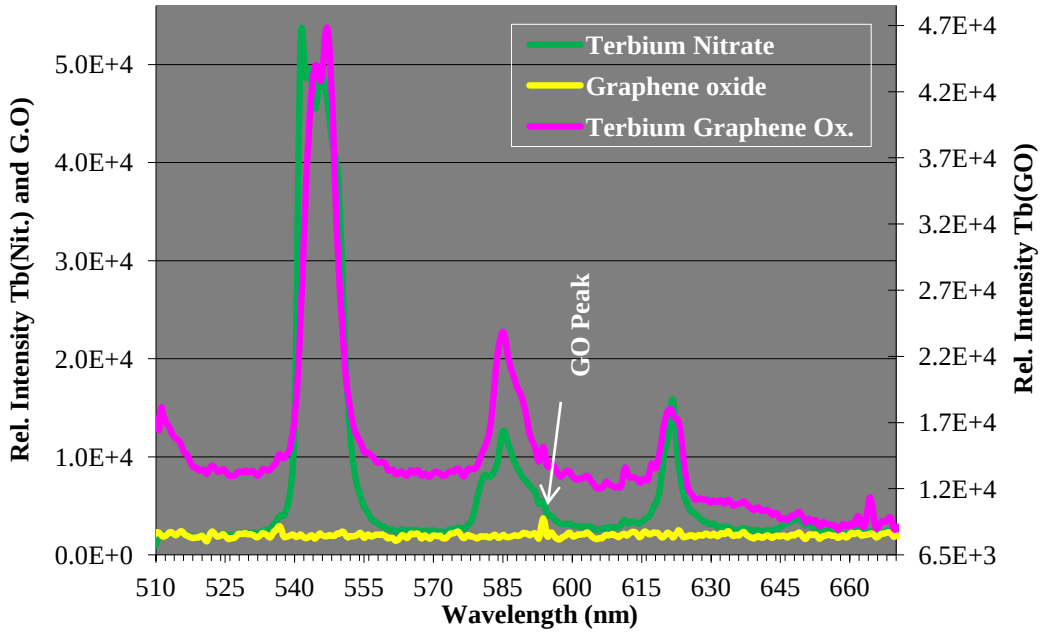

Figure 2. Results of the terbium study. Excitation wavelength was 514.0 nm.

3.2 SEM analysis

The SEM analysis of the graphene oxide showed the nice sheet like structure as expected (Figure 3). The elemental analysis showed traces of sulfur, oxygen, magnesium, and potassium left over from preparation by the Humer method. In the europium graphene oxide (Figure 4) as well as the terbium graphene oxide (Figure 5) SEM images the lanthanide can be seen on the surface of the graphene oxide. The sheets are a bit less visible and the large lanthanides are covering the surface. The SEM elemental analysis shows the europium and terbium respectively as expected but also shows a large amount of sodium and oxygen. This is residual from the NaOH washes, and shows that more extensive washing steps will be needed to completely remove it. Results from the TEM study are forthcoming.

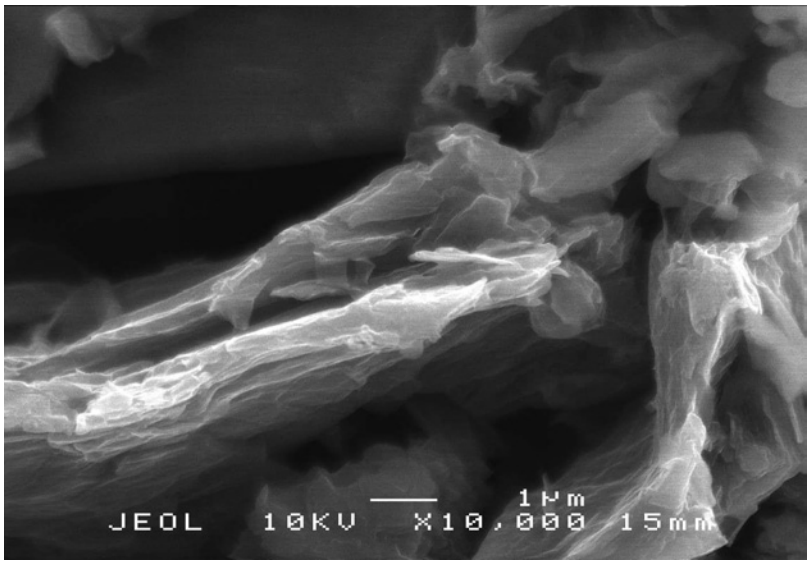

Figure 3. SEM image of the graphene oxide taken at 10 KV.

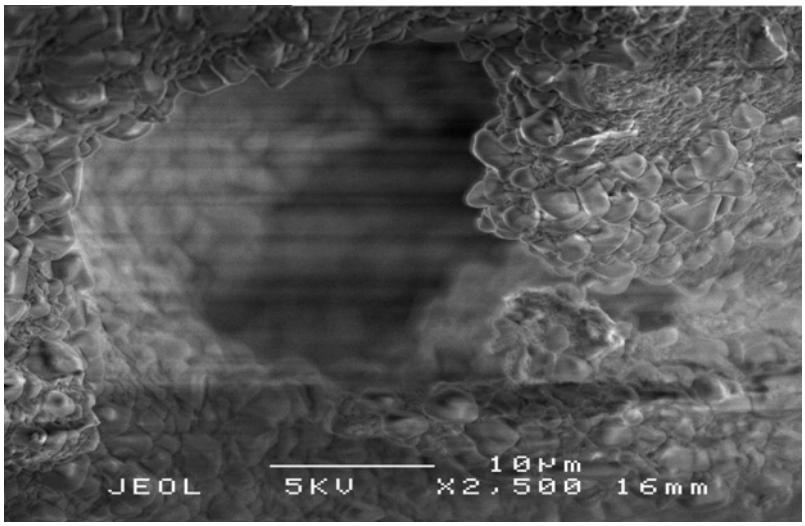

Figure 4. SEM image of the europium graphene oxide taken at 5 KV.

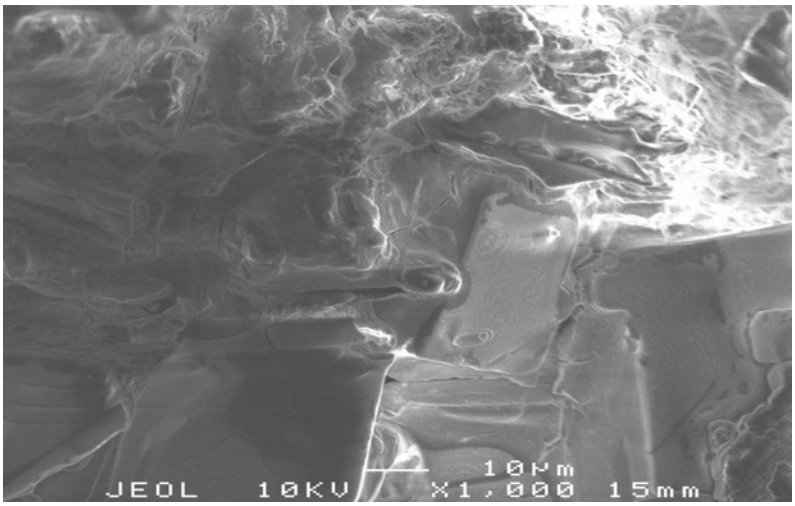

Figure 5. SEM image of the terbium graphene oxide taken at 10 KV.

3.3 Molecular modeling

Thus far, the molecular modeling of the lanthanide graphene complexes is progressing in a deliberative manner due to the large number of electrons involved in modeling the lathanides. Europium, picolinate, naphthalene carboxylate, phenalene carboxylate, europium nitrate, europium picolinate, europium-naphthalene carboxylate, europium-phenalene carboxylate, europium-naphthalene carboxylate-picolinate, and europium-phenalene carboxylate-picolinate complex(es) are under investigation. The carbon-oxygen and europium-oxygen bond lengths in the various compounds as well as the geometry optimized structures are shown below. Previous preliminary results indicate that the europium-oxygen bond lengths of these graphene oxide model compounds are comparable to europium-fluoride bond lengths [44] and somewhat shorter than other europium-oxygen non-graphene ligands.[45] In addition, qualitatively, the bidentate ligand attachment of the carboxylate oxygen to europium is longer than the europium-oxygen bond length found in europium oxide[46] and europium-oxygen bond length of europium-water complexes.[47] A more comprehensive compilation of the results of the modeling effort will be published shortly.

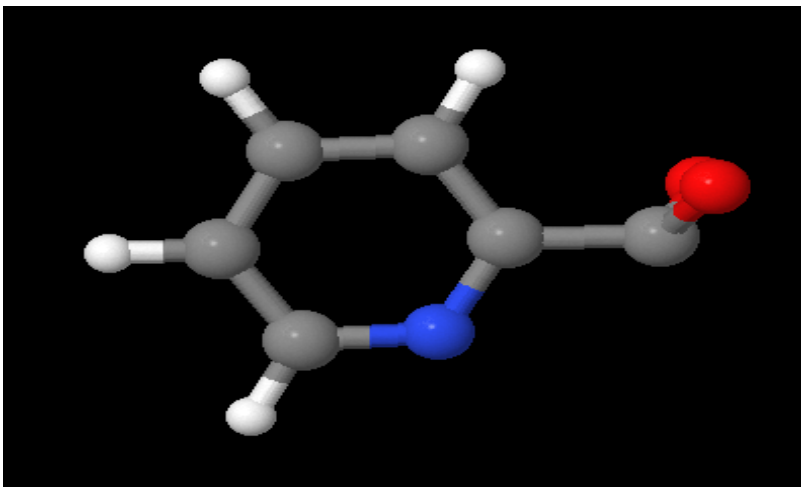

Figure 6. Calculated structure of picolinate (C-O bond lengths of 1.40 Å).

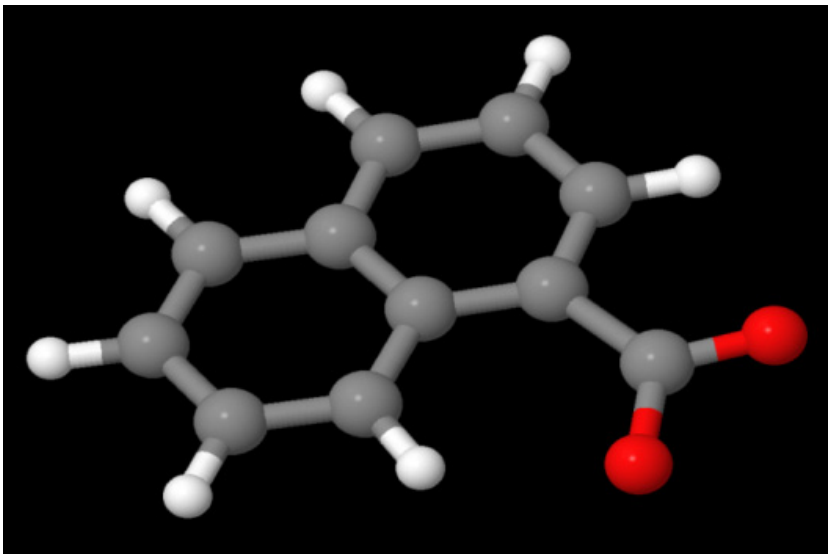

Figure 7. Calculated structure of naphthalene carboxylate (C-O bond lengths of 1.24 and 1.39 Å, respectively).

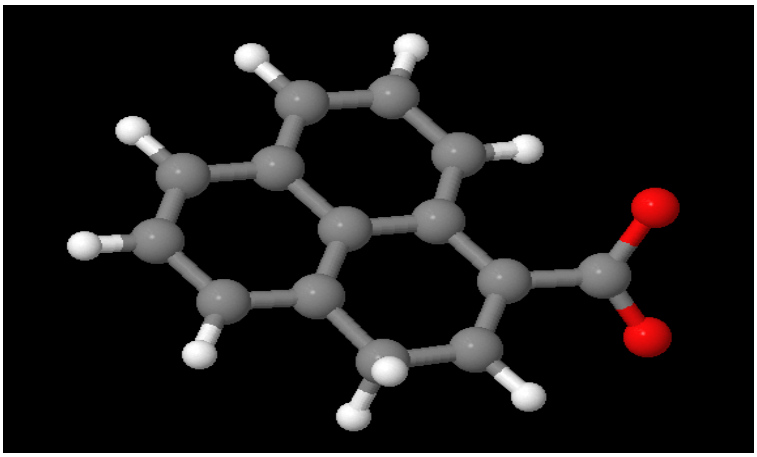

Figure 8. Calculated structure of phenalene carboxylate (C-O bond lengths of 1.26 and 1.39 Å, respectively).

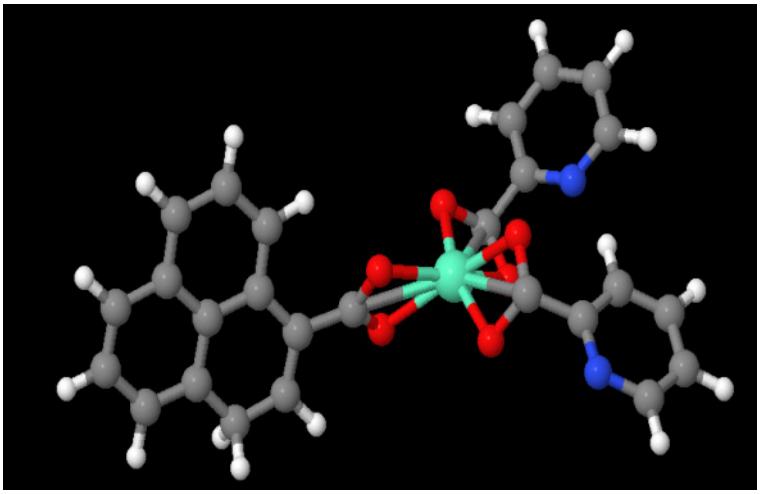

Figure 9. Calculated structure of europium-phenalene carboxylate-(picolinic acid)$_2$ complex (Eu-O distance ~2.22-2.25 Å, picolinate C-O bond lengths 1.42 Å, and phenalene carboxylate C-O bond lengths of 1.27 and 1.40 Å, respectively).

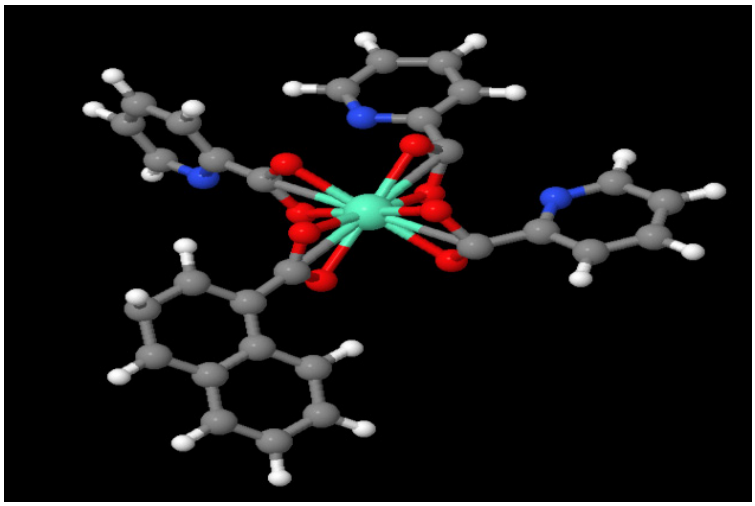

Figure 10. Calculated structure of europium-naphathalene carboxylate-(piolinic acid)$_3$ complex (Eu-O distance ~2.27-2.31 Å, picolinate C-O bond lengths 1.37-1.39 Å, and naphathalene carboxylate C-O bond lengths of 1.25 and 1.37 Å, respectively).

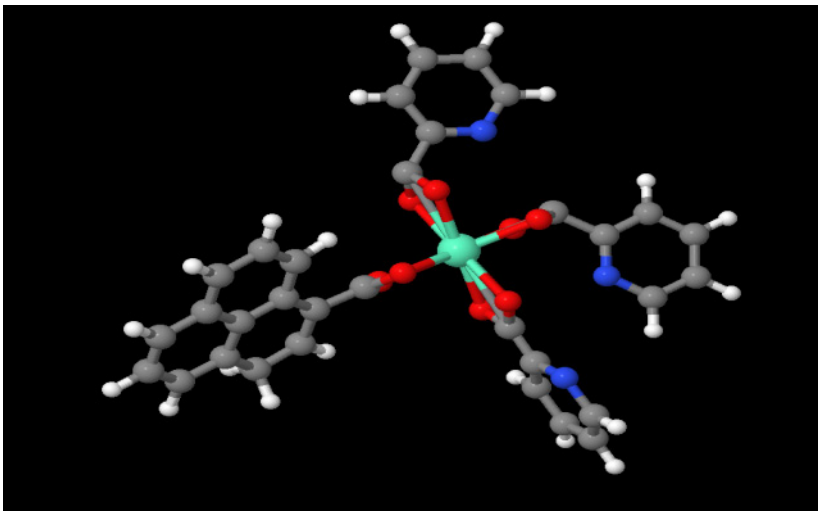

Figure 11. Calculated structure of europium-phenalene carboxylate-(piolinic acid)$_3$ complex (Eu-O distance ~2.27-2.31 Å, picolinate C-O bond lengths 1.37-1.39 Å and phenalene carboxylate C-O bond lengths of 1.25 and 1.37 Å, respectively).

4. CONCLUSIONS

The ability to label graphene oxide with luminescent lanthanides has been validated. Europium and terbium were both successfully complexed with graphene and the resulting spectra collected and verified. Based on this work, the addition of other luminescent lathanides (samarium, dysprosium, etc.) to graphene oxide should be relatively straightforward. Thus far the molecular modeling of these species is lagging slightly behind the actual complex preparation; however, once the modeling data is available it will be used to help optimize the ratio of lanthanide to graphene. Modeling will also be used to direct the complexation of the newly prepared lanthanide graphene species with organic ligands to further enhance the luminescence of complex as well as add specificity and functionality to the materials for future applications such as sensors or electronic devices.

WORK CITED

[1] Tien, H. et al. 2011. *Carbon* 1550-1560.
[2] Vadukumpully, S. et al. 2009. *Carbon* 47(14), 3288–94.
[3] Yoon, B. J. et al. 2005. *J. Am. Chem. Soc*. 127(23), 8234–5.
[4] Sun, Q. et al. 2010. *Appl. Phys. Lett*. 96(10), 103301–3.
[5] Ratcliff, E. L. et al. 2010. *J. Mater. Chem*. 20(13), 2672–9.
[6] Wang, S.J. et al. 2010. *Carbon* 48(6), 1815-23.
[7] Hellstrom, S. L. et al. 2009. *ACS Nano* 3(6), 1423–30.
[8] Kaempgen, M. et al. 2005. *Appl. Surf. Sci*. 252(2), 425–9.
[9] Kim, J. Y. et al. 2010. *Bull. Korean Chem. Soc*. 31(6), 1485-88.
[10] Seredych, M. and Bandosz, T. 2007. *J. Phys. Chem.* 111, 15596-15604.
[11] Bünzli, J.-C. G. and Choppin, G. R. 1989. Lanthanide Probes in Life, Chemical, and Earth Sciences, Elsevier: New York.
[12] Cotton, S. 1991. Lanthanides and Actinides, Oxford University Press: New York.
[13] Murray, G. M. et al. 1989. *Inorg. Chem.* 28, 1994-1998.
[14] Stump, N. A. 1991. Dissertation Thesis, University of Tennessee.
[15] Wright, J. C. and Wehry, E. L. 1981. Modern Luminescence Spectroscopy, Ed., Pleniun Press: New York, Vol. 4, pp 51-109.
[16] Murray, G. M. 1988. Dissertation Thesis, University of Tennessee.

[17] Deike, G. H. 1968. Spectra and Energy Levels of Rare Earth Ions in Crystals, Interscience Publishers.
[18] Hufner, S. 1978. Optical Spectra of Transparent Rare Earth Compounds, Academic Press: New York.
[19] Wybourne, B. G. 1965. Spectroscopic Properties of the Rare Earths, Interscience Publishers: New York.
[20] Jenkins, A. L. and Murray, G. M. 1996. *Anal. Chem*. 68, 2974-2980.
[21] Gualtieri, D. M. et al. 1991. *J. Appl. Phys*. 69, 5978-5981.
[22] Dakin, J. and Culshaw, B. 1988. Optical Fiber Sensors, Artec House Inc: Norwood, MD, pp 267.
[23] Stump, N. A. et al. 1993. *Spectroscopy Letters* 26, 1073-1083.
[24] Klakamp, S. L. and Horrocks, W. D. 1992. *Journal of Inorganic Biochemistry* 46, 175-205.
[25] Cronce, D. T. and Horrocks, W. D. 1992. *Biochemistry* 31, 7963-7969.
[26] Bünzli, J.-C. G. et al. 1994. *Journal of Physical Chemistry* 93, 980-984.
[27] Walters, J. D. and Johnson, J. D. 1990. *Journal of the Biochemical Society* 265, 4223-4226.
[28] Coruh, N. and Riehl, J. P. 1992. *Biochemistry* 31, 7970-7976.
[29] Susetyo, W. et al. 1990. *Analytical Chemistry* 62, 1215-1221.
[30] Thompson, J. W. et al. 1996. *Applied Spectroscopy* 50.
[31] Rizk, M. et al. 1995. *Spectroscopy Letters* 28, 1235-1249.
[32] Mayer, A. et al. 1994. *Chem. Int. Ed*., 33, 1044-1051.
[33] Hurskainen, P. et al. 1991. *Nucleic Acids Research* 19, 10567-1061.
[34] Wright, J. C. and Evans, T. R. 1982. Applications of Laser to Chemical Problems, Interscience-Wiley: New York, pp 81-85.
[35] Jenkins, A. L. et al. 1999. *Anal. Chem*. 71, 373.
[36] Jenkins, A. L. et al. 2001. *Analyst* 126, 798–802.
[37] Parker, D. 2000. *Coordination Chemistry Reviews*, 205, 109–130.
[38] Orcutt, K. M. et al. 2010. *Sensors* 10(2), 1326-1337.
[39] Ai, K. et al. 2009. *Ang. Chem. Int. Ed*., 48(2), 400-401.
[40] Gao, F. et al. 2009. *Talanta* 80(1), 202-6.
[41] *Gaussian 09, Revision B.01*. Gaussian, Inc., Wallingford CT, 2009.
[42] Rappé, A. K. et al. 1992. *J. Am. Chem. Soc*., 114 10024-35.
[43] Buenzli, J-C. G. and Yersin, J. R. 1979. *Inorg. Chem.* 18(3), 605-607.
[44] Chaumont, A. and Wipff, G. 2005. *Phys. Chem. Chem. Phys*. 7, 1926-1932
[45] Katia, N. N. et al. 2011. *J. Inorg. Chem*. 50(5), 1689-1697.
[46] Dolg, M. et al. 1990. *Chemical Physics* 148(2-3), 219-227.
[47] Ricca, A. and Bauschlicher, C. W., Jr. 2002. *Chemical Physics Letters* 366(5-6), 623-627.


SEEDLING PROJECTS

The role of turbulence intensity in establishing a critical Stokes number that demarks the breakdown of isokinetic sampling principles

Daniel Wise, Daniel Weber, Elias Yoon, Donna Carlile
Edgewood Chemical Biological Center, Research & Technology Directorate, 5183 Blackhawk Rd., Aberdeen Proving Ground, MD 21010

ABSTRACT

Inlet efficiency measurements were made for a range of thin-wall tube sampling probes by comparing them to a probe of fixed size co-located in a uniform aerosol stream with a wind velocity of 10 mph. Free stream turbulence intensity was varied as part of the experimental matrix. The various levels of turbulence intensity were created using classical types of turbulence grids and a unique new class of "fractal grids", which are reported to have unique turbulence qualities. In our study, isokinetic sampling did not provide the same aerosol concentration across scales of probe diameter. The inlet efficiency increased with increasing probe Stokes number for low levels of free stream turbulence, but not for high levels of turbulence.

1. INTRODUCTION

Isokinetic sampling is a primary concept in the referencing of aerosols.[1] This sampling technique avoids aerosol collection size and concentration biasing by sampling air isoaxially, and matching the velocity of the flow going into the inlet to the approaching wind velocity. This arrangement eliminates streamline curvature as the air moves into the inlet; therefore, it should aspirate aerosol particles with 100% efficiency. For this reason, isokinetic sampling probes are employed in reference sampling systems used in aerosol research.

Interesting observations have been made that indicate there is a point in the scale of aerosol sampling equipment (particularly isokinetic reference probes) where there is a significant increase in loss of particles due to turbulent particle dispersion (either due to turbophoresis or energetic impaction).[2-4] One conjecture is that the free-stream turbulence intensity which can be significantly higher than the intensity inside the sampling equipment.[5] This mismatch then causes particle aspiration losses because the trajectories of the particles transported by the flow are coupled to the flow turbulence. Although there is some information relating turbulence to particle aspiration loss [6], this data does not extend over a wide range of probe diameters and there is a lack of information that relates turbophoresis or energetic impaction dependence on scale for various levels of turbulence. Furthermore, this dependency is difficult to computationally model because turbulence models for aerosols are ill-suited to handle phenomena such as laminar to turbulent transition and bluff-body aerodynamics that are probably major effects in aerosol aspiration in isokinetic conditions.

An experimental program was performed to determine a critical Stokes number (Stk) (which relates to scale, particle size, and flow velocity) at which turbophoresis or energetic impaction affects aerosol aspiration. The relationship of this critical Stk to free-stream Turbulence Intensity will also be observed.

The result will identify whether Turbulence Intensity is the primary underlying phenomena in the breakdown of isokinetic reference methods and if so, its correlation to a "critical inlet Stokes number". This study has a two-fold relevance. The first is in accurate referencing of aerosols in experimental studies. Anecdotal advice is given to experimenters that selection of reference sampling probes must be

made in context of scale. Ignorance of this "rule-of-thumb" guidance can result in unrecognized inaccurate data. Secondly, validation of the approaches used in numerical simulations (computational fluid dynamics-CFD) is often lacking. In addition, the models for many physical phenomena are not well developed and are not implemented in commercial CFD codes. In particular, aerosol particle tracking capabilities for purposes of aspiration and transport modeling rely on proper implementation the effect of turbulence intensity and adequate turbulence models with particle trajectory-turbulence coupling. Performing basic CFD simulations for reference probe geometries and comparing the numerical results with the experimental data obtained from wind tunnel tests, can provide necessary confidence in the chosen turbulence model.

2. METHOD

2.1 Overview

Aerosol aspiration experiments using different scale isokinetic sampling probes in an aerosol wind tunnel where free-stream turbulence intensity and Reynolds number, and Stokes number can be controlled and varied. The turbulence induced loses will be assessed by aspiration efficiency characterization (per a co-located unity probe) as the scale of the test probe is reduced. The experiment is repeated with different levels of turbulence intensity by tailoring of the free-stream with turbulence grids' overall inlet efficiency is a product of aspiration and transport of the particles and will assessed by aerosol concentration collected by the probes, including their internal losses, so that differences in the inlet efficiency are attributed only to aspiration. The aspiration efficiency of the test probe should be near unity until the interaction of turbulence intensity with probe scale becomes significant, at which point the aspiration efficiency would drop noticeably. This drop-off would correspond to a particular probe Reynolds number (the ratio of inertial to viscous forces referenced to the probe diameter), and Stokes number (the ratio of particle response time to fluid time scale-or more generally, the ratio of fluid pressure forces to the viscous forces). This would designate a "critical" Reynolds and Stokes number for that turbulence intensity level.

2.2 Experimental facility

The experiments were performed in an aerosol wind tunnel with a 20 x 20-inch test section. The test aerosol is generated using a Vibrating Orifice Aerosol Generator (VOAG) with a fluorescently tagged oleic acid solution. The wind tunnel was operated at a test section velocity of 10 mph for all trials. The VOAG produces 5 μm monodispersed particles, which are introduced to the wind tunnel where they are mixed by an array of mixing fans with incoming HEPA filtered air to produce a uniform aerosol challenge. The seeded air flow then passes through a turbulence/fluctuation dampening screen. The aerosol then passes through a contraction to achieve the desired test velocity in the test section. The free-stream turbulence is then created at the desired intensity by a grid in the fetch upstream of the test section.

2.3 Test probes

The experiment is conducted using isokinetic probes of various diameters. The test probes were attached to a 47 mm glass fiber filter holder via a diverging cone and designed in accordance to guidance for thin-wall tube sampling.[7] Thin wall tubes have been studied extensively and a deep literature base for reference and comparison exists. The probes used in this study ranged from 0.125 inches to 1.20 inches in diameter and are shown in Figure 1.

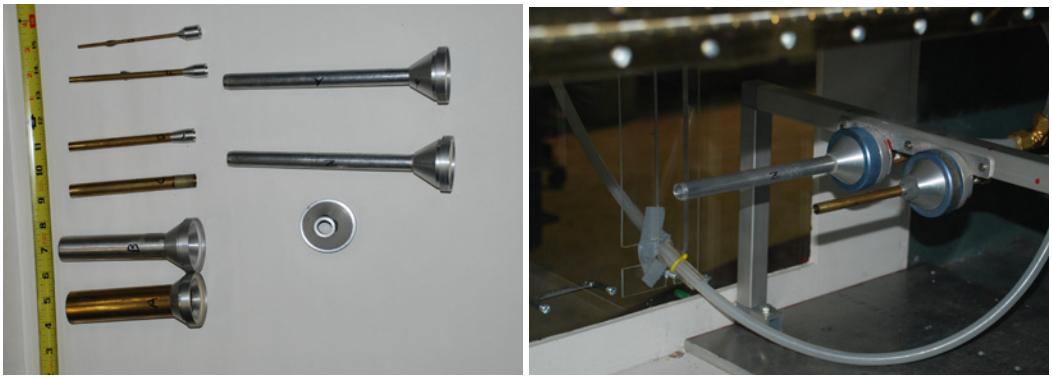

Figure 1. Test probes and test section installation.

2.4 Turbulence manipulation

The test requires different levels of turbulence. This can be done by placing a turbulence generating grid in the wind tunnel upstream of the test probes. Two types of grids were used in the course of the experiments, a classical square lattice grid, and a novel "fractal grid" (briefly discussed in Section 3) are shown in Figure 2.

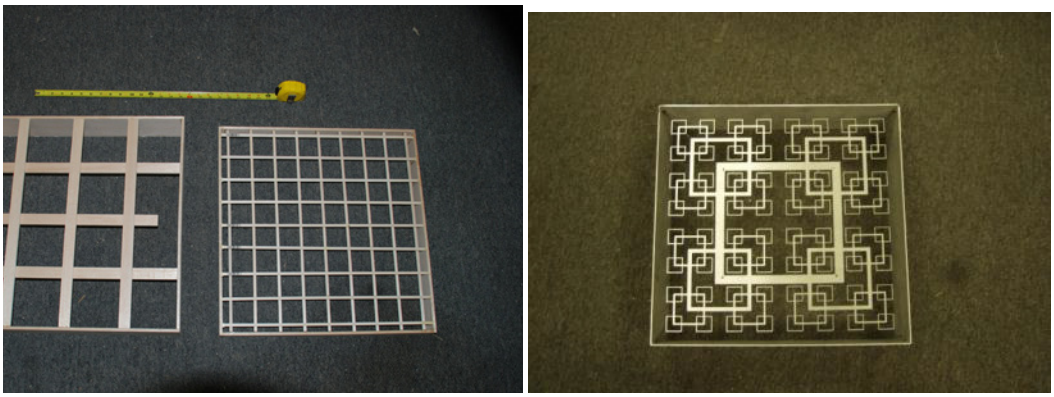

Figures 2. Lattice grids and fractal grid.

2.5 Turbulence measurements

The centerline test section turbulence level measurements were made in the wind tunnel as different turbulence generating grids were placed at various upstream locations, relative to the test section, that influenced the magnitude of turbulent energy reaching the test section. A TSI IFA300 Thermal Anemometry System with ThermoPro software version 4.6 was used to make the needed turbulence measurements. A single component, TSI model 1262A miniature hotwire probe with a wire diameter of 3.8 µm was used. The probe was calibrated for a velocity range of 0.11 to 6.5 m/s. In order to properly capture the turbulent influence on the flow field, the velocity must be sampled at a rate sufficient to capture high frequency fluctuations and for a sufficient duration to acquire the low frequency components. The following settings were used: sampling rate 50k samples/s, low pass filter 10k Hz and sampling time of 20.5 s. A statistical analysis is performed on these samples to determine the average velocity and turbulence intensity. Turbulence intensity is defined as the RMS value of the velocity (turbulence) divided by the average velocity.

3. RESULTS AND DISCUSSION

3.1 Turbulence manipulation

A key issue in the experimental method was the ability to create turbulence levels of three distinct magnitudes. While we have much experience in dampening existing turbulence for aerodynamic studies and creating turbulence for mixing of test aerosols, the creation of turbulence of selectable levels was unprecedented in our lab. Research into methods to select turbulence led us beyond classical turbulence grids to a new class referred to as “fractal grids”. These grids consist of a multi-scale array of planar shapes all based on a single pattern that is repeated in increasing number of copies as the scale decreases.[8] The great lure of this class of grid was that it should produce high levels of turbulence with relatively low pressure drops. In addition, the structure of the turbulence, is reported to not follow typical Kolmogorov decay, and should produce well documented varied turbulence at specific down-wind distances. This is an extremely attractive attribute for our experiment (also, this class of grids creates unique initial conditions for turbulence which opens new areas of basic research applicable to robust modeling of turbulence). A fractal grid was fabricated and evaluated (Figure 3a); however, we were not able to reproduce published turbulence structures, and as such, the fractal grid was not a solution for all our turbulence test conditions. The fractal grid was used to produce our mid-range turbulence; however a classical, high pressure drop, rectangular grid array was necessary to produce the highest levels of turbulence.

Turbulence measurements were made at the following conditions. The free stream velocity was approximately 10 mph. A single turbulence screen was placed in the settling chamber just upstream of the contraction. The all four settling chamber mixing fans were operating at a setting of 4 in the reverse direction. A centerline test section velocity and turbulence measurement was made with the screen installed and fans operating. Next measurements were made with classical grids and the novel fractal grid positioned at several distances from the measuring hotwire in the test section. The results are shown in Figure 3b.

(a) 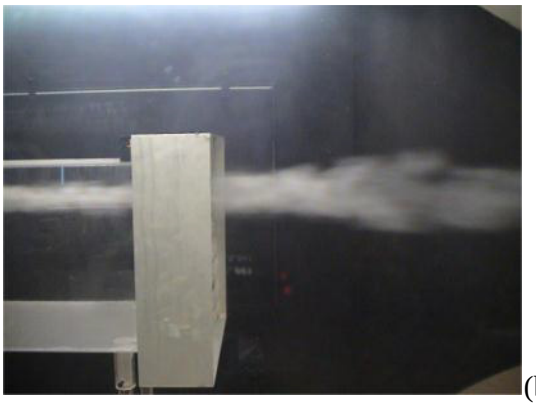

(b) 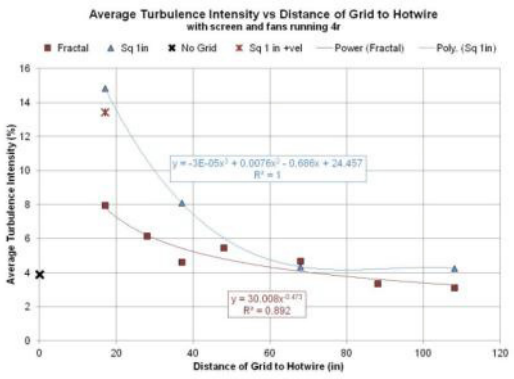

Figure 3. (a) Smoke visualization of fractal grid turbulence and (b) turbulence intensity as a function of grid distance from test section.

3.2 Aerosol uniformity

The uniformity of the aerosol challenge was assessed using two identical, 0.5 inch probes, located at the test and reference probe positions. The overall inlet efficiency determined by comparing these two probes (their concentration ratio) should be unity in a uniform aerosol profile, and the spread of the data over several trials indicates the lowest level of inherent experimental uncertainty. The concentration ratio was 1.06, with a standard deviation of 0.13 confirming the test probe arrangement for our study.

3.3 Inlet efficiency (η_i) over a range of probe diameters and turbulence levels

Inlet efficiency (η_i) for different sized isokinetic probes as turbulence intensity varies is shown in Figure 4. These two plots represent the same data just plotted as a function of either Reynolds number (Re), or square root of the Stokes number ($\sqrt{Stk}$). In expressing similarity of flow and particle inertia conditions both the Re and Stk are considered. As the Stokes number includes both probe diameter and particle size it is perhaps the best representation to compare to other experimental studies. The error bars are omitted in the $\sqrt{Stk}$ plot for clarity of presentation, but retained in the Re plot so the degree of uncertainty is shown.

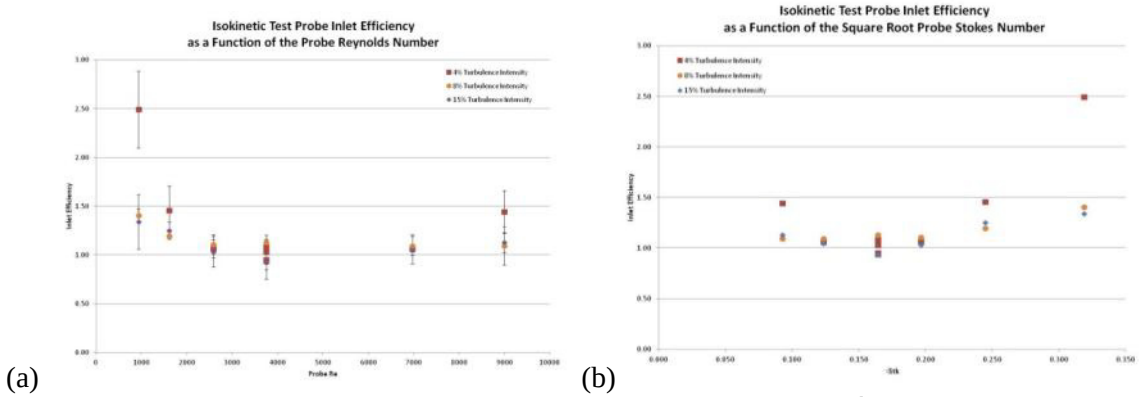

Figure 4. (a) Inlet efficiency as a function of probe Re and (b) $\sqrt{Stk}$

A better understanding of the mechanism of the aspiration and transport of aerosol through the sampling probe can be facilitated by identifying the percent of the aspirated aerosol that is subsequently deposited on the internal surface of the probes. This data was obtained by recovering several rinses of the internal probe surface and is plotted as function of $\sqrt{Stk}$ and turbulence intensity. This was supplemented by concurrent but separate data from a setup at much higher wind velocities which enable the extension of the data range to higher Stokes numbers that were not possible in the small wind tunnel. The rinse data shows no strong correlation of internal probe deposition to turbulence intensity except at extreme Stokes number (Figure 5). It is interesting and validating to note that the supplementing data from the independent wind tunnel test matches the rinse data from the primary test setup. This extended data shows that as the Stokes number increases there is a point where the amount deposited on the inside of the probe increases quite quickly. This has been noted in previous testing of Unmanned Aerial Vehicle (UAV) mounted samplers at high wind speeds and is of practical concern “rule-of-thumb” guidance to testing at high wind speeds.

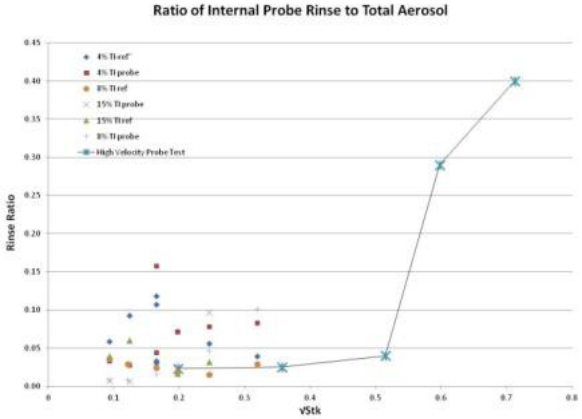

Figure 5. Ratio internal tube aerosol deposition to total aerosol collected.

The inlet efficiency for the range of probe size and turbulence intensities shown in Figure 4 indicates an increase in inlet efficiency with increasing Stokes number (i.e., decreasing probe size and Reynolds number). This result is surprising as previous studies on thin-wall probes show no effect of turbulence on aspiration efficiency.[6] Therefore, inlet efficiency greater than unity, in any case of our experiment, does not have an explanation at this time.

When unexplained results occur, the experimental uncertainties should be explored to determine if the data is truly a physical effect not just an artifact of the experiment. Admittedly, the measurement of true particle concentration over our wide range of test probes (and therefore air flow rates) is extremely difficult. This is reflected to some extent by the magnitude of the error bars for each data point; however, the trend lies outside the trial to trial variability. Likely sources of error include the ability to recover deposition from the interior surface of the probes, non-linearity of the fluorometric analysis, and errors in probe sampling air flow rate. Figure 5 rinse data showed that internal probe deposition was not a large percentage of the total signal (except for the highest Stokes number trials, which were not included in the concentration ratio data), and that the rinses did effectively recover the interior deposition. Any scenario with inadequate probe rinsing would have produced an effect opposite of that observed. The fluorimeter linearity was verified, and the air flow rates which were held constant from trial to trial by critical orifices, were checked with several different calibrated mass flow meters. None of these likely sources of experimental error can account for the unexpected data trend. Therefore, this data suggests that there is a critical Reynolds number (or more comprehensively, a critical Stokes number) which demarks the breakdown of isokinetic sampling principles, but the observed effect is opposite our expectations.

The scale aspect of this phenomenon has been observed and mentioned previously [2-4] and it is often attributed to experimental uncertainty or inability to account for internally deposited aerosols. One of our objectives was to obtain experimental data on this phenomenon of non-unity concentration ratios for small scale probes and eliminate these two possibilities. The observed non-unity concentration ratio seems to be beyond quantifiable experimental uncertainty; therefore, other theories to support these results might be pursued. The theory of the probes' *aspiration efficiency* affected by a mismatch in turbulence intensity between free-stream levels and those inside the probe can be strengthened by assessing the turbulence levels inside the probes. This is very difficult to do on such small probes, but it is possible. Furthermore, CFD modeling may be able to shed light on the magnitude of the turbulence mismatch if several different turbulence models were used to see if any predict these results. If so, then the difference in the models would be a clue to the mechanism for the non-unity concentration ratio. Also, if a turbulence mismatch effect is identified then our experiment could serve as a verification data set in the choice of turbulence models used in CFD aerosol sampling design applications.

4. CONCLUSIONS

Inlet efficiency measurements were made for a range of thin-wall tube sampling probes by comparing them to a probe of fixed size co-located in a uniform aerosol stream with a wind velocity of 10 mph. Free stream turbulence intensity was varied as part of the experimental matrix. The various levels of turbulence intensity were created using classical types of turbulence grids and a unique new class of "fractal grids", which are reported to have unique turbulence qualities.

The data indicates that isokinetic sampling does not provide the same aerosol concentration across scales of probe diameter. The inlet efficiency increased with increasing probe Stokes number for low levels of free stream turbulence, but not so much for high levels of turbulence. We do not have an understanding of how this concentration ratio can increase beyond unity, and the experimental uncertainties alone do not seem to account for it. It is suggested that this is possibly a real effect of turbulence intensity mismatch and follow on work with turbulence measurements inside the probes and CFD modeling of the sampling situation with different turbulence models can provide a better understanding of these experimental results and possibly support the mismatch theory.

5. ACKNOWLEDGEMENTS

The authors would like to thank Dr. Igor Novosselov for suggesting a CFD analysis of the observed phenomena and possible mechanisms by which it could occur and general guidance on experimental combinations. Mr. Daniel VanReenen for fabricating several test fixtures and the ECBC Advanced Design and Manufacturing team for fabricating the novel fractal grid.

WORK CITED

[1] Hinds, W. Aerosol Technology. 2nd edition. New York, NY. John Wiley & Sons.
[2] Ranade et al. “EPA Project Summary: The PM-10 Samper Evaluation Program: January 1985 to July 1986.
[3] Wise, D. et al. “Edgewood Chemical Biological Center’s Evaluation of Generation-3 Vendor Aerosol Collection Subsystems”; December 2010; Test Report for Department of Homeland Security’s Office of Health Affairs.
[4] Novosselov et al. “DFU Inlet Test Report”, Enertechnix Inc. January 2010.
[5] “Numerical and experimental study of particle behavior in isokinetic probes” proposal draft to Daniel Wise by Dr. Igor Novosselov, based on conversations at 2010 AAAR conference.
[6] Vincent, J. 1989. Aerosol Sampling: Science and Practice. Wiley, London.
[7] Durham, M. and Lundren, D. 1980. *J. Aerosol Sci.* Vol. 11, pp. 179 to 188.
[8] Mazellier, N. and Vassilicos, J. 2010. *Physics of Fluids* 22, 075101.

Enhanced recovery of agents by selective recombinational enrichment

Brady W. Redmond*[a], Matthew W. Lux[a], Lauren A. McNew[a], Bryan A. Rivers[b], James P. Carney[a]
[a]Edgewood Chemical Biological Center, Research & Technology Directorate, 5183 Blackhawk Rd., Aberdeen Proving Ground, MD 21010
[b]Science Applications International Corporation, McLean, VA 22102

ABSTRACT

The goal of Enhanced Recovery of Agents by Selective Recombinational Enrichment (ERASRE) is to enable pathogen characterization by genomic sequencing in complex environmental samples. Currently the only option available to reduce the complexity of the DNA sequenced from environmental samples is via bioinformatics. All of the DNA isolated from an environmental sample must be sequenced and data from pathogens of interest must be teased out with complicated algorithms and a heavy investment of computing resources. ERASRE is an attempt to reduce the complexity of an environmental sample by subtracting out unwanted "background" DNA prior to genomic sequencing. In this project we attempted to apply the ERASRE concept to a simple mixture of DNA isolated from two different bacterial populations, enriching the DNA from one population by removing the DNA from the other population. The method did not work as envisioned as we saw no enrichment of *Y. pestis* DNA from a mixture of *B. anthracis* and *Y. pestis* DNA following qPCR analysis.

1. INTRODUCTION

Advances in genomic sequencing technology have renewed interest in the possibilities of metagenomic analysis, the study of genetic material from environmental samples. Metagenomic analysis is of use to the biodefense community when microbial communities possibly contain biological threat agents. Unfortunately, in environmental samples the complexity of the microbiome may inordinately increase the difficulty of the metagenomic analysis.[1] The number of microbial genomes in a gram of soil has been estimated at somewhere between 3000 and 11000.[2] Additionally, a study of farm soil resulted in a high sequence yield but a very low percentage of overlaps and no contigs.[3] It would be very useful for monitoring or forensic biodefense purposes to be able to reduce this complexity in the analysis stream and focus only on a segment of interest. ERASRE could make it possible to enrich a sample for DNA from potential biological threat agents by removing the DNA from common bacterial flora.

We proposed to demonstrate the applicability of ERASRE to enrich samples for targets of interest. The DNA from two bacterial species will be was mixed and ERASRE was used in an attempt to enrich the mixture for DNA from one species (target) by removing most of the DNA from the second bacterial species (background). We included multiple controls in an attempt to elucidate reaction conditions for optimum RecA activity and removal of background DNA. Enrichment would be demonstrated by increased quantitative PCR signal relative to that exhibited by the starting material. In future experimentation we will start with varying ratios of background and target DNA to determine the effectiveness of enrichment. Finally, mixed samples and enriched target DNA will be sent to the ECBC Genomic Sequencing Center for DNA sequence analysis. Enriched samples should provide higher resolution sequence data that can be interpreted with much greater confidence.

2. METHODOLOGY

2.1 Biotinylation of genomic DNA

Genomic DNA isolated from *B. anthracis*, *Y. pestis*, *Erwinia herbicola*, and *B. thuringiensis* was obtained from ECBC stocks. Initial attempts to biotinylate these DNA stocks (approximately 1 µg DNA per reaction) was performed with Klenow fragment and biotinylated dNTPs (New England Biolabs Inc., Ipswich, MA). Later attempts to biotinylate these DNA stocks were accomplished using biotinylated random hexamers (bio-World, Dublin, OH) according to the manufacturer's protocol.

2.2 RecA mediated recombination

Purified biotinylated DNA was heated to 95°C for 2 minutes (except the Not Denatured control) to denature and then flash cooled on ice for 5 minutes. Biotinylated DNA was bound to M-270 Streptavidin Dynabeads (Dynal, Carlsbad, CA) according to the manufacturer's protocol. Briefly, 0.5 mg of suspended Dynabeads (50 µL) were washed two times and added to the flash cooled, denatured, biotinylated DNA. The mixture was incubated at room temperature for 30 minutes with rotation. The Dynabeads were then pulled to the tube wall for 3 minutes with an Invitrogen Magnetic Particle Concentrator (MPC) so that the supernatant (S1) could be removed. The beads were then washed two more times. Several recombination test samples and controls were then set up by adding some of the following to the washed Dynabeads (Table 1): 700 µM ATP (New England Biolabs, Ipswich, MA), 700 µM ATPγS (New England Biolabs, Ipswich, MA), 20 µg *E. coli* $RecA_f$ (New England Biolabs, Ipswich, MA), 50 ng *Y. pestis*YERS078 DNA, and 50 ng *B. anthracis* BACl225 DNA. All reactions had a final volume of 56 µL and were incubated at 37°C for 30 minutes. The Dynabeads were then pulled to the tube wall for 3 minutes with an Invitrogen MPC, the supernatant was collected (S2), and the Dynabeads were discarded.

Table 1. Breakdown of subtractive recombination test samples and various controls.

Sample	BA DNA	ATP	ATPγS	DNA Denatured?	RecA	Free DNA
BACl225.ATP1,2	+	+	-	+	+	+
BACl225.ATPγS1,2	+	-	+	+	+	+
NTC, ATPγS	-	-	+	+	+	+
Not Denatured, ATPγS	+	-	+	-	+	+
No RecA, ATPγS	+	-	+	+	-	+
No ATP or ATPγS	+	-	-	+	+	+
No Free DNA, ATPγS	+	-	+	+	+	-

2.3 Quantitation of recovered DNA

DNA in the recovered supernatants (S1 and S2) was quantified with the Invitrogen Quant-iT dsDNA BR Assay Kit using the Invitrogen Qubit (Invitrogen, Carlsbad, CA). The final supernatant (S2) was used as template for quantitative PCR on an ABI 7900 HT platform (Life Technologies, Carlsbad, CA) using CRP PCR Wet Frozen FastBlock Assay Kits for *B. anthracis* (PCR-BAT-3R-K) or *Y. pestis* (PCR-YPT-4R-K) according to the manufacturer's protocols (Critical Reagents Program, Frederick, MD).

3. RESULTS

Initial experiments relied on the activity of Klenow fragment to incorporate biotinylated dNTPs into the target DNA without any prior restriction enzyme treatment. When this failed to produce the desirable

yield we switched to random priming with biotinylated hexamers. Random priming with biotinylated hexamers has routinely produced low yields after purification with either the Qiaquick kit or the AmPure kit. After running the entire protocol several times and realizing abnormally low DNA concentrations and little enrichment of non-recombinationally targeted DNA we analyzed the biotinylated DNA on the Agilent Bioanalyzer. The biotinylated products were in the 12-15 kb range, obviously too large to be purified by either kit. We have now removed the purification step from the protocol. Tables 2 through 5 show typical results. QPCR following attempted removal via ERASRE of *B. anthracis* DNA from an added mixture of *B. anthracis* and *Y. pestis* DNA has indicated the presence of all added DNA in the final supernatant.

Table 2. Summary of recovered DNA concentrations measured by Quant-IT dsDNA analysis following subtractive recombination

Sample	Prior to RecA addition (µg/mL)	Total DNA (µg/mL)	After RecA addition (µg/mL)	Total DNA (µg/mL)	Total DNA differential (ng)
BACI225.ATP1	5.61	224.4	3.62	202.72	-22.2
BACI225.ATP2	11.1	444.0	9.46	529.76	85.76
BACI225.ATPγS1	10.33	413.2	10.33	578.48	165.28
BACI225.ATPγS2	7.58	303.2	7.12	398.72	95.52
NTC, ATPγS	5.38	215.2	9.99	559.44	344.25
Not Denatured, ATPγS	41.2	1648.0	11.17	625.52	-1022.48
No RecA, ATPγS	10.96	438.4	9.71	543.76	105.36
No ATP or ATPγS	7.71	308.4	7.15	400.40	92.00
No Free DNA, ATPγS	5.85	234.0	4.78	287.68	33.68

Table 3. qPCR results for amplification of *B. anthracis* target from free DNA in final supernatant

Sample Name	Ct	Quantity (pg)	Dilution Factor	Corr. Quantity (pg)	Mean Qnty (pg)	Mean Qnty (ng)	Vol Sample (uL)	Concentration (ng/uL)
Sample1__BA3_1000	22.225935	372.5891	18.1	6743.86	5376.39	5.38	5	1.08
Sample1_BA3_100	26.200981	22.148706	181	4008.92				
Sample2__BA3_1000	23.82662	119.56053	47.3	5655.21	4737.00	4.74	5	0.95
Sample2_BA3_100	27.62216	8.073555	473	3818.79				
Sample3__BA3_1000	23.83443	118.89925	51.66	6142.34	4901.27	4.90	5	0.98
Sample3_BA3_100	27.806059	7.0851893	516.6	3660.21				
Sample4__BA3_1000	23.66512	134.08917	35.6	4773.57	4378.47	4.38	5	0.88
Sample4_BA3_100	27.16257	11.189212	356	3983.36				
Sample5__BA3_1000	24.071974	100.443565	49.96	5018.16	4374.34	4.37	5	0.87
Sample5_BA3_100	27.732141	7.4670167	499.6	3730.52				
Sample6__BA3_1000	23.927094	111.32751	49.86	5550.79	4709.92	4.71	5	0.94
Sample6_BA3_100	27.677973	7.759835	498.6	3869.05				
Sample7__BA3_1000	23.33237	169.82884	48.56	8246.89	7670.36	7.67	5	1.53
Sample7_BA3_100	26.789967	14.578357	486.6	7093.83				
Sample8__BA3_1000	23.786377	123.02645	35.76	4399.43	4641.39	4.64	5	0.93
Sample8_BA3_100	26.882017	13.6559105	357.6	4883.35				
Sample9_BA3_1000	27.825563	6.9877334	23.9	167.01	146.63	0.15	5	0.03
Sample9_BA3_100	31.462128	0.5282512	239	126.25				

Table 4. qPCR results for amplification of *Y. pestis* target from free DNA in final supernatant

Sample Name	Ct	Quantity (pg)	Dilution Factor	Corr. Quantity (pg)	Mean Qnty (pg)	Mean Qnty (ng)	Vol Sample (uL)	Concentration (ng/uL)
Sample1__YP4_1000	23.562534	207.55	18.1	3756.66				
Sample1_YP4_100	26.812796	20.22	181	3659.62	3708.14	3.71	5	0.74
Sample2__YP4_1000	24.48118	107.47	47.3	5083.17				
Sample2_YP4_100	28.03427	8.43	473	3986.02	4534.59	4.53	5	0.91
Sample3__YP4_1000	24.92151	78.39	51.66	4049.60				
Sample3_YP4_100	28.276846	7.08	516.6	3658.91	3854.26	3.85	5	0.77
Sample4__YP4_1000	24.212917	130.24	35.6	4636.58				
Sample4_YP4_100	27.976475	8.78	356	3126.88	3881.73	3.88	5	0.78
Sample5__YP4_1000	24.566286	101.11	49.96	5051.43				
Sample5_YP4_100	28.460608	6.21	499.6	3101.98	4076.70	4.08	5	0.82
Sample6__YP4_1000	24.725565	90.20	49.86	4497.61				
Sample6_YP4_100	28.497757	6.05	498.6	3014.46	3756.04	3.76	5	0.75
Sample7__YP4_1000	24.243713	127.40	48.56	6186.47				
Sample7_YP4_100	27.61908	11.35	486.6	5521.32	5853.90	5.85	5	1.17
Sample8__YP4_1000	24.050913	146.27	35.76	5230.64				
Sample8_YP4_100	27.63407	11.23	357.6	4014.24	4622.44	4.62	5	0.92
Sample9_YP4_1000	Undetermined	0	23.9	0				
Sample9_YP4_100	Undetermined	0	239	0	0.00	0.00	5	0.00

Table 5. Comparison of concentrations of *B. anthracis* and *Y. pestis* free DNA in final supernatant

Sample	Qubit (ng/µL)	Concentration B. anthracis DNA (ng/µL)	Concentration Y. pestis DNA (ng/µL)
BACI225.ATP1	3.62	1.08	0.74
BACI225.ATP2	9.46	0.95	0.91
BACI225.ATPγS1	10.33	0.98	0.77
BACI225.ATPγS2	7.12	0.88	0.78
NTC, ATPγS	9.99	0.87	0.82
Not Denatured, ATPγS	11.14	0.94	0.75
No RecA, ATPγS	9.71	1.53	1.17
No ATP or ATPγS	7.15	0.93	0.92
No Free DNA, ATPγS	4.78	0.03	<0.48

4. CONCLUSIONS

To date we have not had any success enriching for *Y. pestis* DNA via subtractive recombination from a mixture of *B. anthracis* and *Y. pestis* DNA. This is despite trying multiple methods for biotinylating capture DNA and multiple attempts at going through the entire procedure with multiple controls. We suspect that the biotinylation reaction primed with biotinylated random hexamers is proceeding efficiently, but we are losing much of the DNA in the initial purification step due to the large fragments generated. Future attempts to optimize the ERASRE process will likely eliminate this purification step. In conclusion, all attempts at ERASRE thus far have resulted in recovery of all added free DNA regardless of species.

WORK CITED

[1] Venter, J. C. et al. 2004. *Science* 304, 66-74.

[2] Schmeisser, C. et al. 2007. *Appl. Microbiol. Biotechnol.* 75, 955-962.

[3] Kowalchuk, G. A. et al. 2007. *Microbial Ecology* 53, 475-485.

Biodegradation of organofluorine compounds

Melissa M. Dixon and Steven P. Harvey
Edgewood Chemical Biological Center, Research & Technology Directorate, 5183 Blackhawk Rd., Aberdeen Proving Ground, MD 21010

ABSTRACT

Enrichment cultures were set up using various organofluorine compounds as sole source of carbon for growth. Growth was confirmed on two of the substrates; benzoyl fluoride and 1H, 1H, 2H, 2H-perfluorooctyltriethoxysilane. Subsequent measurements of defluorination rates showed that benzoyl fluoride defluorinated very rapidly; therefore the growth observed was probably on the hydrolysis product benzoic acid. Both cultures appeared to be consortia; single colony isolates capable of growth on either compound have not yet been identified. A continuous loop UV mutagenesis reactor was also set up to create segregants with newly-derived abilities to utilize organofluorine compounds as sole carbon source; this work is continuing.

1. INTRODUCTION

Organofluorines comprise an important group of compounds used as refrigerants and agricultural chemicals. Although useful in these roles, they are frequently toxic and can exhibit environmentally deleterious effects such as ozone depletion.[1] The challenge associated with their remediation and detoxification is largely related to their stability. The C-F bond is the strongest covalent bond a carbon atom can form, and will typically survive even extremes of pH, temperature, and oxidation-reduction.[2] New and improved means of detoxifying these compounds are highly sought after and a few enzymes have been identified that are capable of cleaving the C-F bond.[3,4] Recently, several of these defluorinases have even been crystallized.[2] Others surely exist, as evidenced by the fact that there are twelve known naturally-occurring organofluorine compounds, all found in microorganisms and plants.[5] As with all compounds in nature, their enzymatic degradation is assumed to occur by virtue of the observation that they have not accumulated infinitely in the environment.

2. MATERIALS AND METHODS

M9 medium was used without glucose and was comprised of 7.25 g Na_2HPO_4, 3.0 g KH_2PO_4, 0.71 g NaCl, 2.0 g NH_4Cl per liter. Salts solution was then added to the following final concentrations: $MgSO_4$ (1 mM), $CaCl_2$ (0.1 mM), and $FeCl_3$ (0.01 mM).

Fluoride electrode assays were conducted at room temperature in 2.5 mL 50 mM bis-tris-propane buffer, pH 7, using 100 µL of supernatant from the lysate as the enzyme sample.

3. RESULTS AND DISCUSSION

3.1 Enrichment cultures

One approach to the identification of degradative enzymes is to “feed” the compound of interest to a consortium of microorganisms as the sole carbon source for growth and energy. This selection is a powerful tool that can be used to isolate organisms and, subsequently, enzymes for the degradation of various organic compounds. Organisms capable of utilizing the compound of interest will overgrow the culture and after a period of time (typically weeks), can be isolated from the consortium. Following isolation, lysates can then be tested for useful enzyme activity; in the specific case of C-F hydrolysis,

activity can be monitored by fluoride electrode. Our specific proposed approach is to use an array naturally-occurring and synthetic organofluorine compounds as carbon sources in separate enrichments.

The compounds used in the enrichments are shown in Table 1. All compounds were initially used at a concentration of 20 mM as sole carbon source in M9 salts medium.

Table 1. Compounds used as carbon sources in enrichments

Compound	MW	Density
Chloropentafluorobenzene	202.51	1.569
1H, 1H, 2H, 2H-perfluorooctyltriethoxysilane	510.35	1.3299
2,2,2-trifluoroethanol	100.04	1.373
4-fluorophenol	112.1	1.246
perfluorononanoic acid	464.08	solid
perfluoro-1-octanesulfonyl fluoride	502.12	1.824
2,2-difluoroethanol	82.05	1.296
2-fluoroaniline	111.12	1.151
2,6-dichloro-4-(trifluoromethyl)pyridine	215.99	1.505
benzoyl fluoride	124.11	1.14
2-fluoro-6-(trifluoromethyl)benzoyl chloride	226.56	1.465
5-fluoro-2-nitrobenzotrifluoride	209.1	1.49
3-chloro-4-fluoro-5-nitrobenzotrifluoride	243.54	1.607
2-fluoro-3-(trifluoromethyl)benzoic acid	208.11	solid
5-fluoro-2-(trifluoromethyl)benzoic acid	208.11	solid
2-fluoro-5-nitrobenzotrifluoride	209.1	1.52
2-fluoro-6-(trifluoromethyl)benzonitrile	189.11	1.373

Enrichment cultures were inoculated with environmental isolates from water, soil and wastewater discharges and incubated at 25°C for up to three months. Two of these enrichments became turbid due to bacterial growth: benzoyl fluoride and 1H, 1H, 2H, 2H-perfluorooctyltriethoxysilane. Initial cultures containing these two substrates were subsequently passed using a 1 µL inoculum placed into a 100 mL flask containing M9 medium with 20 mM of the same compound as sole carbon source. Both cultures continued to grow with several subsequent passages and bacteria from each were repeatedly streaked for single colonies, none of which were capable of growth on either substrate as sole carbon source.

Both cultures were grown in 1 L volumes to their maximum density on their respective substrates, pelleted at 5,000 x g, lysed in a microfluidizer, pelleted at 20,000 x g, and the supernatants were tested for defluorination activity using a fluoride electrode calibrated against known standards. Assays were run with all the compounds in Table 1 against lysates from cultures grown on both benzoyl fluoride and 1H, 2H, 2H-perfluorooctyltriethoxysilane. This screening did not identify any significant activity from either culture on the organofluorine compounds tested. A typical result is shown in Figure 1.

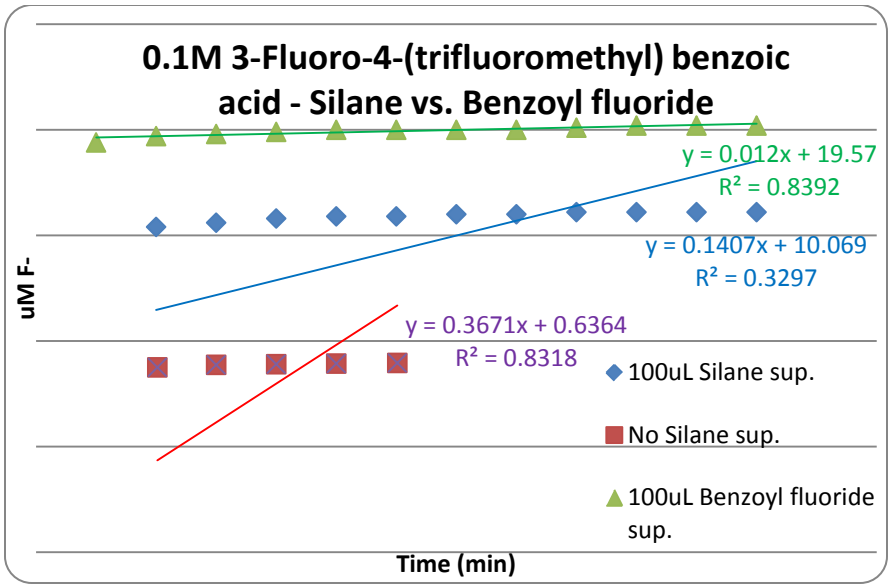

Figure 1. Typical defluorination assay results. Typical results of an assays comparing defluorination rates in the presence and absence of the bacterial lysates. In all cases rates were similar with and without the lysates, consistent with little or no enzymatic activity.

Table 2. Observed defluorination rates of some organofluorine compounds. Rates are composite for those compounds with more than one fluoride leaving group.

Compound	Hydrolysis Rate (nM F-/min)
chloropentafluorobenzene	1.0
2,2,2-trifluoroethanol	0.14
4-fluorophenol	4.6
perfluoro-1-octanesulfonyl fluoride	90
2,2-difluoroethanol	0.4
2-fluoroaniline	4
2,6-dichloro-4-(trifluoromethyl)pyridine	6.0
benzoyl fluoride	980,000
2-fluoro-6-(trifluoromethyl)benzoyl chloride	4.0
3-chloro-4-fluoro-5-nitrobenzotrifluoride	16
3-fluoro-4-(trifluoromethyl) benzoic acid	3.0
2-fluoro-3-(trifluoromethyl)benzoic acid	3.3
5-fluoro-2-(trifluoromethyl)benzoic acid	2.0
2-fluoro-5-nitrobenzotrifluoride	3.0
2-fluoro-6-(trifluoromethyl)benzonitrile	4.0

While most of the organofluorine compounds exhibited very slow hydrolysis, one compound, benzoyl fluoride, hydrolyzed approximately six orders of magnitude faster than the others (Figure 2).

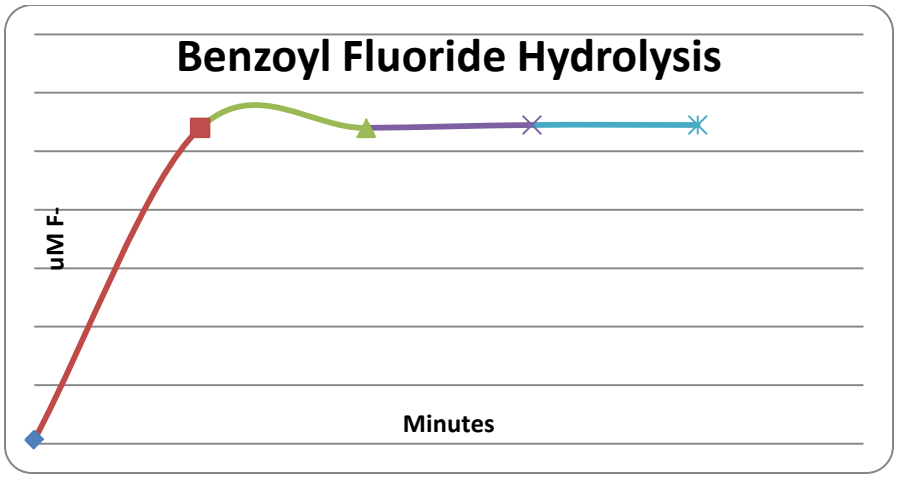

Figure 2. Defluorination of benzoyl fluoride, assayed in 50 mM bis-tris-propane, pH 7 at room temperature.

Presumably the primary product of the reaction in Figure 2 would be benzoic acid (reaction 1 below).

(1)

Accordingly, the cultures that were isolated using benzoyl fluoride as sole carbon source are most likely actually utilizing benzoic acid as their carbon source.

3.2 Continuous-loop UV mutagenesis reactor

In order to pursue a parallel approach to the isolation of organofluorine-degrading bacteria, a continuous-loop UV mutagenesis reactor was set up (Figure 3). The reactor is essentially a chemostat [6], designed with the purpose of continuously mutagenizing and selecting, through growth, for the ability to utilize the organic compounds provided as sole sources of carbon.

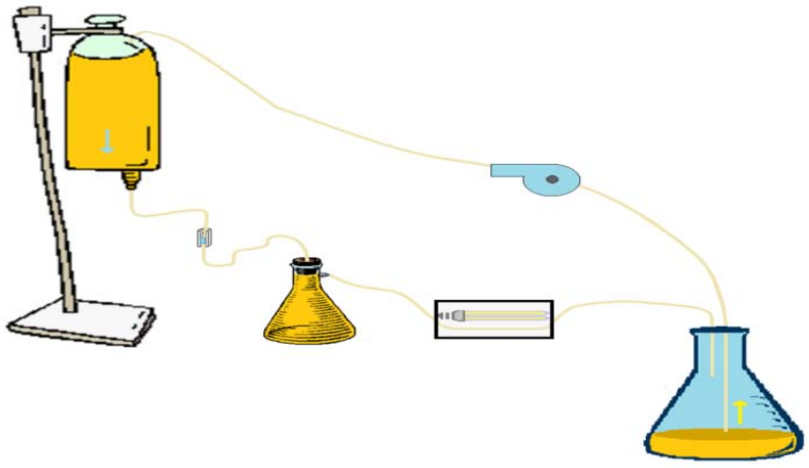

Figure 3. Continuous-loop UV mutagenesis reactor. Environmental isolates are placed in a drip bag and gravity-fed to a continuously-stirred Erlenmeyer flask which overflows into a UV mutagenesis chamber calibrated to kill 90-99% of cells. The overflow from the UV mutagenesis is then cycled back to the beginning of the process. Growth (turbidity) can be detected visually in the Erlenmeyer flask.

In an effort to maximize simplicity, the reactor was fed from a drip bag and the mutagenesis was calibrated to the drip rate from the bag. Using a gravity-fed system avoids the possibility of spills related to clogging and pressure build-up which are common to pump-fed systems. In order to produce useful mutants, we sought to calibrate the flow through the UV light source to produce approximately 90-99% killing.

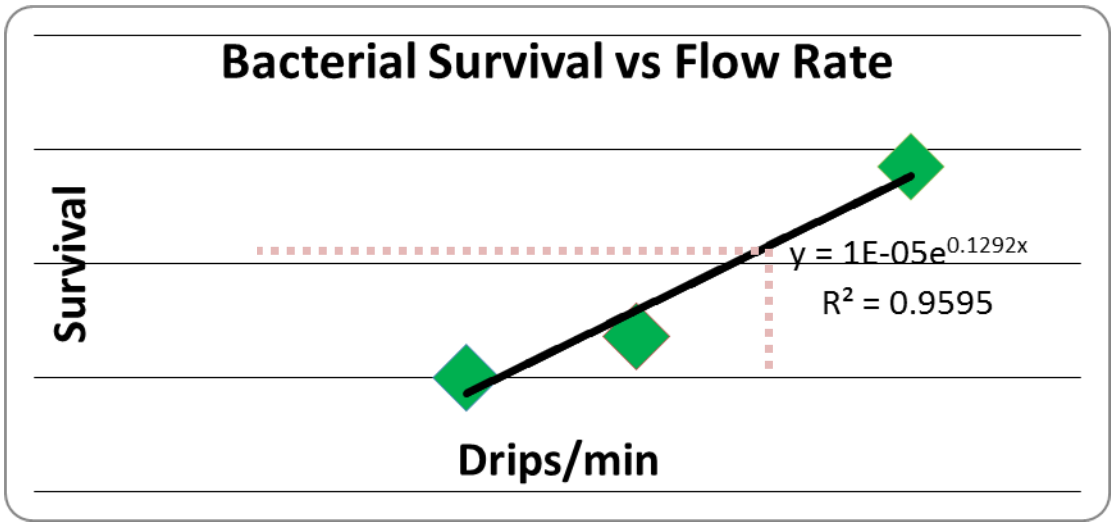

Figure 4. Calibration of mutagenesis reaction. A drip rate of approximately 50/min corresponded to a kill rate of 90-99%. This rate was confirmed with five subsequent tests at a steady drip rate of 50/min which yielded between 96.63% and 97.83% killing.

Using the calibrated flow rate of 50 drips/minute, the mutagenesis reactor was operated continuously for one week using 10 mM each of the compounds listed in Table 1. The recycled effluent from that run is now contained in a large flask which is being monitored for any increase in turbidity.

4. CONCLUSIONS

This work is not complete, so this report might best serve as a progress report. The chemical hydrolysis data will be used to inform the selection of compounds for use in the chemostat. The primary criterion for selection as a substrate for enrichment is that the compound must be stable enough (i.e. relatively little hydrolysis occurs over a period of days to weeks). With the exception of benzoyl fluoride, all the compounds tested meet that criterion. For the enrichment cultures, further efforts will be made to identify single colony isolates capable of utilizing the organofluorine compounds as sole source of carbon for growth.

WORK CITED

[1] Key, B.D. et al. 1998. *Environ. Sci. Technol*. 32: 2283-2287.
[2] Chan, K. et al. 2008. *Life Science* 45: 104-105.
[3] Barnett, J.E.G. et al. 1967. *Biochem. J.* 103: 699.
[4] Goldman, P. and Milne, G.W.A.. 1966. *J. Biol. Chem*. 241: 5557-5559.
[5] O'Hagan, D. et al. 2002. *Nature* 416: 279.
[6] Fussmann, G. McGill University. Chemostats: Eco-evolutionary dynamics in chemostats. Web. 26 Jul 2011. http://biology.mcgill.ca/faculty/fussmann/chemostats.html

Aerosol particle size distribution in relation to material surface science

Daniel Wise, Brendan DeLacy, Daniel Weber, Elias Yoon, Donna Carlile
Edgewood Chemical Biological Center, Research & Technology Directorate, 5183 Blackhawk Rd., Aberdeen Proving Ground, MD 21010

ABSTRACT

Laboratory experiments were performed to explore a relation between an aerosol producing devices' dissemination shear force and the resulting aerosol size distribution as a function of the bulk powder surface energy. Test particles of titanium dioxide (TiO_2) were treated to produce a range of surface energies. These powders were disseminated using a two-fluid entrainment nozzle which enabled variation in the deagglomerating shear stress. The resulting aerosol size spectrum was then observed as a function of these two parameters. Computational Fluid Dynamics (CFD) modeling of the dissemination device was used to quantify the shear stress imparted by the disseminator. The variation in particle size spectrum as a function of surface energy and shear force varied as expected, clearly demonstrating the relationship. The first mode of the spectrum shifted to a larger size as the shear stress was decreased and the surface energy of the particles was increased. The large particle fraction follows this same trend, but the differences in the spectrum as these parameters were varied were not significant. An unexpected second mode growth, however, was noticed as the shear stress increased, independent of surface energy.

1. INTRODUCTION

Analytical models that predict the particle size distribution, shape distribution, and cloud size of energetically disseminated aerosols are of great interest to the Defense community, especially in the CBR and Obscurant subject areas. These models should consider any physical or chemical property that impacts the post-dissemination particle cloud characteristics. Many dissemination methods can be used to produce such aerosol clouds and the particle size, particle shape, and concentration distribution will be related to dissemination parameters and bulk particle material surface properties. Source Term characterizations for these analytical models have been performed for various material and disseminator combinations. Our understanding is that, currently, the source term input is characterized for each emerging combination, but an underlying dominant material property is not considered to provide a generic source term strategy. Is it possible to relate source term input to a dominant material surface property and the energy by which it is disseminated?

Laboratory observations show that the surface energy of the particles comprising the feed stock (powders, micro-particles, or biological organisms) has a distinct effect on the size and the narrowness of the size distribution under energetic dissemination.[1] Our goal is to relate aerosol particle surface properties generically described as "Surface Energy" (which subsequently impacts the Hamaker Constant, Flow Quality number, and Geldhart classification of the powder) to the characteristic aerosol cloud size distribution, for varied dissemination fluid shear stress parameters. The experimental results will contribute to the understanding of the relationship between intrinsic inter-particulate cohesion properties fundamental to resulting aerosol cloud characteristics, and provide a more comprehensive aerosol cloud characterization for practical combinations of surface energy and dissemination shear force.

2. METHOD

2.1 Overview

An experimental study to obtain a relationship between dry powder surface properties and aerosol cloud characteristics was performed. This study focused on a primary surface property, surface energy, which affects the deagglomeration and subsequent coagulation of energetically disseminated feed particles. The approach varied (a) surface energy and (b) dissemination parameters, and the subsequent aerosol cloud characteristics were measured.

The experiment consisted of disseminating TiO_2 powders which have been treated with various coatings to affect their surface energy. The surface energies of the bulk powder with various coatings were classically determined by measuring the contact angle of droplets of various liquids placed on pressed pellets of the various bulk materials. These powders were then disseminated into an interrogating chamber by a controlled dissemination method, (standardized entrainment tube, known as an "SRI-nozzle"- Figure 1) where the primary dissemination mechanism of shear stress was varied through a range representative of typical disseminations from threat devices. This shear stress was controlled by total pressure input to the SRI nozzle, and quantified by CFD modeling. The resulting aerosol cloud properties were characterized using appropriate instrumentation for the particle size range. Three distinct efforts were required to accomplish this study: powder preparation and surface energy measurement, CFD modeling of the SRI nozzle to quantify shear stress as a function of supply pressure, and finally the aerosol dissemination and subsequent cloud characterization through the range of powder surface energies and shear stresses.

Figure 1. SRI-nozzle used to disseminate the test powders.

2.2 Test powder preparation and surface energy

Coatings play a vital role in the prevention of agglomeration, the control of particle size, and the dissemination properties of a given powder in aerosolized form. TiO_2, like other oxides of aluminum, zirconium, and nickel is amenable to surface modification with organosilanes. These surface modifiers can create either a hydrophobic surface or hydrophilic surface, depending upon the chosen organosilane.

Organosilanes contain hydrolyzable groups such as alkoxy, amine, or halogen functionalities. Upon hydrolysis of these groups, silanol groups (-SiOH) are formed which can subsequently condense with other silanol groups or hydroxyl groups on the surface of particles. Typically, condensation first occurs between silanol groups of adjacent organosilanes producing oligomers. The oligomers subsequently form hydrogen bonds with the hydroxyl groups that are present on a substrate surface or particle. Covalent bonds between the oligomer and substrate are finally formed via further condensation and curing.

Surface modifications of titanium dioxide were achieved using two different organosilanes. These included tridecafluoro-1,1,2,2-tetrahydroctyltrimethoxysilane (TDFTMS), and diphenyldimethoxysilane (DPDMS) (Gelest, Morrisville, PA). Coating was achieved using a Gemco slant-cone blender (0.5 ft^3

working capacity) equipped with an airless liquid injection system and agitator (Gemco, Middlesex, NJ). The liquid injection system was used to introduce the dissolved silane during blending. Millennium TiO_2, grade RCL-9, was used as the substrate for all coating experiments. RCL-9 was chosen for its high purity and absence of organic coating.

In addition to the modifications involving the hydrophobic organosilanes, trimethylolethane (TME), a coating that imparted a degree of hydrophilicity was explored. TME is an organic polyols which is commonly used in the surface modification of pigments. The presence of the three hydroxyl groups allows TME to covalently bond to the substrate particle via condensation and curing. Upon completion of bonding, the presence of the free hydroxyl groups imparts a degree of hydrophilicity to the particle surface, which is in contrast to the more hydrophobic organosilane coatings.

2.3 Shear stress quantification using CFD

A CFD model of the SRI nozzle was created using ANSYS CFX version 13.0. The solid geometry was modeled with ANSYS DesignModeler and meshed with ANSYS ICEM Mesh Generation Software. Inflation layers were added to the walls of the SRI nozzle in order to properly depict the near-wall boundary layer. Further mesh face sizing was added, specifically at the nozzle exit. In total, the mesh had 571,947 nodes and 2,016,574 elements.

Seven CFX analyses were completed for the seven different gauge pressures corresponding to the 5, 10, 20, 25, 30, 50, and 60 psig experimental test matrix. The solutions were run at 0.1 time step for 10 steps, 1 time step for 10 steps, 10 time steps for 30 steps, and finally 100 time steps until acceptable convergence. Solutions converged to an average RMS residual value of 2.96E-5 at 157 time steps

Post processing of the computational runs included, velocity, pressure, and temperature data along four consecutive lines, perpendicular to the nozzle axis. The lines were of distance 0.05, 0.2, 0.35, and 0.5 inch away from the nozzle exit (Figure 2). The data was then used to determine the fluid shear stress corresponding to the SRI nozzle experimental pressure settings.

A second commercial CFD code, FloEFD version 9.0 (Mentor Graphics), was also used to model the flow field of the disseminator. Although the CFX solutions were used as the prime flow field and subsequent stress field analysis, the second independent analysis was used as a confidence check.

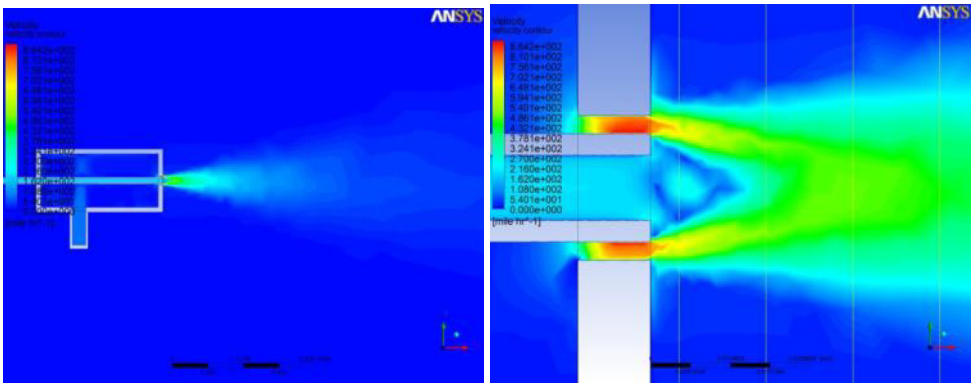

Figure 2. CFD modeling of the SRI-nozzle. The enlarged view shows vertical lines where the flow field data was pulled to determine the fluid shear stress.

2.4 Aerosol cloud characterization

The SRI disseminating device shown in Figure 1 operates by supplying pressure to a cylindrical shell which surrounds an entrainment tube. Pressurized air escapes the shell through an annular gap around the

entrainment tube. The low pressure created by the escaping air entrains a second flow through a tube which in turn aspirates powder stock. As the entrained powder stock passes through the primary air escaping the shell via the annular gap, it is deagglomerated by the shear stress imparted by the velocity gradient and turbulence in this "two-fluid" jet. The supply pressure to the shell can be varied to provide a range of dissemination effects. Normally the SRI-nozzle is operated at pressures sufficient to provide sonic velocity in the annual gap, but for this study the pressure ranged from far below that pressure to well above it. The SRI nozzle was chosen for this study as it has been used as a recognized standard for the study of floc deagglomeration for several decades [2]; therefore, there is a great deal of experience and published data to guide our study. Furthermore, the dissemination parameter of shear stress is easy to vary (via the total pressure input) and the geometry is simple, facilitating the CFD modeling of the two-fluid jet which is our method of quantifying the shear stress. In this study, the SRI nozzle was positioned at a corner of our large, cube-shaped 70-cubic meter chamber which was equipped with air mixing fans. An aerodynamic particle sizer (TSI-APS3321) was positioned in the center of this chamber and continually sampled the air. The air in the chamber was cleaned via a large HEPA filtrations system to prove a very low particle background. When the particle background was sufficiently low, the test powder was disseminated by the SRI-nozzle, (taking care to feed the powder at a rate well below the maximum recommended for the SRI-nozzle) at a selected pressure into the center of the chamber where it was mixed and subsequently sampled by the APS. The density of the TiO_2 is much greater than unity; therefore the APS must invoke a "stokes-correction" in the determination of aerodynamic diameter. This limits its upper range of operation to about 15 μm. The initial results suggested that additional data in the large particle size range beyond the capability of the APS could provide useful insight. Therefore a selected case was measured utilizing a laser diffraction sizer (Sympatek). These measurements were performed by disseminating the powders through the interrogating path of the Sympatek, drawing the resulting cloud into the inlet of a large wind tunnel to prevent it from remaining in the interrogation area and consequently skewing results.

3. RESULTS AND DISCUSSION

3.1 Surface energy measurements

Contact angle and surface energy measurements were determined for all powders using a Future Digital Scientific Corporation (Garden City, NY) OCA 15 contact angle goniometer. Contact angle is the measurement at which a given liquid meets a solid surface. Typically, the contact angle of a water droplet is used on a solid surface that is flat. Contact angle measurements provide a means of determining the hydrophobicity of a given solid surface. A liquid water droplet will for example spread onto a hydrophilic solid surface and the contact angle will be minimal. Conversely, if the solid surface is hydrophobic, the liquid droplet will minimize its interaction with the solid surface and the contact angle will be in the range of 90 to 150 degrees. Hence, contact angle measurements are pertinent to studying the integrity of powder coatings used in this study since the coatings will impact the contact angle at which a given liquid adheres to the powder surface.

Contact angle measurements also provide a means of determining the surface energy of a given solid if the surface tension of the liquid is known. The surface tension of a liquid, in common terms, is the force that holds a liquid together. It is proportional to the strength of the interactions between the molecules that make up the liquid. In the absence of other forces, these intermolecular interactions cause the liquid to form a droplet; however, if a droplet with a given surface tension comes into contact with a solid surface, the energy of the solid surface will interact with the liquid droplet. The energy of the solid surface will impact the angle at which the droplet adheres to the solid surface. If the surface energy of the solid is stronger than the surface tension energy of the liquid droplet, the energy of the solid surface will overcome the surface tension forces within the liquid and decrease the contact angle of that liquid on the

solid surface. Conversely, if the surface energy of the solid is less than the surface tension energy of the liquid droplet, the contact angle will not be altered, or perhaps minimally altered.

For the contact angle measurements made on the coated powders described in this study, the Owens-Wendt-Rabel and Kaelble (OWRK) method was used to determine the surface energy. This method describes the polar interactions between solids and liquids and requires the determination of contact angle for two or more liquids on a given surface. Water, ethanol, n-hexane, and tetrahydrofuran were chosen as the solvents used in the OWRK calculations. The experimental results for the contact angle and surface energy measurements for the various solvents and coated powders are provided in Table 1.

Table 1: Surface Energy measurements of TiO_2 with various coatings

Powder	Water Contact Angle	Ethanol Contact Angle	n-Hexane Contact Angle	Tetrahydrofuran Contact Angle	Surface Energy (mN/m)
Uncoated TiO_2	36.3°	38.6°	16.7°	45.8°	56.69
TME Coated TiO_2	75.3°	65.8°	20.0°	68.9°	24.18
TDFTMS TiO_2	111.1°	94.7°	21.6°	61.3°	13.18
DPDMS TiO_2	116.5°	96.7°	65.9°	40.0°	11.05

As expected, the DPDMS and TDFTMS coated materials have the lowest surface energies. TME coating is more hydrophilic than DPDMS and TDFTMS, therefore it has a higher surface energy, with the uncoated TiO_2 having the highest.

3.2 Shear stress quantification

The shear stress correlation to the SRI nozzle total pressure supply was done through modeling of the disseminating jet through CFD as describe in the Methodology section. The accuracy of the flow field modeling is hard to verify without experimental data; however, we did perform two independent models: ANSYS CFX, and Mentor Graphics FloEFD. Though there were differences in the flow details, probably due to differences in computational grid refinement, the general results were in agreement. The results from the CFX analysis were used in the determination of the fluid shear stress correlation to experimental SRI nozzle pressure parameters.

The shear stress (τ) imparted by the dissemination process that is responsible for deagglomerating the flocs of bulk powder is comprised of a velocity gradient effect and a turbulent energy effect.

$$\tau = \mu \frac{\partial u}{\partial y} - \rho \overline{u'} \overline{v'}$$

The velocity gradient (first term on the left hand side of the above equation) and turbulent shear (second term) were determined from the computed velocity, pressure, and temperature values at various distances from the nozzle exit. This task was much more difficult than anticipated, as we were a bit naïve about the significance of the turbulent shear and the uncertainty in the proper approximation model using standard commercial codes. The velocity gradient at selected axial distances from the nozzle was used to calculate the average and maximum fluid shear stresses from the CFD flow field data and are shown in Figure 3. The value of the maximum shear stress at station 0.35 –inch axial distance seems to be the best representation of the shear stress experience by the flocs, based on the path they take through the jet which we approximate by the velocity vectors originating from the entrainment tube. In addition the turbulent kinetic energy was computed (Figure 4), however it was not included in the total shear stress characterization at this time. This is an important part of accurate quantification of the stress field and should be included in follow-on work. With the turbulent stress component not included in the analysis at

this time, the CFD simulation results in a correlation between input pressure to the SRI-nozzle and approximate shear stress experienced by the bulk powder flocs as they pass through the nozzle and de-agglomerate.

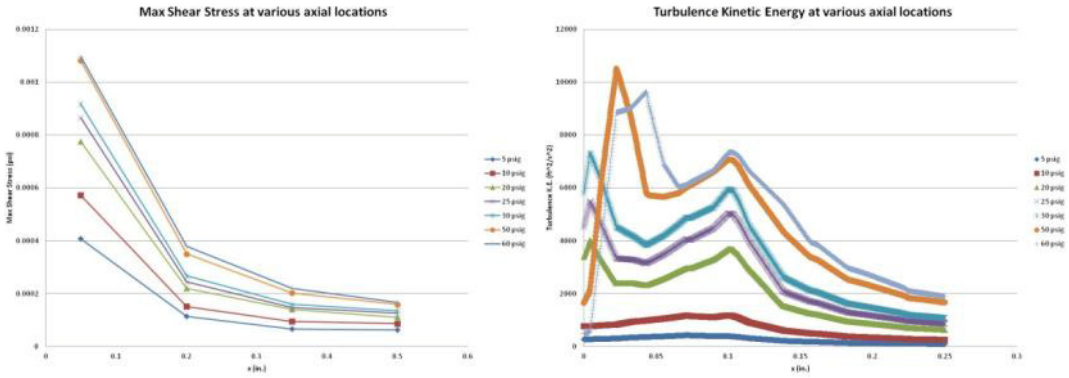

Figures 3 and 4. Maximum shear stress and turbulent kinetic energy at various axial distances from nozzle exit, for the range of nozzle operating pressures.

3.3 Aerosol size distribution as a function of powder surface energy and dissemination shear stress

The four different powders representing a range of surface energies were dispersed into the interrogating chamber over a range of disseminating shear stresses, resulting in a corresponding particle size spectrum. The measured particle size spectrum over the range of surface energy and dissemination shear stress is shown in Figure 5 and is primarily deduced from APS data with overlapping data for select cases from a laser diffraction instrument. This figure depicts all the experimental trials and shows the evolution of the distributions as the shear stress and surface energies are varied and the mass concentration is normalized by the maximum concentration found in a size bin below 10 µm. Note that these size distributions are expressed in mass concentration versus aerodynamic diameter. Since our test powders have a density greater than unity, the actual physical size of these particles should be found by dividing the aerodynamic diameter (AD) by the square root of the actual density. The size distributions for the extremes of the test parameter combinations (the highest shear/lowest surface energy, lowest shear/lowest surface energy) are shown in Figure 6. In general the resulting size distributions follow an expected trend, in that the size attributed to the primary mode is smaller for higher disseminating stresses and lower surface energies, growing as those parameters decrease and increase respectively. The first mode in general lies around 1-µm AD, which is to be expected for a feed stock material that has a submicron native physical particle size as our test powders of TiO_2 (with a density of 4g/cc, and native size of 0.250 µm). As explained by Whitham and Gates [3], the van der Waals forces ordinarily cannot be overcome by aerodynamic drag (which corresponds to aerodynamic shear stress) for flocs of particles smaller than 1 µm AD, meaning that they would not be broken up into smaller particles by shear force alone. Therefore it was expected that differences in the size distribution would be more dramatic in the larger size range where shear force is the major deagglomeration mechanism and differences in surface energy would be dramatically obvious, but this is not really the case. As evident in Figure 5, the mass concentration contribution decreases to less than 10% of total mass by the time the distribution reaches 2 µm for all test cases. At the other end of the measured size spectrum, there are a few flocs that escape effective deagglomeration, resulting in a rise in mass contribution due to large particles. While this rise is very noticeable, generally starting in the 7 µm range, it is important to remember that the mass is attributable to relatively small number of particles when compared to the first mode. It is also notable that the laser diffraction trials did not resolve this large particle aspect except in the case of high surface energy powders, probably due to its reliance on optical concentration and the relatively few particles in this size range. Nevertheless, the size trend in this area follows expectations in that the low shear stress/high surface energy case produces more

mass in large particle sizes than that produced by the higher shear stress/lower surface energy combinations.

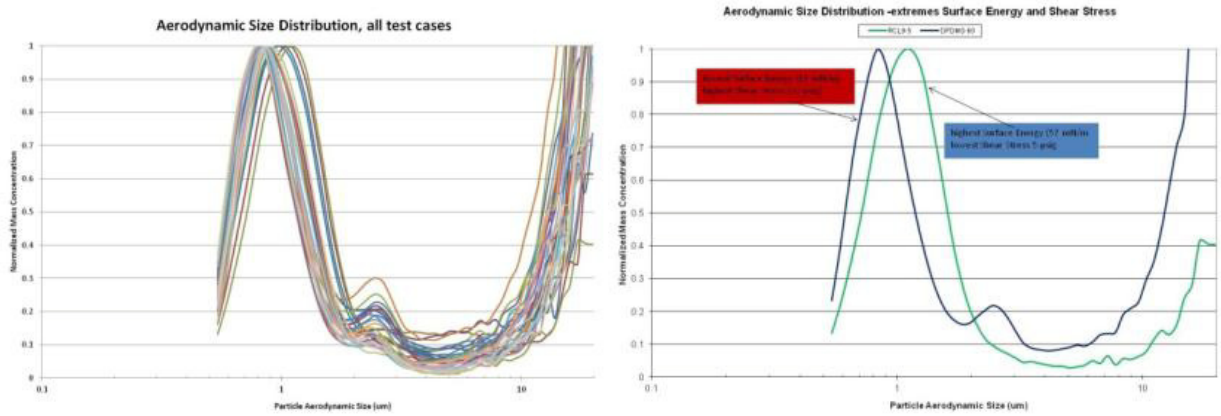

Figures 5 and 6. The aerodynamic size distribution for a range of surface energies and dissemination pressures.

The most surprising result is noticed in the occurrence of a second mode around 2.5 µm. This effect is seen for all treated powders implying that this mode arises as a result of increasing shear stress, rather than a reliance on particle surface energy. This effect is most prominent in during the 25 psig dissemination trials. There is no obvious explanation for this occurrence and may be of further theoretical interest.

The aerodynamic particle size spectrum is a critical input parameter to the "source-term" used in modeling aerosol plume propagation. Current algorithms assume a log-normal distribution and use the Mass Median Aerodynamic Diameter and geometric standard deviation as the inputs to determine cloud propagation. The differences in those two values for the range of spectrums observed in this experimental study would not likely produce a noticeable difference in cloud propagation. However the "fresh" cloud spectrum observed is not purely log-normal and a "look-up table" approach may be more appropriate for certain applications. The growth of the second mode around 2.5 µm AD may make a noticeable difference in this case, though after the aerosol ages for a few minutes it may eventually resemble the classical log-normal distribution. These speculations by the authors should be confirmed by follow-on work involving a few simple runs of the propagation models using the extreme curves of Figure 5.

4. CONCLUSIONS

Laboratory experiments were performed to explore a relation between an aerosol producing devices' dissemination shear force and the resulting aerosol size distribution as a function of the bulk powder surface energy. Test particles of TiO_2, which have a very small (0.250 µm) native particle size, were treated to achieve a range of surface energies. These powders were disseminated using a two-fluid entrainment nozzle which enabled variation in the deagglomerating shear stress. The resulting aerosol size spectrum was then observed as a function of these two parameters. CFD modeling of the dissemination device was used to quantify the shear stress imparted by the disseminator.

The variation in particle size spectrum as a function of surface energy and shear force varied as expected. The first mode of the spectrum shifted to a larger size as the shear stress was decreased and the surface energy of the particles was increased. The large particle fraction follows this same trend. Also, an unexpected second mode growth was noticed as the shear stress was increased, independent of the surface energy. This may be a significant characteristic of aerosols clouds disseminated from high energetic devices. Therefore, toward the goal of this study, it is possible to relate this type of source term input to material surface energy and the energy by which it is disseminated. However the differences in the

spectrum as these parameters were varied were disappointingly small for our choice of test powder and from a practical standpoint this relationship may not be significant to affect models of cloud propagation.

Interesting follow-on efforts that may be pursued involve verifying the CFD results against experimental data, some of which may already exist.[2] Also, an understanding of the mechanism responsible for the second mode growth as the disseminating shear is increased may be a fruitful pursuit if it is a characteristic of energetic dissemination. Finally, since this study focused on the deagglomeration of very small particles, it may be useful to explore the same effect for larger particles for which the van der Waals forces are less significant. This extension of the experimental powder stock size range may yield the dramatic changes in size distribution that would be of significance to cloud propagation modeling.

5. ACKNOWLEDGEMENTS

The authors would like to thank Mr. Robert Doherty, Mr. Paul Deluca, and Mr. Mike Williamson for their quick response in performing the laser diffraction sizing measurements, Mr. Clayton Moury for preparing the CFD solid geometry model, Dr. Arun Ranade for his guidance and advice, and finally, Mr. Larry Bickford for his encouragement and his assistance in forming the study team.

WORK CITED

[1] Delacy et al. ECBC-TR-835.
[2] Calabrese, R. and Ranade, M.B. Pneumatic Nozzle Dissemination of Powders into Air, CRDEC SSP91-2, 1993.
[3] Witham, C. and Gates, R. Dry Dispersion with Sonic Velocity Nozzles, Dissemination Techniques for Aerosols (Edited by Adarsh Deepak, 1983).

Decontamination of single spores and bioclusters using UV-C and simulated sunlight

Jana Kesavan, Deborah Schepers, Jerold Bottiger, and Jason Edmonds
Edgewood Chemical Biological Center, Research & Technology Directorate, 5183 Blackhawk Rd., Aberdeen Proving Ground, MD 21010

ABSTRACT

The aerosols released by sneezing and coughing as well as aerosols generated by crude methods produce bioaerosol clusters and the outer layer of a cluster protects the organisms in the center. Almost all the previous studies that evaluated the kill effect of UV-C and sunlight were conducted with single spores on surfaces and in air, and the effect of UV-C and sunlight on killing of all the organisms in a cluster has not been studied by researchers. Therefore, this study evaluated the effect of UV-C and simulated sunlight on killing organisms in different size clusters and single spores of *Bacillus atrophaeous* (Bg). The results show that single spores are decontaminated faster than the clusters. The outer layers of clusters protect the organisms in the center and a stronger and longer UV exposure is needed to decontaminate all the organisms in a clusters. The kill curve predictions based on previous single spore tests may not be applicable for biocluster decontamination; therefore, decontamination of clusters needs to use information from cluster studies.

1. INTRODUCTION

Bioaerosols are a big concern because of the potential for terrorist and state sponsored releases as well as natural disease epidemics. Germicidal UV lights are increasingly used to disinfect the air and surfaces because of the ease of use of these UV lights in indoor settings. The sunlight is relied upon for disinfection of outdoor contamination because of its germicidal effects.

It is important to understand the UV wavelength regions. The lower wavelength of the UV region is 10 nm and the upper wavelength limit of the UV is 380 nm (or 400 nm), where human vision starts. The far UV or vacuum UV (< 190 nm) has little relevance to inactivation of organisms since it does not reach the earth. The remaining UV region is divided into three regions, UV-A, UV-B, and UV-C, as shown in Table 1. The boundaries of UV-A, UV-B, and UV-C vary between authors depending on whether the division was based on health effects or illumination. In general, the health based wavelengths are defined so that UV-B and UVC are germicidal and UV-A is non-germicidal. The UV-A is emitted from tanning lamps and it covers the wavelengths between 320 and 380 (or 400 nm), UV-B covers the wavelengths between 290 and 320, and UV-C covers the wavelengths between 190 and 290 nm. The alternate definition by International Commission on Illumination defines UV-B as having wavelengths between 280 – 315 nm.

Table 1. Wavelength Ranges of UV Regions vacuum UV, UV-C, UV-B, UV-A

Region	Wavelengths, nm
Vacuum UV	10 – 190
UV-C	190 - 290
UV-B	290 – 320
UV-A	320 - 380

Even though the sunlight has substantial amounts of UV components, only UV wavelengths longer than 290 nm reach the earth due to the ozone filtration. The UV-A and UV-B parts of the sunlight are less efficient in killing organisms compared to the germicidal UV-C lamps. The UV light kills organisms by chemically modifying their genetic materials (DNA and RNA).[1]

Researchers also have been studying cell death due to solar exposure since solar UV radiation disinfects organisms in the outdoor environment. In addition to direct irradiation, highly reflecting environment such as white sand and fresh snow can significantly increase the UV irradiance in the environment. The effect of solar radiation in killing influenza viruses is supported by the correlation found in Brazil that showed increased influenza hospital admissions during burning season where the smoke blocked the UV irradiation and reduced the inactivation of viruses in the air.[2]

UV-C lights have been proposed as supplemental control in healthcare facilities due to its low cost, ease of application, and potential efficiencies. UV-C lamps are also used in enclosed mechanical ventilation system ducts, enclosed in locally recirculating units, and in open configuration in a room. One study [3] showed that UV lights installed in office ventilation systems reduced 99% of microbial and endotoxin concentrations on irradiated surfaces within the ventilation systems and reduced respiratory and musculoskeletal symptoms. Other studies [4,5] showed that upper room (ceiling) UV light significantly reduced the concentration of culturable bacteria in the lower room.

Almost all the previous studies of evaluating the kill effect of UV-C and sunlight were conducted with single spores on surfaces and in the air.[6,7] The aerosols released by sneezing and coughing as well as aerosols generated by crude methods produce bioaerosol clusters and the outer layer of a cluster of spores protects the organisms in the center. The effect of UV-C and sunlight on killing of all the organisms in a cluster has not been studied by researchers. Therefore, this study evaluated the effect of UV-C and simulated sunlight on killing organisms in different size clusters and single spores.

2. TEST METHODOLOGY

2.1 Equipment

Single and clustered *Bacillus atrophaeus* (Bg) spores were used in this test. A combined UV-A and UV-B light was used to simulate the sunlight to determine the decontamination in the outdoor settings. The UV-C light was used to simulate the indoor decontamination. Single spore Bg exposed and unexposed to UV were examined using the SEM to determine any change in shape or size.

An Ink Jet Aerosol Generator (IJAG) was used to generate clusters and single spores for the surface disinfection studies. A collision nebulizer was used to generate single spores for the aerosol disinfection studies and a SonoTek aerosol generator was used to generate clusters for the aerosol testing. A short description of each instrument is given below.

Ink Jet Aerosol Generator (IJAG)
The IJAG (manufactured by U.S. Army, ECBC) was used to generate dried clusters and un-dried primary droplets. A 12-nozzle ink jet cartridge (HP 51612A), purchased empty, was filled with a slurry of clean water and Bg. Droplets were fired downward as a 65 μm primary droplet. With the heated drying tube turned off the primary droplets exited the IJAG and was collected for the single spore surface studies. With the heated drying tube turned on the water from the primary droplets evaporated leaving aggregate residue particles. These residue particles were collected on filters for the cluster testing.

Since the size of the primary ink jet droplet is fixed, ≈ 65 μm diameter, the size of the residue particle depends only on the concentration of the slurry. We have prepared different concentrations of slurries to produce different size monodisperse particles and the IJAG is capable of producing monodisperse particles at a rate of 1–500 particles/s.

Collison Nebulizer
A collison nebulizer (BGI Inc., Waltham, MA) was used to generate single spore Bg for the aerosol tests. The nebulizer was connected to a compressed air source that exited from small holes inside the nebulizer at high velocity. The low pressure created in the exit region caused liquid to be drawn from the bottom of the nebulizer through a second tube due to Bernoulli Effect. The liquid exited the tube as a thin filament that was stretched out as it accelerated in the air stream until it broke into droplets. The spray stream was directed onto the wall where larger droplets were impacted and removed from the air and the small particles were carried out of the nebulizer.

SonoTek Aerosol Generator
A Sono-Tek ultrasonic atomizing nozzle (Sono-Tek Corporation, Milton, NY) was used to produce bioclusters that were dried to leave an aerosol of residue material particles for the cluster aerosol testing. The final particle size depended on the concentration of material in the feed liquid and the characteristic size of the Sono-Tek droplet. The rate of aerosol generation depended on the rate at which the mixture fluid is fed to the Sono-Tek nozzle. Five Sono-Tek models are available with number mean diameters ranging from 23 to 70 μm (120 kHz to 25 kHz operating frequencies) and flow rates from a few microliters per second to about 6 gallons per hour. In this test, the 120 kHz model, with a liquid flow rate of 170 μL/min was used in our laboratory to make the cluster aerosols.

2.2 Surface exposure test methodology

This experiment was conducted to determine the effect of UV-C and simulated sunlight on single spore and clustered bacteria on surfaces. Single spore and clustered bacteria were deposited on polycarbonate membrane filters for the UV exposure. Single spores were deposited on membrane filters by pipetting a bacteria suspension or using the primary droplets from the IJAG onto membrane filters. A pump pulled air through the filters to dry the particles before UV exposure.

IJAG was also used to generate different size bacteria clusters for this experiment. In this case the IJAG heating tube was turned on to evaporate the water from the primary droplets and to produce the clusters. The clusters generated by the IJAG were deposited on the filters by the sampling process. The filter was moved under the IJAG output to prevent particles falling on top of each other and shielding the UV exposure to the clusters on the bottom.

Filters with the organisms were removed gently from the filter holders and placed on cardboard.The filter edges were pinned to the cardboard to prevent the filters from curling during the UV exposure. The test filters were placed inside the exposure chamber on the bottom as shown in Figure 1 and exposed to either UV-C or simulated sunlight for different lengths of time. The filters were removed from the exposure chamber after the irradiation, and the bacteria were extracted using a validated recovery procedure. This procedure consists of putting the filters in to 50 mL centrifuge tubes with 20 mL of phosphate buffered saline with 0.01% triton X, and vortexing on a multitube vortexer (VWR Scientific, Radnor, PA) for 5 min. One hundred micro liters of the solution was plated in triplicate for the determination of culturable fraction of the organisms. The survival fraction was determined by comparing the test filter results to reference filter results that were not exposed to UV irradiation. The UV flux at the location of the filters was measured by a UV meter (Model UV-3718-4 Radiometric Detector, Gigahertz-Optik, Newburyport, MA). The UV dose or fluence was calculated by multiplying the flux by the exposure time.

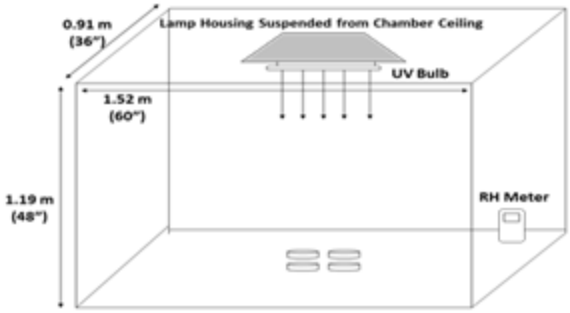

Figure 1. Surface exposure chamber

2.3 Aerosol exposure test methodology

This test was conducted to determine the effect of UV-C and simulated sunlight on single and clustered Bg aerosols. Aerosol experiments were conducted in a 0.14 m^3 chamber as shown in Figure 2. Single spore bacteria were generated with a collison nebulizer and bacteria clusters were generated with a SonoTek aerosol generator. Experiments were conducted with the UV light on and off to determine the bacteria kill due to the UV exposure. One minute air samples were taken periodically on gel filters and the filters were dissolved and the samples were plated to determine the culturable quantity.

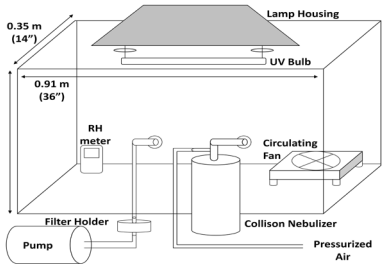

Figure 2: UV Exposure Chamber

3. RESULTS AND DISCUSSION

The single and clustered Bg spores (2.7 and 4.5 µm) on surfaces exposed to UV-C light is shown in Figure 3. The single spores are killed faster compared to the clusters and the 2.7 and 4.5 µm clusters have similar overall kill curves (Figure 3A). Evaluating the first 1000 J/m^2 exposure shows that 4.5 µm particles have a slower kill compared to the 2.7 µm particles (Figure 3B).

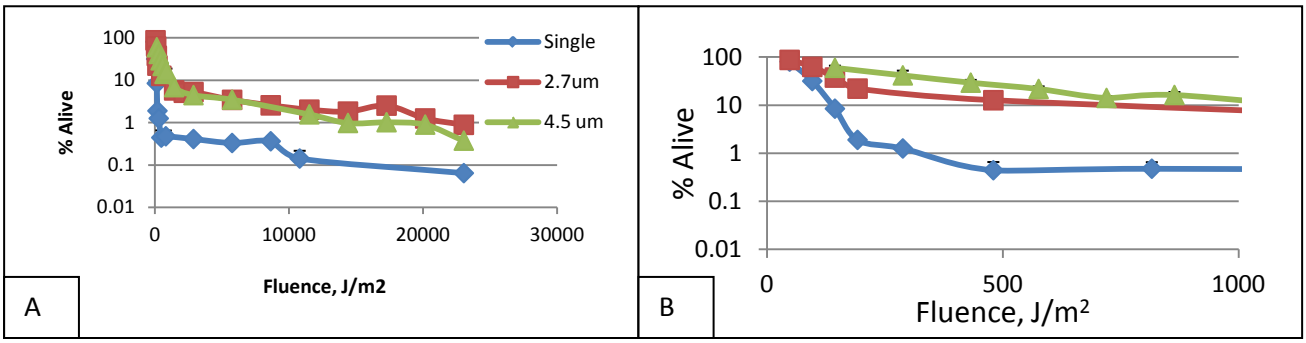

Figure 3. The UV-C kill curve for the single and clustered Bg (2.7 and 4.5 µm) deposited on filter surfaces. (A) Kill curve for fluence up to 30,000 J/m^2. (B) Kill curve for fluence up to 1,000 J/m^2.

The single and 2.7 µm clustered bacteria spore aerosols exposed to UV-C light is shown in Figure 4. The graph shows that single spores are killed faster than the organisms in the 2.7 µm clusters.

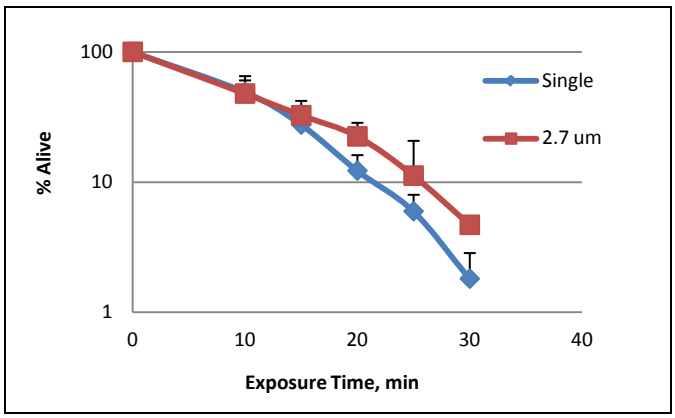

Figure 4. The UV-C kill curve for aerosolized single spore and 2.7 µm bioclusters

The percent alive results of single and 2.7 µm clustered bacteria spores on surfaces exposed to simulated sunlight is shown in Figure 5. The results show that at some time points, single spores are killed significantly higher compared to the clusters.

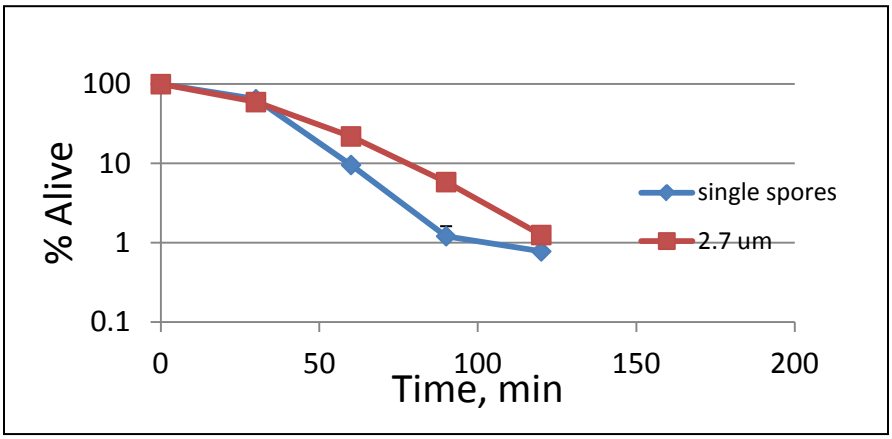

Figure 5. Simulated sunlight kill curve for the single and 2.7 µm clustered Bg on surfaces.

The UV exposed and unexposed single spores on surfaces were observed using the SEM. The SEM pictures of UV exposed and unexposed Bg showed no observable difference in shape and size. This experiment was conducted with the simulated sunlight and more experiments need to be conducted with UV-C to determine any changes due to UV-C.

4. CONCLUSION

The results of UV-C and simulated sunlight exposure to single and clustered Bg on surfaces and in air show that single spores are decontaminated faster than the clusters. The outer layer of clusters protects the organisms in the center and a stronger and longer UV exposure is needed to decontaminate clusters. The kill curve predictions based on previous single spore tests may not be applicable for biocluster decontamination; therefore, decontamination of clusters must use information from cluster studies.

WORK CITED

[1] Lytle, C. D., and Sagripanti, J-L. 2005. *J. Virol*. Vol. 79. No. 22. 14244-14252.
[2] Mims, F. M. 2005. *Environ. Health Perspect.* 113(12), A806-A807.
[3] Menzies, D. et al. 2003. *Lancet*. 362:1785-91.
[4] Ko, G. et al. 2002. *Environ. Health Perspect*. 110(1):95-101.
[5] Xu, P. et al. *Atmos. Environ.* 37 (2003) 405–419.
[6] King, B. et al. 2011. *Aerosol Sci. Tech.* 45: 1-9.
[7] Coohill, T.P. and Sagripanti, J-L. 2009. *Photochem. Photobiol*. 85: 1043-1052.

Peptide selectivity study on the Cu_2O surface

Jerry Cabalo
Edgewood Chemical Biological Center, Research & Technology Directorate, 5183 Blackhawk Rd., Aberdeen Proving Ground, MD 21010

ABSTRACT

It has been observed that many inorganic materials such as Ag, Au, GaAs, ZnO, ZnS, and Cu_2O are capable of selectively binding peptide sequences based on the content of particular amino acids or amino acid sequences. The ability of some metal oxides to selectively bind materials also translates into interesting catalytic properties, such as the potential of Cu_2O to reduce CO_2 to CH_3OH. The objective of this study is to understand some of the fundamental mechanisms that govern the selective binding between these biological molecules and an inorganic substrate. Geometry of the inorganic surface and the peptide, surface defects, and formation of chemical bonds play key roles in the binding event. We utilized classical dynamics using the Forcite module of Materials Studio in our attempt to understand the influences of these processes on the selective binding. Classical molecular dynamics were used to examine the dynamic behavior of several amino acids and peptides placed near a model Cu_2O surface. To capture the behavior of the inorganic metal oxide surface, a modified DREIDING forcefield was used. DFT calculations using the B3LYP functional and the LANL2DZ basis set were used to determine unparameterized quantities such as the Cu-O bond length, Cu-O-Cu bond angles, and force constants. Partial charges were assigned with DFT and the Mullekin population analysis for the metal oxide surface and the organic molecules. Molecular dynamics (MD) runs of up to 100 ps were run with 300 K and 373 K temperature settings with the NVT ensemble with the Andersen thermostat, and timesteps of 0.5 fs for glycine, phenylalanine, arginine, and peptides of Gly-Gly, Gly-Gly-Gly, Phe-Phe, Phe-Phe-Phe, Arg-Arg, and Arg-Arg-Arg. Relaxation runs were performed with geometry optimizations followed by short MD runs with the Velocity Scale thermostat. For the longer runs, distances between analyte molecules were tracked. The MD simulations did not show a clear pattern of affinity for the Arginine containing peptides as is observed experimentally. It was noted that DFT calculations show a weak positive charge that is nearly neutral for the singly bonded Cu atoms on the surface. It is likely chemistry or charge transfer can occur on this site, and the purely classical MD that considers only electrostatic interactions cannot take such interactions into account.

1. INTRODUCTION

Many inorganic materials such as Ag, Au, GaAs, ZnO, ZnS, and Cu_2O are capable of selectively binding particular amino acids or amino acid sequences.[1,2] The opposite is also true where a particular inorganic substrate repels a given amino acid, such that some of the materials could be used as anti-clogging agents in microfluidics. It has also been observed that some organisms use particular proteins or peptides that are adept at selectively binding particular metals and participating in bio-mineralization processes.[1,3,4] Materials formed from bio-mineralization processes possess many desirable properties because they inherit nano-scale order from the biological systems they originate from. The ability of some metal oxides to selectively bind materials also translates into interesting catalytic properties, such as the potential of Cu_2O to reduce CO_2 to CH_3OH.[5-9] An understanding of the underlying mechanisms governing this selective binding or repulsion between metal/metal oxides and peptides can potentially impact a number of technology areas that are of interest to the Army. Although a number of inorganic metal oxide materials exhibit selective binding, Cu_2O was the focus due to its catalytic [5-9] and semiconductor [10,11] properties.

A nano-structured surface appears to provide much of the selective adhesion properties of Cu_2O. A combined experimental and theoretical study by Baneyx [3] that used MD simulations of dodecameric peptides in solution showed similarities in shape to molecules that selectively bind to ZnO and Cu_2O surfaces. This makes sense if one considers the interaction between a molecule on the surface and the substrate as a "lock and key" interaction, where the selectivity is driven by interaction between complementary shapes. The objective of this study is to understand some of the fundamental mechanisms that govern the selective binding between these biological molecules and an inorganic substrate, and the hypothesis is that the interaction is driven by matching of the molecular geometry to nanostructures on the inorganic substrate.

2. METHODS

We modeled the (1,1,1) surface of Cu_2O with the density functional theory (DFT) electronic structure code DMOL3, a generalized gradient approximation (GGA) type PBE functional, and a triple zeta basis set with polarization functions. First, the unit cell of the Cu_2O crystal was energy optimized with DMOL3. A surface model was created by cleaving the unit cell on the (1,1,1) plane, and placing a vacuum slab 30 angstroms thick above the surface, and forming a 5 X 5 supercell that was seven surface layers thick. The bottom 4 layers were motion constrained to simulate the bulk crystal, and the top three layers were permitted to relax. Cleaving the crystal (Figure 1A) to form a surface created a number of vacancies, so that reoptimization of the surface, that is, relaxation, allowed the surface to rearrange in response to the presence of the surface.

The resulting surface, shown in Figure 1B and 1C, shows interesting nano-structure that would not be expected from the chemical formula. Unlike the surrounding O which have an average partial charge of -0.62e or Cu atoms which have an average partial charge of +0.27e, there are singly bound Cu atoms that have a partial charge of +0.046e, which is nearly neutral. The result is a regular pattern of pockets in the Cu_2O surface with a nearly neutral metal atom in the center of the pocket that is capable of participating in chemistry. It is this pattern that we attribute the selective binding capabilities of the material.

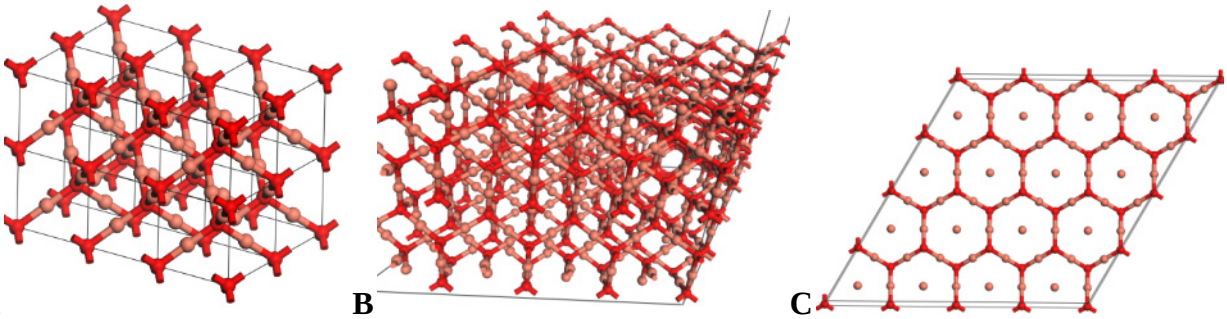

Figure 1. A) Bulk crystal structure of Cu_2O with 3-D boundary conditions, B) Surface model of the (1,1,1) crystal face of Cu_2O with 2-periodic boundary conditions, and C) Top view of B) with only the top layer visible. The active surface of this material consists of periodic hexagonal rings formed from six Cu atoms and six O atoms. A near neutrally charged copper atom lies at the center of each hexagonal ring.

The Cu_2O bulk and surface have a number of atom types that are not included in the standard force fields. From the DFT simulation, there are two atomic types each of oxygen and copper atoms. For oxygen, there is the standard atom type with sp^3 atomic orbital hybridization that has two molecular bonds and a -2 charge, and there is also a type that bonds to four different copper atoms and has tetrahedral geometry. For the copper, there is the atomic type that links the two different oxygen atoms, and at the surface of the metal oxide crystal, there is a copper ion bound to a single oxygen that sits in a hexagonal pocket formed by linked copper and oxygen atoms. Each of these atom "types" require parameterization in order to perform the MD simulations. To capture the behavior of the inorganic metal oxide surface, a modified

DREIDING forcefield was used. Several new atom types were added and the new equilibrium bond lengths, angles, and force constants were determined from DFT calculations using the B3LYP functional and the LANL2DZ basis set. Rigid scans of the potential energy surface (PES) were performed for both the Cu-O bond stretch and the O-Cu-O bond angle. The results were fitted with a third order polynomial, and an equilibrium bond length of 1.92 angstroms for the Cu-O bond and an equilibrium bond angle of 180 degrees resulted. The bond stretch force constant was determined to be 0.255 Hartree/Angstrom^2 and the angle bend force constant was determined to be 0.023 Hartree/radian^2. Partial charges were assigned with DFT and the Mullekin population analysis for the metal oxide surface and the organic molecules. For simulations treating water molecules explicitly, the Amorphous Cell module of Materials Studio was used, which populates a volume with molecules to a set density using a Monte Carlo approach.

Amino acids and peptides were first treated with DFT and geometry optimized with the PBE functional and the DNP basis wet within Materials Studio. Partial charges were assigned at this time. These structures were then imported into the models.

The first set of simulations utilized explicit representations of water molecules. Depending on the volume occupied by the amino acid or peptide, the Amorphous Cell code placed approximately 800 water molecules into the empty space within the model. Relaxation of the system first started with a geometry optimization of the system using the modified DREIDING forcefield. Short MD runs with 0.1 fs timesteps of up to 2 ps were performed with the Velocity Scale thermostat and the NVT ensembles were performed to fully relax the system, with the atom centered summation method for calculating non-bonding interactions. Production runs on the relaxed systems were performed with the Andersen thermostat for up to 50 ps and with 0.5 fs timesteps. Simulations were attempted with both Ewald and atom centered summation methods, although the Ewald summations did not complete for most of the systems that had water treated explicitly.

Additional simulations were performed where water was treated as a dielectric continuum. Systems without explicit water were relaxed in the same way as above, with an initial geometry optimization followed by a short dynamics run with the NVT ensemble and the Velocity Scale thermostat. Simulations were performed for longer timescales of up to 100 ps with 0.5 fs timesteps. The NVT ensemble, the Andersen thermostat, and temperatures of 300 K and 373 K were utilized. These were performed for glycine, phenylalanine, and arginine, and peptides of Gly-Gly, Gly-Gly-Gly, Phe-Phe, Phe-Phe-Phe, Arg-Arg, and Arg-Arg-Arg. These amino acides and peptides were selected to provide a comparison between molecules known to bind to the Cu_2O surface and peptides that would not bind as strongly. From the resulting trajectories, it was possible to track the molecule-surface distance to look for surface binding.

3. RESULTS AND DISCUSSION

The first results from modeling showed how critical correct parameterization and assignment of electric charge in the metal oxide are. Because only a few inorganic materials are parameterized in standard force fields, it is clear that a modified force field is necessary. Figure 2A shows the result of a failed simulation using the COMPASS forcefield, which is a consistent valence force field that also contains assigned charge. The result was a complete collapse of the metal oxide surface. A similar result was found when the partial charges were not assigned with a quantum mechanical calculation. Figure 2B shows the failed simulation of Arginine on the surface with explicitly treated water. When charge was assigned with the Qeq (an empirically based charge assignment algorithm) on the metal oxide substrate, the singly bound Cu atoms were no longer nearly neutral in charge. As a result, they became attracted to the negatively charged O atoms resulting in a large release of potential energy and a sharp rise in system temperature. The modified force field and quantum mechanically assigned charge resulted in a stable metal oxide model.

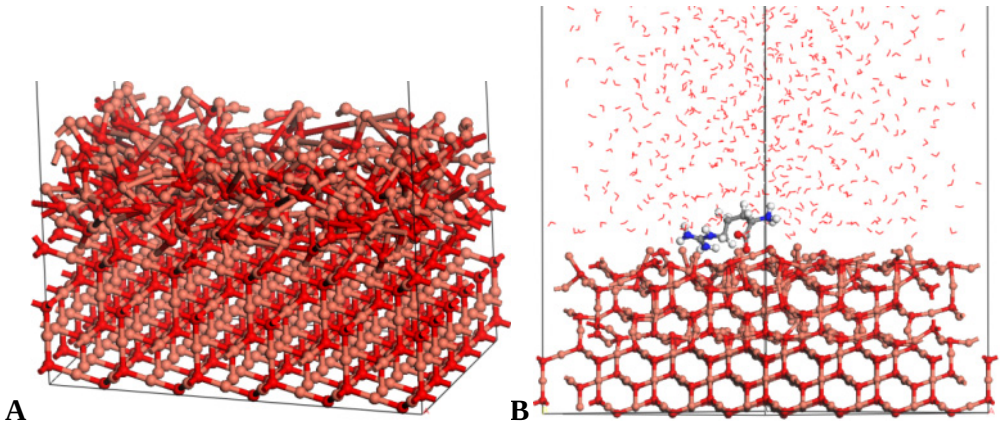

Figure 2. Results of poor parameterization of the MD model. A) Example of the collapse of the metal oxide crystal when an unsuitable force field is utilized. B) Result of a molecular dynamics simulation of arginine acting on a (1,1,1) Cu_2O surface with water molecules treated explicitly. An incorrect assignment of charge resulted in distortion of the surface structure.

Other issues became apparent in the course of the MD simulations. Many simulations were performed for various amino acids and peptides using explicit water molecules. When atom centered summation was used for the calculation of non-bonding interactions, no translational movement of either the water molecules or peptides was observed, only intramolecular vibrations. Increasing the temperature to induce movement did not result in translational motion. To understand this issue, a similar volume was filled with water molecules and a peptide molecule without the metal oxide surface. When the Ewald summation was utilized, translational motion was observed. When the atom centered summation was utilized, no noticeable translation motion was observed. Clearly, the method of calculating the intermolecular forces affects the possible translation motion. When Ewald sums were used with the system containing both explicit water molecules and the inorganic substrate, a random atom would have potential energy focused into it and a non-physical velocity introduced, and the simulation failed. The exact cause of this effect in the model was not determined within the Forcite/Materials Studio code, but a strong possibility is a scalability issue since the total model exceeded over 1000 atoms. To remedy this issue, other MD codes such as NAMD and LAMMPS were attempted, but the task of modifying the standard AMBER or CHARMM forcefields to accommodate the metal oxide did not complete.

To obtain results, the water was then modeled as a continuum with a dielectric constant of 88 rather than 1 with explicit water molecules. While this approach neglects the influence of water molecules and the shells of solvation, nevertheless, some useful observations were extracted. Below are plots of distance for the ends and midpoint of both Phe-Phe and Arg-Arg peptides from reference points on the Cu_2O substrate as a function of time at 300 K. Ewald sums were used to compute the intermolecular interactions. The results of these two simulations are in disagreement with the experimental observation that peptides containing the Arg-Arg sequence have enhanced affinity for the Cu_2O substrate. Based on experimental observations, it would expected that the Phe-Phe peptide should be more weakly bound to the surface than the Arg-Arg peptide, and that it would detach more readily. The opposite is observed where the Arg-Arg peptide detatches and is much more mobile than the Phe-Phe peptide. Additional simulations were performed with slightly modified initial positions, but no detachment event was observed for the Phe-Phe peptide. In fact, the amide carbonyl oxygen and the acid and amine charge groups on the peptides appeared to interact with the surface as strongly as the Cu_2O surface. This did not indicate additional affinity for the surface for the arginine containing peptides.

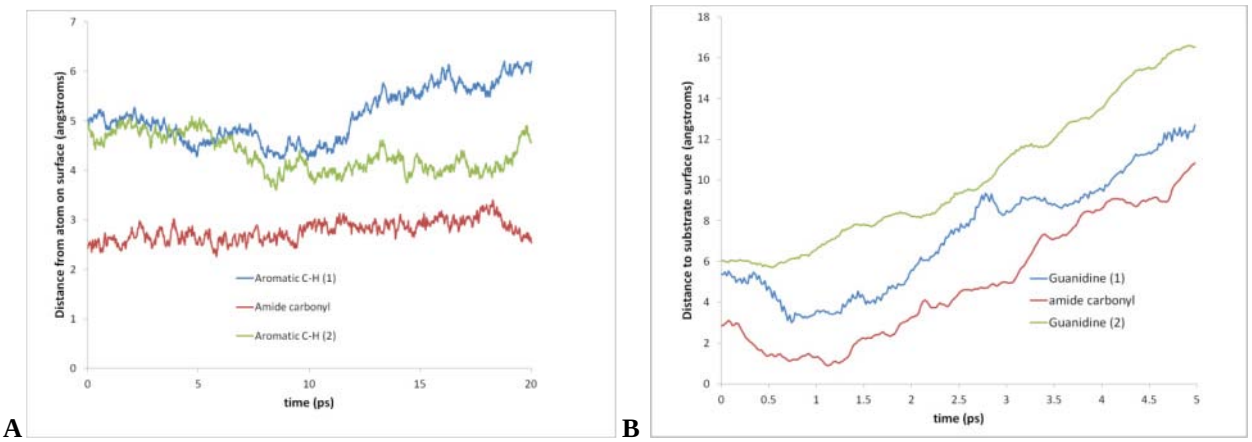

Figure 3. Plots of distance between points on the Cu_2O substrate and reference points on the A) Phe-Phe and B) Arg-Arg peptides. For Phe-Phe, the reference points were aromatic hydrogens at opposite ends of the molecule and the amide carbonyl oxygen at the midpoint of the molecule. For Arg-Arg, the reference points were the centers of the guanidine functional groups at either end of the molecule and the amide carbonyl at the midpoint of the molecule. The reference points on the Cu_2O surface were chosen based on closeness at the beginning of the simulation. As shown, only the Arg-Arg peptide actually detaches from the Cu_2O surface during a simulation.

Although the nearly neutral singly bound copper atoms are known to participate in many interactions on the Cu_2O surface, interaction with these metal atoms was not observed in these simulations. Yet these atoms have electrons with which to perform chemistry. Because classical MD were used, charge transfer or bond forming interactions are neglected. Since this Cu atom has a weak charge, the MD simulation almost completely neglects interaction with this atom because the simulation primarily considers electrostatic interactions as one of two primary nonbonding interactions. Thus the possibility of bond formation with the nearly neutral metal atom is ignored.

4. CONCLUSIONS

Classical MD simulations were performed for Glycine, Arginine, Phenylalanine, and two-mer and three-mer peptides of these residues acting on the (1,1,1) face of Cu_2O. It had been expected that the affinity of Arginine containing peptides could be explained by a complementary match between the geometry of partial atomic charges on the Arginine side chain and the nano-structured arrangements of negatively charged O and positively charged Cu atoms on the surface. Within the simulations performed here, no additional affinity for the surface is demonstrated by Arginine or its two-mers or three-mers in comparison to Phenylalanine, Glycine or their two-mers or three-mers. Given that the molecular geometry of Arginine does not enhance the binding of the partial atomic charges on its side chain to the Cu_2O substrate over the other peptides, the result strongly suggests that charge transfer or chemistry involving the singly bound Cu atom is a factor in the selective binding. This indicates that ab initio or Carr-Parrinello MD are necessary to fully account for the selectivity.

WORK CITED

[1] Sarikaya, M. et al. 2003. *Nature Mater.* 2577-585.
[2] Vallee, A. et al. 2010. *Accounts Chem. Res.* (10), 1297-1306.
[3] Thai, C. K.et al. 2004. *Biotech. Bioengin.* 87(2), 129-137.
[4] Choe, W. S. et al. 2007. *Langmuir* 23(23), 11347-11350.
[5] Le, M. et al. 2011. *J. Electrochem. Soc.* 158(5), E45-E49.
[6] Zhang, R. et al. 2011. *Appl. Surf. Sci.* 2574232-4238.

[7] Xu, C. et al. 2010. *J. Hazard. Mater.* 176(1-3), 807-813.
[8] Huang, L. et al. 2010. *Scripta Mater.* 63(2), 159-161.
[9] Cao, H. et al. 2010. *Chem.-Eur. J.* 16(34), 10553-10559.
[10] Minami, T. et al. 2011. *Appl. Phys. Express* 4(6).
[11] Septina, W. et al. 2011. *Electrochim. Acta* 56(13), 4882-4888.

Click chemistry on self-assembled monolayers (SAMs)

George Hondrogiannis, Stanley Ostazeski, and Erica Valdes
Edgewood Chemical Biological Center, Research & Technology Directorate, 5183 Blackhawk Rd., Aberdeen Proving Ground, MD 21010

1. INTRODUCTION

The purpose of this seedling proposal was to discover compatible organic reactions which can be performed on 1,7-dicarba-closo-dodecaborane m-9-carboranethiol (m-9-carboranethiol) SAMs leading to the introduction of any desired organic functionality to the surface. To this end, we wanted to develop a method to couple an azide functionalized building block to a gold thin film modified with an ethynyl terminated alkyl m-9-carboranethiol SAMs.

2. RESULTS AND DISCUSSION

The process of achieving these goals involved three steps. First, a gold thin film was modified with SAMs derived from m-9-carboranethiol. Second, the m-9-carboranethiol SAMs was functionalized with an ethynyl terminated moiety at both carbon atoms of the carborane cage via reaction with sec-butyl lithium, followed by propargyl bromide, and third CuAAC reaction of a wide variety of azide terminated molecular species with gold thin films coated with an ethynyl terminated m-9-carboranethiol SAMs.

This proposal addresses steps one and two above. During the first step, we attempted to achieve the packing of the gold thin film with m-9-carboranethiol. The coating of the gold thin films was accomplished by their immersion into a solution of 10 mmoles of m-9-carboranethiol in acetone for 12 hours and 48 hours, respectively. The gold thin films were then removed from solution and rinsed multiple times with reagent grade acetone, and dried under nitrogen. The progress of the reactions on the gold surfaces during steps one and two was followed by imaging the lateral distribution of the surface adsorbates using SEM and low voltage energy dispersive x-ray spectroscopy (EDS). In SEM materials contrast occurs, because different materials have different backscattered and secondary electron yields under primary electron bombardment. Thus morphology is indicated by secondary imaging while atomic number contrast is visible via backscattered imaging. Thus in backscatter Au appears brighter than B (boron) if the two materials are in the same field of view of the scanning microscope, since Au emits more secondary electrons than B. In addition to that, surface adsorbates are known to change the magnitude of the secondary electron yield from many materials by changing the sample potential of the material or by scattering the secondary electrons once they are emitted from the substrate.

In order to obtain a better understanding of the reactions steps, despite the fact that properties of SAMs on gold thin films are different from those in the bulk, the alkylation reactions of m-9-carboranethiol were also attempted on the bulk solid under identical conditions and in parallel to those on the thin films. Thus, the reactivity of the bulk solid was studied by the reaction of m-9-carboranethiol anion (generated by a 10 molar excess of sec-butyl lithium at -5°C under nitrogen) with an equivalent amount of propargyl bromide. This reaction was allowed to stir at 25°C for 12 hours. Analysis of the crude products by GC-MS and NMR spectroscopy showed that the m-9-carboranethiol was 99% alkylated at the sulfur atom and only 1% alkylated at the carbon atom of the carborane cage.

This finding is in accordance with the pKa value of 9.45 of the m-9-carboranethiol, compared with the pKa value of m-carborane of 27.9. The higher the pKa of the m-carborane indicates that it is the weaker acid. This is in agreement with the reactivity of alkylthiol SAMs which attach to gold thin films through the acidic thiol groups.

From these experiments it can be concluded that at least in the bulk the alkylation of the m-9-carboranethiol carbon bonds does not occur at room temperature even under excess of reagents, and long reaction times.

The alkylation of the SAMs of m-9-carboranethiol gold thin films was carried out as follows; the SAMs were first treated with sec-butyl lithium in cyclohexane at -5°C, and then allowed to react for 3 hours at 25°C. The excess of sec-butyl lithium was removed under nitrogen and the gold thin films were treated with excess propargyl bromide for 12 hours at 25°C. The gold films were removed from solution, washed with reagent acetone and dried under nitrogen. The films were then analyzed by SEM and EDS.

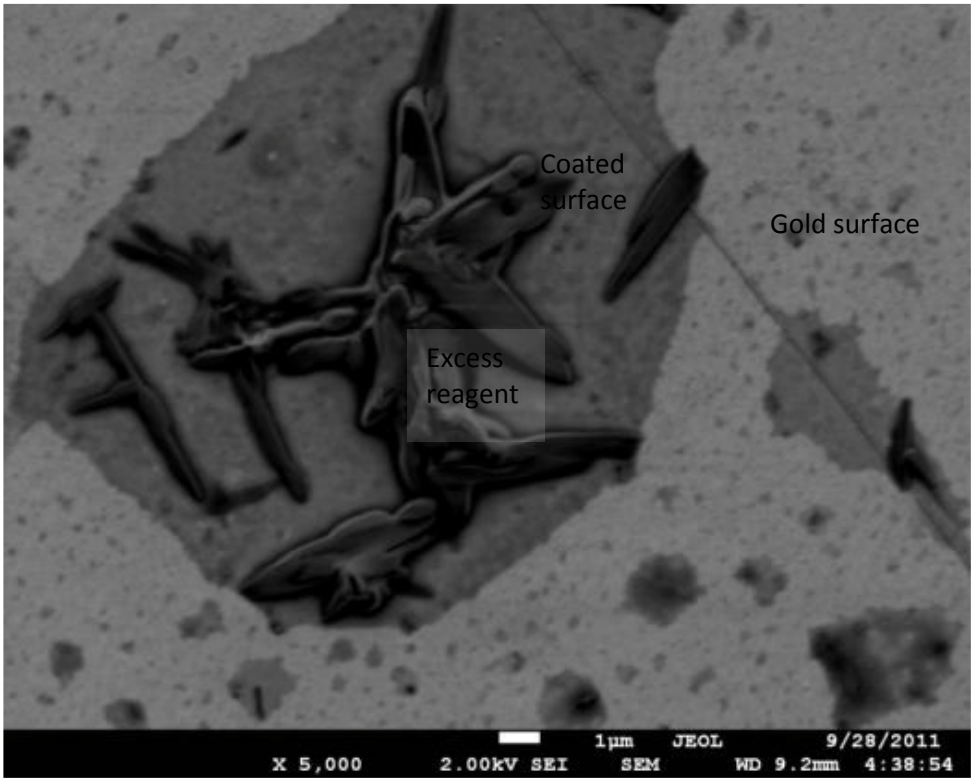

Figure 1. SEM photomicrograph of gold surface following treatment with excess propargyl bromide.

One major limitation encountered in the direct chemical transformation of the alkylthiolate SAMs is the thermal instability of the bond between the gold and thiol substrates. This dictates that all chemical reactions performed with alkylthiols attached to gold surfaces should be done at temperatures of 60°C or less. The carborane molecules exhibit extraordinarily high stability towards heating—up to 400°C unaffected. Therefore, it was reasonable to expect that some of their thermal stability would stabilize the gold-thiol bond; however, during the alkylation of the SAMs of m-9-carboranethiols on gold films at 70°C the solution turned gold-orange, and the gold thin films showed significant loss of gold coating. The reaction was then stopped after an hour. After cooling, the gold films were removed from the solution, washed, dried, and examined by SEM.

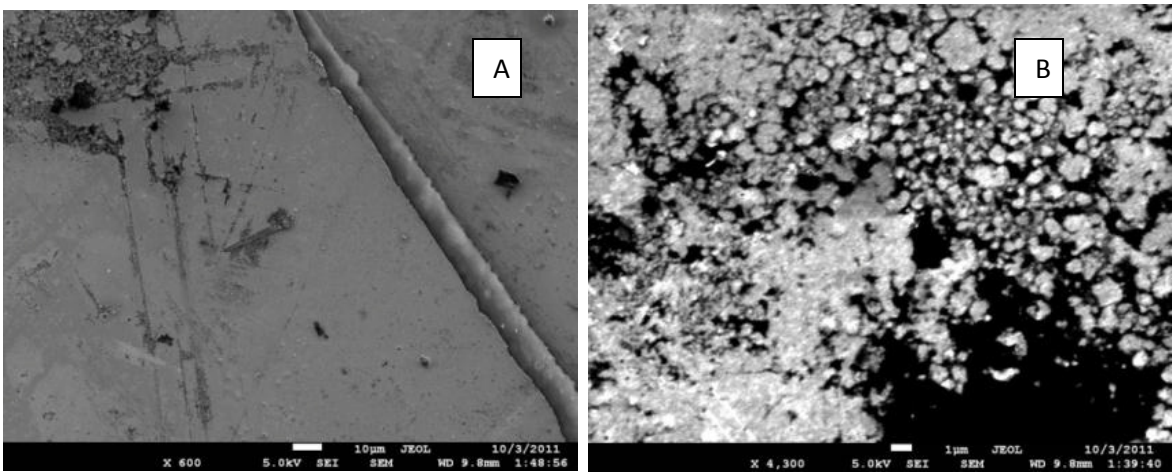

Figure 2. SEM photomicrographs of the surfaces after alkylation of the SAMs of m-9-carboranethiols on gold films at 70°C (A and B above) and EDS elemental maps and spatially specific spectra (C through J below).

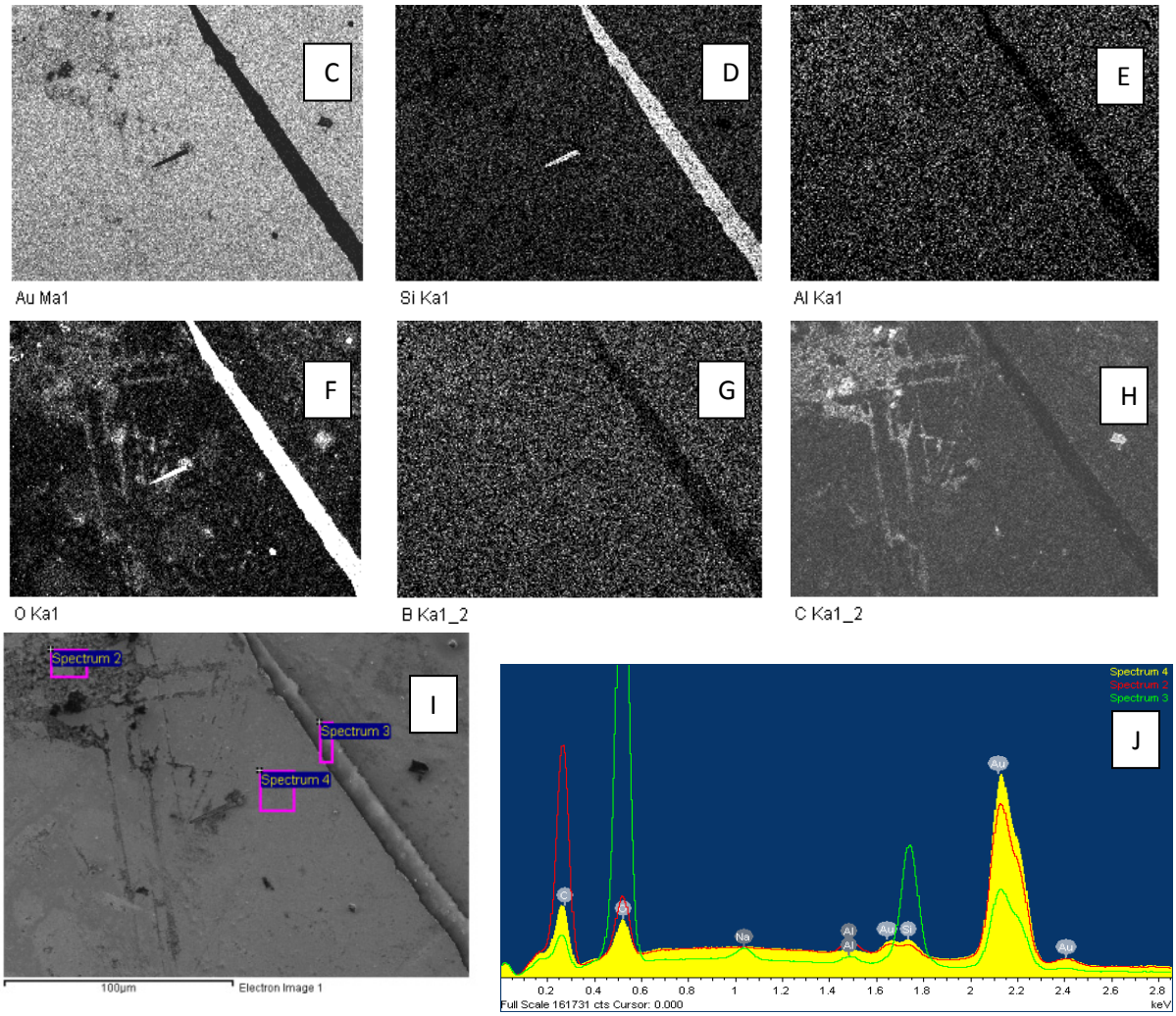

The reaction was then repeated in the bulk solid under identical conditions. Analysis of the crude products by GC/MS and NMR spectroscopy gave the following product distribution: 1.7% m-9-carboranethiol,

68.4% sulfur-alkylated m-9-carborane sulfide, 28.8% sulfur and one carborane carbon di-alkylated m-9-carborane sulfide, and only 1.1% of sulfur and both carborane carbons tri-alkylated m-9-carborane sulfide. These results, therefore suggest that in the bulk solid the desired tri-alkylated product does not form readily, and it requires longer reaction times and higher temperatures. Unfortunately, as it was observed before, these conditions are not compatible with the SAMs of m-9-carboranethiols on gold thin films.

3. CONCLUSION

In conclusion, we have gathered evidence by SEM and EDS that the modification of the surfaces of gold nanoparticles can be accomplished by chemisorption of m-9-carboranethiol from a solution in acetone at room temperature. At higher temperatures SEM seem to suggest an interesting observation consisting of the incorporation of the carborane cage into the gold metal core as well as on its surface. At the present time, the SEM and EDS data are not conclusive as to the success of the direct alkylation of the chemisorbed m-9-carboranethiol by propargyl bromide.

AFM data (when operational) to be collected in the future from samples obtained in this study will assist in the determination of the extent and nature of the direct alkylation reaction. Bulk results suggest that such reactions are feasible provided that sufficient heat and reaction times are allowed. These conditions (heat) however, are generally not compatible with the properties of SAMs. It should be reminded however, that the properties of compounds confined to a surface are significantly different from that in bulk.

REFERENCES

- Nuzzo, R. G. et al. 1987. *J. Am. Chem. Soc*. 109, 733–740.
- Poirier, G. E. 1997. *Chem. Rev.* 97, 1117–1127.
- Poirier, G. E. and Tarlov, M. J. 1994. *Langmuir* 10, 2853–2856.
- Poirier, G. E. et al. 1994. *Langmuir* 10, 3383–3386.
- Ulman, A. et al. 1989. *Langmuir* 5, 1147–1152.
- Ulman, A. 1996. *Chem. Rev.* 96, 1533–1554.
- Evans, S. D. et al. 1991. *J. Am. Chem. Soc*. 113, 4121–4131.
- Nuzzo, R. G. et al. 1990. *J. Chem. Phys*. 93, 767–773.
- Edinger, K. et al. 1993. *Langmuir* 9, 4–8.
- Poirier, G. E. and Pylant, E. D. 1996. *Science* 272, 1145–1148.
- Ogawa, H. et al. 1999. *Jpn. J. Appl. Phys.* 2 38, 6019–6023.
- Noh, J. and Hara, M. 2002. *Langmuir* 18, 1953–1956.
- Dameron, A. A. et al. 2005. *J. Am. Chem. Soc.* 127, 8697–8704.
- Yang, G. H. et al. 2000. *J. Phys. Chem. B* 104, 9059–9062.
- Ishida, T. et al. 2000. *J. Phys. Chem. B* 104, 11680–11688.
- Dhirani, A. A. et al. 1996. *J. Am. Chem. Soc.* 118, 3319–3320.
- Collman, J. P. et al. 2006. *Langmuir* 22, 2457–2464.
- Plesek, J. and Hermanek, S. 1977. *Bull. Acad. Sci. USSR, Div. Chem. Sci.* 36, 2227.
- Basˇe, T. et al. 2005. *Langmuir* 21, 7776–7785.
- Knyazev, S. P. et al. 2006. *Russ. Chem. Bull*. 55, 2154–2160.